POLISH ACADEMY OF SCIENCES
ELECTRICAL ENGINEERING COMMITTEE

ARCHIVES OF ELECTRICAL ENGINEERING

Volume 66(260) • 2/2017

QUARTERLY JOURNAL

www.aee.put.poznan.pl
www.degruyter.com/view/j/aee

POZNAŃ 2017

www.aee.put.poznan.pl
www.degruyter.com/view/j/aee

ISSN 1427-4221
eISSN 2300-2506

Edition co-sponsored by
Polish Academy of Sciences

EDITORIAL OFFICE

Archives of Electrical Engineering
Piotrowo 3A (room: 612X)
60-965 Poznań, Poland
tel.: +48 616652636, *fax*: +48 616652381
e-mail: aee@put.poznan.pl

Centrum Poligrafii Sp. z o.o.
ul. Łopuszańska 53
02-232 Warszawa

Printed in Poland

Contents

ARCHIVES OF ELECTRICAL ENGINEERING VOL. 66(2), pp. 229-239 (2017)

DOI 10.1515/aee-2017-0017

Finite-time integral sliding mode control for chaotic permanent magnet synchronous motor systems

ABDELILAH CHIBANI, BACHIR DAAOU, ABDELMADJID GOUICHICHE, AHMED SAFA, YOUCEF MESSLEM

Laboratoire de Génie Electrique et des Plasmas
LGEP, Université Ibn Khaldoun, Tiaret, Algérie
e-mail: abdelilah.chibani@gmail.com

(Received: 11.02.2016, revised: 17.08.2016)

Abstract: In this paper, an integral finite-time sliding mode control scheme is presented for controlling a chaotic permanent magnet synchronous motor (PMSM). The controller can stabilize the system output tracking error to zero in a finite time. Using Lyapunov's stability theory, the stability of the proposed scheme is verified. Numerical simulation results are presented to present the effectiveness of the proposed approach.

Key words: chaos control, control chaotic Permanent Magnet Synchronous Motor, finite-time, sliding mode

1. Introduction

A permanent magnet synchronous motor (PMSM) plays an important role in industrial applications due to its simple structure, high power density, low maintenance cost, and high efficiency [1-4]. However, investigations show that PMSM displays chaotic behavior when motor parameters lie in a certain range [3, 4]. Chaos in PMSM, which decreases the system performance, is highly undesirable in most engineering applications.

Several researchers have investigated the problem of control chaos in PMSM [5-16]. Decoupling control [5], entrainment and migration control [6], optimal Lyapunov exponents placement [7], sensorless control [8-10], time delay feedback control [11], feedback control [12], backstepping control [13], passivity control [14], sliding mode control [15], and fuzzy control [16, 17]. During the last three decades, variable structure systems (VSS) and sliding mode control (SMC) have received significant interest and have become well-established research areas with great potential for practical applications. The theoretical development aspects of SMC are well documented in many books and articles [7, 16, 20, 25, 27, 29, 31].

The principle of the sliding mode control is to forcibly constrain the system [18, 19, 21], by suitable control strategy, to stay on the sliding surface on which the system will exhibit

desirable features [24, 26, 28]. The advantages of SMC are robustness, computation speed, compact implementation, controller order reduction, disturbance rejection, and insensitivity to parameter variations. The main disadvantage of the SMC strategy is the chattering phenomenon. SMC has been applied in many control fields which include robot control [30], motor control [5, 22], flight control [23], control of power systems [9, 30, 32, 33], and chemical process control [4].

In this paper, an integral sliding mode control law is designed to achieve the finite-time chaos suppression for the permanent magnet synchronous motor system. The finite-time stability of the closed-loop system is proved using the Lyapunov theory.

This article is organized as follows: the dynamic model of PMSM is presented in Section 2; this model is normalized so that PMSM exhibits chaotic behavior under certain conditions. Section 3 describes in detail the proposed approach design and verifies the stability of the controller according to Lyapunov stability. Effectiveness of the proposed schemes is demonstrated by simulation in Section 4. Finally, the conclusion is given in Section 5.

2. Modeling of permanent-magnet synchronous motor (PMSM)

The mathematical model of PMSM [3] is given by:

$$\begin{cases} \dfrac{\mathrm{d}\,\omega}{\mathrm{d}\,t} = \dfrac{1}{J}\left(n_d\ \psi\ i_q + n_p(L_d - L_q) i_d\, i_q - T_L - \beta\omega\right), \\ \dfrac{\mathrm{d}\,i_q}{\mathrm{d}\,t} = \dfrac{1}{L_q}\left(u_q - R\, i_d - \omega L_d i_d - \omega\psi_r\right), \\ \dfrac{\mathrm{d}\,i_d}{\mathrm{d}\,t} = \dfrac{1}{L_d}\left(u_d - R\, i_d + \omega L_q i_q\right), \end{cases} \tag{1}$$

where i_q, i_d and u_d, u_q are three d-axis and q-axis stator currents and voltage L_q, L_d are q-axis stator inductances, R corresponds to the stator resistor. J is the polar moment of inertia; β is the viscous friction constant, ψ_r is the rotor magnetic flux linking the stator and n_p is the number of pole-pairs, T_L represents the external load torque and ω corresponds to the rotor angular velocity.

By employing an affine transformation $(.) = \lambda^{-1}(.)$ and a time-scaling transformation,

$$t = \frac{R}{L_q} t', \text{ where } \boldsymbol{\lambda} = \begin{bmatrix} \boldsymbol{\tau k} & \mathbf{0} & \mathbf{0} \\ \mathbf{0} & \mathbf{k} & \mathbf{0} \\ \mathbf{0} & \mathbf{0} & \mathbf{R/L_q} \end{bmatrix}, \quad \tau = \frac{L_d}{L_q}, \quad k = \frac{\beta R}{L_q n_p \psi_r}, \quad \gamma = \frac{\psi_r}{k L_q}, \quad \sigma = \frac{\beta L_q}{LJ}.$$

Then system (1) can be transformed to the following form, which is more suited for control-design purpose:

$$\begin{cases} \dfrac{\mathrm{d}\omega}{\mathrm{d}t} = \sigma(i_q - \omega) - T_L, \\ \dfrac{\mathrm{d}i_q}{\mathrm{d}t} = -i_q - i_d\omega + \gamma\omega + u_q, \\ \dfrac{\mathrm{d}i_d}{\mathrm{d}t} = -i_d + i_q\omega + u_d, \end{cases} \tag{2}$$

where ω is the angle speed, i_q and i_d denote the quadrature and the direct-axis currents of the motor, respectively σ and γ are the system parameters, T_L is the load torque, u_q and u_d are the quadrature and direct-axis stator voltage components, respectively. In our paper, we only take the case $u_q = u_d = 0$ then, system (2) becomes:

$$\begin{cases} \dfrac{\mathrm{d}\omega}{\mathrm{d}t} = \sigma(i_q - \omega), \\ \dfrac{\mathrm{d}i_q}{\mathrm{d}t} = -i_q - i_d\omega + \gamma\omega, \\ \dfrac{\mathrm{d}i_d}{\mathrm{d}t} = -i_d + i_q\omega. \end{cases} \tag{3}$$

Fig. 1 and Fig. 2 illustrate the typical chaotic attractor's behavior of PMSM for a certain range of its parameters. In our paper we choose the case of $(\sigma, \gamma) = (5.45,\ 20)$ and initial condition. $\omega(0) = 0.5$, $i_q(0) = 0.6$, $i_d(0) = 0.5$.

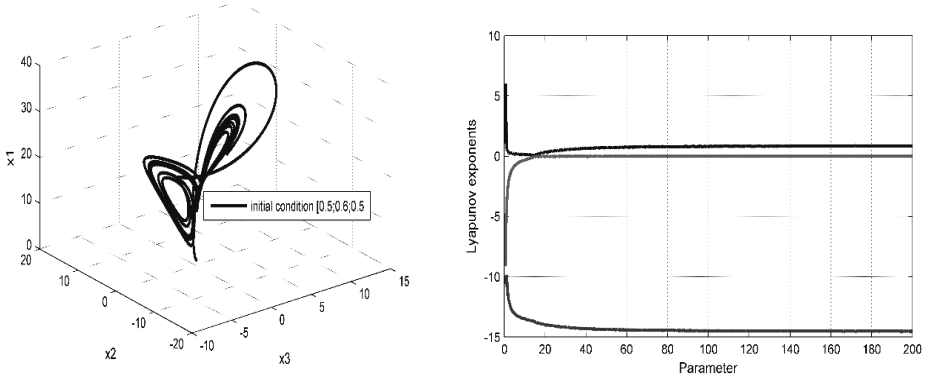

Fig. 1. Characterizations of chaos in PMSM: (a) chaotic attractor; (b) lyapunov exponent

3. Integral terminal sliding mode control for PMSM

Consider a nonlinear system as follows:

$$\dot{x} = f(x) + g(x)u, \tag{4}$$

where $x \in R$, $f(x) \in R$, $g(x) \in R$ and $g^{-1}(x) \neq 0 \in R$.

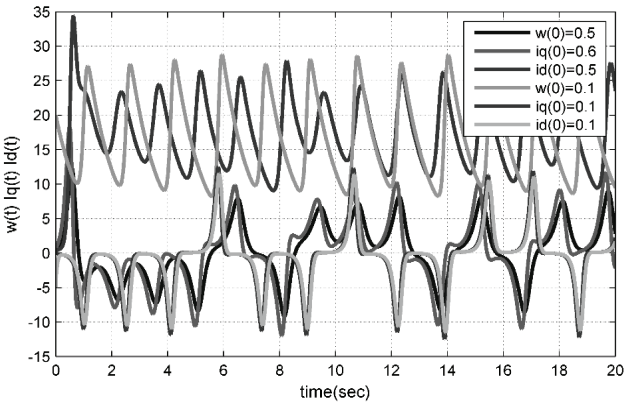

Fig. 2. Time response of the state of PMSM for two initial conditions (0.5, 0.6, 0.5)-(0.1, 0.1, 0.1)

Let us introduce a sliding variable:

$$S = x + \theta x_1 , \tag{5}$$

$$\dot{x}_1 = \operatorname{sgn}(x) \text{ with } x_1(0) = -\frac{x(0)}{\theta} , \text{ where } \theta > 0 .$$

According to [20], x will be always kept on S. If we guarantee that the surface S is always zero then x will converge to zero in a finite time.

Let (ω^r, i_q^r, i_d^r) denotes an equilibrium point (ω^r, i_q^r, i_d^r). The aim of this paper is to design a controller that stabilizes the system (3) to the equilibrium point and guarantees chaos suppression. We add the single control $u(t)$ to system (3) and then the controlled PMSM system can be expressed by:

$$\begin{cases} \dfrac{\mathrm{d}\omega}{\mathrm{d}t} = \sigma(i_q - \omega), \\ \dfrac{\mathrm{d}i_q}{\mathrm{d}t} = -i_q - i_d\omega + \gamma\omega + u, \\ \dfrac{\mathrm{d}i_d}{\mathrm{d}t} = -i_d + i_q\omega. \end{cases} \tag{6}$$

Let the error states of system be:

$$e_1 = \omega^r - \omega, \quad e_2 = i_q^r - i_q \text{ and } e_3 = i_d^r - i_d .$$

Then dynamical system can be expressed as:

$$\begin{cases} \dot{e}_1 = \sigma(e_2 - e_1), \\ \dot{e}_2 = -(e_1 e_2 + \omega e_3 + i_d e_1) \ - e_2 + \gamma e_1 + u, \\ \dot{e}_3 = e_1 e_3 + \omega e_2 + i_q e_1 - e_3 . \end{cases} \tag{7}$$

A suitable sliding surface can be chosen as:

$$S = e_2 + \theta e_{2I}, \tag{8}$$

$\dot{e}_{2I} = \text{sgn}(e_2)$ with $e_{2I}(0) = -\dfrac{e_2(0)}{\theta}$.

If e_2 reaches S it will converge to zero in a finite time $T_S = \dfrac{|e_2(0)|}{\theta}$.

The time derivative of S is

$$\dot{S} = \dot{e}_2 + \theta \,\text{sgn}(e_2). \tag{9}$$

By letting $S = 0$, one can get the equivalent control as:

$$u_{eq} = e_1 e_3 + \omega e_3 + i_d e_1 + e_2 - \gamma e_1 - \theta \,\text{sgn}(e_2). \tag{10}$$

The reaching control is selected as follows:

$$u_{rech} = -\mu \,\text{sgn}(S), \tag{11}$$

where $\mu > 0$ is a positive number.

The sliding mode controller law is designed as:

$$u = u_{eq} + u_{rech}. \tag{12}$$

Theorem

Consider dynamic error system (7).The integral sliding mode controller (12) yields convergence of e_2 and $\dot{e}_2$ to 0 in a finite time, and the errors e_1 and e_3 are globally asymptotically stable at (0, 0).

Proof

Let the Lyapunov function $V(S)$ be defined by:

$$V(S) = \frac{1}{2} S^2. \tag{13}$$

The time derivative of this function with respect to time along (7):

$$\dot{V}(S) = S\dot{S}, \tag{14}$$

$$\dot{V}(S) = S(-(e_1 e_3 + \omega e_3 + i_d e_1) - e_2 + \gamma e_1 + \theta \,\text{sgn}(e_2) + u). \tag{15}$$

Substituting (12) into (15) gives:

$$\dot{V}(S) = -\mu |S|. \tag{16}$$

According to the sliding condition [20], e_2 and $\dot{e}_2$ converge to zero in a finite time. After e_2 has converged to 0, the dynamical errors e_1 and e_3 can be written as:

$$\begin{cases} \dot{e}_1 = -\sigma e_1, \\ \dot{e}_3 = i_q e_1 - e_3. \end{cases} \tag{17}$$

If the candidate Lyapunov function is defined as:

$$V(e) = \frac{1}{2}(e_1^2 + e_3^2), \tag{18}$$

then the time derivative of $V(e)$ is:

$$\dot{V}(e) = e_1\dot{e}_1 + e_3\dot{e}_3, \tag{19}$$

$$\dot{V}(e) = -\sigma e_1^2 - e_3^2 + i_q e_1 e_3. \tag{20}$$

Inequality (21) can be rewritten as:

$$\dot{V}(e) = -e^T \Gamma e \ < 0, \tag{21}$$

with $e = [\boldsymbol{e_1} \ \ \boldsymbol{e_3}]^T$ and $\Gamma = \begin{bmatrix} \boldsymbol{\sigma} & \boldsymbol{0} \\ -\boldsymbol{i_q} & \boldsymbol{1} \end{bmatrix} > 0 \ \ (\sigma > 0)$.

4. Simulation results

Simulations, using MATLAB Software Package, are carried out to verify the effectiveness of the proposed method. The parametric values of PMSM are the same as those in Section 3. Without loss of generality, we select $(\omega^r, i_q^r, i_d^r) = (0, 0, 0)$ as the desired equilibrium point. The control method takes effect after $t = 4.5$ s. Fig. 3 shows the dynamic error system states of PMSM and the manipulated signals u.

From the results, it can be seen that the proposed integral sliding mode controller structure shows good performance in achieving the output regulation.

Next, we examine the robustness of the proposed controllers in the presence of the model uncertainty and external disturbances. Fig. 4 shows the performances of controllers for 40% increase in the parameters and external disturbance were added to PMSM: omiga 1 = $= 0.2\cos(0.3t)$, $omiga\ 2 = 0.3\cos(0.4t)$, $omiga\ 3 = 0.6\cos(0.6t)$. Therefore, it can be concluded that the proposed control schemes are robust to changes in the parameters and to disturbances acting on the system.

Finally, we examine the robustness of the proposed controllers in the presence of the measurement noise. In this case, white Gaussian noises with variances of 3% are simultaneously added to the outputs measurements. The system transient's responses for the controller and the control action are shown in Fig. 5.

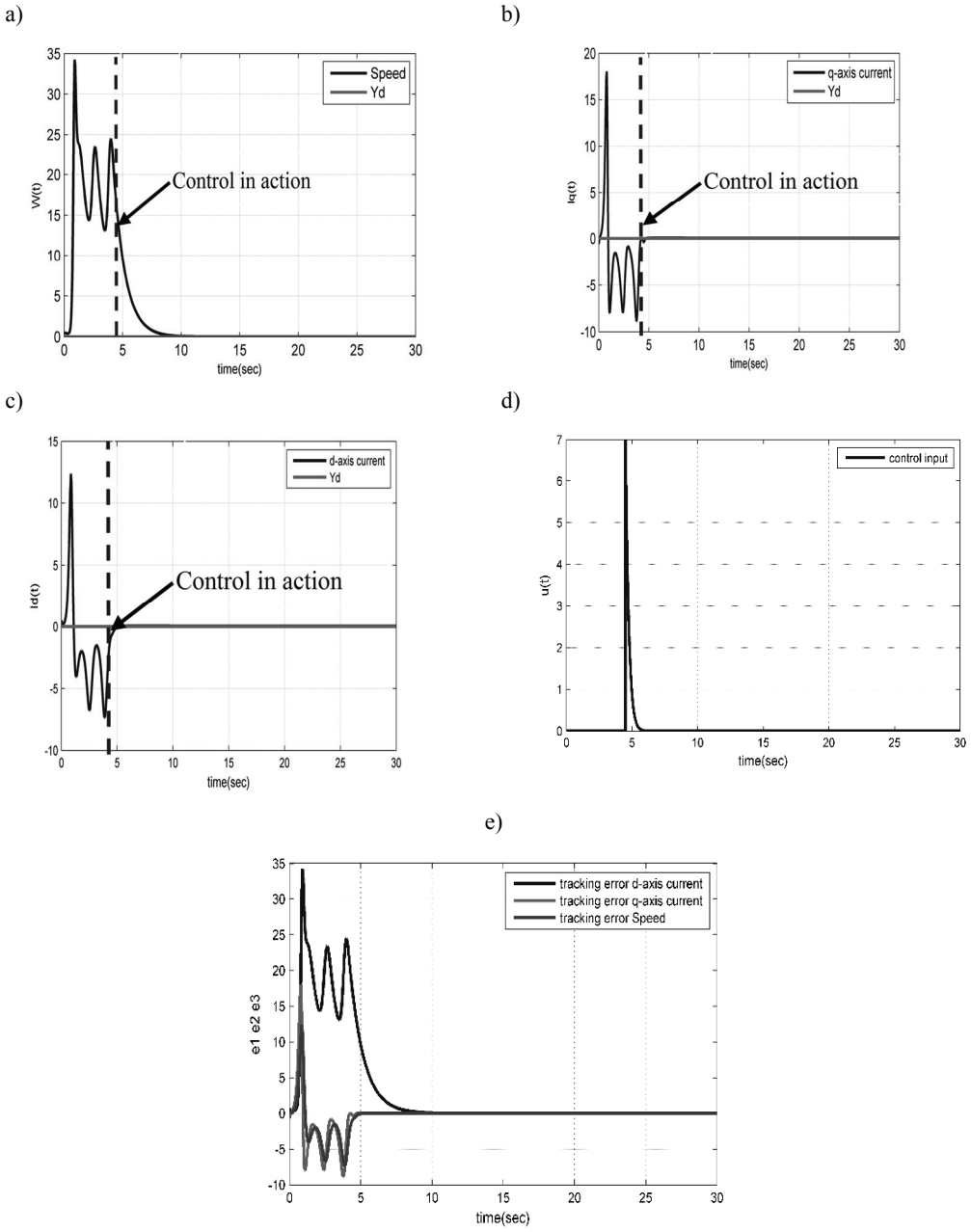

Fig. 3. System responses with the control in action at $t = 4.5$ s: (a) speed; (b) q-axis current; (c) d-axis current; (d) control input; (e) tracking error

It can be seen that the set-point tracking behavior is very satisfactory. Note that the proposed controller maintains the PMSM state in a small neighborhood of the desired value despite the noise on the measurement.

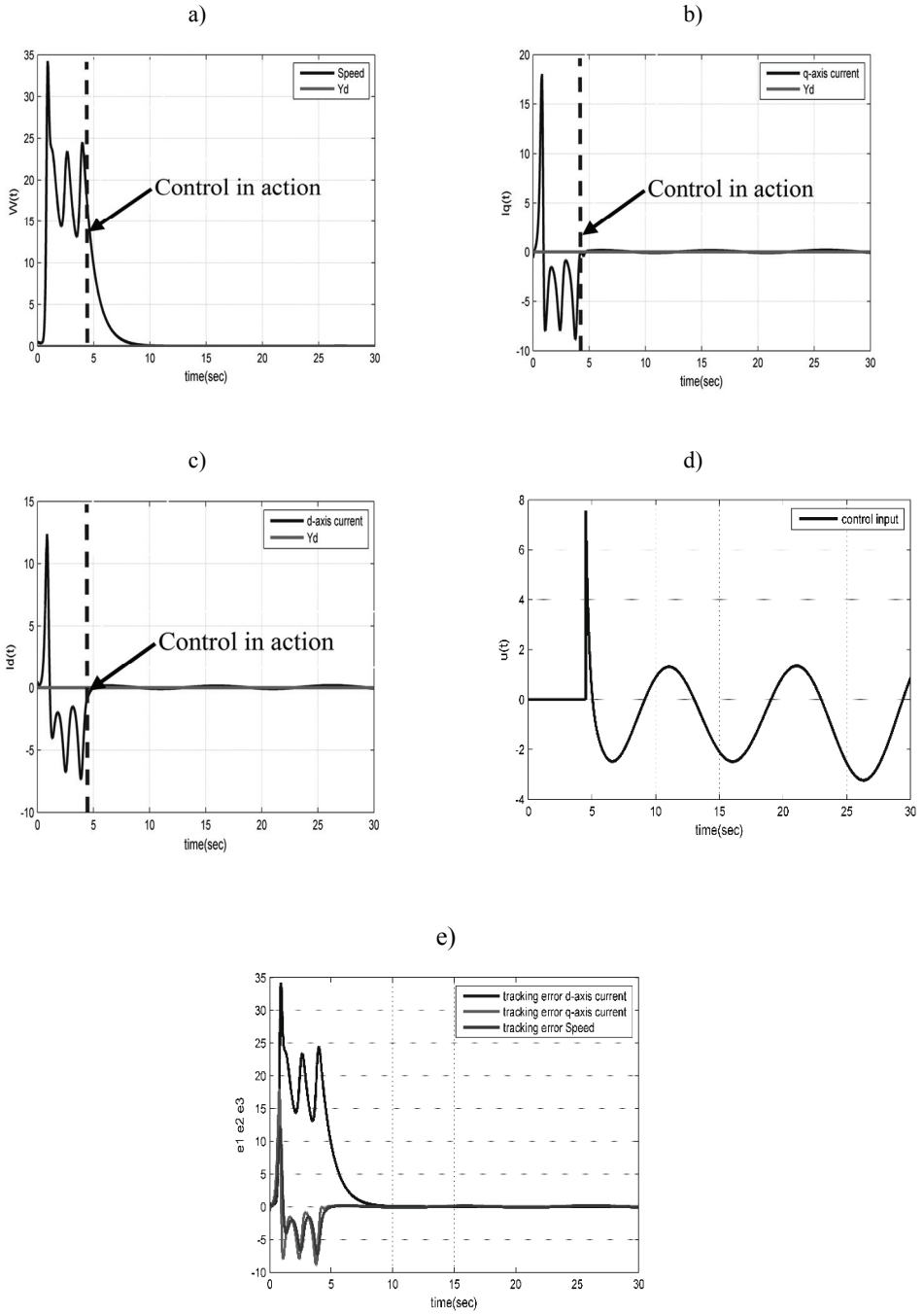

Fig. 4. System responses in the presence of the model uncertainty and external disturbances with the control in action at $t = 4.5$ s: (a) speed; (b) q-axis current; (c) d-axis current; (d) control input; (e) tracking ing error

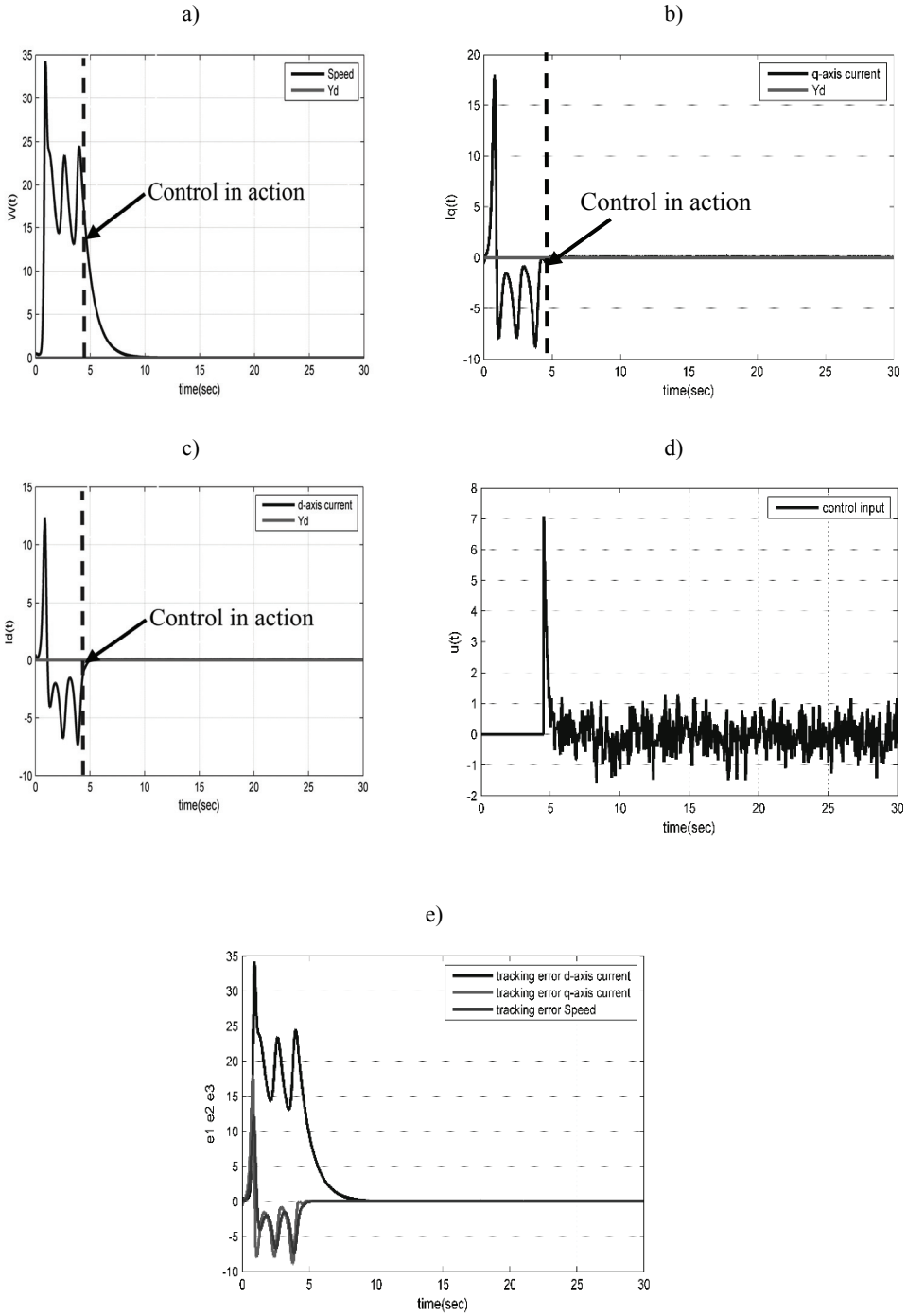

Fig. 5. System responses with the presence of the white noise with the control in action at $t = 4.5$ s: (a) speed; (b) q-axis current; (c) d-axis current; (d) control input; (e) tracking error

5. Conclusion

In this paper, we presented an integral finite-time sliding mode control scheme for a permanent-magnet synchronous motor. The closed-loop stability is proved. Through numerical simulations, we illustrated the feasibility of the designed control system. Moreover, the proposed control exhibits a satisfactory performance when used with disturbance and dynamics uncertainty.

References

[1] Babak N.M., Farid M.T., Sargos F.M., *Mechanical Sensorless Control of PMSM with Online Estimation of Stator Resistance*, IEEE Trans. Ind. Appl., vol. 40, no. 2, pp. 457-471 (2004).
[2] Bolognani S., Zigliotto M., Zordan M., *Extended-Range PMSM Sensorless Speed Drive Based on Stochastic Filtering*, IEEE Trans. Power Electron., vol. 16, no. 1, pp. 110-117 (2001).
[3] Li Z., Park J., Zhang B., Chen G., *Bifurcations and chaos in a permanent-magnet synchronous motor*, IEEE Trans. Circuits Syst.-I, vol. 49, no. 3, pp. 383-287 (2002).
[4] Jing Z., Yu C., Chen G., *Complex dynamics in a permanent-magnet synchronous motor model*, Chaos, Solitons and Fractals, no. 22, pp. 831-848 (2004).
[5] Li J., Ren H., *Partial decoupling control of chaos in permanent magnet synchronous motor*, Control Theory & Applications, vol. 22, no. 4, pp. 637-640 (2005).
[6] Zhang B., Zhong L., Zongyuan M., *Entrainment and Migration Control of Permanent-Magnet Synchronous Motor System*, Journal of Control Theory and Applications, vol. 19, no. 4, pp. 53-56 (2002).
[7] Ataei M., Kiyoumarsi A., Ghorbani B., *Control of chaos in permanent magnet synchronous motor by using optimal Lyapunov exponents placement*, Physics Letters, vol. 374, no. 41, pp. 4226-4230 (2010).
[8] Seok J.K., Lee J.K., Lee D.C., *Sensorless speed control of nonsalient permanent-magnet synchronous motors using rotor-position-tracking PI controller*, IEEE Trans. Ind. Appl., no. 53, pp. 399-405 (2006).
[9] Wallmark O., Harnefors L., *Sensorless control of salient PMSM drives in the transition region*, IEEE Trans. Ind. Appl., vol. 53, no. 4, pp. 1179-1187 (2006).
[10] Brock S., Pajchrowski T., *Sensorless and energy-efficient PMSM drive for fan application*, Arch. Electr. Eng., vol. 62, no. 2, pp. 217-225 (2013).
[11] Ren H.P., Liu D., Li J., *Delay feedback control of chaos in permanent magnet synchronous motor*, Proceedings of the CSEE, vol. 23, no. 6, pp. 175-178 (2003).
[12] Ren H.P., D Liu., *Nonlinear feedback control of chaos in permanent magnet synchronous motor*, IEEE Trans. Circuits Syst.-II., vol. 53, no. 1, pp. 45-50 (2006).
[13] Hu J., Zou J., *Adaptive backstepping control of permanent magnet synchronous motors with parameter uncertainties*, Control and Decision, vol. 21, no. 11, pp. 1264-1269 (2006).
[14] Wu Z.Q., Tan F.X., *Passivity control of permanent magnet synchronous motor chaotic systems*, Proceedings of the CSEE, vol. 26, no. 18, pp 159-163 (2006).
[15] Huang C.F., Liao T.L, Chen C.Y, Yan J.J., *The design of quasi-sliding mode control for a permanent magnet synchronous motor with unmatched uncertainties*, Comp. Math. Appl., vol. 64, no. 5, pp. 1036-1043 (2012).
[16] Wu Z.Q., *Optimal fuzzy guaranteed cost control for nonlinear system and its application in permanent magnet synchronous motor chaos system*, Proceedings of the CSEE, vol. 23, no. 9, pp. 152-157 (2006).
[17] Li D., Zhang X.H., Yang D., Wang S.L., *Fuzzy control of chaos in permanent magnet synchronous motor with parameter uncertainties*, Acta Phy. Sin., vol. 58, no.3, pp. 1432-1440 (2009).
[18] Bartolini G., Zolezzi T., *Variable structure systems nonlinear in the control law*, IEEE Trans. Autom. Control, vol. 30, Issue 7, pp. 681-684 (1985).

[19] Decarlo R.A., Zak S.H, Matthews G.P., *Variable structure control of nonlinear multivariable systems: a tutorial*, Proceedings of the IEEE, vol. 76, no. 3, pp. 212-232 (1988).
[20] Utkin V.I., *Sliding modes in control and optimization*, Springer-Verlag, Berlin (1992).
[21] Hung J.Y., Gao W., Hung J.C., *Variable structure control: a survey*, IEEE Trans. Ind. Electron., vol. 40, no. 1, pp. 2-22 (1993).
[22] Zinober A.S.I., *Variable structure and Lyapunov control*, Springer-Verlag, Berlin (1994).
[23] Young K.D., Utkin V.I., Ozguner U., *A control engineer's guide to sliding mode control*, IEEE Trans. Control Syst. Technol., vol. 7, no. 3, pp. 328-342, (1999).
[24] Koshkouei A.J., Zinober A.S.I., *Robust frequency shaping sliding mode control*, IEE Proceedings - Control Theory Appl., vol. 147, no. 3, pp. 312-320 (2000).
[25] Sira-Ramirez H., Ahmad S., Zribi M., *Dynamical feedback control of robotic manipulators with joint flexibility*, IEEE Trans. Syst. Man Cybern., vol. 22, no. 4, pp. 736-747 (1992).
[26] Zribi M., Sira-Ramirez H., Ngai A., *Static and dynamic sliding mode control schemes for a permanent magnet stepper motor*, International Journal of Control, vol. 74, pp. 103-117 (2001).
[27] Alrifai M.T., Zribi M., Sira-Ramirez H., *Static and dynamic sliding mode control of variable reluctance motors*, International Journal of Control, vol. 77, pp. 1171-1188 (2004).
[28] Sira-Ramirez H., Zribi M., Ahmad S., *Dynamical sliding mode control approach for vertical flight regulation in helicopters*, IEE Proceedings – Control Theory Appl., vol. 141, pp. 19-24 (1994).
[29] Bengiamin N.N., Chan W.C., *Variable structure control of electric power generation*, IEEE Trans. Power Apparatus Syst., vol. 101, pp. 376-380 (1982).
[30] Shtessel Y., Zinober A.S.I., Shkolnikov I., *Sliding mode control of boost and buck-boost power converters using the dynamic sliding manifold*, Int. J. Robust Nonlinear Control, vol. 13, pp. 1285-1298 (2003).
[31] Aguilar R., Martinez-Guerra R., Maya-Yescas R., *Temperature Regulation via PI High-Order Sliding-Mode Controller Design: Application to a Class of Chemical Reactor*, International Journal of Chemical Reactor Engineering, vol. 7 (2009).
[32] Baba M., Lascu C., Boldea I., Blaabjerg F., *Parallel and series 4 switch Z-source converters in induction motor drives*, in Proceedings of the International Conference on Optimization of Electrical and Electronic Equipments, Optim (2014).
[33] Lascu C., Blaabjerg F., *Super-twisting sliding mode direct torque control of induction machine drives*, IEEE Energy Conversion Congress and Exposition ECCE, 2014, pp. 5116-5122 (2014).

ARCHIVES OF ELECTRICAL ENGINEERING VOL. 66(2), pp. 241-251 (2017)

DOI 10.1515/aee-2017-0018

A control strategy of hybrid solar-wind energy generation system

HIMANSHU SHARMA, NITAI PAL, PANKAJ KUMAR, ASHIWANI YADAV

Department of Electrical Engineering, IIT (ISM)
Dhanbad, Jharkhand, India, 826004
e-mail:himanshu26sharma@gmail.com

(Received: 17.04.2016, revised: 11.10.2016)

Abstract: Synchronization in the energy generated by renewable energy sources is one of the significant issue associated with the converter used in the system module. The presented paper concentrates on the design aspect of a PV and wind power input to a DC-DC converter which can be practically useful in hybrid renewable energy power systems. In this regard, the proposed converter can be utilized to obtain a smooth regulated output voltage from the given input renewable energy power sources. The proposed converter can be efficiently work under critical conditions having very few ripple in current waveform of input or output. A major advantage with this type of converter is the simple circuit with respect to the conventional converters in some critical situations. At the end, the result based on the simulation exercise and various experiments, performance of the converter in different situations is presented so that the efficiency of the designed converter arrangement is accepted.

Key words: distributed PV/wind power system, double-input DC-DC converter, multi-variable controller, voltage regulation

1. Introduction

A hybrid system can be defined as an electrical system having one or more energy sources along with at least one source as renewable energy source. Wind energy as well as solar energy using a photovoltaic array are two major environmentally friendly sources of energy [1]. There are mainly two types of hybrid systems, one is grid connected and the other one is in standalone mode [2, 3]. The hybrid photovoltaic (PV) and wind turbine system (WT) can be mainly applied in the systems like water pumping, domestic as well as street lighting, surface mine lighting, various vehicle applications etc.

The projected hybrid structure comprises of one wind blade, one fluctuating speed wind alternator, an AC/DC converter attached to the wind side, a PV module, a DC/DC chopper, a DC/DC converter to get the controlled DC output with a desired voltage level and a DC/AC converter is used to get the controlled output AC voltage as required by the load as shown in Fig. 1 [4, 5].

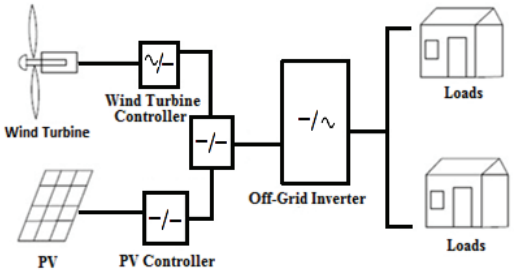

Fig. 1. Hybrid generation system model

A typical DC capacitor is also attached in addition to an applied load to suppress the harmonics. From a common DC line, a parallel connection is provided for two power sources [6].

2. Operation principle of designed converter

In this survey, the principle is to synthesize different DC/DC converters to create MIC. Two Cuk converters have been used for the structure of the given converter. The circuit diagram of this converter is given in Fig. 2. It includes two DC input sources (V_1, V_1).

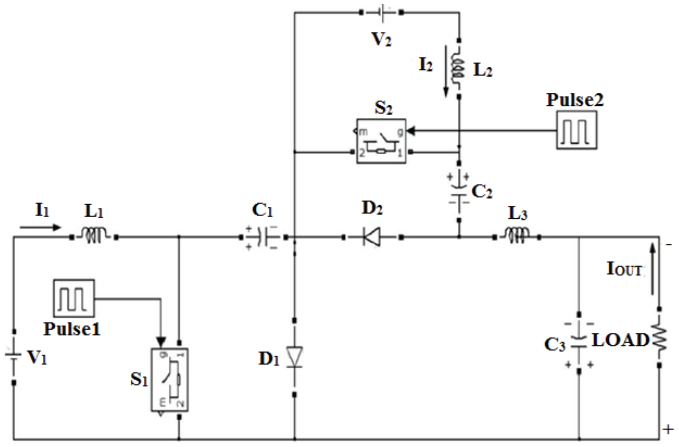

Fig. 2. Designed circuit of proposed converter

The bypass path for the inductors L_1 and L_2 currents to flow continuously is provided by power diode D_1 and D_2. The projected dual input DC-DC converter can take power from two voltage sources separately or simultaneously, by applying an appropriate control scheme to the pulse generator of the power switches S_1 and S_2. On the other hand, based on the control scheme and input sources, the output voltage can be regulated at the reference value [7]. The energy transfer elements are capacitors C_1 and C_2. The duty of capacitor C_3 is to eliminate the ripple of the output voltage like in the conventional converters.

It has four modes of operation, which are categorized with respect to the status of the power switches (S_1 and S_2):

Mode I (S_1 ON and S_2 ON): in this mode, the input voltage sources V_1(Solar) [8] and V_1(Wind) charge the input inductors L_1 and L_2 and at the same time, C_1 and C_2 discharge and supply energy to the output load [9]. Since, S_1 and S_2 are conducting, power diodes D_1 and D_2 are reversed biased and should be considered as an open circuit (OC).

Mode II (S_1 ON and S_2 OFF): in this mode, the power diode D_1 is reversed biased, thus, operates as an open circuit and D_2 is forward biased and acts as a short circuit (SC). During operation, V_1 charges the inductor L_1 and V_1 charges capacitor C_2. The inductor L_2 releases its energy to the capacitor C_2.

Mode III (S_1 OFF and S_2 ON): here, D_1 is forward biased and conducts, whereas the D_2 is reversed biased, so it is blocked. In this mode, V_1 and L_1 charges the capacitor C_1. Similarly, inductor L_2 is charged by voltage produced by V_1. Capacitor C_2 is discharged to provide energy to the load.

Mode IV (S_1 OFF and S_2 OFF): the diodes (D_1 and D_2) are forward biased and taken as a short circuit (SC). Here, the capacitors C_1 and C_2 are charged by V_1 and V_1, respectively.

Inductor L_3 is needed to diminish the ripple present in the output current waveform. As shown in Fig. 3, $t1$ and $t2$ represent the conducting time for the power switches S_1 and S_2 respectively. Fig. 3 represents analytical voltage and current waveforms of the designed converter taking $t1 > t2$. Starting from the top, the analytical waveform of power switches, voltage across the switches (V_{S1} and V_{S2}), current in the inductors (I_{L1} and I_{L2}), voltage across the capacitors (V_{C1} and V_{C2}) and current output across the inductor (I_{L3}) are determined.

3. Steady state analysis of the system

Correlation between input voltage and output voltage can be derived from the steady state volt-second balance investigation of the inductors. For the voltage and current waveforms represented in Fig. 3, the corresponding operational circuit of the projected converter through one switching sequence will follows the order of modes I, II, and IV.

Using the volt-second balance theorem on the inductors L_1, L_2 & L_3 the below equations can be achieved:

For L_1: by applying the volt-second balance theorem,

$$(V_1 \times t_2) + V_1(t_1 - t_2) + (V_1 - V_{C_1})(1 - t_1) = 0\,, \tag{1}$$

$$V_{C_1} = \frac{1}{(1-t_1)} \times V_1\,. \tag{2}$$

For L_2:

$$(V_2 \times t_2) + (V_2 - V_{C_2})(t_1 - t_2) + (V_2 - V_{C_2})(1 - t_2) = 0\,, \tag{3}$$

$$V_{C_2} = \frac{1}{(1-t_2)} V_2\,. \tag{4}$$

For L_3:

$$(V_{C_1}+V_{C_2}+V_0)\times t_2+(V_{C_1}-V_0)(t_1-t_2)-V_0(1-t_1)=0\,, \tag{5}$$

$$V_0=(V_{C_1}\times t_1)+(V_{C_2}\times t_2)\,, \tag{6}$$

$$V_0=\frac{t_1}{(1-t_2)}V_1+\frac{t_2}{(1-t_2)}V_2\,. \tag{7}$$

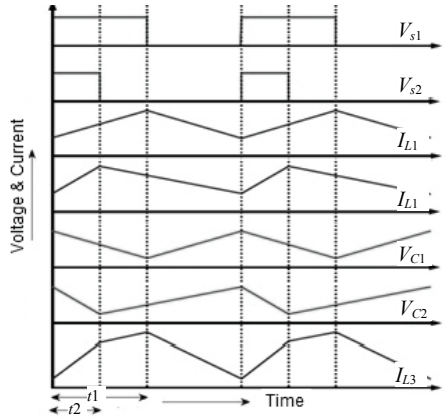

Fig. 3. Voltage and current waveforms of the designed converter vs time

4. Multivariable control strategy for distributed hybrid power system

Usually, in a distributed power system, to control the voltage of different buses, the controller regulates the time duration of power switches which exist in power electronics devices. In this paper, to design the controller, multivariable control strategy as an efficient method is selected [10], [11]. The basic idea of this method is to shape a family of open-loop transfer function matrixes of power system by minimizing the summation of the squared second norm of the errors between the open-loop transfer function matrixes of the system, obtained at several operating points of interest, and a desired open-loop transfer function matrix [12]. The step by step method of controller designing is explained as below:

4.1. Determination of an open-loop transfer function of a power system

In this step, based on the power system characteristics, the open loop transfer function of the power system is determined. The open loop transfer function of this system is defined as Eq. 8.

$$\begin{bmatrix}V_{01}(jw)\\V_{02}(jw)\\V_{03}(jw)\end{bmatrix}=\begin{bmatrix}G_{i,11(jw)}\;G_{i,12(jw)}\\G_{i,21(jw)}\;G_{i,22(jw)}\\G_{i,31(jw)}\;G_{i,32(jw)}\end{bmatrix}\begin{bmatrix}d_1(jw)\\d_2(jw)\end{bmatrix}. \tag{8}$$

In this equation, V_{01}, V_{02} and V_{03} are the voltages of PQ buses and D_1, D_2 are the time durations of converter switches. In addition, matrix $\boldsymbol{G_{i\ (jw)}}$ is the transfer function matrix of the power system. The elements of this matrix are determined by measuring the frequency response of the power system within the frequency range of interest.

At the next step, the elements of the transfer function matrix are calculated at several operating points. The chosen operating points are the closest points to the most probable operational conditions of the distributed power system. The family of transfer function matrixes is formed as:

$$\phi = \{G_i(jw), i = 1 \text{ to } 2, \omega \varepsilon \text{ R}\}. \tag{9}$$

4.2. Determination of the controller class

In this section, the class of controller is determined. The main objective of this survey is to design a linearly parameterized multivariable controller. So, the class of the controller should be determined in the *Z*-domain. The parametric model of such a multivariable controller in the *Z*-domain is given by Eq. 10.

$$K(Z) = \begin{bmatrix} K_{11}(Z)\, K_{12}(Z)\, K_{13}(Z) \\ K_{21}(Z)\, K_{22}(Z)\, K_{23}(Z) \end{bmatrix}. \tag{10}$$

The elements of the controller matrix have the same form which is stated by Eq. 11. The definition of the equation parameters is presented in Eq. 12.

$$K_{ij}(z,\rho) = \rho_{ij}^T \phi(z), \tag{11}$$

$$\left\{ \begin{array}{l} \rho_{ij}^T = [\rho_{ij,0}, \rho_{ij,1}, \rho_{ij,2}, \ldots, \rho_{ij,n}] \\ \phi^T(Z) = \left[\dfrac{1}{1-Z^{-1}}, \dfrac{Z^{-1}}{1-Z^{-1}}, \dfrac{Z^{-2}}{1-Z^{-1}}, \ldots, \dfrac{Z^{-n}}{1-Z^{-1}} \right] \end{array} \right\}. \tag{12}$$

In the above equations, the variable n is the number of zeros for each element. To calculate this parameter, the initial value of 2 is considered. Then this parameter is increased until the controller achieves appropriate dynamic performance. In this survey, the minimum value to satisfy the goals of accuracy and fast dynamic performance is $n = 4$. Based on this selection, the element forms of matrix $\boldsymbol{K(z)}$ are stated as:

$$K_{ij}(z) = \frac{\rho_{ij,0} + \rho_{ij,1}.z^{-1} + \rho_{ij,2}.z^{-2} + \rho_{ij,3}.z^{-3} + \rho_{ij,4}.z^{-4}}{1 - z^{-1}}. \tag{13}$$

For more clarification, the block diagram of the controller to determine the conduction time of the switch (S_1) is presented in Fig. 4. As the figure shows, based on the difference between the actual value of buses voltage and their reference values, the elements of the first row of the matrix $\boldsymbol{K(z)}$ determine the conduction time of converter switches. The elements of other rows of this matrix, determine the conduction time of switches S_2, S_3 and S_4, respectively.

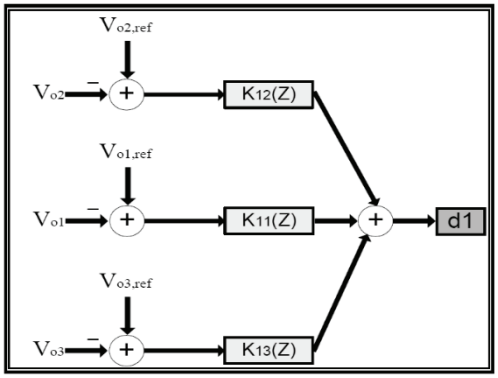

Fig. 4. Controller block diagram for determining D_1

After calculating the elements of the transfer function of ***K*(*z*)**, based on Eq. 14, the elements of the open-loop transfer function matrix of the overall power system are obtained.

$$L(jw) = G(jw) \times K(jw) . \tag{14}$$

So, based on Eq. 15, the family of open-loop transfer function matrixes can be calculated.

$$\Lambda = \{L_i(jw),\ i = 1,2 \text{ and } \omega \varepsilon R\} . \tag{15}$$

4.3. Loop Shaping by Optimization Process

At the next step, the loop shaping of the open-loop transfer function matrixes family is done via minimizing the summation of the squared second norm of the errors between L_i and L_d. The matrix L_i is the open-loop transfer function matrix of the overall power system, and matrix L_d is the desired matrix that the user expected from the power system. So, for the controller design, the procedure solves the optimization problem which is stated in Eq. 16.

$$\min \sum_{i=1}^{4} \left\| L_i - L_d \right\|^2 . \tag{16}$$

The elements of L_d are determined based on the controller objectives. The diagonal elements of the matrix L_d are considered to regulate the voltages of PQ buses with appropriate dynamic performance. In other words, by adjusting ω_c an appropriate dynamic response is achieved. In this paper, to provide a reasonable bandwidth and guarantee stability, $\omega_c = 8 \times 10^4$ r/s.

$$L_D(S) = \begin{bmatrix} L_{D_1}(S) & 0 & 0 \\ 0 & L_{D_2}(S) & 0 \\ 0 & 0 & L_{D_3}(S) \end{bmatrix} = \begin{bmatrix} \frac{\omega_c}{S} & 0 & 0 \\ 0 & \frac{\omega_c}{S} & 0 \\ 0 & 0 & \frac{\omega_c}{S} \end{bmatrix} . \tag{17}$$

The closed-loop sensitivity function of diagonal elements is:

$$S_i = \frac{1}{1 + L_{i,q}},$$

$$\left|W_i(jw)[1 + L_{D,qq}(jw,\rho)]\right| < \mathrm{Re}\left\{\left[1 + L_{D,qq}(-jw)\right]\left[1 + L_{i,qq}(jw,\rho)\right]\right\}, \quad \forall\, \omega \in R \text{ for } i = 1,\ 2 \text{ and } q, p = 1,\ 2,\ 3, \tag{18}$$

where, $W_i(jw)$ is the weighting filter. In this survey, $W_1 = 0.6$ to guarantee the phase margin of greater than 29°. In addition to guarantee the stability of the power system. The parameterized controller can satisfy the stability of the power system if:

$$r_{i,pq}(jw,\rho) < \frac{Re\{[1 + L_{D,q}(-jw)][1 + L_{i,q}(jw,\rho)]\}}{\left|W_1(jw)[1 + L_{D,qq}(jw,\rho)]\right|}, \quad \forall\, \omega \varepsilon R \text{ for } i = 1, 2 \text{ and } q, p = 1,\ 2,\ 3, \tag{19}$$

where, parameters of $r_{i,pq}$ are the off-diagonal elements of matrix L_i.

5. Dynamic performance analysis of designed controller at different situations

In this section, the dynamic performance and stability of proposed control strategy have been studied in different conditions. In order to have a comprehensive evaluation of the controller performance, several examinations including all the normal and critical conditions that a power system may experiences are tested. It must be mentioned that at these tests, the initial values of quantitative parameters that have been selected for a distributed power system are similar to the ones that are mentioned in the previous section. In addition, as the B_2 bus is connected to all of the PQ buses as shown in Fig. 5, then it is not necessary to measure the voltage of each PQ bus and the voltage of the B_2 bus is a comprehensive representative of the overall power system voltage [13, 14]. It is necessary to mention that in following tests, the RMS value of the B_2 bus voltages is measured. The reference value of this parameter at a normal condition is $V = 20$ kV. These tests are described as below:

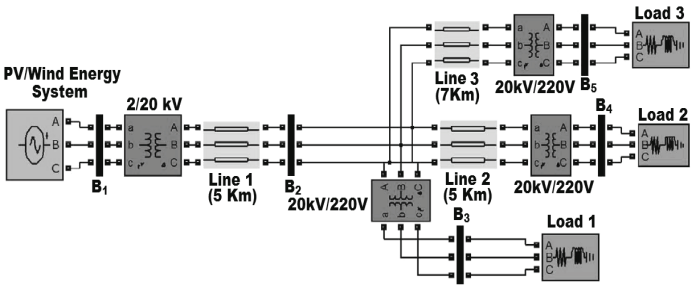

Fig. 5. Simulated distributed hybrid PV/wind power system in MATLAB/SIMULINK

5.1. Changing the power demand at PQ bus

In this examination, the ability of a controller to respond to different power demands at PQ buses has been analyzed. This test is divided into two parts. In the first section, the variation of active power and at the second part, reactive power alternation has been studied.

For this reason, at the first evaluation, at $t = 4$ s, the power demand of three PQ buses has been increased from 1.1 MW to 1.7 MW. For the second scenario, like in the previous test, the reactive power demand has been changed and at $t = 4$ s, the amount of reactive power that was consumed at three PQ buses is increased from 350 kvar to 550 kvar as shown in Fig. 6.

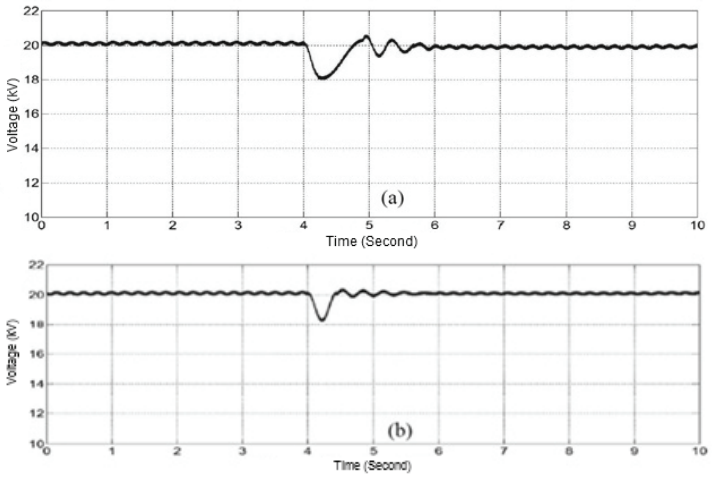

Fig. 6. The voltage of B_2 bus in Test A, during a) increase of demanded active power, b) increase of demanded Reactive power

At the first examination, normal conditions are considered for the power system. The quantitative characteristics of the power system are: $\lambda = 1$, $T = 320$ K, Wind Speed (vw) = 8 m/s, the reference value of the B_2 bus voltage = 20 kV.

5.2. Variations of ambient conditions at renewable energy sources

In this part, two of the prevalent incidents that affect the performance of distributed renewable power systems are studied. These incidents are caused by the reduction of sun irradiation ($\lambda = 1$ to $\lambda = 0.2$) and continuous variation of wind speed ($vw = 10$ m/s to $vw = 1$ m/s). The voltage of the B_2 bus is measured and is presented in Fig. 7.

5.3. Variations of the reference voltage value

In this test, by changing the quantity of reference voltage, the flexibility of a power system in changing bus voltage has been tested. The reference voltage $V = 20$ kV is increased to $V = 25$ kV at $t = 4$ s and then is decreased to $V = 17$ kV at $t = 6$ s. The voltage of the B_2 bus is measured and shown in Fig. 8.

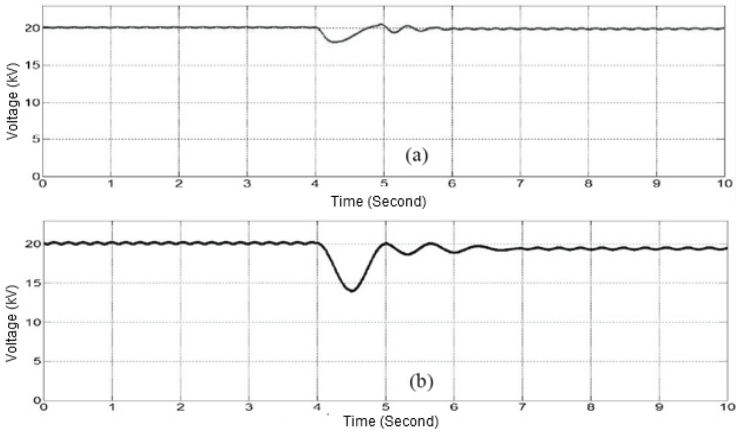

Fig. 7. The voltage of B_2 bus in Test B, during a) decrease of sun irradiation, b) decrease of wind speed

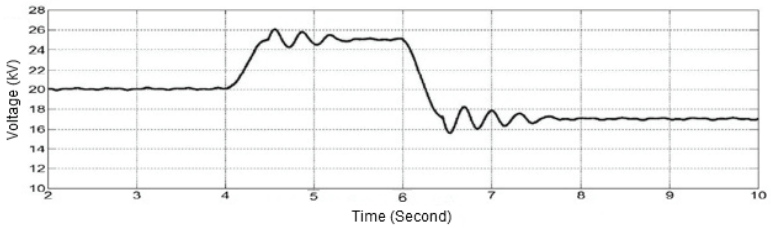

Fig. 8. The voltage of B_2 bus in Test C

5.4. Occurrence of fault condition in one of the PQ buses

In this test, by inserting the symmetrical fault condition to one of the PQ buses (B_3) and observing the voltage of other PQ buses, the independence of PQ buses voltage has been analyzed and shown in Fig. 9(a).

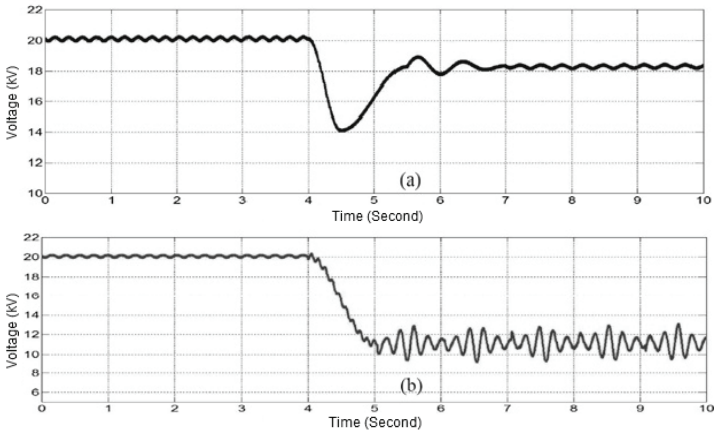

Fig. 9. The voltage of B_2 bus in Test D with a) multivariable controller, b) conventional controller

As the figure shows, occurrence of electrical fault at $t = 4$ sec at one of the buses has negligible influences on the other parts of the power system. For instance, this test has been repeated with a conventional controller (PID controller) and the voltage of the B_2 bus has been measured again and is shown in Fig. 9(b).

As this figure shows, the PID controller cannot maintain the stability of the voltage of the distributed power system. By comparing the results of these two controllers, the efficiency of a multivariable controller is revealed.

5.5. The changing structure of a hybrid power supply distribution system

In this test, the response of a multivariable controller to the power system structure changes is evaluated. To analyze this feature, at $t = 5$ s, the power line that connects the B_5 bus to B_2 bus is cut off. As Fig. 10 shows, inserted perturbation doesn't make the voltage of the power system unstable and after about 0.5 second, the controller regulates the voltage of a common bus of B_2 at predetermined value again. In addition, during transient time, the increase of voltage at the proposed bus is insignificant.

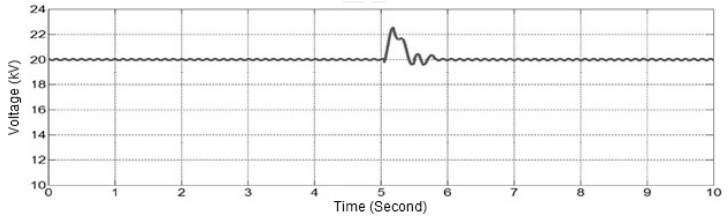

Fig. 10. The voltage of B_2 bus in Test E

6. Conclusions

This paper proposes two important subjects. In the first part, a novel double-input DC-DC converter that can be applied in a distributed power system is introduced. The theoretical principles of the proposed converter are presented, and based on these principles; the current of converter's inductors, the voltage of converter's capacitors and the output voltage are discussed. In the second section, by applying a designed converter, a distributed hybrid PV/wind power system is simulated. To control the power switches of power system's converters, a multivariable controller is designed. This controller has some exclusive features that are: 1) regulating the voltage of a power system in normal and critical conditions, 2) isolating the voltage of different buses from each other, 3) changing the reference value of power system voltage with appropriate dynamic performance. The simulation and experimental results confirm satisfactory performance of the proposed multivariable controller in regulation of the distributed hybrid power system voltage at different conditions. The proposed methodology is general and applicable to different distributed renewable power systems with any number of energy sources and PQ buses.

Acknowledgements

Authors are thankful to the IIT(ISM), Dhanbad and UNIVERSITY GRANTS COMMISSION, Bahadurshah Zafar Marg, New Delhi, India for granting financial support under Major Research Project entitled "Development of Hybrid Off-grid Power Supply System for Remote Areas [UGC Project: F. No. 42 152/2013(SR), w.e.f. 01/04/2013]" and also grateful to the Under Secretary and Joint Secretary of UGC, India for their active co-operation. Authors are also thankful to the National Institute of Solar Energy, Gurgaon-Faridabad Road, Gwalpahari, Gurgaon, Haryana, India for allowing the opportunity to work at their campus and for their active co-operation.

References

[1] Luque A., Hegedus S., *Handbook of Photovoltaic Science and Engineering*, Wiley (2003).

[2] Dali M., Belhadj J., Roboam X., *Hybrid solar-wind system with battery storage operating in grid-connected and standalone mode: Control and energy management – Experimental investigation*, 7th International Conference on Sustainable Energy Technologies, pp. 2587-2595 (2010).

[3] Bogaraj T., Kanakaraj J., Kumar K.M., *Optimal sizing and cost analysis of hybrid power system for a stand-alone application in Coimbatore region: a case study*, Archives of Electrical Engineering, vol. 64, no. 1, pp. 139-155 (2015).

[4] Ciampichetti S., Corradini M.L., Ippoliti G., Orlando G., *Sliding Mode Control of Permanent Magnet Synchronous Generators for Wind Turbines*, IEEE Conference on IECON – 37th Annual Conference on IEEE Industrial Electronics Society, Poland, pp. 740-745 (2011).

[5] Izadbakhsh M., Rezbani A., Gandomkar M., *Dynamic response improvement of hybrid system by implementing ANN-GA for fast variation of photovoltaic irradiation and FLC for wind turbine*, Archives of Electrical Engineering, vol. 64, no. 2, pp. 291-314 (2015).

[6] Izadbakhsh M., Rezvani A., Gandomkar M., *Improvement of microgrid dynamic performance under fault circumstances using ANFIS for fast varying solar radiation and fuzzy logic controller for wind system*, Archives of Electrical Engineering, vol. 63, no. 4, pp. 551-578 (2014).

[7] Nejabatkhah F., Danyali S., Hosseini S.H., Sabahi M., Niapour S.M., *Modeling and Control of a New Three-Input DC-DC Boost Converter for Hybrid PV/FC/Battery Power System*, IEEE Transactions on Power Electronics, vol. 27, no. 5, pp. 2309-2324 (2012).

[8] Pandiarajan K., Babulal C.K., *Fuzzy ranking based non-dominated sorting genetic algorithm-II for network overload alleviation*, Archives of Electrical Engineering, vol. 63, no. 3, pp. 367-384 (2014).

[9] Mangaiyarkarasi S.P., Sree Renga Raja T., *PSO based optimal location and sizing of SVC for novel multi objective voltage stability analysis during N – 2 line contingency*, Archives of Electrical Engineering, vol. 63, no. 4, pp. 535-550 (2014).

[10] Qi W., Liu J., Chen X., Christofides P.D., *Supervisory predictive control of standalone wind/solar energy generation systems*, IEEE Transactions on Control Systems Technology, vol. 19, no. 1, pp. 199-207 (2011).

[11] Uzunoglu M., Onar O.C., Alam M.S., *Modeling, control and simulation of a PV/FC/UC based hybrid power generation system for stand-alone applications*, Renewable Energy, vol. 34, no. 3, pp. 509-520 (2009).

[12] Dash P.K., Padhee M., Barik S.K., *Estimation of Power Quality Indices in Distributed Generation Systems during Power Islanding Conditions,* International Journal of Electrical Power & Energy Systems, vol. 36, no. 1, pp. 18-30 (2012).

[13] Xiao W., Edwin F.F., Spagnuolo G., Jatskevich J., *Efficient Approaches for Modeling and Simulating Photovoltaic Power Systems*, IEEE Journal on Photovoltaics, vol. 3, no. 1, pp. 500-508 (2013).

[14] Said S., Massoud A., Benammar M., Ahmed S., Guy C., Gerard R., *A Matlab/Simulink Based Photovoltaic Array Model Employing Sim Power Systems Toolbox*, Journal of Energy and Power Engineering, vol. 6, no. 12, pp. 1965-1975 (2012).

ARCHIVES OF ELECTRICAL ENGINEERING VOL. 66(2), pp. 253-263 (2017)

DOI 10.1515/aee-2017-0019

Magnetic characterization of the nickel layer protecting the copper wires in harsh applications

DANIEL ROGER, STEPHANE DUCHESNE, VADIM IOSIF

Universitet Artois
daniel.roger@univ-artois.fr

(Received: 26.09.2016, revised: 26.11.2016)

Abstract: High Temperature (HT°) motor coils open new perspectives for extending the applications of electrical motors or generators to very harsh environments or for designing very high power density machines working with high internal temperature gradients. Over a temperature of 300°C, the classic enameled wire cannot work permanently, the turn-to-turn insulation must be inorganic and made with high temperature textiles or vitro-ceramic compounds. For both cases, a diffusion barrier must protect the copper wire against oxidation. The usual solution consists of adding a nickel layer that yields an excellent chemical protection. Unfortunately, the nickel has ferromagnetic properties that change a lot the skin effect in the HT wire at high frequencies. For many applications such as aeronautics, electrical machines are always associated with PWM inverters for their control. The windings must resist to high voltage short spikes caused by the fast fronted pulses imposed by the feeding inverter. The nickel protection layer of the HT° inorganic wire has a large influence on the high frequency behavior of coils and, consequently, on the magnitude of the voltage spikes. A good knowledge of the non-linear magnetic characteristics of this nickel layer is helpful for designing reliable HT inorganic coils. The paper presents a method able to characterize non-linear electromagnetic properties of this nickel layer up to 500°C.

Key words: high temperature motor winding, nickel diffusion barrier, temperature dependent magnetic properties

1. Introduction

Electrical machines able to work at high temperatures (300-400°C) for short times are now standard products; they are used for smoke extractors. These machines are built with an improved Electrical Insulation System (EIS) able to withstand high temperatures during short lifespans. They use high performance polymers such as polyimide (PI) strengthened by inorganic particles [1]. However, these conventional organic technologies reach their limits, continuous operations at such high temperature are not possible.

Electrical machines able to operate continuously at 400°C have been developed by the petroleum industry for deep drilling [2]. Their EIS are built with composite materials that

combine fiberglass and mica. The large thicknesses of these inorganic insulating layers (100-200 µm) limits this inorganic technology to big machines using large wire sections.

Many applications, in ground transports or in aeronautics require compact actuators of low and medium powers. With higher permanent internal temperatures, it is possible to design machines with higher current densities and consequently higher power densities. The coils of such machines are built with a wire insulated by a thin inorganic layer made of a glass-ceramic compound. Unfortunately, this inorganic insulating layer is porous; it is no longer able to protect the copper against oxidation. Therefore, the copper must have an additional protection layer made of nickel, between the copper and the inorganic insulation layer. The copper wire can be used up to 230°C without any protection and with a porous inorganic insulation. A nickel protection layer must be added for higher temperatures. Manufacturers propose wires with a higher nickel thicknesses for the products able to operate at the most elevated temperatures [3].

Nickel is a ferromagnetic material, therefore the protection layer changes the electromagnetic global behavior of the coil, especially in the higher part of the frequency spectrum because of skin and proximity effects. The paper presents an experimental method able to characterize the non-linear magnetic properties of the nickel protection layer of HT° inorganic wires, it gives details on the research works presented in the conference EPNC 2016 [4].

2. High temperature coils

Fig. 1 is the picture of such a motor coil after tests at 500°C. This rigid coil is made with an available inorganic HT° wire [5] protected by a high temperature cement based on alumina [6]. These coils are placed on the stator teeth of concentrated winding permanent magnet synchronous machines (CW-PMSM) [7].

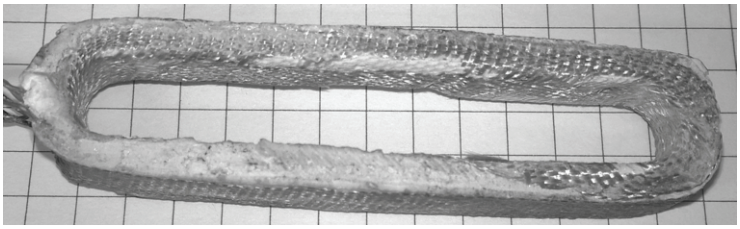

Fig. 1. HT° inorganic coil after tests at 500°C

Fig. 2 is a microscopy of the cross section of a HT° inorganic wire, which diameter is 800 µm. The nickel layer thickness is 65 µm and the inorganic insulation one 10 µm. For modeling the high frequency behavior of HT° coils made with such a wire, the magnetic permeability of the nickel, for several temperature, is required. A study made a long time ago shows a strong dependence of the permeability to the magnetic field and the temperature [8]. Deeper investigations are useful for considering the non-linear phenomena of this nickel layer.

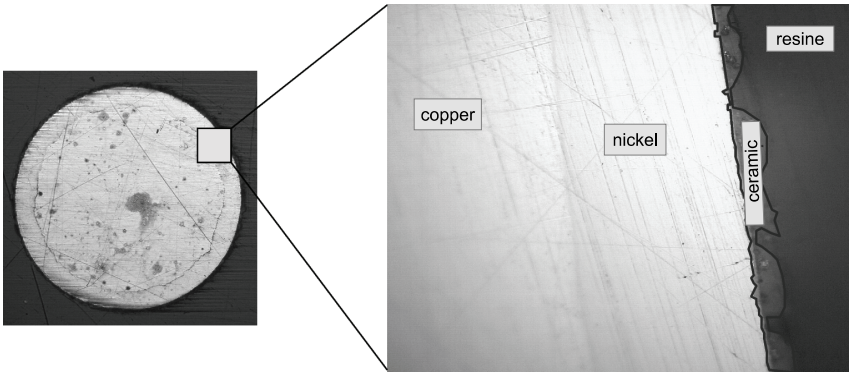

Fig. 2. HT° inorganic wire cross-section

3. Measurements at low temperatures

The experimental setup defined for measuring the $B(H)$ curve of the nickel layer is inspired from the Epstein frame. Measurements are performed at low frequency, the skin effects is negligible. The HT° inorganic wire is wound to form the magnetic core of the experimental system presented in Fig. 3. The two primary coils connected in series produce the magnetic field and the secondary coils measure the global magnetic flux. Fig. 4 gives the electric circuit for measurements.

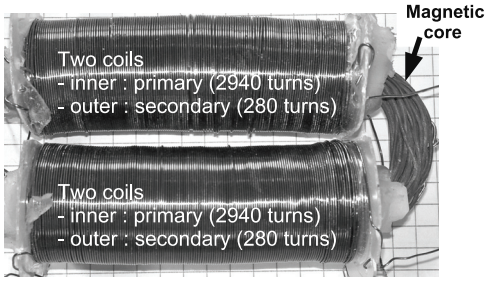

Fig. 3. Measurement device at ambient temperature

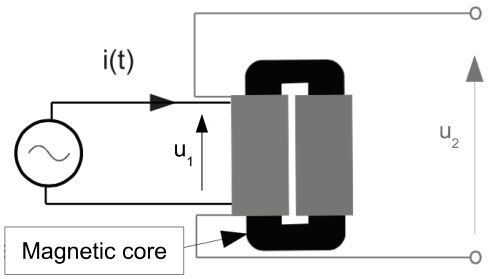

Fig. 4. Electric circuit for measurements at ambient temperature

In the magnetic core the nickel clad wire follows the field lines created by the primary coils. Therefore, the magnetic field is tangent to the nickel layer at any point of the wire periphery as shown in Fig. 5. With this geometry, the principle of conservation of the tangential component of the field on each side of the border between the materials impose the equality of the magnetic field in the air, the nickel and the copper.

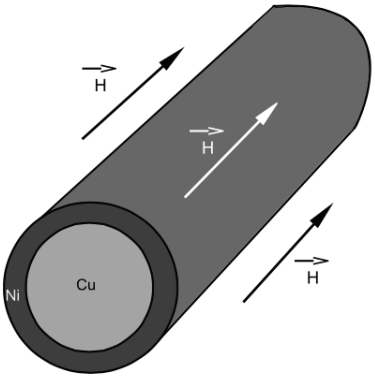

Fig. 5. Detail of the magnetic field in the experimental core

The magnitude of this field can be estimated by the Ampere law from the primary current i, the turn number of the primary winding N_1 and the average length of the experimental core l.

$$H = \frac{N_1 i}{l}. \tag{1}$$

The Faraday law yields the voltage induced in the secondary from the total flux φ and the number of secondary turns N_2.

$$u_2 = N_2 \frac{\mathrm{d}\varphi}{\mathrm{d}t}. \tag{2}$$

The flux is computed by integrating the secondary voltage. The results are presented in Fig. 6 for $f = 50$ Hz. The straight-line gives the flux computed considering only the uniform flux in the air inside a virtual tube following the core and of the same diameter as the secondary coils. The non-linearity caused by the nickel layer is clearly visible.

The flux density in the nickel layer is computed from the flux measurements by subtracting the flux in the tube of air and dividing by the nickel section. The resulting hysteresis loop is presented in Fig. 7.

The hysteresis loop shows the ferromagnetic properties of the nickel layer with a saturation shoulder at approximately $B_S = 0.35$ T for a field $H_S = 4000$ A/m. The width of the loop is quite large but the eddy currents induced in the copper central wire artificially increase this value. The key information from this experience is an estimation of the current that corresponds to the saturation shoulder of the nickel layer. Considering a single conductor, which radius is a, away from any external electromagnetic influence, the current corresponding to the

saturation shoulder is that corresponds to a current of 10 A peak, for a wire of diameter 0.8 mm. The corresponding average current density is 19.9 A/mm^2, which is very high, even for a HT motor.

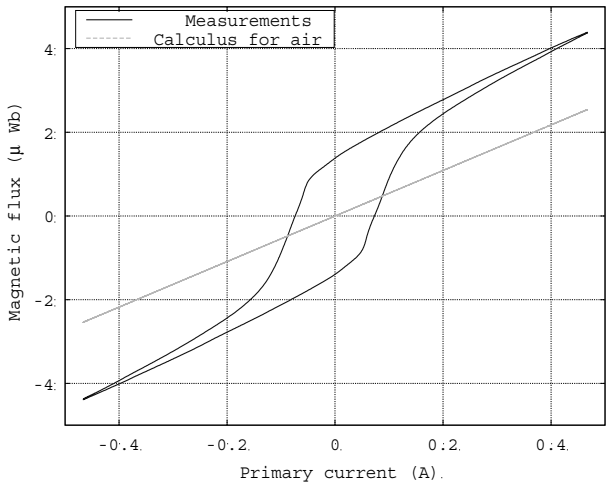

Fig. 6. Flux in the core as a function of the primary current

The hysteresis loop is very similar to that for iron, but with a saturation shoulder at a lower level. Consequently, the relative permeability is very difficult to define because of the non-linear behavior of this ferromagnetic material, it depends on minor hysteresis loops, dc magnetic polarization and ac field magnitude.

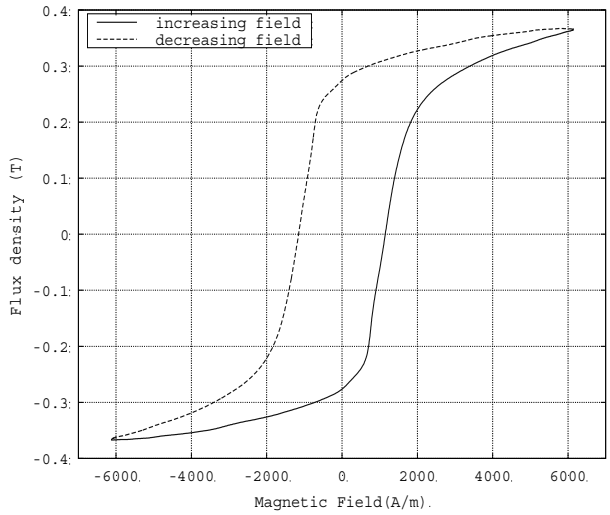

Fig. 7. Hysteresis loop of the nickel protection layer

4. Investigations at high temperatures

For testing the influence of the nickel layer at high temperatures, a simpler experimental setup has been made, it consists of two adjacent HT° wires attached to a mica plate by spots of HT° cement. Fig. 8 shows a small part of the experimental bifilar line, which total length is 3 m.

Fig. 8. Small part of the 3m length bifilar line set on a mica plate

The end of the pair is short-circuited and its input is connected to the measurement device by a much shorter twisted pair made with mica fiberglass HT° wire. The inductance measurements are used for estimating the nickel layer properties. Fig. 9 presents the inductance measurements performed on the bifilar experimental line versus temperature for two currents imposed by the measurement system. The low current imposed by the impedance analyzer corresponds to a low field between the two wires yields lower inductance that measurements performed at higher currents.

The measurements show a strong dependence of the inductance to the temperature and the magnetic field due to the nickel protection layer.

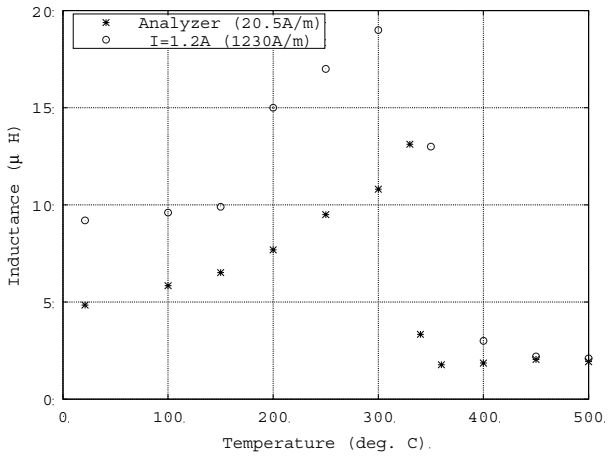

Fig. 9. Temperature dependence of the experimental bifilar line inductance

The nickel layer permeability at any temperature can be deduced from the bifilar line inductance measurement. Unfortunately, the actual distance between the wires of the experimen-

tal bifilar line is not known with a relevant accuracy as it can be seen on Fig. 8. Therefore, the average value of this parameter is computed from electrical measurements performed above the Curie point, when the ferromagnetic properties of the nickel layer are nullified. For these temperatures and for low frequencies, the bifilar line inductance can be estimated using the classical analytic approach that consider homogeneous wires, which geometric parameters are defines in Fig. 10.

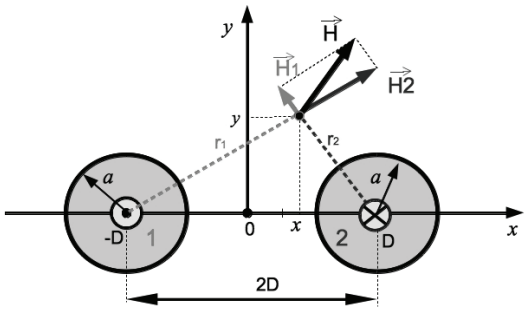

Fig. 10. Cross-section of the bifilar line and geometric parameters

The magnetic field is computed applying the Ampère's law and considering currents in opposite direction in the two wires. The flux is obtained by performing the integration along the x axis between the points corresponding the null value of the flux density. Then, the inductance L, for a length l of the bifilar line, is obtained dividing the flux by the current. Considering the geometric parameters defined in Fig. 10, the global result is:

$$\frac{L}{l} = \frac{\mu_0}{\pi}\left(Ln\frac{D+\sqrt{D^2+a^2}}{a} + \frac{1}{a^2}\left(D\sqrt{D^2+a^2} \right) \right). \tag{3}$$

This analytical approach is based on 2 wires made of homogeneous materials, but the real wire over the Curie point is not homogeneous because the resistivity of the nickel is much higher than the copper one ($26.10^{-8}\,\Omega \cdot$ m and $4.19.10^{-8}\,\Omega \cdot$ m respectively at 400 °C). A Finite Element (FE) simulation has been made for observing the differences between the analytical approach and the reality. Fig. 11 highlights this approximation showing the fields on the x axis.

The difference between the curves H and EF denotes an under-evaluation of the flux therefore of the inductance. A lower error of the analytical model is obtained choosing $a = r_{Cu}$, the radius or the copper core of the wire. Fig. 12, drawn with this hypothesis, shows the lower under-evaluation for the improved model.

The parameter D, corresponding to the half of the average distance between the center of the wires of the experimental bifilar line is determined from the analytical formulae (3) of the improved model where $a = r_{Cu}$. The input data are: the inductance measured at 400 °C (L = 1.94 µH); the radius of the copper core of the wire ($a = r_{Cu}$ = 325 µm) and the length of the line (l = 3 m). D is the only unknown parameter of Eq. (3) that can be computed by a numerical method. The result is D = 485 µm.

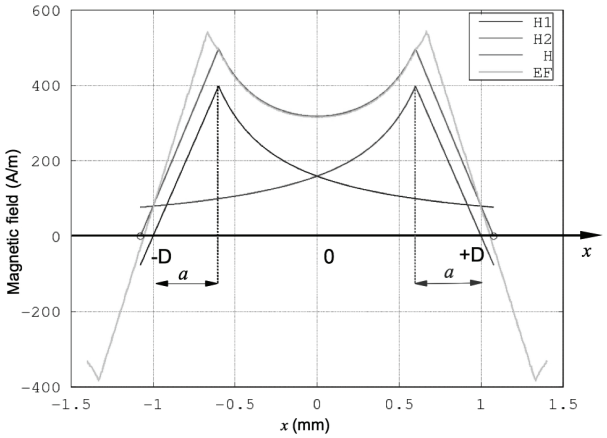

Fig. 11. Magnetic field on the x axis ($H1$: left wire, $H2$: right wire, H: resulting field, EF: field computed taking the higher resistivity of the nickel at 400°C into account

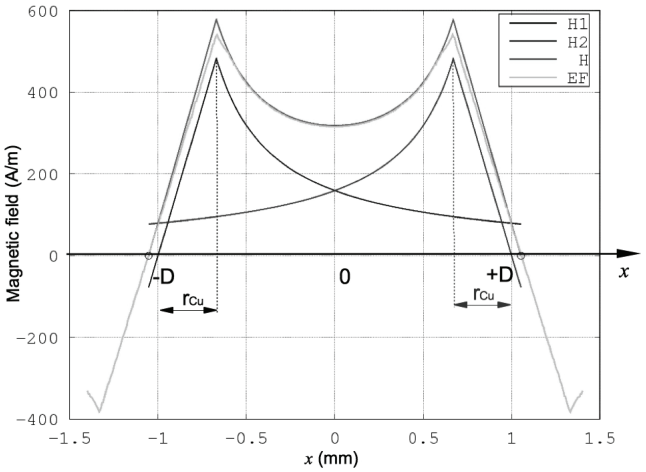

Fig. 12. Improved analytical model obtained with $a = r_{Cu}$ in the same conditions

With an accurate determination of the average distance $2D$ between the wire center of the experimental line and the inductance measurements at temperature under the Curie point, it is possible to determine the magnetic permeability of the nickel layer at any temperature.

The flux density is $\mu_0 H$ in the copper and in the air and $\mu_0 \mu_R H$ in the nickel layer as illustrated in Fig. 13. The flux increase $\Delta\phi$ due to the relative permeability μ_R of the nickel layer is due to its ferromagnetic properties under the Curie point and corresponds to the hatched areas in Fig. 13. This increase, for a length l of the bifilar line and nickel thickness e_n is:

$$\frac{\Delta\phi}{l} = 2(B_2 - B_1)e_n . \tag{4}$$

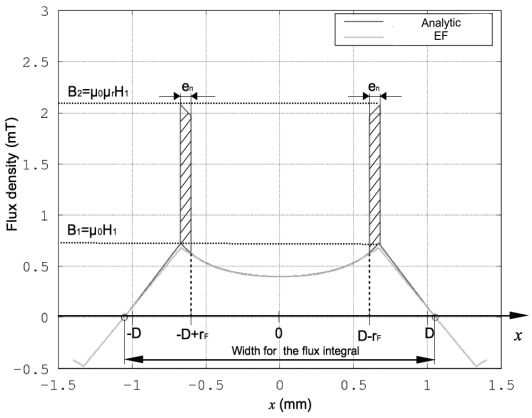

Fig. 13. Increase of the flux density in the nickel layers

The improved analytical model gives the maximum value H_1 of the magnetic field; therefore the increase of the inductance ΔL, comparing to the value measured over the Curie point, can be used for determining the relative permeability of the nickel at any temperature and current measurement. The final formulae is given by Eq. (5) were e_N is the nickel thickness and r_F the total wire radius with the nickel layer.

$$\mu_R = 1 + \frac{\Delta L}{l} \frac{\pi}{\mu_0 \left[\frac{1}{2D - (r_F - e_n)} + \frac{1}{r_F - e_n} \right]}. \tag{5}$$

The application of this equation to the inductance measurements performed up to 400°C are presented in Fig. 14.

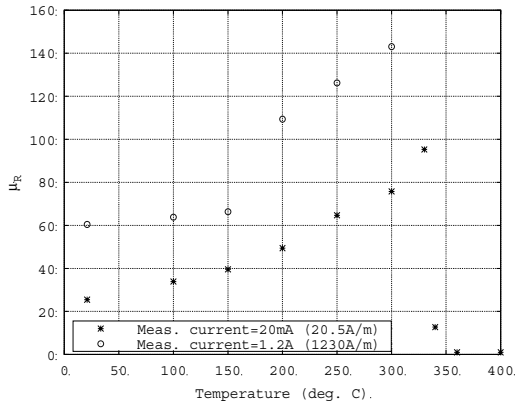

Fig. 14. Relative permeability of the nickel layer versus temperatures at two current levels

There is a significant increase of the magnetic permeability below the Curie point (360°C) and a brutal decrease over the Curie point as expected for a ferromagnetic material [9]. These

results show that the relative permeability is also strongly dependent of the ambient field in the neighborhood of the nickel layer.

5. Conclusions

The proposed experimental approach describes a method able to characterize the non-linear magnetic characteristics of the nickel layer used as a diffusion barrier in HT° wires used in a harsh environment. The proposed method is based on the analysis of the behavior of a bifilar short-circuited line placed in an oven.

The preliminary measurements made at ambient temperature show the hysteresis loop of the thin nickel layer and a saturation shoulder at more or less 0.3 T. This hysteresis loop, which is similar to the one measured on classic iron, predicts a very non-linear behavior. Consequently, the high frequency model of the motor coils used for predicting the voltage spikes during transients will be more complex. Such a model is all the more useful as the electrical performances of the HT° inorganic insulating materials are poor compared to those of conventional polymers [10]. A fine modeling of the high frequency electromagnetic behavior of the coils is crucial for designing HT° machines powered by PWM inverters, which impose very stiff and repetitive voltage edges [11].

For temperature below the Curie point of nickel, the nickel diffusion barrier modifies strongly the skin and proximity effects: the higher damping effects mitigate the voltage spikes after each voltage edge. Consequently, the dielectric stress on the turn-to-turn insulation is lower. A good knowledge of the non-linear magnetic characteristics of the diffusion barrier added to the copper wire is helpful for designing reliable HT° inorganic machines that will be able to withstand the fast fronted voltages imposed by the PWM inverter that feed the machine. When this HT° winding technology is mature, it will be possible to design large power generators working in the near vicinity or the propulsion turbines of aircrafts.

Acknowledgements

This work is a part of the project ”Compact Electric Actuator with Integrated Converter for Extreme temperatures – ACCITE” supported by the French Foundation for Aeronautics and Espace (FRAE).

References

[1] Aymonino F., Lebey T., Malec D., Petit C., Michel J., Anton A., Gimenez A., *Degradation and dielectrics measurements of rotating machines insulation at high temperature (200-400 °C)*, IEEE International Conference on Solid Dielectrics, July 2007, pp. 130-133 (2007).

[2] Hooker M., Hazelton C., Kano K., Tupper M., *High-temperature electrical insulation for EGS downhole equipment*, Thirty-Fifth Workshop on Geothermal Reservoir Engineering, Stanford University, Stanford, California (2010).

[3] Vonroll, *Mica-taped wires samicafirewall*, www.vonroll.com (2015).

[4] Iosif V., Roger D., Duchesne S., *Magnetic characterization of the nickel protection layer of wires used for high temperature motors,* XXIV Symposium on Electromagnetic Phenomenon and Non-linear Circuits (EPNC), Helsinki *(*2016).
[5] Plastec Group, *Cerafil500.* www.cables-cgp.com/.
[6] *Cotronics, Adhesifs, ciments, revetements ceramiques hautes temperatures – 1000 à 3000 °C*, www.cotronics.com/.
[7] Iosif V., Roger D., Takorabet N., Duchesne S., Meibody-Tabar F., *Technological assessments for designing machines able to work at very high internal temperatures (450-500 °C)*, International Conference on Electrical Machines (ICEM), Lausanne (2016).
[8] Zaimovski A., *On the temperature dependence of magnetic permeability in weak fields*, Journal of Physics (1941).
[9] Néel L., *Propriétés magnétiques du nickel pur a proximité du point de curie*, Société Française de physique (1933).
[10] Iosif V., Roger D., Duchesne S., Malec D., *Assessment and improvements of inorganic insulation for high temperature low voltage motors*, IEEE Transactions on Dielectrics and Electrical Insulation, vol. 23, no. 5, pp. 2534-2542 (2016).
[11] Iosif V., Duchesne S., Roger D., *Voltage stress predetermination for long-life designof windings for electric actuators in aircrafts*, IEEE - Annual Report Conference on Electrical Insulation and Dielectric Phenomena (CEIDP), Ann Arbor, pp. 319-321 (2015).

ARCHIVES OF ELECTRICAL ENGINEERING VOL. 66(2), pp. 265-277 (2017)

DOI 10.1515/aee-2017-0020

Statistical analysis and dimensioning of a wind farm energy storage system

BARTOSZ WAŚKOWICZ

Institute of Electrical Engineering, University of Zielona Góra
Szafrana 2, 65-980 Zielona Góra, Poland
e-mail: b.waskowicz@iee.uz.zgora.pl

(Received: 23.09.2016, revised: 03.11.2016)

Abstract: The growth in renewable power generation and more strict local regulations regarding power quality indices will make it necessary to use energy storage systems with renewable power plants in the near future. The capacity of storage systems can be determined using different methods most of which can be divided into either deterministic or stochastic. Deterministic methods are often complicated with numerous parameters and complex models for long term prediction often incorporating meteorological data. Stochastic methods use statistics for ESS (Energy Storage System) sizing, which is somewhat intuitive for dealing with the random element of wind speed variation. The proposed method in this paper performs stabilization of output power at one minute intervals to reduce the negative influence of the wind farm on the power grid in order to meet local regulations. This paper shows the process of sizing the ESS for two selected wind farms, based on their levels of variation in generated power and also, for each, how the negative influences on the power grid in the form of voltage variation and a short-term flicker factor are decreased.

Key words: energy storage, power quality, renewable energy, wind power

1. Introduction

With the ever-increasing demand of energy consumption and numerous environmental concerns it is of increasing significance to modernize the energy grid [1]. Modern day energy grids are more efficient, produce more energy, use more distributed energy generating units and put less emphasis on fossil fuels. This approach means that maintaining high power quality indices becomes harder due to a much higher number of generating stations which experience greater output variation than traditional power plants [1]. However, it is possible to make renewable energy generating stations more stable by adding energy storage.

Depending on local law and legal regulations it is possible to achieve required parameters by using appropriate energy storage to stabilize the power output of such generating stations as wind farms. According to the Polish power transmission regulations [2, 3], a wind farm

should not generate output with sudden dips or spikes exceeding 1.5% of the reference power level and should have a short-term flicker factor below 0.35.

Many methods are being used for storage sizing but there is no generally accepted framework. The two most commonly used methods are the deterministic approach and the stochastic approach. More uncommon methods include genetic algorithms [4], artificial neural networks [5], application of low-pass filter methodology [6], and using inventory models [7].

1.1. Storage role and type

Energy storage can be used in conjunction with a wind farm for several reasons. One of which is to minimize the influence of the wind farm on the power grid by either reducing the Pst, or making it possible to meet the day-ahead forecast. However one of most important reasons is to meet the short-circuit criterion in certain areas where grid parameters do not allow for connecting additional wind generation stations. Also incorporation of a storage system makes it possible to use wind farms on the power balance market. The economic aspect of storage systems is complicated and largely unregulated. It seems intuitive that DSOs should create new possibilities for incorporating new renewable energy plants. Thus they should be interested in implementing energy storage as a simpler, faster and cheaper way to open the grids to new distributed energy sources. On the other hand, in some cases (when technical issues have not been resolved and the whole project is doubtful) investors in renewables should also be interested in financing energy storage systems. To make a 24 hour forecast it is impossible to do so based on statistical data alone [8]. Therefore it is necessary to use historical meteorological data. Even though this is proven to work by many case studies it requires energy storage with huge capacity because of the power balancing over many hours. Additionally, uncertainty of the forecast requires even larger storage capacity to account for the possible deviation from the forecast. Typical capacities of such storages are around few MWh [1, 6, 9], depending on wind characteristics and wind farm rated power, and they are very costly. Typically used energy storage technologies for long forecasts are pumped hydroelectric storage, sodium-sulfur batteries, among others. Using an ESS to reduce destabilizing influences on the power grid does not require the use of historical data nor meteorological data. This role requires storage capacities two orders of magnitude smaller than the balancing storage, as shown in this paper. While the energy capacity required is relatively small it is still necessary to supply a large power output for smoothing brief power fluctuations. Different storage technologies are being used for these two roles because of the aforementioned reasons. Possible storage technologies here are supercapacitors, flywheel energy storage and superconducting magnetic energy storage.

1.2. Method types

Deterministic methods use mathematical models to analyze the system and calculate the capacity of the storage needed. Such methods are often used for long term forecasts (24 h or over) and they often include historical meteorological data and sometimes take into account multisite correlation. Such models are very complicated and require the determination of values of numerous parameters. This, along with the uncertainty of meteorological and histo-

rical data, makes such methods difficult to implement and determine the accuracy of such methods. Also, forecast tools are not widespread [9] and forecast error greatly impacts on the necessary storage capacity [8, 9]. Although deterministic methods are able to make 24 h forecasts and wind farms have been proven to function using forecasting in many case studies [10] they require very large capacities of ESS. Also due to unpredictability of weather forecasting it is impossible to determine the confidence level of the system in question.

The stochastic approach may appear more appropriate to deal with such an unpredictable element as wind speed. It is best suited for short-term prediction and balancing. It is impossible to make a 24 h forecast based on statistical data alone. There are cases where stochastic methods were applied but they had to be combined with weather data for making a 24 h forecast [1, 9]. Analyzing the required storage capacity using statistical methods is convenient because it does not require the determining of numerous parameters and it is always possible to get an accurate confidence level using a histogram of power generation variation which is useful especially when dealing with the customer. Statistics alone can be useful for determining storage capacity for short or very short forecast applications.

As already stated, there is no established method or framework of optimal storage sizing. Often, authors in their papers do not reveal all technical details of their methods, diminishing the transparency of their research. Existing methods are quite difficult to adequately compare in terms of efficiency, and therefore do not show a clear superiority of one over the others. There are a few reasons for this, one of which is that there are different types of methods and while different deterministic methods can be analytically compared, it cannot be done between deterministic and stochastic or more exotic approaches. But the main reason is different wind data and wind farm characteristics. There is no benchmark data that could be fed to tested methods to calculate a fair result. This may be caused by the fact that detailed (1 s intervals) wind data are very hard to come by and are often tied to a non-disclosure agreement.

1.3. Proposed method

The purpose of the proposed method is the reduction of negative influence from wind farm dynamics on the power grid using as small an energy storage capacity as possible. To achieve this the method optimizes the storage size by setting constant levels of output power at 1 min intervals. This power level of i-th cycle is determined by calculating the average power value P_{wf} in the previous 1 min interval and adding a correction $A_{i\text{-}1}$, which is determined on the basis of the current storage charge level according to the formula:

$$P_{\mathrm{ref},i} = \frac{1}{n}\sum_{j=1}^{n} P_{\mathrm{wf},i-1}\left(t_j\right) + A_{i-1}\left(t_0\right), \tag{1}$$

where: $P_{\mathrm{ref},i}$ is the power level set in i-th interval, P_{wf} is the wind farm power, $A_i(t)$ correction parameter determined by current storage discharge level.

An advantage of this method is its simplicity, robustness and the fact that it does not require the determination of numerous parameters to function nor any historical data or meteorological data. It can be deployed virtually anywhere and can reduce unwanted power fluctuations and thus the short-term flicker factor (P_{ST}).

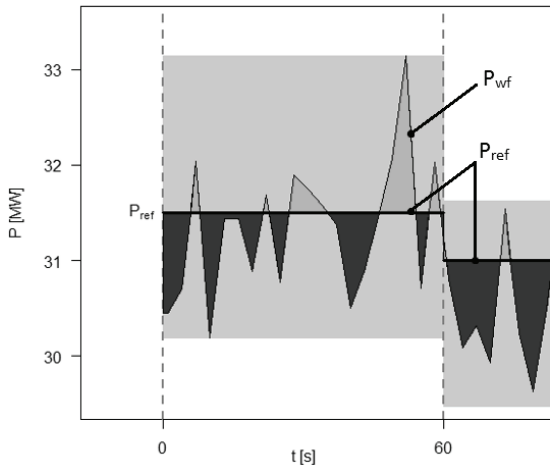

Fig. 1. Fluctuations of active power (P_{wf}) compared to constant power levels (P_{ref}) at 1 min intervals

Fig. 1 illustrates the method and its influence on the output power. The method only allows one rise or fall of power level every minute. Also the magnitude of this fall or rise will virtually always be a lot lower than the magnitude of regular wind farm power fluctuations, thus significantly smoothing power output.

Further sections of this paper include statistical analysis, its purpose, different steps taken, simulation assumptions and the conditions the simulation was conducted in, experimental results in different conditions illustrated with active power fluctuations, histograms of active power variation, a histogram of storage charge levels, detailed tables, summary tables and the impact of the wind farm connected to high-voltage grid.

2. Input data

The data used in this article consist of the result of experimental 10 min measurements of power outputs of two wind farms:

1) Location A Wind Farm (12×3.3 MW = 39.6 MW) – over the period of 31 months.
2) Location B Wind Farm (12×2.5 MW + 2×3.3 MW = 36.6 MW) – over 37 months.

It is important to emphasize that the abovementioned data do not allow for in-depth analysis of output power level dynamics, though they do allow, for active power output estimation over long periods of time (months/years). Knowledge of short-term (one minute and below) power fluctuations is necessary in power prediction and regulation.

Fig. 2a illustrates the averaged values of active power obtained for different wind speeds presented with histograms. Based on these power levels, the power curve was estimated. It is worth noting that the power curve determined on the basis of the measurements differs (is greater) than the power curve declared by the manufacturer. Further study is based on the power curve obtained from the analysis.

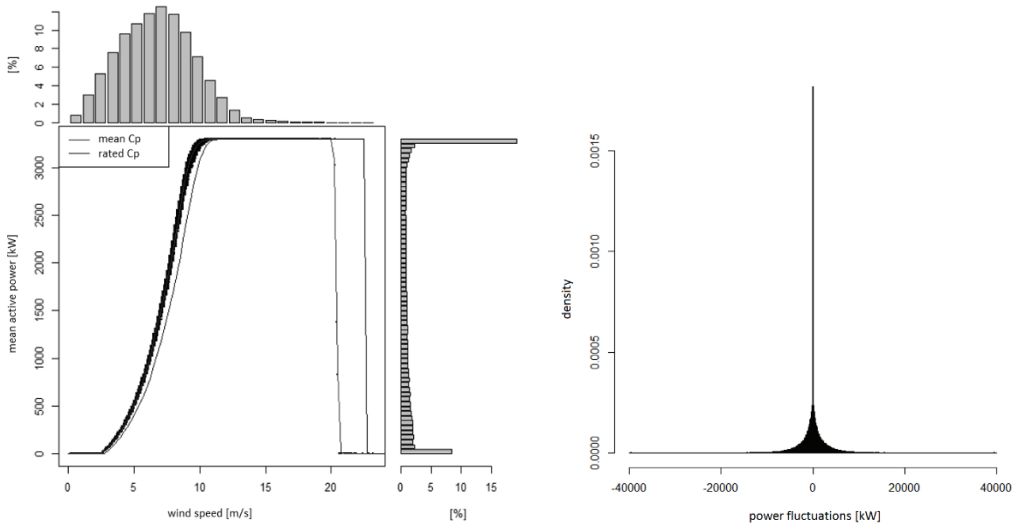

a) b)

Fig. 2. a) Power curves and histograms of wind speed and active power generated by one of the wind farm turbines in Location A; b) Distribution of power changes generated by the wind farm

Having solid information of short-term fluctuations is most important for simulating power distribution and the state of charge for 1 min intervals. Information on 10 min power changes will be the starting point for further assumptions. The graph above (Fig. 2b) shows the distribution of total wind farm power.

The distribution of average power increases over 10 min periods is symmetrical with respect to 0, which means that in every subsequent interval an increase or decrease in output power is equally likely. As shown in Table 1, the changes are within the range of – 39.6 MW to 39.6 MW. Also around 99% of changes are in the range of – 11 MW to 11 MW. Analysis of 99% of cases is especially important, keeping in mind the Polish power distribution regulations. These regulations require the power quality indices to be above a certain level 99% of the time in a one-week period [2]. Table 1 shows how the selection of a storage unit for 99% of cases of power changes between intervals (0.5% to 99.5%) allows for a significant reduction of storage capacity.

Table 1. Ranges of power changes generated by Location A wind farm

Quantile of power change [kW/10 min]						
min	0.5%	25%	50%	75%	99.5%	max
–39600	–11313.09	–875.37	0.0	845.67	11857.93	39600

Identical analysis was conducted for Location B wind farm receiving very similar results.

3. Statistical analysis

The purpose of the simulation is to determine the required storage capacity in different conditions and compare results. Storage capacities will be determined according to the proposed 1 min interval method, which sets every subsequent power level according to Eq. 1.

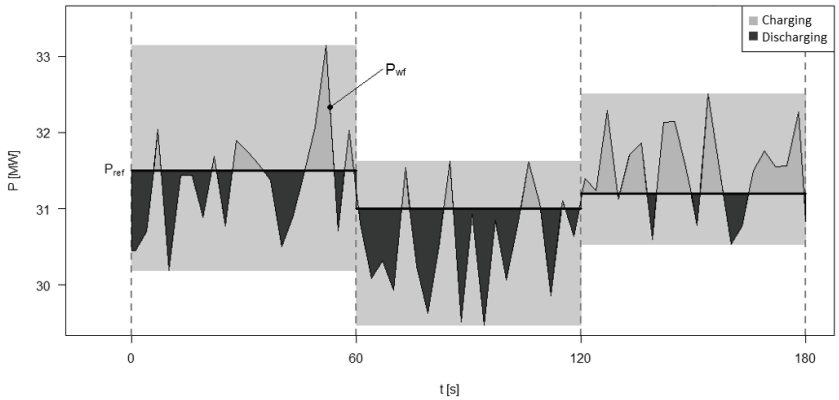

Fig. 3. Power fluctuations of the wind farm without magazine (P_{wf}) and with energy storage (P_{ref})

This model allows for control of the level of charge of the storage by setting prediction of active power in subsequent one-minute intervals for large active power fluctuations with no apparent trend shown in Fig. 3. The obtained power prediction values along with the amount of power required to compensate the power fluctuations constitute the basis for determining the energy storage capacity. For the sake of analysis it is assumed that the base level of charge storage is 50%, which enables charging or discharging of the successive instants of time. The capacity obtained from simulation has to be treated as usable capacity. If the battery type does not allow for total discharge it is necessary to oversize the energy storage.

Fig. 3 illustrates the changes of wind farm power output with and without storage in the form of a graph. Power output with storage is identical to predicted power values (P_{ref}). The maximum fluctuation range is used to analyze the influence of the wind farm on the power quality indices at the point of connection as well as the required storage capacity.

4. Simulation assumptions

Simulation only concerns power changes corresponding to ranges between starting speed and rated rotational speed of the rotor. In other cases with speed exceeding the maximum, the power plant experiences no fluctuation.

In order for the short-term simulations to be meaningful at all there has to be data from fluctuations of said time interval. Therefore, short-term fluctuation magnitude has been simulated and injected into the received data on the basis of experimental study results published

in [11], maintaining consistency of variability indices with provided experimental data. The power curve used in the analysis was estimated using the supplied simulation data.

Supplied data were enriched with simulated short-term data (1 s interval) in a few scenarios to illustrate the effectiveness of the sizing method in favorable and unfavorable conditions and to determine the required storage capacity. Therefore simulations were carried out for power following trend lengths of 1 min and 10 min. Both simulations of trend lengths were carried out in two trend slopes variants of 0.9 MW/10 min to 11 MW/10 min and the range from 0 to 0.9 MW/10 min.

With reference to the above, a list of executed simulations is given below. All four simulations were conducted for both considered wind farms:

Simulation 1 – Trend slope is a random value from the range of 0.9 to 11 MW/10 min. Direction of trend is changed randomly every 10 min.

Simulation 2 – Trend slope is a random value from the range of 0.9 to 11 MW/10 min. Direction of trend is changed randomly every minute.

Simulation 3 – Trend slope is a random value from the range of 0 to 0.9 MW/10 min. Direction of trend is changed randomly every 10 min.

Simulation 4 – Trend slope is a random value from the range of 0 to 0.9 MW/10 min. Direction of trend is changed randomly every minute.

5. Simulation results

Simulation 1 was chosen as an example to illustrate the methodology, with partial results obtained. An identical procedure was performed for all scenarios and both wind farms. Summary results of all variants of conditions are presented in Table 3. The table illustrates the influence of the trend slope and trend length on required the storage capacity (C_{min}).

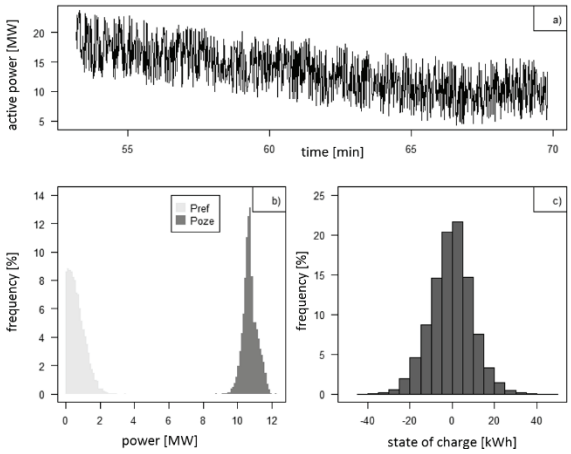

Fig. 4. a) Active power fluctuations over 15 min period; b) histogram of reference and active power level changes; c) histogram of storage charge levels

Table 2. Estimation of the minimum ESS capacity (C_{min}) based on 99% reference power (P_{ref}) changes

Reference power [kW]		**Energy storage [kWh]**				
max	99% range	max	min	99% range		C_{min}
3420.7	2079.2	−44.1	46.4	−26.4	25.8	**52.8**

Table 3. Consolidated list of estimates of the minimum usable energy storage capacity (C_{min}) based on 99% power change reference (P_{ref}) for all the analyzed cases

	Reference power [kW]		**Energy storage [kWh]**				
	max	99%	max	min	99% range		C_{min}
Location A Wind Farm							
Sim. 1.	**3420.7**	2079.2	−44.1	46.4	−26.4	25.8	52.8
Sim. 2.	**3404.7**	1980.5	−43.0	49.5	−25.1	25.1	50.1
Sim. 3.	**2270.6**	1538.3	−35.2	36.4	−19.8	19.6	39.7
Sim. 4.	**2409.5**	1532.3	−35.0	36.5	−19.7	19.8	39.6
Location B Wind Farm							
Sim. 1.	**3252.8**	1697.0	−36.5	39.6	−23.0	21.2	45.9
Sim. 2.	2526.3	1704.0	−36.0	36.4	−21.1	21.2	42.4
Sim. 3.	1969.7	1137.6	−27.8	29.4	−15.0	14.9	30.1
Sim. 4.	1730.1	1148.6	−28.5	27.9	−14.7	15.0	30.1

As shown in Table 3 the proposed method is not influenced greatly by the length of the trend, performing similarly in favorable and unfavorable conditions. However the magnitude of power fluctuations in the said trends understandably influences the calculated capacity.

The robustness of this method is a result of its simplicity. It can be widely used however it is best suited to environments where there are very short or no clear trends. Also as a result of its simplicity it is easy and cheap to implement.

6. Energy storage technologies

Having determined the exact storage parameter requirements, it is now possible to determine the real characteristics of the ESS by choosing the type of ESS technology. Some of the best suited storage systems are considered below with all their characteristics taken into account in respect of both technical and economic aspects. Both wind farms have different power and energy requirements and thus different ideal C parameter. Location A storage requirements would be fulfilled with a technology having charge and discharge currents of 39.4°C as showed below (2).

$$C_{RATE} = \frac{P}{E} = \frac{2079.2[\text{kW}]}{52.8[\text{kWh}]} \cong 39.4\left[\frac{1}{\text{h}}\right], \tag{2}$$

where: C_{RATE} is the C factor, P is the storage power, E is the storage capacity.

Location B storage requirements on the other hand would be satisfied with a technology with charge and discharge currents of 37.1 C as showed below (3).

$$C_{RATE} = \frac{P}{E} = \frac{1704.0[\text{kW}]}{45.9[\text{kWh}]} \cong 37.1\left[\frac{1}{\text{h}}\right]. \tag{3}$$

Li-Ion – Lithium Ion batteries are one of the most common and widely used battery types. They exhibit high specific energy of 200 Wh/kg and 400 Wh/l [12], relatively high power for an electrochemical battery of 300 W/kg, and have a life of around 6000 cycles and discharge current of up to 0.5°C. The dimensioning process is problematic because it requires massive oversizing of the storage system to meet the power requirements.

Location A – Because the Li-Ion technology's characteristics are very different power-wise (0.5°C) than the characteristics for this specific storage implementation (39.4°C) it is required to oversize the Li-Ion storage to get the necessary power, which is shown below.

$$E = \frac{P}{C_{RATE}^{\text{Li-Ion}}} = \frac{2079.2[\text{kW}]}{0.5[\frac{1}{\text{h}}]} \cong 4158.5[\text{kWh}]. \tag{4}$$

The calculated capacity is almost 80 times the required capacity thus the theoretically cheapest technology (900 $/kWh) no longer has the lowest cost.

$$IM_{\text{Li-Ion}} = E \cdot M_{\text{Li-Ion}} = 4158.4[\text{kWh}] \cdot 900\left[\frac{\$}{\text{kWh}}\right] = 3742560\ [\$], \tag{5}$$

where: $IM_{\text{Li-Ion}}$ is the total investment cost of considered Lithium Ion storage, $M_{\text{Li-Ion}}$ is the cost of Lithium Ion batteries per kWh, E is the storage capacity [kWh].

Location B – Similarly in the case of location B power is the limiting factor again. The wind farm has different parameters and all calculations were made in the same way.

$$E = \frac{P}{C_{RATE}^{\text{Li-Ion}}} = \frac{1704\,[\text{kW}]}{0.5[\frac{1}{\text{h}}]} \cong 3408[\text{kWh}], \tag{6}$$

$$IM_{\text{Li-Ion}} = E \cdot M_{\text{Li-Ion}} = 3408.4[\text{kWh}] \cdot 900\left[\frac{\$}{\text{kWh}}\right] = 3067200\ [\$]. \tag{7}$$

The smaller wind farm (location B) naturally requires smaller and less expensive energy storage. Additionally, the 2000 cycle life of a Li-Ion storage system can pose a problem, however the vast capacity can also be used for other uses than fluctuation suppression.

EDLC – Electric double-layer capacitors are based on different phenomena than electrochemical batteries. They accumulate electrical charge rather than storing energy in chemical form, therefore they have much higher rated power, charge and discharge currents and power ramp. Their estimated lifetime often exceeds 1000000 cycles or 20 years [13]. This type of storage is mainly used in short cycle, power intensive uses [14]. EDLC supercapacitors have a high power density of over 10000 W/kg and low energy density or around 5 Wh/kg [14-16].

Location A – Since EDLC supercapacitors have a C factor of over 100°C and power is no longer the limiting factor there is no need to oversize the storage system. The estimated price per kWh is 44500 $/kWh. An additional important point is the 0 to 100% voltage operating range. It becomes necessary to limit the operating range to enable correct operation of converters. For the purpose of calculations the voltage range is reduced to 25 to 100%.

The reduced voltage range has been taken into account by increasing the storage capacity and multiplied by EDLC's cost per kWh to determine the investment cost in the equation:

$$IM_{\text{EDLC}} = \frac{E}{DOD} \cdot M_{\text{EDLC}} = \frac{52.8[\text{kWh}]}{0.75} \cdot 44500 \left[\frac{\$}{\text{kWh}}\right] = 3132800\ [\$]\,. \tag{8}$$

Location B – The same calculations were carried out for Location B.

$$IM_{\text{EDLC}} = \frac{E}{DOD} \cdot M_{\text{EDLC}} = \frac{45.9[\text{kWh}]}{0.75} \cdot 44500 \left[\frac{\$}{\text{kWh}}\right] = 2723400\ [\$]\,. \tag{9}$$

Even taking the reduced depth of charge into account the most expensive technology per kWh becomes more economically justified because no significant oversizing is required. Storage based on supercapacitors will have a very long life, require little to no maintenance and pose no environmental threat.

LIC – Lithium Ion Capacitors are supercapacitors that combine high power with increased capacity from 5 Wh/kg to about 20 Wh/kg. LIC supercapacitors have different voltage ranges than EDLC of around 40% of rated voltage, which guarantees full utilization of stored energy. LIC supercapacitors have low inner resistance, high charge and discharge currents (30C).

Location A – Although lithium supercapacitors have high currents up to 30C the storage will still have to be oversized but a lot less than the Li-Ion storage variation.

$$C_{RATE}^{\text{LIC}} = \frac{P}{E} = \frac{2079.2[\text{kW}]}{30[\frac{1}{\text{h}}]} \cong 69.3[\text{kWh}]\,. \tag{10}$$

LIC are slightly less expensive than regular EDLC supercapacitors costing around 40000 $/kWh resulting in lower investment costs.

$$IM_{\text{LIC}} = E \cdot M_{\text{LIC}} = 69.3[\text{kWh}] \cdot 40000 \left[\frac{\$}{\text{kWh}}\right] = 2771167\ [\$]\,. \tag{11}$$

Location B – The same calculations were carried out for Location B.

$$C_{RATE}^{\text{LIC}} = \frac{P}{E} = \frac{1704.2[\text{kW}]}{30[\frac{1}{\text{h}}]} \cong 56.8[\text{kWh}], \tag{12}$$

$$IM_{\text{LIC}} = E \cdot M_{\text{LIC}} = 56.8[\text{kWh}] \cdot 40000 \left[\frac{\$}{\text{kWh}}\right] = 2272266.7[\$]\,. \tag{13}$$

Although they are not ideal and still require a slightly oversized capacity, lithium supercapacitors seem to have the closest C parameter to the calculated storage system.

Cost Summary – Costs of each individual storage type for the two considered wind farms are shown in the table below.

Table 4. Summary table of initial cost of considered storage technologies

	Investment Cost [$]		
Site	**Li-Ion**	**EDLC**	**LIC**
Location A	3 742 560	3 132 800	2 772 267
Location B	3 067 200	2 723 400	2 272 267

Storage based on LIC supercapacitors is the best suited parameter-wise and also the best from an economic standpoint, both in initial investment and maintenance costs.

7. Impact analysis

According to local regulations [2, 3] sudden power changes (ΔP_{wf}) cannot exceed 1.5% for 100 dips or spikes an hour, and short-term flicker factor (P_{ST}) cannot be greater than 0.35. Both the above-mentioned indices were calculated taking all required transformer and line characteristics into account [17] and are illustrated below.

Table 5. Summary of power quality indices improvement

	ΔP_{wf} [%]		P_{ST}	
	No ESS	With ESS	No ESS	With ESS
Allowed	1.5		0.35	
Location A	1.78	0.50	0.64	0.18
Location B	1.38	0.47	0.5	0.17

As shown in Table 5, the incorporation of ESS in two cases of separate wind farms enables them to operate in the grid, whereas both wind farms would be unable to participate in energy exchange in the power system without energy storage.

8. Conclusions

The situation on the energy market today makes it necessary to take into account penetration of the power grid by renewable energy generation which has a large variation in output power. Thus, the aim of this article has been to present an efficient means of dimensioning of energy storage using a specially developed control algorithm, which has been demonstrated in the case of two selected wind farms.

A storage control method has been developed and proposed in this paper as a way to reduce the required storage capacity of energy storage systems used to decrease wind farm

power fluctuations. The method relies on the setting of one-minute intervals at a constant output level for the wind farm, using the storage system to absorb all deviations from the reference level. The power level of each subsequent interval is calculated taking the mean power value of the previous interval and the level of charge in the ESS as shown in Eq. 1. Such a system causes the output power to be constant, with only a single rise or fall of power between the intervals. In this way, the method reduces power variation and the negative influence of the wind farm on the power system. Depending on local regulations different wind farms may be required to employ an ESS to be allowed to operate within the power system and a control strategy is an effective way to reduce the required storage capacity and thus the cost of the ESS. The simulation study shown the robustness of the developed method and that it can substantially decrease storage capacity even taking into account the most unfavorable conditions of a short or non-distinguishable trend in output power, establishing the variation amplitude as the only impactful factor for this method.

The Lithium Ion Capacitor was chosen as the best suited technology for the designed storage system. It has the right proportion of power and energy, and while it is expensive it is still a better and less problematic option than EDLC and Lithium Ion batteries. EDLC are more expensive and difficult to fully discharge while Li-Ion batteries require massive oversizing and have a shorter estimated life.

The capacities calculated using the developed method are quite small compared to other methods found in the literature. The result is 52.8 kWh for a 39.6 MW wind farm which makes 1.3 kWh per MW and 45.9 kWh for a 36.6 MW which makes 1.25 kWh per MW. The P_{ST} factor has been successfully reduced from 0.5 to 0.17, which is a 68% reduction. For instance in [6] a storage capacity of 5 kWh per MW reduces the standard deviation of generated power by 10% and a storage capacity of 25 kWh per MW reduces the standard deviation by 50% in most cases.

Further studies will consider further development by using a linear, exponential or a polynomial function instead of a constant value. Other more specialized control methods may use more sophisticated prediction algorithms. A different challenge is to adjust the methods to work with hybrid storage systems, which although they need to be developed to suit each individual deployment, look like being the most cost efficient way to satisfy every ESS need.

Acknowledgement

The research was supported by the National Centre for Research and Development (Narodowe Centrum Badań i Rozwoju) within the project No. PBS3/A4/13/2015 entitled “Superconducting magnetic energy storage with a power electronic interface for the electric power systems” (original title: “Nadprzewodzący magazyn energii z interfejsem energoelektronicznym do zastosowań w sieciach dystrybucyjnych”), 01.07.2015 – 30.06.2018.

References

[1] Shokrzadeh S., Jozani M. J., Molinski T., *A statistical algorithm for predicting the energy storage capacity for baseload wind power generation in the future electric grids*, Energy (2015).

[2] *Power grid codes of transmission network. Terms of use, operation and planning of network development. Version 2.1* (in Polish), The consolidated text of the Charter of renovation CK / 1/2012 approved by the President of URE No. DPK-4320-2 (16) / 2010 – 2013 / LK (2013).
[3] PN-EN 50160: 2002 *Voltage characteristics of electricity supplied by public distribution networks*
[4] Luo Y., Shi L., Tu G., *Optimal sizing and control strategy of isolated grid with wind power and energy storage system*, Energy Conversion and Management, vol. 80, pp. 407-415 (2014).
[5] Zhang Y., Tang X., Qi Z., Liu Z., *The Ragone plots guided sizing of hybrid storage system for taming the wind power*, Electrical Power and Energy Systems, vol. 65, pp. 246-253 (2015).
[6] Paatero J.V., Lund P.D., *Effect of Energy Storage on Variations in Wind Power*, Wind Energy, vol. 8, no. 4, pp. 421-441 (2005).
[7] Schneidera M., Bielb K., Pfallera S., Schaedea H., Glockb C.H., *Optimal sizing of electrical energy storage systems using inventory models*, Energy Procedia, vol. 73, pp. 48-58 (2015).
[8] Jaworsky C., Turitsyn K., Backhaus S., *The Effect of Forecasting Accuracy on the Sizing of Energy Storage*, ASME 2014 Dynamic Systems and Control Conference (2014).
[9] Haessig P., Multon B., Ahmed H.B., Lascaud S., Bondon P., *Energy storage sizing for wind power: impact of the autocorrelation of day-ahead forecast errors*, HAL (2013).
[10] Korpaas M., Holen A.T., Hildrum R., *Operation and sizing of energy storage for wind power plants in a market system*, Electrical Power & Energy Systems, vol. 25, issue 8, pp. 599-606 (2003).
[11] Lubośny Z., *Wind farms in the power system, monograph*, WNT Publishing House, Warsaw (2013).
[12] William E.J., Gupta V., Huff M., Linda O., Govar J., *A Comparative Study of Lithium Poly-Carbon Monoflouride (Li/CFx) and Lithium Iron Phosphate (LiFePO4) Battery Chemistries for State of Charge Indicator Design*, Contract M67854-08-C 6530 (2009).
[13] Gualous H., Alcicek G., Diab Y., Hammar A., Venet P., Adams K., Marumo C., *Lithium Ion capacitor characterization and modelling*, ESSCAP' (2008).
[14] Abbey C., Joos G., *Supercapacitor energy storage for wind energy applications*, IEEE Transactions on Industry Applications, vol. 43, no. 3, pp. 769-776 (2007).
[15] Jayalakshmi M., Balasubramanian K., *Simple capacitors to supercapacitors-an overview*, Int. J. Electrochem. Sci., col. 3, no. 11, pp. 1196-1217 (2008).
[16] Díaz-González F., Sumper A., Gomis-Bellmunt O., Villafáfila-Robles R., *A review of energy storage technologies for wind power applications*, Renewable and Sustainable Energy Reviews, vol. 16, no. 4, pp. 2154-2171 (2012).

ARCHIVES OF ELECTRICAL ENGINEERING VOL. 66(2), pp. 279-293 (2017)

DOI 10.1515/aee-2017-0021

Optimized design of a high-power-density PM-assisted synchronous reluctance machine with ferrite magnets for electric vehicles

XIPING LIU, YA LI, ZHANGQI LIU, TAO LING, ZHENHUA LUO

School of Electrical Engineering and Automation
Jiangxi University of Science and Technology
No.86 Hongqi Road, Ganzhou, China
e-mail: ly122810@163.com

(Received: 14.04.2016, revised: 17.12.2016)

Abstract: This paper proposes a permanent magnet (PM)-assisted synchronous reluctance machine (PMASynRM) using ferrite magnets with the same power density as rare-earth PM synchronous motors employed in Toyota Prius 2010. A suitable rotor structure for high torque density and high power density is discussed with respect to the demagnetization of ferrite magnets, mechanical strength and torque ripple. Some electromagnetic characteristics including torque, output power, loss and efficiency are calculated by 2-D finite element analysis (FEA). The analysis results show that a high power density and high efficiency of PMASynRM are obtained by using ferrite magnets.

Key words: permanent magnet (PM)-assisted synchronous reluctance machine, ferrite magnet, demagnetization, mechanical strength, torque ripple, finite element analysis

1. Introduction

Recently, a permanent magnet synchronous machine (PMSM) that contains rare-earth permanent magnets (PMs) is popular for its hybrid electrics vehicles (HEVs) and electric vehicles (EVs) [1-2]. Many kinds of PMSMs for traction application are actively studied [3-5]. PMSM, which use rare-earth PMs have some advantages, such as high torque density, high power density, a high power factor, a wide constant power speed range, and high efficiency, etc. However, there is a limitation for rare-earth PMs because of the high price of rare-earth material. Therefore, the electrical machines with less or no rare-earth PMs are required in EVs and HEVs application.

The reluctance motor is one type of electrical machine without PMs. A switched reluctance motor (SRM) has some advantages, such as a simple structure, rotor robustness, the potential to operate at high temperature and torque-speed range, which can be competitive to PMSMs employed in EVs and HEVs [6-10]. Nevertheless, SRM has the problem with a high level of vibration and acoustic noise in general [11-13]. A synchronous reluctance machine (SynRM)

is also a candidate for a rare-earth-free machine, but its torque density, power density, power factor and efficiency are inferior compared to PMSMs [14-15]. By adding the proper amount of PMs in SynRM, the torque density and power density of a PM-assisted SynRM (PMASynRM) can be improved [16-28]. The total costs of PMASynRM with ferrite magnets can be reduced because some rare-earth materials such as neodymium and dysprosium, needed for automotive applications are not used in this machine.

The rotor structure of PMASynRM must be designed to achieve satisfying high power density, high efficiency, and a wide speed range used in EVs and HEVs. Furthermore, the irreversible demagnetization of the ferrite magnets in cold weather and the mechanical strength of rotor at the maximum speed should be considered [29-32]. Meanwhile, the torque ripple should also be taken into account for the design of PMASynRM based on a finite-element method (FEM).

In this paper, some characteristics of PMASynRM with ferrite magnets are studied, including the demagnetization behavior, mechanical strength, torque ripple, torque, output power, loss and efficiency.

2. Target and structure of PMASynRM with ferrite Magnet

2.1. Target

Table 1 shows the specification of an interior permanent magnet synchronous machine (IPMSM) in HEV (Toyota Prius 2010) [33-34], which is called a target IPMSM in this paper. The maximum output power is 60 kW, and its speed varies from 2768 to 13900 r/min (maximum speed). The outer diameter of the stator is 264 mm, and the stack length is 50 mm. However, the axial length of IPMSM considering the end winding is 108 mm. The volume of the motor core is 5.9 L, which does not include the casing and cooling system. A power density is 10.17 kW/L. The power density of 10.17 kW/L and a maximum speed of 14000 r/min are the targets of the proposed PMASynRM. The highest efficiency of the target IPMSM is estimated to 95% for another target of PMASynRM.

Table 1. HEV IPMSM and target

Item (Unit)	Value
Stator outer diameter (mm)	264
Stack length (mm)	50
Machine axial length (mm)	108
Air gap length (mm)	0.73
Max. DC side voltage (V)	650
Max. current (A)	141*
Max. output power (kW)	60
Max. power speed range (r/min)	2768-13900*
Max. torque (N·m)	205

Max. power density (kW/L)	10.17
Max. torque density (N·m/L)	34.67
Max. efficiency (%)	95*
Efficiency at knee point (%)	91*
Winding resistance at 21°C (Ω)	0.077
Stator turns per coil	11
Winding type (%)	distributed
Slot fill factor (%)	54*

*Estimated value

The aim of this paper is to investigate a PMASynRM design competitive to the Prius 2010 IPMSM in the point of view of power density, efficiency, a torque-speed region and maximum torque. The proposed PMASynRM with ferrite magnets (Y30BH) are shown in Table 2. The coercive force of ferrite magnet is 232 kA/m at 20°C, which is about one-fourth of common rare-earth PMs. Therefore, for achieving high power density, high torque density and high efficiency, a rational rotor structure of PMASynRM should be designed into a multi-layer structure and embed more ferrite magnets by making full use of reluctance torque.

To achieve the maximum torque, the stack length of PMASynRM is one of the most important factors. The number of turns per coil is 8, which is less than that of Prius 2010 IPMSM. The stator slot depth of PMASynRM is shallower than that of Prius 2010 IPMSM, which results the stator outer diameter of PMASynRM is smaller. As shown in Fig. 1, the stator outer diameter of PMASynRM is set to 245 mm comparing to the stator outer diameter 264 mm of Prius 2010 IPMSM. However, the axial length of the motor is 128 mm, and the stack length is 70 mm, so the volume of PMASynRM's core is same as Prius 2010 IPMSM. In addition, the air gap length, maximum dc-side voltage and winding type is the same. Nevertheless, the winding resistance is 0.0646 Ω at 21°C, which is less than that of Prius 2010 IPMSM.

Table 2. The proposed PMASynRM

Item (Unit)	**Value**
Number of poles	8
Stator outer diameter (mm)	245
Machine axial length (mm)	128
Stack length (mm)	70
Air gap length (mm)	0.73
Max. DC side voltage (V)	650
Max. output power (kW)	60
Max. power speed range (r/min)	3000-14000
Max. torque (N·m)	205
Max. efficiency (%)	95
PM material	Y30BH

Coercive force of PM (kA/m)	232
Winding type	distributed
Stator turns per coils	8
Slot fill factor (%)	52.3
Winding resistance at 21°C (Ω)	0.0646

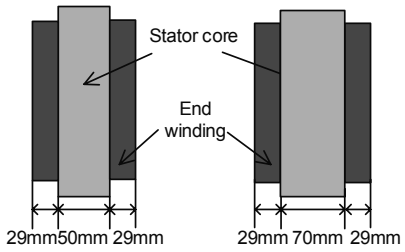

Fig. 1. Machine axial length: Prius 2010 IPMSM (a); the proposed PMASynRM (b)

2.2. Structure of PMASynRM with ferrite magnets

Fig. 2 shows the stator of PMASynRM, which has 48 slots and a distributed winding. In this paper, the optimal rotor structure is discussed for the irreversible demagnetization, torque ripple and mechanical strength at the maximum speed of 14000 r/min.

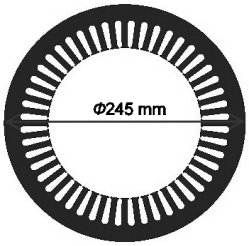

Fig. 2. Stator of the proposed PMASynRM

Fig. 3 shows several representative design schemes of a rotor. The rotor structure mainly includes the shape and thickness of ferrite magnets, the shape of flux barriers, the size of central ribs and iron bridges. Fig. 3(a) shows Rotor-A without center ribs, which includes ferrite magnets, flux barriers and iron bridges. Rotor-B is given in Fig. 3(b), which has the center rib to add the mechanical strength of the rotor. Considering the processing of ferrite magnets and irreversible demagnetization, the forth-layer PMs of Rotor-C is designed to a right angle. Moreover, an appropriate flux barrier is designed in center ribs in order to reduce magnetic leakage and achieve sufficient mechanical strength. The same size of PMs and center ribs are adopted for Rotor-C, Rotor-D and Rotor-E, but the shape of flux barriers in the second-layer and third-layer is different. In summary, the rotor structure should be designed by trial and error for decreasing the demagnetization and obtaining sufficient mechanical strength of the rotor.

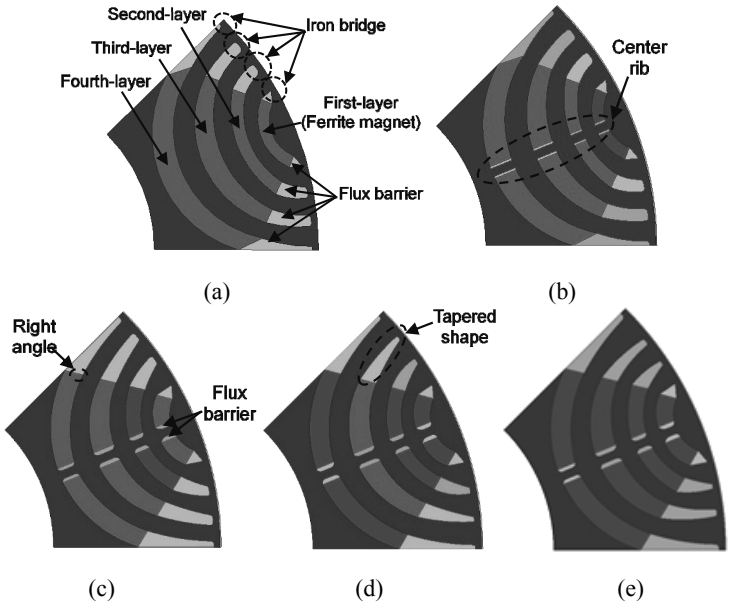

Fig. 3. Rotor structure of the examined PMASynRM: Rotor-A (a); Rotor-B (b); Rotor-C (c); Rotor-D (d); Rotor-E (e)

3. Rotor optimization

3.1. Evaluation of irreversible demagnetization

Fig. 4 shows the demagnetization curve of ferrite magnet (Y30BH) used in the proposed PMASynRM. The irreversible demagnetization will occur when the flux density of PMs is lower than the critical flux density at the knee of demagnetization curve. For the purpose of calculating the demagnetization, the flux density of PMs was evaluated. The rate of ireversible demagnetization is defined as the ratio of demagnetizing PMs' area to the total PMs' area, which is called the "demagnetization rate" (DR). In order to assume the severest condition, the temperature of PMs is set to −40°C, the current in the opposite direction of PM's demagnetization magnetomotive force (MMF) is increased to 585 A, which is 1.5 times of the maximum current. The critical flux density of irreversible demagnetization was assumed to be 0.15 T at −40°C (with margin).

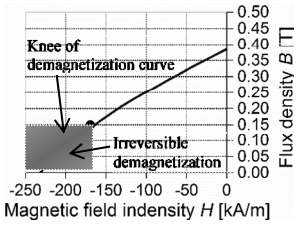

Fig. 4. Demagnetization curve of ferrite magnet (Y30BH) at -40 °C

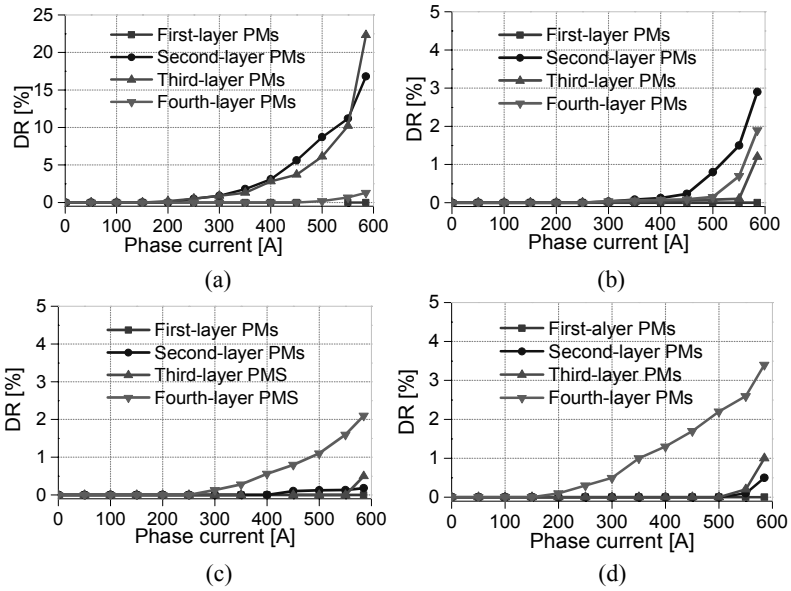

Fig. 5. Demagnetization rate of PMASynRM at −40°C: Rotor-B (a); Rotor-C (b); Rotor-D (c); Rotor-E (d)

The demagnetization rate at −40°C for some rotors is shown in Fig. 5. The demagnetization of Rotor-A is ignored because it has an obvious problem of mechanical strength. As shown in Fig. 5(a), the demagnetization rate of third-layer ferrite magnet in Rotor-B reaches 22.3% at 585 A. The demagnetization rate can be improved by changing the rotor structure such as shape, thickness of ferrite magnets and shape of flux barriers. The flux can flow along the iron bridges easily because the reluctance becomes small. As a result, the demagnetization rate of fourth-layer and second-layer ferrite magnets in Rotor-C, Rotor-D and Rotor-E is larger. However, the demagnetization rate is no more than five percent in fourth-layer and second-layer PMs.

Fig. 6 shows the contour plots of flux density at 585 A. It shows that the side part of ferrite magnets in the second-layer and third-layer are irreversible demagnetized in Fig. 6(a). Moreover, the demagnetization also occured in the side part of ferrite magnets in Rotor-C, Rotor-D and Rotor-E, as shown in Figs. 6(b), (c) and (d) respectively.

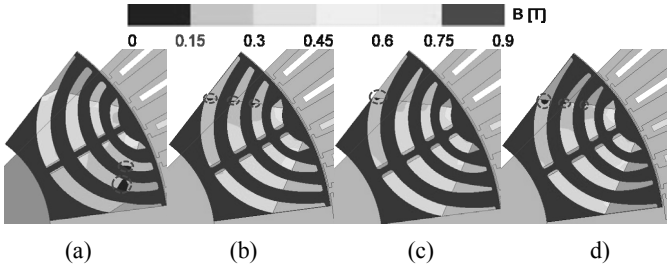

Fig. 6. Contour plots of flux density at 585 A: Rotor-B (a); Rotor-C (b); Rotor-D (c); Rotor-E (d)

This is because the flux due to the MMF from the stator winding flows primarily through the center ribs and iron bridges. However, the flux also flows over the flux barriers because the thickness of the flux barrier is smaller than that of the ferrite magnet. The result shows that the flux density is too low in the side part of the ferrite magnets, and irreversible demagnetization is occurred. Therefore, the rotor structure such as the shape and thickness of the ferrite magnets, the width of iron bridges and center ribs, the shape of flux barriers were modified to reduce a demagnetization rate by trial and error.

3.2. Evaluation of mechanical strength

The mechanical strength of rotor is examined by FEM. Fig. 7 shows the distribution of the von Mises stress at the maximum speed. The ferrite magnets were hidden in those pictures. Rotor-C, Rotor-D and Rotor-E have the same width of center ribs and iron bridges, as the maximum stress area occurred in center ribs and iron bridges. However, it has been confirmed that the proposed rotor structure can withstand the centrifugal force at the maximum speed.

Fig. 7. Von Mises stresses distribution: Rotor-C (a); Rotor-D (b); Rotor-E (c)

3.3. Torque ripple minimization

The torque ripple for adopting the different rotor structures is shown in Fig. 8. The torque ripple ratio is defined as ratio of peak-to-peak instantaneous torque to average torque.

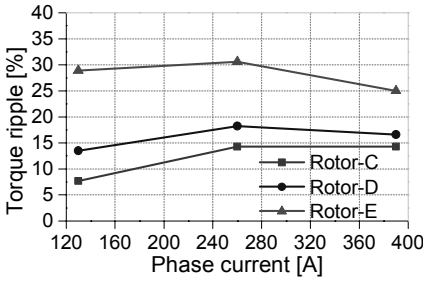

Fig. 8. Torque ripple characteristics

Although a little difference among Rotor-C, Rotor-D and Rotor-E, which is in the shape of flux barriers in the second-layer and third-layer, may cause a great effect on the flux density and reluctance variations around the air gap. Despite a low torque ripple of Rotor-C compared

to Rotor-D and Rotor-E, the torque ripple is still more than 10% of the maximum torque. Therefore, the asymmetric flux barrier was used in PMASynRM to reduce the torque ripple [14, 35-40]. Rotor-F and Rotor-G were proposed in Fig. 9. Rotor-G combines the structures of Rotor-C and Rotor-F, and it has an asymmetric flux barrier in the second-layer.

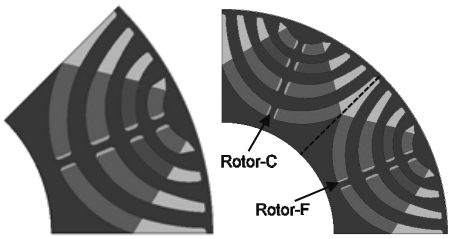

Fig. 9. Rotor structures with different flux barrier shape: Rotor-F (a); Rotor-G (b)

Current I_{em} (rms value of phase current) was set to 130, 260, 390 A as well as the instantaneous torque characteristics of Rotor-C, Rotor-F and Rotor-G are shown in Fig. 10, and the torque ripple characteristics are given in Fig. 11. Despite of the fact that the torque ripple (only 7.7%) of Rotor-C is low when I_{em} is 130 A, it reaches 14.3% when I_{em} is 260 and 390 A. The torque ripple of Rotor-F is 8.5% at the maximum output torque. However, the torque ripple is more than 10 percent when I_{em} is 130 and 260 A. Nevertheless, a mutual compensation of the transient torque is realized for Rotor-G by using asymmetric flux barriers, and its torque ripple can be reduced significantly, as shown in Figs. 10(a), (b) and (c).

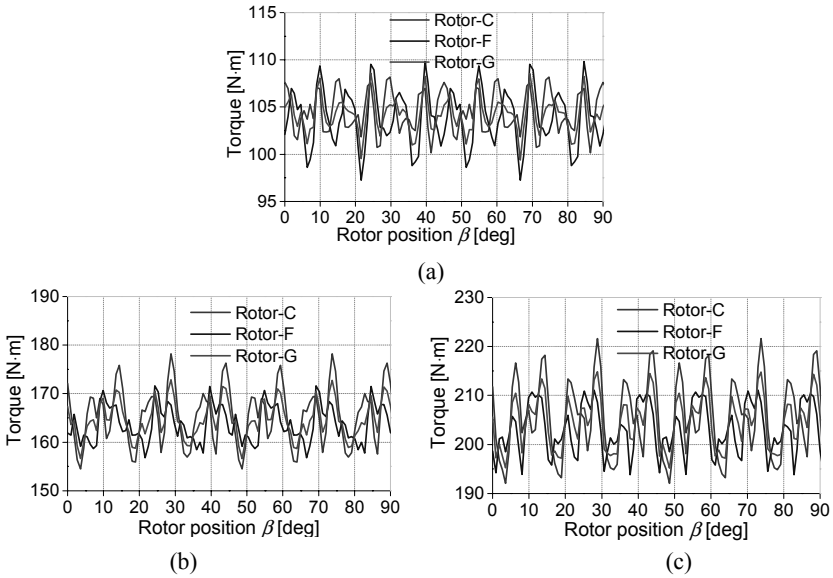

Fig. 10. Instantaneous torque characteristics: I_{em}=130 A (a); I_{em}=260 A (b); I_{em}=390 A (c)

Although the torque ripple of PMASynRM increased to 8.8%, 9.6% when I_{em} was 130 and 390 A, respectively, it is less than 10%. In summary, Rotor-G with asymmetric flux barriers has a great effect on reducing torque ripple. Meanwhile, the average torque of Rotor-G is not reduced by comparing with Rotor-C and Rotor-F, as shown in Fig. 12. This characteristic demonstrates that the proposed PMASynRM has a lower torque ripple by using asymmetric flux barriers, which is competitive to theToyota Prius 2010 IPMSM.

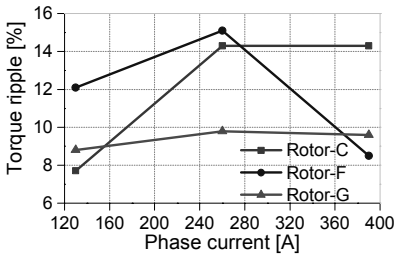

Fig. 11. Torque ripple characteristics

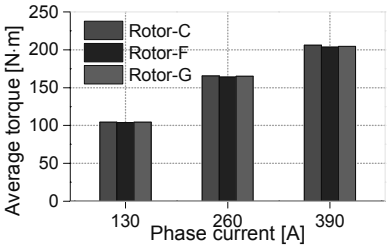

Fig. 12. Average torque

4. Performance evaluation

4.1. Torque and output power versus speed

Because the dc-side voltage is assumed to be 650 V, the voltage limit V_{em} (rms value of line-to-line voltage) was set to 450 V. The current limit I_{em} was set to 130, 260 and 390 A. It is noted that I_e becomes smaller than I_{em} when the maximum torque per ampere (MTPA) control is applied during flux-weakening operation, and I_{em} is a ceiling value of current.

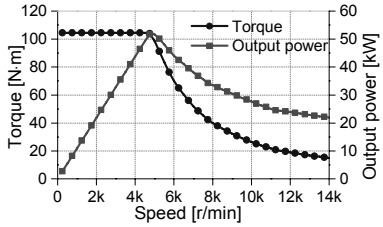

(a)

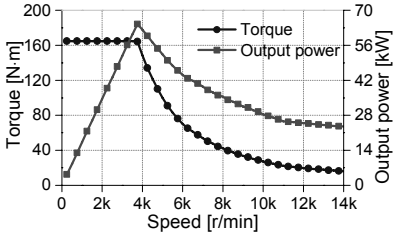

(b)

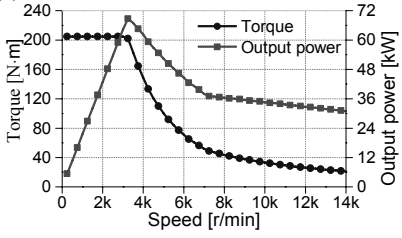

(c)

Fig. 13. Torque and output power versus speed: I_{em} = 130 A (a); I_{em} = 260 A (b); I_{em} = 390 A (c)

The torque and output power versus speed relationships are shown in Fig. 13. With the proposed rotor structure, the maximum output power is 49.2 kW at 4500 r/min in Fig. 13(a), and constant torque is 104.4 N·m. When I_{em} was set to 260 A, the maximum output power reaches to 64.4 kW at 3750 r/min. However, the peak torque is only 164.8 N·m, which is less than the target of the maximum output torque 205 N·m, as shown in Fig. 13(b). Fig. 13(c) shows that the maximum output power is 68.7 kW at 3250 r/min, which reaches the target maximum output power. Meanwhile, the maximum torque is 204.8 N·m when I_{em} is 390 A, which is very close to the target torque. It indicates that a reasonable design of the rotor structure in the proposed PMASynRM could achieve a high power density and high torque density by using low-cost ferrite magnets.

4.2. Loss and efficiency characteristics

The loss and efficiency versus speed relationships is given in Fig. 14. The iron loss, copper loss and efficiency were calculated by the following equations

$$W_i = W_h + W_e, \tag{1}$$

$$W_c = 3R_a I_e^2, \tag{2}$$

$$\eta = \frac{\omega T - W_i}{\omega T + W_c} \times 100\%, \tag{3}$$

where W_h is the hysteresis loss [W], W_e is the eddy current loss [W], W_i is the iron loss [W], W_c is the copper loss [W], R_a is the armature winding resistance [Ω], I_e is the RMS value of phase current [A], η is the efficiency [%], T is the torque [N·m], and ω is the mechanical angular velocity [rad/s].

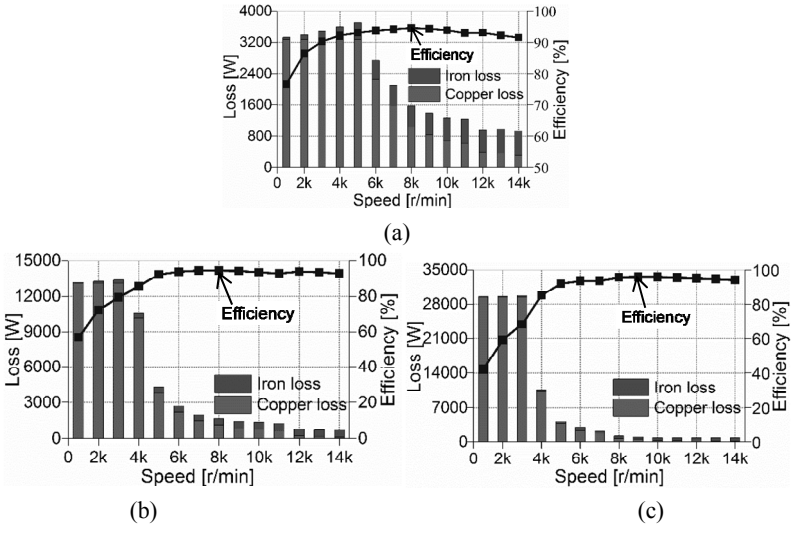

Fig. 14. Loss and efficiency versus speed: I_{em} = 130 A (a); I_{em} = 260 A (b); I_{em} = 390 A (c)

As shown in Fig. 14(a), when the speed exceeds 4000 r/min, the copper loss is signify-cantly decreased by a field-weakening control strategy. Although the iron loss has been in-creased, the total loss is reduced, which leads to the efficiency of PMASynRM increased during flux weakening operation at high speed. The iron loss gradually increases with speed up to 4000 r/min, as shown in Figs. 14(b) and (c). This is because the applied MTPA control is above 4000 r/min. In the speed region from 4000 to 14000 r/min, the current gradually decreases even if the current limit value I_{em} is set to 260 or 390 A, and copper losses decreases with the increase of speed. The maximum efficiency is 95.6% at the speed of 7000 r/min when the rated current is 260 A, which satisfies the target of the maximum efficiency.

4.3. Efficiency map

The efficiency maps of the proposed PMASynRM is shown in Fig. 15. V_{em} is set to 450 V, and I_{em} is set to 130, 260 and 390 A. The maximum efficiency reaches to 95.8%, 96.6% and 96.9%, when I_{em} is set to 130, 260 and 390 A, respectively. The efficiency of PMASynRM is over 90% across a wide operating range, as shown in Figs. 15(a), (b) and (c). When the maximum phase current is 390 A, the maximum efficiency is 96.9% and the maximum torque is 204.8 N·m, which satisfies the target efficiency and the target maximum torque in Table 2.

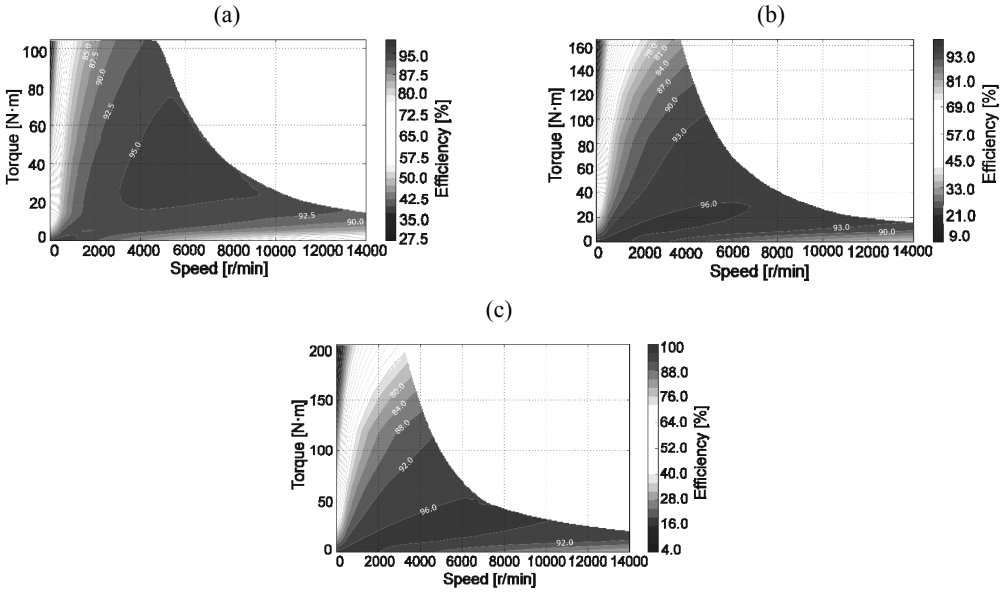

Fig. 15. Efficiency maps of the proposed PMASynRM: I_{em} = 130 A (a); I_{em} = 260 A (b); I_{em} = 390 A (c)

5. Compare to Prius 2010 IPMSM

Some parameters of PMs were compared in Toyota Prius 2010 IPMSM and the proposed PMASynRM in Table 3, which includes PM dimensions, magnet volume, the maximum work-

ing temperature, price and cost of PMs. It should be noted that the coercive force of N36_Z20 is about four times of Y30BH. However, the price of N36_Z20 is 4342.1 ¥ per kilogram, which caused that the total costs of PMs in Toyota Prius 2010 IPMSM are 116 times of the proposed PMASynRM. Furthermore, the maximum working temperature of ferrite magnets (Y30BH) is 460°C, which is about two times of N36_Z20. Therefore, the proposed PMASynRM with low-cost ferrite magnets could meet high-power density, high torque density, high efficiency and a wide range speed operation, and a higher working environment temperature is obtained.

Table 3. Some parameter of PMs

Parameter	**Toyota Prius2010 IPMSM**	**Proposed PMASynRM**
PM material	N36_Z20	Y30BH
Coercive force of PM (kA/m)	920	232
PM dimensions (mm)	49.3×17.88×7.16*	arc-shaped
Magnet volume (cm^3)	100.98	262.08
Total mass of magnets (kg)	0.768	1.991
PM price** (¥)	4342.1	14.4
PM total cost (¥)	3334.7	28.7
Max. working temperature (°C)	200	460

*One magnet **2016

6. Conclusions

The novel rotor structures of PMASynRM with ferrite magnets have been examined in this paper, which considered irreversible demagnetization, mechanical strength and torque ripple. In order to reduce the torque ripple, the asymmetric flux barrier was used in the rotor, and the torque ripple is less than 10% when I_{em} is 130, 260 and 390 A. Some characteristics including the torque, output power, loss and efficiency were calculated by FEA. The maximum efficiency is 96.9% when adopting the maximum phase current, which satisfies the target efficiency of 95%. Meanwhile, the high-power density and high torque density of PMASynRM are obtained compared to Prius 2010 IPMSM. It can be found that the torque, efficiency and operating speed-torque region of PMASynRM are competitive when applied in HEVs/EVs. However, its phase current is increased and the power factor is low, which needs further study or looking for new materials to replace the rare-earth PMs. A prototype of the proposed PMASynRM should be manufactured to validate the loss, maximum torque, output power, efficiency, and thermal analysis.

Acknowledgements
This work is supported by National Natural Science Foundation of P.R.China (No.51267006), Plan Project of Jiangxi Province of P.R.China (20151BBE50109, 20153BCB23012), Program of Qingjiang Excellent Young Talents (JXUST).

References

[1] Jurkovic S., Rahman K.M., Savagian P.J., *Design, Optimization and Development of Electric Ma chine for Traction Application in GM Battery Electric Vehicle*, 2015 IEEE International Electric Machine & Drives Conference (IEMDC), Coeur d'Alene, USA, pp. 1814-1819 (2015).

[2] Santiago J.D., Bernhoff H., Ekergard B., Eriksson S., Ferhatovic S., Waters R., Leijon M., *Electrical Motor Drivelines in Commercial All-Electric Vehicles: A Review*, IEEE Transactions Vehicular Technology, vol. 61, no. 2, pp. 475-484 (2012).

[3] Nerg J., Rilla M., Ruuskanen V., Pyrhonen J., Ruotsalainen S., *Direct-Driven Interior Magnet Permanent-Magnet Synchronous Motors for a Full Electric Sports Car*, IEEE Transactions Industrial Electronics, vol. 61, no. 8, pp. 4286-4294 (2014).

[4] Galioto S.J., Reddy P.B., EL-Refaie A.M., Alexander J. P., *Effect of Magnet Types on Performance of High-Speed Spoke Interior-Permanent-Magnet Machines Designed for Traction Applications*, IEEE Transactions on Industry Applications, vol. 51, no. 3, pp. 2148-2150 (2015).

[5] Abdel-Khalik A.S., Ahmed S., Massoud A.M., *Effect of Multilayer Windings with Different Stator Winding Connections on Interior PM Machine for EV Applications*, IEEE Transactions on Magnetics, vol. 52, no. 2, 8100807 (2016).

[6] Ding W., Hu Y., Wu L., *Analysis and Development of Novel Three-Phase Hybrid Magnetic Paths Switched Reluctance Motors Using Modular and Segmental Structures for EV Applications*, IEEE/ASME Transactions on Mechatronics, vol. 20, no. 5, pp. 3427-2451 (2015).

[7] Kiyota K., Kakishima T., Sugimoto H., Chiba A., *Comparison of the Test Result and 3D-FEM Anlysis at the Knee Point of a 60 kW SRM for a HEV*, IEEE Transactions on Magnetics, vol. 49, no. 5, pp. 2291-2294 (2013).

[8] Nezamabadi M.M., Afjei E., Torkaman H., *Design, Dynamic Electromagnetic Analysis, FEM, and Fabrication a New Switched Reluctance Motor with Hybrid Motion*, IEEE Transactions on Magnetics, vol. 52, no. 4, 8201708 (2016).

[9] Takeno M., Chiba A., Hoshi N., Ogasawara S., Takemoto M., Rahman M.A., *Test Results and Torque Improvement of the 50-kW Switched Reluctance Motor Designed for Hybrid Electric Vehicles*, IEEE Transactions on Industry Applications, vol. 48, no. 4, pp. 2874-2883 (2012).

[10] Chiba A., Takano Y., Takeno M., Imakama T., Hoshi N., Takemoto M., Ogasawara S., *Torque Density and Efficiency Improvements of a Switched Reluctance Motor Without Rare-Earth Material for Hybrid Vehicles*, IEEE Transactions on Industry Applications, vol. 47, no. 3, pp. 1240-1246 (2011).

[11] Kiyota K., Kakishima T., Chiba A., Rahaman M.A., *Cylindrical Rotor Design for Acoustic Noise and Windage Loss Reduction in Switched Reluctance Motor for HEV Applications*, IEEE Transactions on Industry Applications, vol. 52, no. 1, pp. 154-162 (2016).

[12] Bayless J., Kurihara N., Sugimoto H., Chiba A., *Acoustic Noise Reduction of Switched Reluctance Motor with Reduced RMS Current and Enhanced Efficiency*, IEEE Transactions on Energy Conversion, vol. 31, no. 2, pp. 1-10 (2015).

[13] Rasmussen P.O., Andreasen J.H., Pijanowski J.M., *Structural Stator Spaces-A Solution for Noise Reduction of Switched Reluctance Motors*, IEEE Transactions on Industry Applications, vol. 40, no. 2, pp. 574-561 (2004).

[14] Ooi S., Morimoto S., Sanada M., Inoue Y., *Performance Evaluation of a High-Power-Density PMASynRM With Ferrite Magnets*, IEEE Transactions on Industry Applications. vol. 49, no. 3, pp. 1308-1314 (2013).

[15] Obata M., Morimoto S., Sanada M., Inoue Y., *Performance of PMASynRM With Ferrite Magnets for EV/HEV Applications Considering Productivity*, IEEE Transactions on Industry Applications, vol. 50, no. 4, pp. 2427-2435 (2014).

[16] Morimoto S., Ooi S., Inoue Y., Sanada M., *Experimental Evaluation of a Rare-Earth-Free PMASynRM With Ferrite Magnets for Automotive Applications*, IEEE Transactions on Industrial Electronics, vol. 61, no. 10, pp. 5749-5756 (2014).

[17] Sanada M., Inoue Y., Morimoto S., *Structure and Characteristics of High-Performance PMASynRM with Ferrite Magnets*, Electrical Engineering in Japan, vol. 187, no. 1, pp. 42-50 (2014).

[18] Cai H., Guan B., Xu L., *Low-Cost Ferrite PM-Assisted Synchronous Reluctance Machines for Electric Vehicles*, IEEE Transactions on Industrial Electronics, vol. 61, no. 10, pp. 5741-5748 (2014).
[19] Kim W.H., Kim K.S., Kim S.J., D. Kang W., Go S.C., Chun Y.D., Lee J., *Optimal PM Design of PMASynRM for Wide Constant-Power Operation and Torque Ripple Reduction*, IEEE Transactions on Magnetics, vol. 45, no. 10, pp. 4660-4663 (2009).
[20] Boldea I., Tutelea L., Pitic C.I., *PM-Assisted Reluctance Synchronous Motor/Generator (PM-RSM) for Mild Hybrid Vehicles: Electromagnetic Design*, IEEE Transactions on Industry Applications, vol. 40, no. 2, pp. 492-498 (2004).
[21] Kondo K., Kusase S., Maekawa T., Hanada K., *A New PM-Assisted Synchronous Reluctance Motor With Three-Dimensional Trench Air Gap*, IEEE Transactions on Industry Applications, vol. 50, no. 4, pp. 2485-2492 (2014).
[22] Bianchi N., Fornasiero E., Soong W., *Selection of PM Flux Linkage for Maximum Low-Speed Torque Rating in a PM-Assisted Synchronous Reluctance Machine*, IEEE Transactions on Industry Applications, vol. 51, no. 5, pp. 3600-3608 (2015).
[23] Chen X., Wang J., Lazari P., Chen L., *Permanent Magnet Assisted Synchronous Reluctance Machine with Fractional-Slot Winding Configurations*, 2013 IEEE International Electric Machine & Drives Conference (IEMDC), Chicago, USA, pp. 374-381 (2013).
[24] Yamazaki K., Tamiya S., Utsuno K., Shima K., Fukami T., Sato M., *Rotor Shape Optimization for Output Maximization of Permanent-Magnet-Assisted Synchronous Machines*, IEEE Transactions on Industry Applications, vol. 51, no. 4, pp. 3077-3085 (2015).
[25] Carraro E., Morandin M., Bianchi N., *Traction PMASR Motor Optimization According to a Given Driving Cycle*, IEEE Transactions on Industry Applications, vol. 52, no. 1, pp. 209-216 (2016).
[26] Kim S.I., Park S., Park T., Cho J., Kim W., Lim S., *Investigation and Experimental Verification of a Novel Spole-Type Ferrite-Magnet Motor for Electric-Vehicles Traction Drive Applications*, IEEE Transactions on Industrial Electronics, vol. 61, no. 10, pp. 5763-5770 (2014).
[27] Barcaro M., Bianchi N., Magnussen F., *Permanent-Magnet Optimization in Permane-Magnet-Assisted Synchronous Reluctance Motor for a Wide Constant-Power Speed Range*, IEEE Transactions on Industrial Electronics, vol. 59, no. 6, pp. 2495-2502 (2012).
[28] Lohninge R., Grabner H., Weidenhozer G., Silber S., Amrhein W., *Modeling, Simulation, and Design a Permanent -Magnet-Assisted Synchronous Reluctance Machine*, IEEE Transactions on Industry Applications, vol. 51, no. 1, pp. 196-203 (2015).
[29] Huang H., Hu Y., Xiao Y., Lyu H., *Research of Parameters and Anti-demagnetization of Rare-Earth-Less Permanent Magnet-Assisted Synchronous Reluctance Motor*, 2015 IEEE Magnetics Conference (INTERMAG), Beijing, China, 8112504, (2015).
[30] Vagati A., Boazzo B., Guglielmi P., Pellegrino G., *Design of Ferrite-Assisted Synchronous Reluctance Machines Robust Toward Demagnetization*, IEEE Transactions on Industry Applications, vol. 50, no. 3, pp. 1768-1779 (2014).
[31] Sanada M., Inoue Y., Morimoto S., *Rotor Structure for Reducing Demagnetization of Magnet in a PMASynRM with Ferrite Permanent Magnet and its Characteristics*, 2011 IEEE Energy Conversion Congress and Exposition (ECCE), Phoenix, AZ, pp. 4189-4194 (2011).
[32] Barcaro M., Meneghetti G., Bianchi N., *Structural Analysis of the Interior PM Rotor Considering Both Static and Fatigue Loading*, IEEE Transactions on Industry Applications, vol. 50, no. 1, pp. 253-260 (2014).
[33] Kiyota K., Chiba A., *Design of Switched Reluctance Motor Competitive to 60-Kw IPMSM in Third-Generation Hybrid Electric Vehicle*, IEEE Transactions on Industry Applications, vol. 48, no. 6, pp. 2303-2309 (2012).
[34] Urase K., Yabu N., Kiyota K., Sugimoto H., Chiba A., Takemoto M., Ogasawara S., Hoshi N., *Energy Efficiency of SR and IPM Generators for Hybrid Electric Vehicle*, IEEE Transactions on Industry Applications, vol. 51, no. 4, pp. 2874-2883 (2015).
[35] Boldea I., Tutalea L.N., Parsa L., Dorrell D., *Automotive Electric Propulsion Systems With Reduced or No Permanent Magnets: An Overview*, IEEE Transactions on Industrial Electronics, vol. 61, no. 10, pp. 5696-5711 (2014).

[36] Ren W., Xu Q., Li Q., Chen L., *Reducing Cogging Torque and Suppressing Torque Ripple in PMASynRM for EV/HEV Applications*, Transportation Electrification Asia-Pacific (ITEC Asia-Pacific), 2014 IEEE Conference and Expo., Beijing, China, pp. 1-6 (2014).

[37] Wang K., Zhu Z.Q., Ombach G., Koch M., Zhang S., Xu J., *Torque ripple reduction of synchronous reluctance machines: using asymmetric flux-barrier*, COMPEL: The International Journal for Computation an Mathematics in Electrical and Electronic Engineering, vol. 34, no. 1, pp. 18-31 (2015).

[38] Sanada M., Hiramoto K., Morimoto S., Takeda Y., *Torque Ripple Improvement for Synchronous Reluctance Motor Using an Asymmetric Flux Barrier Arrangement*, IEEE Transactions on Industry Applications, vol. 40, no. 4, pp. 1076-1082 (2004).

[39] Pina A.J., Xu L., *Modeling of Synchronous Reluctance Motors Aided by Permanent Magnets with Asymmetric Rotor Poles*, 2015 IEEE International Electric Machine & Drives Conference (IEMDC), Coeur d'Alene, USA, pp. 412-418 (2015).

[40] Bianchi N., Bolognani S., Bon D., Pre M.D., *Rotor Flux-Barrier Design for Torque Ripple Reduction in Synchronous Reluctance and PM-Assisted Synchronous Reluctance Motors*, IEEE Transactions on Industry Applications, vol. 45, no. 3, pp. 921-927 (2009).

ARCHIVES OF ELECTRICAL ENGINEERING VOL. 66(2), pp. 295-312 (2017)

DOI 10.1515/aee-2017-0022

Research on the influence of driving harmonic on electromagnetic field and temperature field of permanent magnet synchronous motor

HONGBO QIU[1], WENFEI YU[1], YONGHUI LI[2], CUNXIANG YANG[1]

[1] *College of electric and information engineering*
Zhengzhou University of Light Industry
Zhengzhou 450002, China
e-mail: {qiuhongbohrb/bijiaohao22/yangcx77777}@163.com

[2] *Luoyang Railway Information Engineering School*
Luoyang 471000, China
e-mail: kidlook@163.com

(Received: 29.06.2016, revised: 15.12.2016)

Abstract: At present, the drivers with different control methods are used in most of permanent magnet synchronous motors (PMSM). A current outputted by a driver contains a large number of harmonics that will cause the PMSM torque ripple, winding heating and rotor temperature rise too large and so on. In this paper, in order to determine the influence of the current harmonics on the motor performance, different harmonic currents were injected into the motor armature. Firstly, in order to study the influence of the current harmonic on the motor magnetic field, a novel decoupling method of the motor magnetic field was proposed. On this basis, the difference of harmonic content in an air gap magnetic field was studied, and the influence of a harmonic current on the air gap flux density was obtained. Secondly, by comparing the fluctuation of the motor torque in the fundamental and different harmonic currents, the influence of harmonic on a motor torque ripple was determined. Then, the influence of different current harmonics on the eddy current loss of the motor was compared and analyzed, and the influence of the drive harmonic on the eddy current loss was obtained. Finally, by using a finite element method (FEM), the motor temperature distribution with different harmonics was obtained.

Key words: air gap flux density, eddy current loss, harmonic, magnetic field decoupling, torque ripple

1. Introduction

At present, because PMSM with variable frequency speed regulation has the advantages of superior starting performance and excellent speed regulation performance, it has been widely used in industrial production and daily life. However, the drive controller power supply con-

tains a lot of time harmonic that will affect the air gap flux density, torque ripple, eddy current loss and so on [1-3]. On one hand, the motor running high-frequency electromagnetic noise is loud [4], and the motor efficiency is reduced. On the other hand, due to the motor rotor has difficult heat dissipation, eddy current loss produced by permanent magnet will cause permanent magnet (PM) temperature rise too high [5-7], even partial irreversible demagnetization, which will seriously influence motor performance and operation reliability [8-9]. So it is significant to study the effect of harmonics on the motor performance.

In recent years, there are many experts and scholars who study the power supply of the driver, and some results have been obtained. Reference [1] proposed an analytical model that can evaluate the influence factors of current harmonics. Reference [6] represented the magnet eddy-current loss was mainly produced by the carrier harmonics of the PWM inverter and that the axial length of the divided magnet should be smaller than the skin depth of the eddy currents produced by the major harmonics for the loss reduction. Reference [10] proposed harmonic current suppression control of a PM motor in αβ coordinates by using repetitive perfect tracking control with the PWM-hold model. Reference [11] studied the relationship between converter parameters and harmonic iron loss, and the formula of the iron loss in the power supply of the inverter was modified. Reference [12] proposed a current filtering strategy which weakened the 5th and the 7th harmonic currents in the stator. Reference [13] proposed a novel design for the elimination of radial air-gap flux density harmonics of permanent magnet motors. Reference [14] proposed and studied the phase-shifted chaotic space vector modulation scheme for harmonic performance improvement in paralleled voltage-source inverters fed permanent magnet synchronous motor drive. Reference [9] focused on the analysis and development of low-current harmonics and presented a zero-axis current estimator auxiliary vector control method to compensate for three multiples of the voltage harmonic. From references [9, 15 and 16], it is seen that, by injecting harmonic currents, resistive losses in the stator can be minimized along with the reduction of torque ripple. The harmonic current in the stator winding is the research object of this paper. The influence of the harmonic current on the performance of PMSM is analyzed, and the influence of the harmonic on air gap flux density, torque ripple, eddy current loss and temperature of PM is determined.

In the present study, firstly, a two dimensional FEM is established. A novel method of decoupling the motor magnetic field is presented. The difference of harmonic content in the air gap magnetic field of the fundamental wave and different order harmonics is studied. By analyzing, the influence of the harmonic current on the air gap flux density is obtained. Secondly, by comparing the motor torque fluctuation wave of the fundamental current with the harmonic current of a different order, amplitude and phase angles, the influence of a harmonic of a different order, amplitude and phase angles on motor torque fluctuation is determined. Then, the influence of the different current harmonics on the eddy current loss of the motor rotor is compared and analyzed, and the influence of the drive harmonic of a different order, amplitude and phase angles on the eddy current loss is obtained. Finally, based on the FEM, the motor temperature distribution under different harmonic conditions is obtained. In this paper, the research results lay the foundation for the study of the loss and vibration of the drive motor, and provide a way to improve the motor performance.

2. Prototype parameters and harmonic analysis

2.1. Prototype parameters

In this paper, taking a 10 kW, 2000 r/min PMSM as an example, the effect analysis of a harmonic on the performance of the PMSM is made. The two dimensional (2D) FEM of the prototype is shown in Fig. 1, and the basic parameters of PMSM are shown in Table 1.

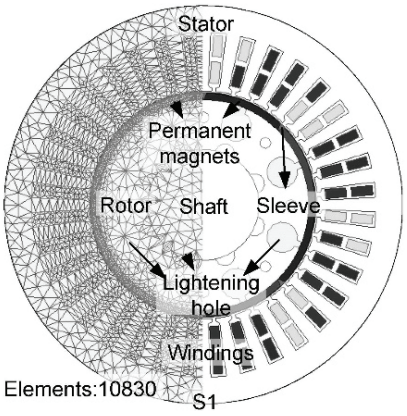

Fig. 1. FEM model of the prototype

In order to facilitate the influence study of a harmonic on the motor, the following assumptions are made:

(a) A displacement current and skin effect in the stator windings are ignored.
(b) Materials are isotropic. Permeability and conductivity of the materials are constant except the stator core and the rotor yoke.
(c) The material permeability and conductivity are constant ignoring the influence of temperature.

Based on the above assumptions, the 2D cross section of the motor perpendicular to axial direction is selected as the analysis model shown in Fig. 1, and the vector magnetic potential A only has z-component. Considering the saturation, the transient 2D electromagnetic field calculation equation would be (1), in which the permanent magnet is simulated by a current density source [17].

$$\begin{cases} \Omega : \left\{ \dfrac{\partial}{\partial x}\left(\dfrac{1}{\mu}\dfrac{\partial A_z}{\partial x}\right) + \dfrac{\partial}{\partial y}\left(\dfrac{1}{\mu}\dfrac{\partial A_z}{\partial y}\right) = -\left(J_z - \sigma\dfrac{\mathrm{d}A_z}{\mathrm{d}t}\right), \right. \\ S_1 : A_z = 0, \\ PM : \dfrac{1}{\mu_1}\dfrac{\partial A_z}{\partial n} - \dfrac{1}{\mu_2}\dfrac{\partial A_z}{\partial n} = J_s, \end{cases} \tag{1}$$

where: Ω is the calculation region, A_z and J_z represent the magnetic vector potential and the source current density in the z-axial component respectively, J_S is the equivalent current density of permanent magnets, n is the normal direction of a permanent magnet boundary, σ is

the conductivity, μ is the permeability, S_1 is the Dirichlet boundary conditions, μ_1 and μ_2 represent the relative permeability, t is the time.

Table 1. Parameters of the model

Parameters	Value	Unit
Rated power	10	kW
Rated speed	2000	r/min
Pole number	8	
Axial length	102	mm
Rotor magnetic circuit structure	surface-mounted type	
Stator outer diameter	180	mm
Stator inner diameter	103	mm
Slot number	36	
Number of parallel branches	1	
Winding connection type	Y	

2.2. The establishment of harmonic and research method

In order to prevent the PMSM demagnetization caused by armature reaction and to optimize the motor performance, in this paper, the vector control mode $i_d = 0$ is chosen in PMSM based on the principle of permanent magnet motor control technology.

The synthetic electromotive force in the stator armature winding not only contains the fundamental wave but also contains each harmonic. The current in windings is obviously not sinusoidal. The fundamental wave rotating magnetic field is generated by a fundamental wave current, and the magnetic field is generated by rotor permanent magnets. The main electromagnetic torque is formed by the fundamental wave rotating magnetic field and the magnetic field. The rotation speed and rotation direction of the synthetic rotating magnetomotive force generated by the harmonics are different from those of the rotor's. The speed of the synthetic rotating magnetomotive force is relatively higher than the rotor speed. The eddy current loss and magnetic hysteresis loss in the rotor are generated by the synthetic rotating magnetomotive force, which causes a phenomenon in which the rotor temperature rise is higher than that of the stator. At the same time, the motor efficiency decreases, and the motor vibration and noise increase [1, 6].

The harmonics affecting the motor are mainly the 5th, 7th, 11th, 13th harmonics. The 5th 7th 11th 13th harmonics are chosen in this paper, for each harmonic, five amplitudes are set, they are 2%, 4%, 6%, 8% and 10% of the fundamental current amplitude respectively. The artificial injection harmonic method was adopted and different orders of harmonic currents and a fundamental current are injected. The superposition of different times of the harmonic currents and fundamental current were taken as the excitation source of the motor, the influence of a different order, amplitude and the phase angle of the harmonic current on the motor performance in the excitation power supply is studied. The input current can be expressed as Eq. (2):

$$\begin{cases} I_A \sin(2\pi ft) + kI_A \sin(2\nu\pi ft + \varphi_0), \\ I_B \sin(2\pi ft - 2\pi/3) + kI_B \sin(2\nu\pi ft - 2\nu\pi/3 + \varphi_0), \\ I_C \sin(2\pi ft - 2\pi/3) + kI_C \sin(2\nu\pi ft + 2\nu\pi/3 + \varphi_0), \end{cases} \tag{2}$$

where: I_A, I_B, I_C are the peak values of the current A, current B, current C respectively. k is the ratio of the harmonic amplitude of the fundamental amplitude. v is the harmonic order. φ_0 is the harmonic initial phase.

3. The influence of harmonic current on air gap magnetic field

3.1. Analysis of air gap magnetic field

During the motor normal operation, because of the non-sine stator armature current waveform and stator slot, the wave of the magnetomotive force is non-sine, which causes a lot of space and time harmonic magnetic fields in the air gap magnetic field. The time harmonic magnetic field is the spatial fundamental magnetic field generated by the harmonic exciting current, and the motor air gap main magnetic field consists of the time harmonic magnetic field and the fundamental magnetic field. The direction of the K-th ($K = 6n - 1$, $n = 1, 2, 3...$) time harmonic magnetic field is reversed to the direction of the fundamental magnetic field and the speed is K times of the fundamental magnetic field. The direction of the K-th ($K = 6n + 1$, $n = 1, 2, 3...$) time harmonic magnetic field is the same as the direction of the fundamental magnetic field and the speed is also K times of the fundamental magnetic field. Therefore, the eddy current is generated in rotor permanent magnets and in a sleeve. Finally, the eddy current loss increases [1, 4].

3.2. Air gap magnetic field decoupling method

According to the electrical machine theory, during the motor operation, the air gap magnetomotive force includes the stator current harmonic magnetomotive force and the equivalent magnetomotive force of the rotor permanent magnets [18]. The space harmonic magnetic field is produced by permanent magnets, and it rotates synchronously with the rotor. The eddy current cannot be induced by these harmonics, and eddy current loss cannot be produce. Therefore, the harmonics produced by the stator armature winding just induce the eddy current in the rotor.

The harmonic current generates a large amount of the eddy current loss in the rotor. The time and space harmonics are the main reasons which cause the eddy current loss [19]. The motor air gap magnetic field is composed of the magnetic field generated by a stator current and that is generated by permanent magnets. A motor magnetic field decoupling method was proposed, which separated the magnetic field generated by the stator current from the motor air gap magnetic field. The influence of the high harmonic content of the stator armature current on the motor air gap magnetic field is analyzed, and the influence of the stator armature current on the air gap flux density is obtained.

An air gap magnetic field decoupling method and procedure are as follows:

(1) Three phase stator armature currents are extracted when the motor operates under the rated condition.
(2) The three-phase stator armature currents are decomposed by FFT and the amplitude and phase of each harmonic wave are determined.
(3) The mixed current of the fundamental current and the ideal harmonic is used as the excitation to the stator armature.
(4) The permanent magnets are demagnetized completely and driven motor rotation at the rated speed.

Fig. 2 shows the air gap flux density waveforms under different motor operating conditions. Curve1 is the air gap flux density waveform at no-load operation, curve2 is the air gap flux density waveform at rated load operation, and curve3 is the air gap flux density waveforms generated by the stator current after the air gap magnetic field decoupling. Actually, due to the influence of armature reaction, the armature field should act in the *q*-axis, and the synthetic magnetic field under load operation lags behind the magnetic field under no-load operation 20 deg. In order to facilitate the contrast analysis, the phase difference of the synthetic magnetic field is artificially adjusted to the same phase.

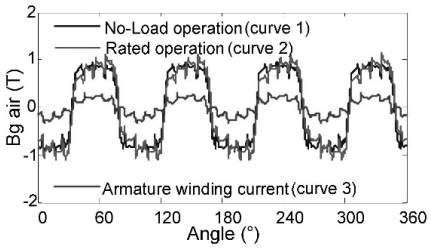

Fig. 2. The motor air gap flux density waveform under different operation conditions

When the harmonic order changes only, the influence of harmonic order variation on the motor electromagnetic field is studied. The fundamental current and the 5th, 7th, 11th, 13th harmonics whose amplitude is 10% of the fundamental current are injected through the method of artificial injection. The influence of the stator armature currents on the harmonic content of the air gap magnetic field in the motor is studied after the air gap magnetic field decoupling. The air gap magnetic field is only generated by the stator armature current. By using the FFT method, the air gap magnetic field of the fundamental current and each harmonic is decomposed respectively, and the harmonic content of the air gap magnetic field is shown in Fig. 3.

The content of the 5th, 7th, 11th and 13th harmonics in the air gap magnetic field is higher than that of others obviously. It can be concluded that the eddy current loss of the motor rotor is mainly caused by the 5th, 7th, 11th, and 13th harmonic currents.

Taking the air gap flux density harmonic content in the fundamental current as a reference value, when the 5th and 11th harmonic currents are input into the stator armature windings, the magnetic field content of the motor air gap fundamental wave decreases; when the 7th and 13th harmonic currents are input into the stator armature windings, the motor air gap funda-

mental wave magnetic field content increases. The maximum air gap magnetic density value caused by the 5th and 11th harmonic becomes smaller, the average value increases. The air gap flux density maximum value caused by the 7th and 13th harmonic becomes large, and the average value decreases.

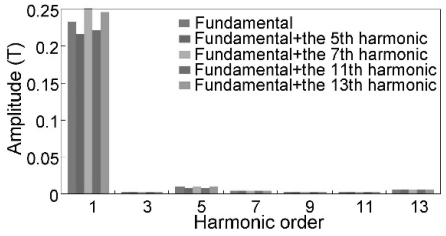

Fig. 3. The air gap magnetic flux harmonic in the fundamental and harmonic current

4. The influence of harmonic current on torque

A torque ripple factor and the average torque are two important parameters which could determine the stability of a permanent magnet motor. On the basis of the fundamental current, the different order harmonics with different amplitudes and phases were injected into the motor armature windings by the method of artificial injection and the influence of the harmonic current of different orders and amplitudes on the motor torque ripple and the average torque is analyzed.

4.1. Effect of harmonic current amplitude on torque

Due to the fact that the input voltage and current contain a lot of harmonic components, the harmonics of different order affects the motor torque ripple to a different degree. For the three-phase PMSM, when Y-type connection is adopted in the stator windings, the $3K$-th ($K = 1, 2, 3...$) harmonics of the motor phase current are eliminated, so the influence of the $3K$-th ($K = 1, 2, 3...$) harmonics on the motor performance is not considered and only the effect of the 5th, 7th, 11th and 13th harmonics on the motor performance are considered [20].

In the research of the PMSM torque ripple, the torque ripple coefficient is usually used to measure the motor stability. Eq. (3) is the torque ripple formula.

$$\delta = \frac{\sqrt{\sum_{i=1}^{n}\left(T_{i\max} - T_{i\text{av}}\right)^2} + \sum_{i=1}^{n}\left(T_{i\text{av}} - T_{i\min}\right)^2}{\sum_{i=1}^{n} T_{i\text{av}}} \tag{3}$$

where: δ is the torque ripple coefficient. $T_{i\max}$ and $T_{i\min}$ are the maximum and minimum values of the torque ripple in the i-th cycle. $T_{i\text{av}}$ is the torque average value in the i-th cycle, n is the number of computation cycles.

Under the motor rated operating condition, the fluctuation curve of the motor output torque is shown in Fig. 4a. The periodic fluctuations of the torque ripple curve appeared. The opera-

tion cycle of the motor is 7.5 ms. The average torque of the motor is 47.6 N·m. The maximum torque is 49.5 N·m and the minimum torque is 45.6 N·m. The motor torque fluctuation range is 3.9 N·m and the torque ripple coefficient is 5.75%.

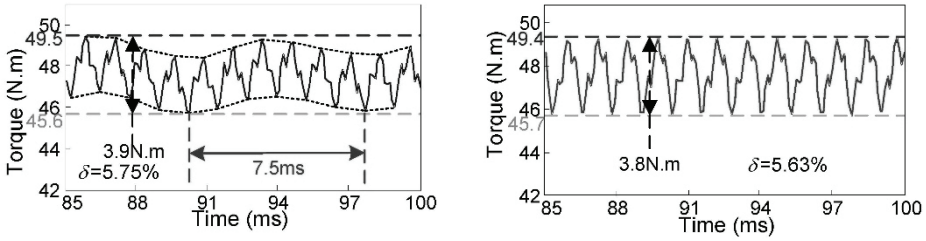

(a) (b)

Fig. 4. The motor torque fluctuation curve under different situation: torque fluctuation curve at rated operation (a); torque fluctuation curve under fundamental current (b)

Firstly, in order to study the harmonic current influence on motor performance, a fundamental current of 133 Hz is injected into the armature windings, and the motor torque curve is shown in Fig. 4b. The data are regarded as the reference and are compared with other conditions when the harmonic current order is different.

When the fundamental current is injected into the stator armature windings, the average torque of the motor is 47.7 N·m, the maximum torque is 49.4 N·m and the minimum torque is 45.7 N·m. The motor torque fluctuation range is 3.7 N·m under stable conditions. The torque ripple coefficient is 5.63%.

On the basis of the fundamental wave current, the influence of the 5th harmonic current with different amplitudes on the motor torque fluctuation curve is studied by the method of artificial injection. As soon as the harmonic amplitude changes, the influence of harmonic amplitude variation on the output torque is studied. The 5th harmonic amplitudes are 0%, 2%, 4%, 6%, 8% and 10% of the fundamental current amplitude respectively. The motor torque fluctuation curve with different amplitude harmonic is shown in Fig. 5.

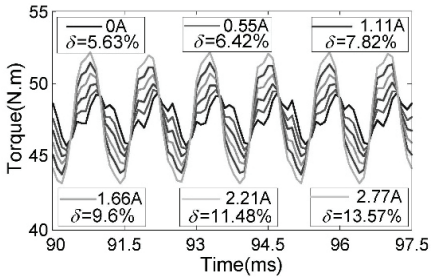

Fig. 5. The torque curve under fundamental wave and the 5th harmonic currents with different amplitudes

As is shown in Fig. 5, on the basis of the fundamental wave current, the larger the amplitude of the 5th harmonic current is, the larger the range of the motor torque fluctuation is, the higher the torque ripple coefficient of the motor is, the worse the stability of the motor is.

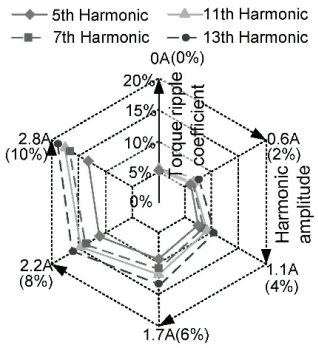

Fig. 6. The influence of the harmonic current with different amplitude on the motor torque ripple

The influences of a different order harmonics on the motor torque ripple are shown in Fig. 6. The fundamental current and different order harmonics current of different amplitudes are injected into the motor stator armature windings respectively.

On the basis of the fundamental wave current, the motor torque fluctuation range is 4.4 N·m, 5.8 N·m, 7.4 N·m, 9.3 N·m and 11.2 N·m when the 7th harmonic current is loaded and the amplitudes are 2%, 4%, 6%, 8%, 10% of the fundamental wave. The torque ripple coefficient is 6.56%, 8.6%, 11.08%, 13.95%, 16.74% respectively. The fluctuation range of the motor torque increases with the increase of the harmonic amplitude.

After analyzing the influence of different order harmonic currents on the motor torque, the following conclusions could be concluded. The motor average torque is not affected by the harmonic currents of different amplitudes. However, with the increase of the harmonic current amplitude, the bigger the range of the motor torque fluctuation is and the higher the torque ripple coefficient of the motor is, the worse the stability of the motor is.

4.2. The influence of harmonic current phase angle on torque

Not only will the amplitude of the harmonic current affect the PMSM torque performance, but also the phase angle difference between the harmonic current and fundamental current will affect the motor average torque and torque ripple.

As soon as the harmonic initial phase changes, the influence of harmonic phase variation on the output torque is studied. When analyzing the influence of harmonic phase, the fundamental phase does not shift. As the current expression shows, the harmonic magnetic field generated by the harmonic current of the same order also shifts when the harmonic current initial phase is shifts from 0 deg to 360 deg. The fundamental current and the 5th harmonic current whose amplitude is 10% of the fundamental current are injected into the motor armature windings. The harmonic initial phase angle changes from 0 deg to 360 deg. The step length is 15 deg. Finally, the average torque and torque ripple coefficient with the change of a harmonic current phase are obtained as shown in Fig. 7.

From Fig. 7, it could be found that when the initial phase φ_0 of the 5th harmonic current increases from 15 deg to 75 deg gradually, the motor torque pulsating coefficient increases from 15.35% to 18.72% gradually. When the initial phase φ_0 increases from 75 deg to 165 deg, the motor pulsating coefficient has a downward trend from 18.72% to 11.95%. When

the initial phase φ_0 increases from 210 deg to 255 deg, the torque ripple coefficient decreases. When the initial phase φ_0 increases from 255 deg to 345 deg, the motor torque ripple coefficient increases from 8.79% to 15.77% gradually.

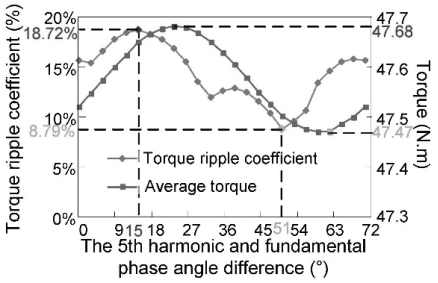

Fig. 7. The influence of the 5th harmonic current initial phase φ_0 on the motor torque ripple

When the 5th harmonic current initial phase φ_0 is 75 deg, the motor torque fluctuation range is maximum and the value is 12.6 N·m, and the motor ripple coefficient is 18.72%. When the initial phase φ_0 is 255 deg, the motor torque ripple range is minimum and the value is 5.9 N·m. The torque pulsation coefficient is 8.79%.

The average torque fluctuation curve changes according to sinusoidal law. The average torque reaches a maximum value of 47.68 N·m when the 5th harmonic initial phase φ_0 is 120 deg. The average torque reaches a maximum value of 47.47 N·m when the 5th harmonic current initial phase φ_0 is 300 deg.

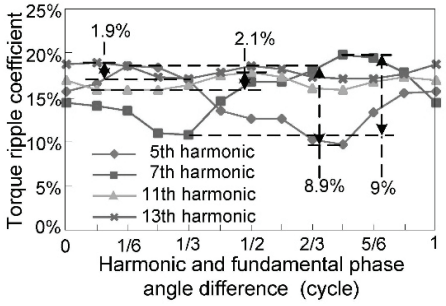

Fig. 8. The influence of harmonic initial phase φ_0 on torque pulsating

Not only does the armature current contain the 5th harmonic, but also contains the 7th, 11th and 13th harmonics. The fundamental current and each harmonic current with 10% of the fundamental current amplitude are injected into the motor armature windings. Fig. 8 shows the torque pulsating changes of different harmonic currents of a different initial phase φ_0.

As shown in Fig. 8, when the 5th, 7th, 11th and 13th harmonic initial phase φ_0 change within 360 deg, the variation range of the motor torque pulsation coefficient is 8.9%, 9%, 2.1%, 1.9% respectively. The change of the torque fluctuating range caused by the 5th and 7th harmonic currents is larger than that caused by the 11th and 13th harmonic currents with the change of the initial phase.

The initial phase φ_0 change not only affects the motor torque pulsation, but also affects the motor average torque. Fig. 9 shows the variation of the motor average torque when each harmonic current initial phase φ_0 changes within 360 deg.

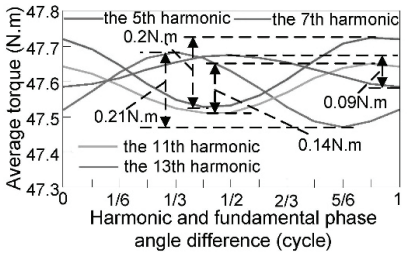

Fig. 9. The influence of harmonic initial phase φ_0 on average torque

With the change of the initial phase φ_0 of the 5th, 7th, 11th and 13th harmonic currents the fluctuation ranges of the motor average torque are 0.21 N·m, 0.2 N·m, 0.14 N·m, 0.09 N·m respectively. When the 5th and 7th harmonic currents flow, the motor average torque is larger than that when the 11th and 13th harmonic currents flow.

5. Influence of harmonic current on eddy current loss and permanent magnet temperature

5.1. Effect of harmonic current amplitude on eddy current loss and temperature rise of permanent magnets

A low order harmonic magnetic field not only generates an eddy current in the sleeve, but also generates a large eddy current in the rotor permanent magnets. When the motor operates under loaded condition, a lot of eddy currents will be generated on the sleeve surface, which will cause additional eddy current loss and hysteresis loss. The motor rotor iron loss increases with the increase of frequency, harmonic will cause the motor iron loss to increase rapidly.

In this paper, the eddy current loss of the rotor caused by a harmonic current is studied by the method of artificial injection harmonic current with different amplitude. As shown in Fig. 10a, the maximum value of motor eddy current density under the action of an ideal fundamental current is 1.61×10^6 A/m^2. The eddy current loss of the permanent magnets and the sleeve is 10.1 W. When the fundamental current and the 13th harmonic current whose amplitude is 10% of the fundamental current are injected into the motor armature windings, due to the impact of the harmonic magnetomotive force, an eddy current was formed on the rotor surface. As shown in Fig. 10b the maximum value of the motor eddy current density is 3.24×10^6 A/m^2.

Based on the FEM, a 2D motor temperature field model is built. In order to simplify the analysis and calculation of the temperature field, the following assumptions are proposed [21]:

1) The motor is continuous along the axial direction, and the axial temperature gradient is zero.

2) Material is isotropic; the influence of temperature on thermal conductivity is ignored.

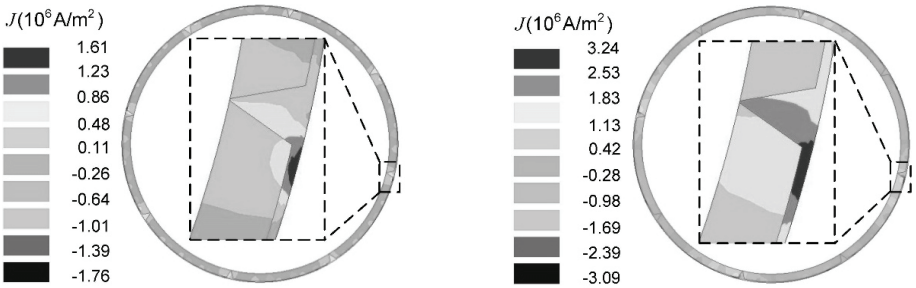

(a) (b)

Fig. 10. The motor rotor eddy current density distribution: under the action of fundamental current (a); under the fundamental and the 13th harmonic current (b)

Based on the above assumptions, the 2D model could be established adopting the FEM. The heat transfer equation can be expressed as Eq. (4):

$$\left.\begin{aligned} &\frac{\partial}{\partial x}\left(\lambda_x \frac{\partial T}{\partial x}\right)+\frac{\partial}{\partial y}\left(\lambda_y \frac{\partial T}{\partial y}\right)=-q_v \\ &\lambda \frac{\partial T}{\partial x}\Big|_{\Gamma}=\alpha\left(T-T_f\right) \end{aligned}\right\}, \tag{4}$$

where: T is the body temperature, λ_x and λ_y represent the thermal conductivity along the directions x and y, q_v is the heat generation density, the stator outer surface is the air natural convection heat dissipation, the third boundary condition is given as Γ (the stator outer circle boundary), α is the heat transfer coefficient, T_f is the temperature of the circumstance.

The ideal harmonic is injected by the method of artificial injection, the influence of harmonic frequency, amplitude and the phase angle on a motor temperature field is studied. Fig. 11a shows the motor temperature field distribution under the action of an ideal fundamental current. Fig. 11b shows the motor temperature field distribution under the action of the fundamental current and the 13th harmonic current whose amplitude is 10% of the fundamental current.

As shown in Fig. 11, when the ideal fundamental wave current is injected into the motor winding, the motor winding temperature is 81.7°C and rotor permanent magnet temperature is 78.9°C. When the fundamental current and the 13th harmonic current whose amplitude is 10% of the fundamental current are injected into the motor armature windings, the motor winding temperature is 94°C and rotor permanent magnet temperature is 128.1°C. Based on the above analysis method, the motor eddy current loss and the permanent magnet temperature distribution under different amplitudes of each harmonic are studied. As shown in Fig. 12, the change of the motor eddy current loss and the temperature increasing trend of the permanent magnet are studied under the fundamental current and the 5th ,7th, 11th and 13th harmonic current whose amplitude is 2%, 4%, 6%, 8% and 10% of the fundamental current respectively.

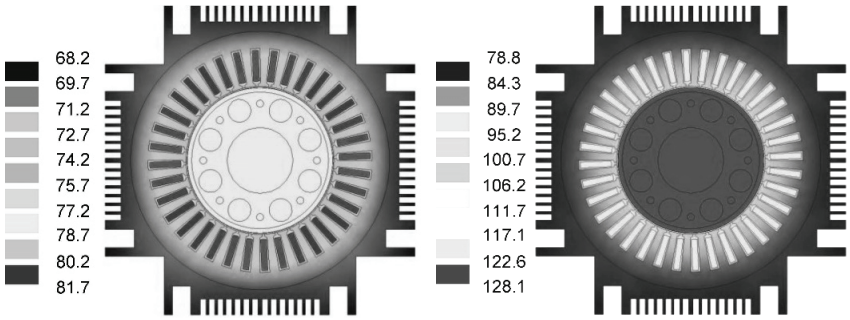

Fig. 11. The motor temperature distribution: under the action of fundamental current (a); under the fundamental and the 13th harmonic current (b)

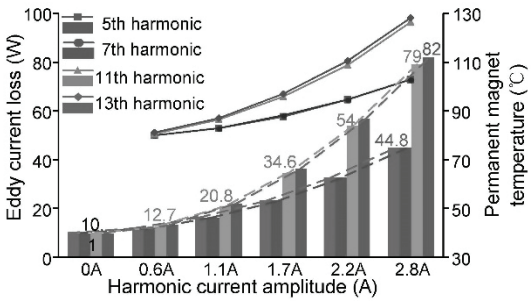

Fig. 12. The influence of the harmonic current with different amplitude on the motor eddy current loss

In general, the higher order harmonics causes the larger rotor eddy current loss and the higher temperature rise of permanent magnets when the amplitude of the harmonic current is constant. As shown in Fig. 12, when the amplitude of each harmonic current is 2.8 A, the rotor eddy current loss generated by the 5th harmonic current is 44.8 W, the temperature of the rotor permanent magnets is increased by 23.7°C, and the permanent magnet temperature is 1.3 times of the permanent magnet temperature when the fundamental current is injected. The rotor eddy current loss generated by the 13th harmonic current is 82 W.

In addition, with the increase of the harmonic amplitude, the eddy current loss of the rotor increases, and the temperature rise of the permanent magnets also increases. When the amplitude of the 11th harmonic current is 0.6 A, 1.1 A, 1.7 A, 2.2 A and 2.8 A respectively, the corresponding eddy current losses are 12.7 W, 20.8 W, 34.6 W, 54 W and 79 W, the temperature rise of the rotor permanent magnets is 2.28%, 9.38%, 21.29%, 38.15% and 59.7% of the permanent magnet temperature when the fundamental current is injected.

However, the increase of the loss caused by the high order harmonic current is signifycantly higher than the increase of the loss caused by the lower harmonic current. When the amplitude of the harmonic current is 2.8 A, the eddy current loss caused by the 5th harmonic current increases by 3.44 times compared with that caused by the fundamental current, and the eddy current loss caused by the 13th current harmonic increases by 7.12 times compared with that caused by the fundamental current.

5.2. The influence of harmonic current phase angle on the eddy current loss and permanent magnets temperature

The harmonic amplitude affects the motor eddy current loss, in addition, the harmonic initial phase is also one of the key factors affecting the motor eddy current loss. The 5th, 7th, 11th and 13th harmonic currents whose amplitudes are 10% of the fundamental current are adopted. The rotor eddy current loss and the permanent magnet temperature rise are studied when harmonic initial phase φ_0 changes within 360 deg. The results are shown in Fig. 13.

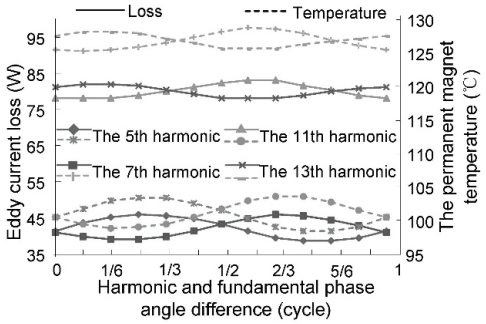

Fig. 13. The influence of harmonic initial phase on eddy current loss and permanent magnet temperature

As shown in Fig. 13, the variation regular of the eddy current loss generated by the 5th, 7th, 11th and 13th harmonic current is sinusoidal with the change of the phase angle. The motor eddy current loss generated by the 5th harmonic current reaches a minimum value of 38.5 W when the 5th harmonic initial phase φ_0 is 270 deg, and the temperature of the permanent magnets is 98.4°C. The motor eddy current loss reaches a maximum value of 45.9 W when the 5th harmonic initial phase φ_0 is 90 deg, and the temperature of the permanent magnets is 103.4°C. The eddy current loss is increased by 19.2%, and the temperature rise of the permanent magnets is 5°C, which is increased by 5.1%.

The motor eddy current loss reaches a minimum value of 39 W when the 7th harmonic initial phase φ_0 is 60 deg, and the temperature of the permanent magnets is 98.8°C. The motor eddy current loss reaches a maximum value of 45.8 W when the 7th harmonic initial phase φ_0 is 240 deg, and the temperature of the permanent magnets is 103.5°C. The eddy current loss is increased by 17.4%, and the temperature rise of the permanent magnets is 4.7°C, which is increased by 4.8%.

The motor eddy current loss reaches a minimum value of 78 W when the 11th harmonic initial phase φ_0 is 30 deg, and the temperature of the permanent magnets is 125.3°C. The motor eddy current loss reaches a maximum value of 83.2 W when the 11th harmonic initial phase φ_0 is 210 deg, and the temperature of the permanent magnets is 128.7°C. The eddy current loss is increased by 6.7%, and the temperature rise of the permanent magnets is 3.4°C, which is increased by 2.7%.

The motor eddy current loss reaches a minimum value of 78.1 W when the 13th harmonic initial phase φ_0 is 210 deg, and the temperature of the permanent magnets is 125.6°C. The motor eddy current loss reaches a maximum value of 82 W when the 13th harmonic initial phase φ_0 is 30 deg, and the temperature of the permanent magnets is 128.1°C. The eddy

current loss is increased by 5%, and the temperature rise of the permanent magnets is 2.5°C, which is increased by 2%.

6. Experimental study

In order to verify the correctness of the electromagnetic field and temperature field model, the experimental test of the prototype is carried out. The test system consists of a Magtrol dynamometer machine, YOKOGAWA power analyzer, industrial condensing unit, DSP data acquisition system, PMSM and other equipment. The experimental platform of the prototype is shown in Fig. 14. Test data and calculation data of the PMSM current are shown in Table 2 when the motor operates at different load conditions.

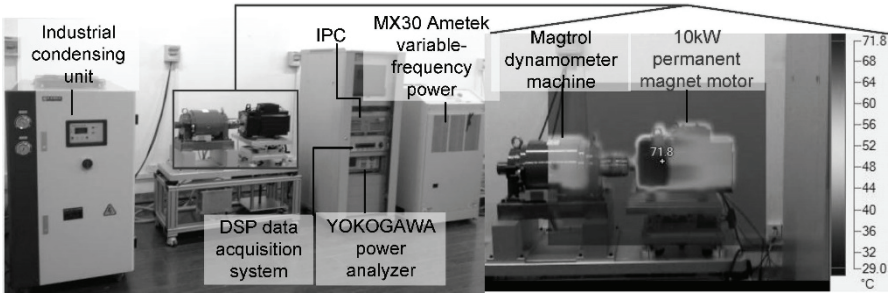

Fig. 14. Test platform of the prototype

In the experimental study, the temperature rise of the PMSM is tested at the rated load (10 kW) for a long time. The infrared thermal imager is adopted to obtain the temperature distribution of the motor outside surface as shown in Fig. 14.

Table 2. Test data and calculation results of PMSM at different conditions

Torque	Experimental current	Simulation current	Change rate
25 N·m	10.62 A	10.23 A	3.8%
36.4 N·m	15.3 A	15.4 A	0.6%
47.7 N·m	19.4 A	19.8 A	2%

Through the comparison of the above data analysis, it can be noticed that the experimental current values are basically consistent with the simulation current values when the permanent magnet motor operates under different loads, and the deviation is less than 5%, which corresponds with the practical requirements of the project.

The motor cooling system is shown in Fig. 15. The motor uses fan and ventilating ducts to accelerate the heat dissipation. It can be seen that the motor surface temperature increases from the inlet to the outlet of the cooling medium (air). The heat amount transferred by the cooling medium decreases with the increase of the temperature. In addition, at the end of the

ventilation system, the wind speed will be significantly reduced, so the hottest area is located at the end of the ventilation system.

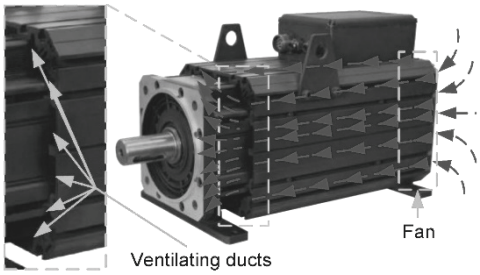

Fig. 15. The motor cooling system

Because the heat source in the motor interior larger and the heat dissipation structure is complex, only the surface temperature of the motor casing is measured. The laboratory environment temperature is 25°C. From the temperature measured by infrared thermal imager, it can be found that the maximum surface temperature of the motor shell is 71.8°C and the finite element result is 69.6°C. The deviation rate is just 3.2%, which is within the allowable deviation range in engineering.

7. Conclusions

In this paper, using the finite element method, the influences of the 5th, 7th, 11th and 13th harmonic currents with different amplitudes on the air gap magnetic field, torque ripple, eddy current loss and temperature field of PMSM are analyzed, the following conclusions can be obtained:

1) When the 5th, 11th harmonic currents were input into the stator armature windings, the motor air gap fundamental wave magnetic field content decreases; when the 7th and 13th harmonic currents were input into the stator armature windings, the motor air gap fundamental wave magnetic field content increases. The air gap magnetic density maximum value caused by the 5th and 11th harmonics becomes small, and the average value increases. The air gap flux density maximum value caused by the 7th and 13th harmonics becomes large, and the average value decreases.

(2) The motor average torque is not affected by the harmonic currents with different amplitudes. However, with the increase of the harmonic current amplitude, the range of the motor torque fluctuation is bigger, the higher the torque ripple coefficient of the motor is, the worse the motor stability is. When the harmonic initial phase changes within 360 deg, the change of the torque ripple coefficient and the average torque ripple range caused by the lower order harmonic is larger than that caused by the higher order harmonic.

(3) With the same amplitude of the harmonic current, the higher the harmonic order is, the greater the eddy current loss is, and the higher the temperature rise of the permanent

magnets is. In addition, with the increase of the harmonic amplitude, the eddy current loss of the rotor increases, and the permanent magnets temperature rise also increases. However, the increase of the loss caused by the higher order harmonics is significantly higher than that caused by the lower order harmonics. The variation regularity of the eddy current loss caused by each harmonic and the temperature rise of the permanent magnet is sinusoidal with the change of the harmonic initial phase. When the harmonic initial phase changes within 360 deg, the change of the eddy current loss and permanent magnet temperature rise caused by the lower order harmonic is larger than that caused by the lower order harmonic.

Acknowledgments

This work was supported in part by the National Natural Science Foundation of China under Grant 51507156, in part by the University Key Scientific Research Programs of Henan province under Grant 17A470005, in part by the Doctoral Program of Zhengzhou University of Light Industry under Grant 2014BSJJ042, and the part by the Graduate Scientific and Technology Innovation Foundation of Zhengzhou University of Light Industry under Grant 2016001.

References

[1] Liang W., Wang J., Luk C.K., Fang W., Fei W., *Analytical Modeling of Current Harmonic Components in PMSM Drive With Voltage-Source Inverter by SVPWM Technique*, IEEE Transactions on Energy Conversion, vol. 29, no. 3, pp. 673-680 (2014).

[2] Cao W., Bradley K.J., Clare J.C., Wheeler P.W., *Comparison of Stray Load and Inverter-Induced Harmonic Losses in Induction Motors Using Calorimetric and Harmonic Injection Methods*, IEEE Transactions on Industry Applications, vol. 46, no. 1, pp. 249-255 (2010).

[3] Yamazaki K., Suzuki A., Ohto M., Takakura T., *Harmonic Loss and Torque Analysis of High-Speed Induction Motors*, IEEE Transactions on Industry Applications, vol. 48, no. 3, pp. 933-941 (2012).

[4] Lee S., Kim Y.J., Jung S.Y., *Numerical Investigation on Torque Harmonics Reduction of Interior PM Synchronous Motor with Concentrated Winding*, IEEE Transactions on Magnetics, vol. 48, no. 2, pp. 927-930 (2012).

[5] Jeong T.C., Kim W.H., Kim M.J., Lee K.D., Lee J.J., Han J.H. et al., *Current Harmonics Loss Analysis of 150-kW Traction Interior Permanent Magnet Synchronous Motor Through Co-Analysis of d\hbox {-}q Axis Current Control and Finite Element Method*, IEEE Transactions on Magnetics, vol. 49, no. 5, pp. 2343-2346 (2013).

[6] Yamazaki K., Abe A., *Loss Investigation of Interior Permanent-Magnet Motors Considering Carrier Harmonics and Magnet Eddy Currents*, IEEE Transactions on Industry Applications, vol. 45, no. 2, pp. 659-665 (2009).

[7] Wang J., *Performance evaluation of fractional-slot tubular permanent magnet machines with low space harmonics*, Archives of Electrical Engineering, vol. 64, no. 4, pp. 655-668 (2015).

[8] Dolecek R., Novak J., Cerny O., Nemec Z., *Research of harmonic spectrum of currents in traction drive with PMSM*, IEEE International Symposium on Industrial Electronics, Gdansk, pp. 710-715 (2011).

[9] Hwang J.C., Wei H.T., *The Current Harmonics Elimination Control Strategy for Six-Leg Three-Phase Permanent Magnet Synchronous Motor Drives*, IEEE Transactions on Power Electronics, vol. 29, no. 6, pp. 3032-3040 (2014).

[10] Nakai T., & Fujimoto H., *Harmonic Current Suppression Method of PMSM Based on Repetitive Perfect Tracking Control*, Industrial Electronics Society, 33rd Annual Conference of the IEEE, Taipei, pp. 3032-3040 (2007).

[11] Boglietti A., Cavagnino A., Ionel D.M., Popescu M., Staton D.A., Vaschetto S., *A General Model to Predict the Iron Losses in PWM Inverter-Fed Induction Motors*, IEEE Transactions on Industry Applications, vol. 46, no. 5, pp. 1882-1890 (2010).
[12] Wang T., Fang F., Wu X., Jiang X., *Novel Filter for Stator Harmonic Currents Reduction in Six-Step Converter Fed Multiphase Induction Motor Drives*, IEEE Transactions on Power Electronics, vol. 28, no. 1, pp. 498-506 (2013).
[13] Chaithongsuk S., Takorabet N., Meibody-Tabar F., *On the Use of Pulse Width Modulation Method for the Elimination of Flux Density Harmonics in the Air-Gap of Surface PM Motors*, IEEE Transactions on Magnetics, vol. 45, no. 3, pp. 1736-1739 (2009).
[14] Wang Z., Chen J., Zhang B., Zheng Y., *Phase-shifted chaotic SVM for harmonic performance improvement in paralleled voltage-source inverters fed PMSM drive*, International Power Electronics and Application Conference and Exposition, Shanghai, pp. 670-675 (2014).
[15] Lu J., Yang J., Ma Y., Ren R., *Compensation for harmonic flux and current of permanent magnet synchronous motor by harmonic voltage,* International Symposium on Knowledge Acquisition and Modeling, Fukuoka, pp. 1-5 (2015).
[16] Lee G.H., Kim S.I., Hong J.P., Bahn J.H., *Torque Ripple Reduction of Interior Permanent Magnet Synchronous Motor Using Harmonic Injected Current*, IEEE Transactions on Magnetics, vol. 44, no. 6, pp. 1582-1585 (2008).
[17] Li W., Wang J., Zhang X., Kou B., *Loss calculation and thermal simulation analysis of high-speed PM synchronous generators with rotor topology*, International Conference on Computer Application and System Modeling, Taiyuan, 2010, pp. V14-612-V14-616 (2010).
[18] Witczak P., Kubiak W., Lefik M., Szulakowski J., *Modal-frequency spectrum of magnetic flux density in air gap of permanent magnet motor*, Archives of Electrical Engineering, vol. 63, no. 1, pp. 29-46 (2014).
[19] Zhou C., Yang G., Su J., *PWM Strategy With Minimum Harmonic Distortion for Dual Three-Phase Permanent-Magnet Synchronous Motor Drives Operating in the Over modulation Region*, IEEE Transactions on Power Electronics, vol. 31, no. 2, pp. 1367-1380 (2016).
[20] Li Y., Zhou J., Xia J., Meng H., *Research on vibration and noise of permanent magnet motor under low order harmonic current*, Transportation Electrification Asia-Pacific IEEE, Beijing, pp. 1-5 (2014).
[21] Li W., Yu Z., Chen Y., *Calculation and Analysis of Heat Transfer Coefficients and Temperature Fields of Air-Cooled Large Hydro-Generator Rotor Excitation Windings*, IEEE Transactions on Energy Conversion, vol. 26, no. 3, pp. 946-952 (2011).

ARCHIVES OF ELECTRICAL ENGINEERING VOL. 66(2), pp. 313-323 (2017)

DOI 10.1515/aee-2017-0023

Impact of inductor current ringing in DCM on output voltage of DC-DC buck power converters

MARCIN WALCZAK

Department of Electronics, Koszalin Technical University of Technology
Śniadeckich 2, 75-453 Koszalin, Poland
e-mail: marcin.walczak@tu.koszalin.pl

(Received: 04.06.2016, revised: 03.01.2017)

Abstract: Ringing of an inductor current occurs in a DC-DC BUCK converter working in DCM when current falls to zero. The oscillations are the source of interferences and can have a significant influence on output voltage. This paper discusses the influence of the inductor current ringing on output voltage. It is proved through examples that the oscillations can change actual value of duty a cycle in a way that makes the output voltage difficult to predict.

Key words: Inductor current ringing, DCM, BUCK converter, parasitic capacitance, electromagnetic compatibility in DC-DC converters

1. Introduction

Basic BUCK and BOOST converters working in discontinuous conduction mode (DCM) are widely used in electronics, especially for power factor correction (PFC). Inertia of the converters working in this mode can be described with a simpler model than in CCM [1]. The small-signal transmittances are presented as second order functions [2-5]. But since the second pole frequency in DCM is usually comparable to the switching frequency (or even higher), in some applications its influence on the frequency characteristics is negligible and a first order function can be used instead [4 chapter 11], [6, 7]. The first order transfer function simplifies the process of control circuit designing compared to a second order description, typical for CCM. One of disadvantages of DCM is the ringing of the inductor current when it reaches zero value [8, 9]. It is known that the ringing can be a source of additional losses, and electromagnetic interferences. In this paper the other consequences of the ringing are observed, namely unwanted changes of the output voltage.

The next section of this paper describes the origin of the inductor current ringing, which appears when a converter works in DCM. Subsequently an impact of the oscillations on the output voltage control is explained and the results of measurements are presented. At the end

some of known methods used to eliminate the oscillations are mentioned and used to improve the response of the output voltage to a duty cycle change.

2. Origin of ringing in DCM

The BUCK and BOOST converters contain a resonant circuit consisted of inductance L and parasitic capacitances of high-side and low-side switches [4, 9-11]. The circuit does not have a noticeable effect on an inductor current when a converter works in CCM. But in DCM a resonance appears in the form of inductor current ringing, when it reaches zero value. The ringing occurs in the inductor current and switch node voltage, which in the BUCK converter is the equivalent to the diode voltage. Waveforms of the BUCK converter in which the ringing occurred have been presented in Figs. 2-4. The waveforms apply to a converter with following parameters: $V_G = 12$ V, $T_S = 5$ µs, $L = 15$ µH, $C = 330$ µF, $G = 0.01$ S, $D = 0.3$, an IDD03SG60C Schottky diode, IRFZ44V transistor. Sometimes additional spikes in the inductor current can be observed. Those spikes are the result of parasitic inductances and often they can be minimized with a proper measurement method [12]. But such current spikes won't be discussed further, as they are not a subject of this paper.

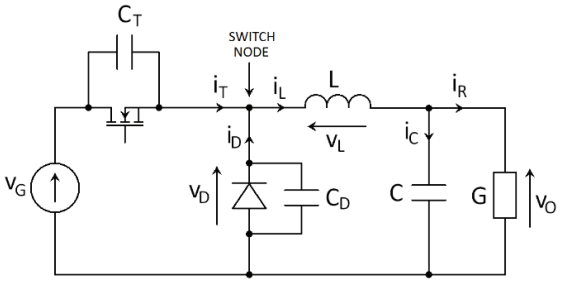

Fig. 1. BUCK converter with parasitic capacitances of switches

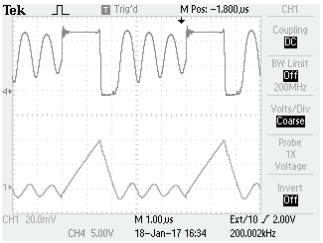

Fig. 2. Diode voltage (top) and inductor current (bottom) of BUCK converter working in DCM

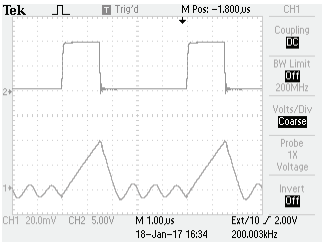

Fig. 3. Gate-source voltage (top) and inductor current (bottom) of BUCK converter working in DCM

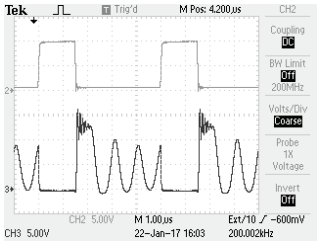

Fig. 4. Gate-source voltage (top) and drain-source voltage (bottom) of BUCK converter working in DCM

The waveform of the ringing can be described as [8]:

$$v_{LX}(t) = v_G + (v_O - v_G)\cos\omega_0(t - t_2), \qquad t_2 \le t \le t_3, \tag{1}$$

$$i_L(t) = \frac{v_G - v_O}{\omega_0 L}\sin\omega_0(t - t_2), \qquad t_2 \le t \le t_3, \tag{2}$$

where: v_{LX} is the voltage drop between a switch node and ground, t_2 is the point of time where an inductor current reaches zero value, t_3 is the point of time where an inductor current starts to rise from zero value.

Value ω_0 can be calculated as the resonant pulsation of inductance L and capacitance C_{PAR}, where C_{PAR} should be calculated as a parallel connection of switches' parasitic capacitance:

$$\omega_0 = \frac{1}{\sqrt{LC_{\mathrm{PAR}}}}. \tag{3}$$

3. Impact of ringing on output voltage

Side effects of the inductor current ringing, mentioned in literature, usually involve increased emission of electromagnetic interferences [13] and higher losses which lead to the lower efficiency of a converter [8]. Another drawback of oscillations which isn't usually mentioned is related to a switching signal and output voltage. When the ringing occurs, the current oscillates between the inductor and parasitic capacitances of high-side and low-side switches. If a new switching cycle begins when an inductor current is equal to zero as shown in Fig. 5 (subinterval 1) then values $t_{\mathrm{ON1}} = t_{\mathrm{ON1}}'$ and the output voltage react to a switching signal accordingly to a known mathematical model (4) [4-7].

$$V_{O(\mathrm{BUCK\,DCM})} = V_G \frac{G_Z D}{2G}\left(\sqrt{D^2 + 4\frac{G}{G_Z}} - D\right), \tag{4}$$

$$G_Z = \frac{T_S}{2L}, \tag{5}$$

where: T_S is the period of a switching signal, D is the duty cycle of a switching signal, G is the output conductance.

Let's consider a situation from Fig 5 (subinterval 2). A new switching cycle starts when an oscillating inductor current is above zero. The duty cycle of control signal v_{GS} can be determined based on t_{ON2}. But if one tries to measure the duty cycle as a time interval when the inductor current is larger than zero, then it would appear that the actual duty cycle, determined by t_{ON2}' is larger than the duty cycle of the control signal (since $t_{\mathrm{ON2}}' > t_{\mathrm{ON2}}$). Therefore the output voltage would be higher than expected. Similar situation appears, when the new switching cycle starts while the inductor current is below zero (Fig. 5 subinterval 3).

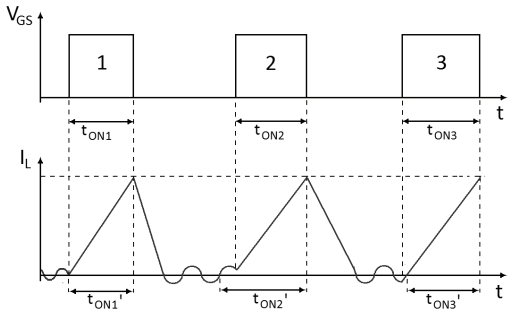

Fig. 5. Intervals of control signal V_{GS} and inductor current I_L in DCM

In that case the measured duty cycle would be smaller than the duty cycle of the control signal (since $t_{ON3}' < t_{ON3}$). This situation would influence the output voltage, making it smaller than expected. The variation of the output voltage would repeat in the wide range of the duty cycle, making the output voltage oscillate around the expected value, determined by (4). This effect can be observed when the peak value of the inductor current is relatively small i.e. when amplitude of oscillations is higher than ~ 5% of the inductor current amplitude. The inductor current amplitude depends on value of the inductor, switching frequency, and load resistance, therefore to prevent noticeable influence of the oscillations proper values of the parameters need to be considered.

An experimental BUCK converter has been designed to verify the presented theory. An APP9962 transistor (high-side) and MBRS340 Schottky diode (low-side) were used as switches. An IRS2186PBF device was used as a transistor driver. Other parameters of the converter during the measurement were as follows: $V_G = 12$ V, $T_S = 10$ µs, $L = 30$ µH, $C = 330$ µF, $G = 0.01$ S. During the experiment output voltage was measured while the duty cycle D of the control signal was changing between 0.1 and 0.6 with a step of 0.01. The result of the experiment is presented in Fig. 6a. Another measurement was made when the transistor was changed to IRFZ44, which has got higher value of output capacitance. The result of the measurement is presented in Fig. 6b.

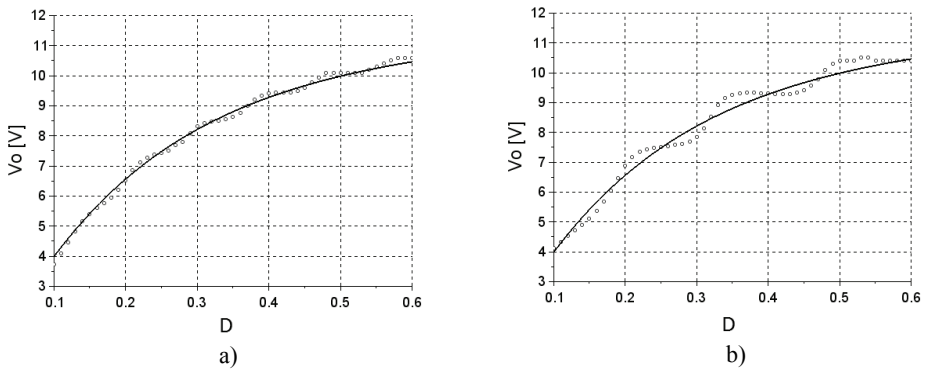

Fig. 6. Output voltage of a BUCK converter in DCM: a) an AP9962 transistor as a high-side switch; b) an IRFZ44 transistor as a high-side switch; solid – calculated from Eq. (4); dots – measured value

As shown in Fig. 6a the measured output voltage not only does not follow the simulation but oscillates around it. Another measurement presented in Fig. 6b indicates that using a switching element with higher parasitic capacitance can increase the difference between theoretical and measured value of the output voltage. If a transistor, diode and the inductor are chosen and parameters of the oscillations are fixed, then influence of the oscillations on the characteristic $V_O(D)$ depends on switching frequency. Such dependency is presented in Fig. 7, where a different BUCK converter was used: $V_G = 12$ V, $L = 15$ µH, $C = 470$ µF, $G = 0.01$ S, an APP9962 transistor, IDD03SG60C Schottky diode. The waveforms of gate-source voltage and inductor current, related to each frequency, are presented in Fig. 8.

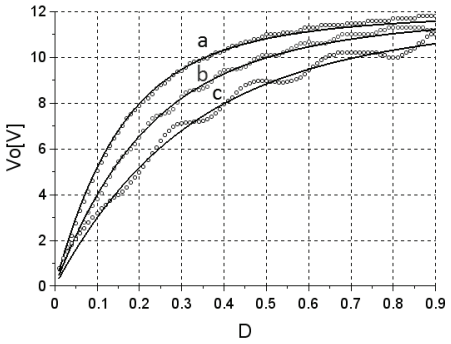

Fig. 7. Output voltage of a BUCK converter (APP9962 transistor, IDD03SG60C diode) in DCM for different frequencies: a – f_S = 100 kHz; b – f_S = 200 kHz; c – f_S = 400 kHz; solid line – calculated from Eq. (4); dotted line – measured value

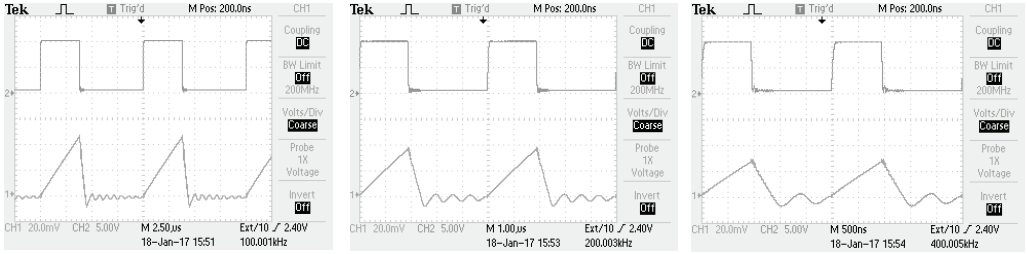

a) b) c)

Fig. 8 Gate-source voltage (top) and inductor current (bottom) of BUCK converter(transistor APP9962, diode IDD03SG60C) in DCM for different frequencies: a – f_S=100kHz, b – f_S=200kHz; c – f_S=400kHz

As shown in Fig. 7 the value of the switching frequency can increase or decrease the impact of the oscillations on converter characteristics. If the switching frequency increases the peak value of inductor current decreases, which makes the characteristics more susceptible to the oscillations.

It can be noticed in Fig. 6 and Fig. 7 that at some points a change in the duty cycle does not influence the output voltage. This can be shown with another experiment, where a step change $\Delta d = 0.02$ was introduced to value D_0 of the duty cycle according to Eq. (6).

$$D = D_0 + \Delta d. \tag{6}$$

The value of step change Δd was constant but D_0 was increased in each step by a constant value. This experiment simulates a situation where a control circuit tries to change the duty cycle in order to regulate the output voltage. Parameters of the converter are the same as for measurement from Fig. 6a. The result of the measurement is presented in Fig. 9.

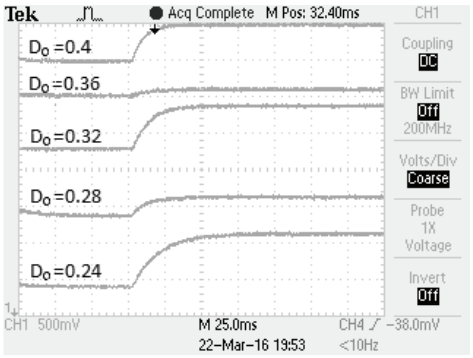

Fig. 9. Response of output voltage to step change of duty cycle

Measurements presented in Fig. 9 show that change in output voltage does not have the same transient character for all D_0 values due to presence of inductor current oscillations. Such differences can lead to incorrect control of the output voltage. In the next section some of methods used to suppress or eliminate ringing are described.

4. Elimination of ringing influence on output voltage

4.1. Proper selection of switches

There are a few methods which can be used to decrease or eliminate the ringing of inductor current [8, 11-16]. One of them includes appropriate selection of switching elements with lower capacitance. This approach increases frequency of the oscillations, which in turn increases the EMI, but it also decreases amplitude of the oscillations which can be further suppressed with a damping resistor or a snubber. An example of using transistor with lower value of C_T is presented in Figs. 10-11. Parameters of the converter are as follows: $V_G = 12$ V, $L = 15$ µH, $C = 470$ µF, $G = 0.01$ S, $D = 0.3$, $T_S = 10$ µs. Using PN diodes instead of Schottky diodes is not recommended because of the reverse recovery charge, which increases the power loss. An example of an inductor current waveform, in the case when a PN diode was used, is presented in Fig. 12. All parasitic capacitances have been evaluated based on characteristics from a datasheet and input voltage $V_G = 12$ V, which corresponds to the transistor and diode voltage when they are turned off.

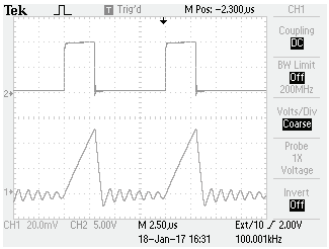

Fig. 10. Gate-source voltage (top) and inductor current (bottom) of a BUCK converter which uses transistor IRFZ44 (C_T = 650 pF) and diode IDD03SG60C (CD = 30 pF)

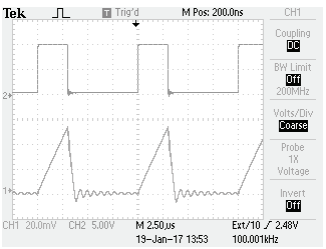

Fig. 11. Gate-source voltage (top) and inductor current (bottom) of a BUCK converter which uses transistor AP9962 (C_T = 250 pF) and diode IDD03SG60C (C_D = 30 pF)

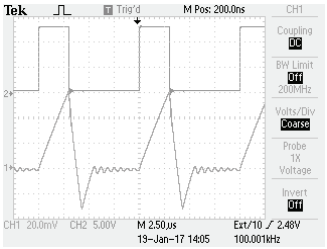

Fig. 12. Gate-source voltage (top) and inductor current (bottom) of a BUCK converter which uses transistor AP9962 (C_T = 250 pF) and diode 1N4007 (C_D = 4.5 pF, *trr* = 1 µs)

4.2. Damping resistor

Apart from proper selection of switches one can use an additional damping resistor, connected in parallel with the inductor [14]. To minimize the influence of the resistor on converter characteristics, its value should be much higher than inductor reactance calculated for specific switching frequency. In the example presented in Fig. 13b a resistor with a value of 1 kΩ has been connected in parallel to a 30 µH inductor. A switching frequency of 100 kHz was used. Other parameters are the same as for measurement from Fig. 6a.

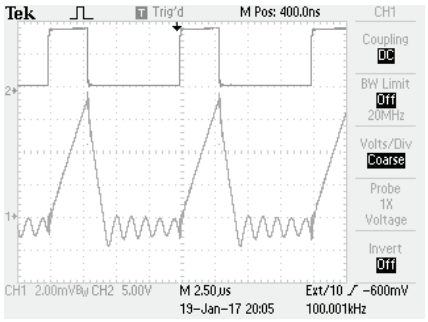

a)

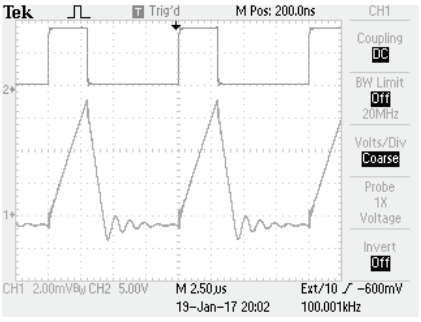

b)

Fig. 13. Gate-source voltage (top) and inductor current (bottom) of a BUCK converter working in DCM, a) without damping resistor; b) with damping resistor connected in parallel to inductor

Fig. 13a shows an inductor current waveform during measurement of the characteristic presented in Fig. 6a. An additional damping resistor not only reduced amplitude of the ringing but it also improved response of the output voltage to a duty cycle as shown in Fig. 14.

A more sophisticated approach is presented in [8] where a transistor, instead of the damping resistor, is connected in parallel to the inductor. The transistor is turned on when the inductor current reaches zero value. Because of small resistance R_{DSON} of the transistor, such solution can eliminate the oscillations more efficiently than the damping resistor. The main

drawback of using a transistor instead of a damping resistor is that it requires additional circuits such as a transistor driver and a circuit that detects the point when the inductor current reaches zero value.

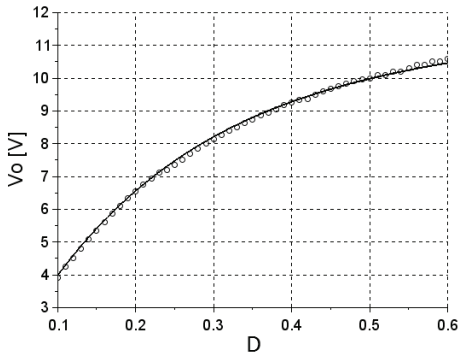

Fig. 14. Output voltage of a BUCK converter in DCM: solid – calculated from Eq. (4); dots – measured value

4.3. Snubber

A method which is frequently used to suppress any kind of oscillations is a *RC* circuit called a snubber. The snubber is usually connected in parallel with a low-side switch (Fig. 15). This solution can be easily found in literature along with methods of calculation R_S and C_S values [11-13, 15-16].

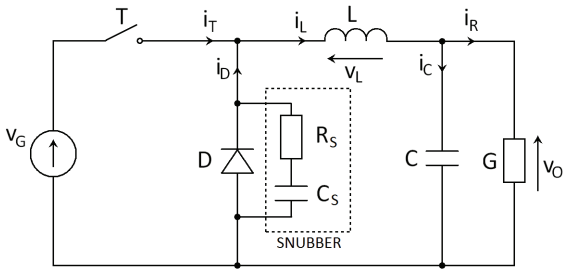

Fig. 15. Snubber circuit in BUCK converter

Values of a snubber capacitor and resistor can be changed to get the highest damping rate of the oscillations. However it is important to point out, that the snubber also dissipates power. In applications where high efficiency is required the snubber capacitance needs to be chosen carefully since it is involved in power dissipation according to the following formula [12]:

$$P_{\mathrm{SNUB}} = \frac{1}{2} C_S V_{\mathrm{SNUB}}^2 f_S \,, \tag{7}$$

where: V_{SNUB} is the voltage across the snubber, f_S is the switching frequency.

As a result of using a snubber in the converter related to Fig. 6a the inductor current oscillations are being suppressed, as shown in Fig. 16.

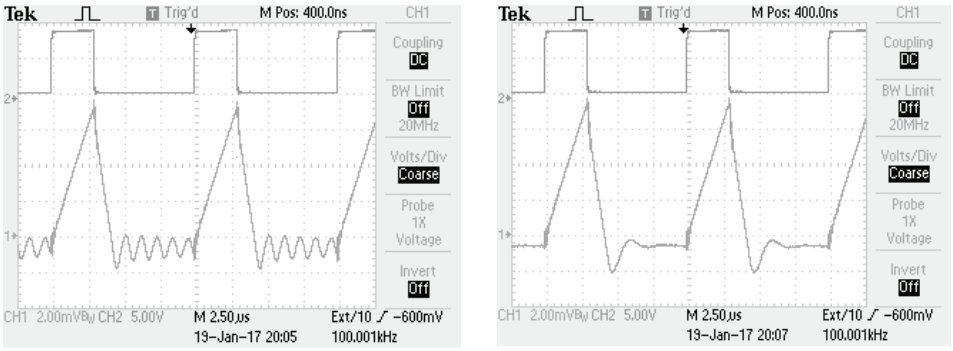

a) b)

Fig. 16. Gate-source voltage and inductor current of a BUCK converter: a) without snubber; b) with snubber connected in parallel with diode

Additional experiments have been performed to evaluate if the snubber circuit improves the voltage response to a change in a duty cycle. The experiments were performed in a similar way to those presented in the previous section (Fig. 6a and Fig. 9). The only difference was that a snubber circuit was used to suppress inductor current oscillations. The results of measurements are presented in Fig. 17-18.

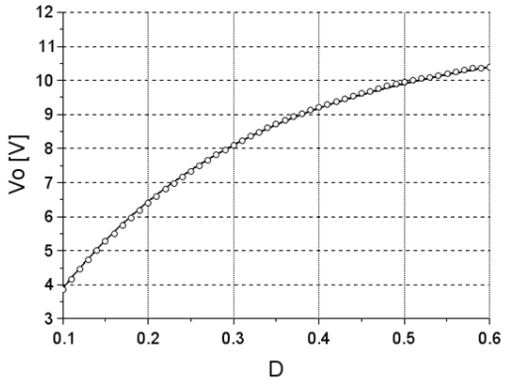

Fig. 17. Output voltage of a BUCK converter in DCM with snubber connected to diode: solid – calculated from Eq. (4); dots – measured value

The results of measurements presented in Figs. 17-18 show improvement in output voltage response to a change in a duty cycle. The value of the output voltage does not oscillate around theoretical value and it is consistent with a mathematical model (4). If the duty cycle is higher than 0.6 the output voltage of the measured converter differs from the theoretical value due to presence of the reverse current (Fig. 16b).

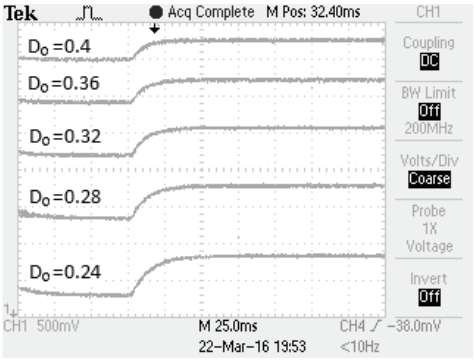

Fig. 18. Response of output voltage to step change of duty cycle in BUCK converter working in DCM with snubber connected to diode

One can notice that the negative current in Fig. 16b has higher amplitude and duration than the first negative oscillation in Fig. 16a. The duration and amplitude can be changed by using different parameters of the snubber [12]. In spite of reverse current presence an improvement has been achieved making the presented converter controllable in the range between $0 < D < 0.6$.

5. Conclusions

A control circuit should be designed based on a proper mathematical model of a converter. As a result of its operation, a PWM signal with a specific duty cycle is applied to the transistor driver. Any disturbance, not included in the assumed model, can substantially affect output voltage. This paper presents an influence of inductor current oscillations (present in DCM) on the response of the output voltage to duty cycle change. It has been shown, that the duty cycle, evaluated based on an inductor current waveform, can be different than the value of the duty cycle introduced to the transistor gate. The difference is a source of inconsistency in the output voltage and it depends on various parameters of a converter. In order to eliminate the oscillations some of known solutions have been presented. Two common methods using a dumping resistor and a snubber circuit were implemented in a real converter and measurements were made. As a result a good consistency between the theoretical and measured values of the output voltage was observed, confirming that the oscillations were the source of differences in the output voltage and proving usefulness of the damping resistor and snubber circuit.

References

[1] Janke W., Walczak M., *Small-signal input characteristics of step-down and step-up converters in various conduction modes*, Bulletin of the Polish Academy of Sciences: Technical Sciences, vol. 64, no. 2, pp. 265-270 (2016).

[2] Sun J., *Averaged modeling of PWM converters operating in discontinuous conduction mode*, IEEE Trans. on Power Electronics, vol. 16, no. 4, pp. 482-492 (2001).

[3] Reatti A., Kazimierczuk M.K., *Small-signal model for PWM converter for the discontinuous conduction mode and its application for the boost converter*, IEEE Trans. Circuits Syst. I, vol. 50, no. 1, pp. 65-73 (2003).
[4] Erickson R.W., Maksimović D., *Fundamentals of power electronics*, *2-nd Edition*, Springer (2004).
[5] Kazimierczuk M.K., *Pulse-Width Modulated DC–DC Power Converters*, J. Wiley (2008).
[6] Janke W., *Averaged models of pulse-modulated DC-DC power converters. Part II. Models based on the separation of variables*, Archives of Electrical Engineering, vol. 61, no. 4, pp. 633-654 (2012).
[7] Janke W., *Equivalent Circuits for Averaged Description of DC-DC Switch-Mode Power Converters Based on Separation of Variables Approach*, Bulletin of the Polish Academy of Sciences, vol. 61, no. 3, pp. 711-723 (2013).
[8] Yajun L., Xinquan L., Qiang Y., Bing Y., *High efficiency and low electromagnetic interference boost DC-DC converter*, Journal of Semiconductors, vol. 35, no. 4, pp. 045002-1 – 040002-8 (2014).
[9] Janke W., Walczak M., *Comparison of transient states in step-down power converter (BUCK) in continuous and discontinuous conduction mode*, Bulletin of the Polish Academy of Science: Technical Sciences, vol. 62, no. 4, pp. 773-778 (2014).
[10] Rich A., *Intersil Integrated Fet DCDC Converters*, Intersil Application Note 1209.0, February 23 (2006).
[11] El-Ghanam S.M., Abdel Basit W., Ismail M., Kamh S.A., Ashry H.A., Soliman F.A.S., *Improvement of Switching Characteristics of Boost Converter Systems*, ARPN Journal Of Science and Technology, vol. 3 no. 3, pp. 254-258 (2013).
[12] *Ringing Reduction Techniques for NexFET™ High Performance MOSFETs*, Texas Instruments, Application Report (2011).
[13] Falin J., *Minimizing Ringing at the Switch Node of a Boost Converter*, Texas Instruments, Application Report (2006).
[14] Maksimović D., *A Unified Analysis of PWM Converters in Discontinuous Modes*, IEEE Transactions of Power Electronics, vol. 6, no. 3, pp. 476-490 (1991).
[15] Choudhary V., *Controlling switch-node ringing in DC/DC converters*, Texas Instruments (2016).
[16] Taylor R., Manack R., *Controlling switch-node ringing in synchronous buck converters*, Texas Instruments, Analog Applications Journal, vol. 2Q, pp. 5-7 (2012).

ARCHIVES OF ELECTRICAL ENGINEERING VOL. 66(2), pp. 325-337 (2017)

DOI 10.1515/aee-2017-0024

Improvement of the finite element method equations conditioning for the magnetic field-circuital problems

MAREK GOŁĘBIOWSKI

Faculty of Electrical and Computer Engineering, Rzeszow University of Technology
Wincentego Pola 2, 35-959 Rzeszów, Poland
e-mail: yegolebi@prz.edu.pl

(Received: 16.09.2016, revised: 16.01.2017)

Abstract: The presented systems with magnetically coupled windings are solved with the finite element method. If the issue of voltage supply is analyzed, a system of linear equations with a partially skew-symmetric sparse matrix is obtained. Iterative methods used to solve a system of equations are particularly effective for symmetric matrices. Resultant equations can be reduced to this symmetrical form by using the method known from the literature [1]. The ratio of the maximum to the minimum eigenvalue of the main matrix of this circuit, which is the condition number, is however very high. This means that the problem is ill-conditioned and leads to a very long iterative solution process. The method presented in the article allows for a direct solution of a system of equations on its part, corresponding to high eigenvalues of the system matrix. The remaining part of the system of equations is solved by iterative methods. This part has much better condition number, and therefore the computational process is fast. The proposed iterative process depends on multiplication of a sparse matrix by vectors. It is not necessary (and possible) to store the entire matrix. This is especially important for larger sizes of a matrix.

Key words: magnetic field-circuital problem, condition number, iterative method

1. Introduction

In many problems a large linear system of algebraic equations of the form (1) must be solved in the following way:

$$[\boldsymbol{A}]\cdot\vec{\boldsymbol{x}}=\vec{\boldsymbol{b}};\quad \overrightarrow{\boldsymbol{res}}=[\boldsymbol{A}]\cdot\vec{\boldsymbol{x}}-\vec{\boldsymbol{b}}\,, \tag{1}$$

where: $\vec{\boldsymbol{b}}$ is a known vector, [$\boldsymbol{A}$] is a square, symmetrical, positive definite $n\times n$ matrix, $\overrightarrow{\boldsymbol{res}}$ is the error of the $\vec{\boldsymbol{x}}$ solution.

We meet often in reality with the issue of this form, e.g. with boundary problems of partial differential equations of elliptic type, when designing a network, trusses, etc. Due to these issues the dimension n is so large that the overall number of elements in the matrix n^2 greatly exceeds the capabilities of a digital machine's memory.

Therefore, one can use the special form of the matrix [$\boldsymbol{A}$], which is usually a sparse matrix [1, 2]. The efficient iterative methods of solving problems of type (1) were developed. The

best of these methods, e.g. a Chebyshev method requires certain additional information about the spectrum of the matrix [$\boldsymbol{A}$] [2, 3].

The minimum information is the knowledge of the smallest possible range containing the spectrum (eigenvalues) of the matrix [$\boldsymbol{A}$]. This information is not always available. On the other hand, there are methods like e.g. the conjugate gradient method or minimal residual method, which do not require any information about the spectrum of the matrix [$\boldsymbol{A}$].

These methods, however, are unstable. What is noteworthy is an idea to combine two methods: the Chebyshev method with the minimal residual method [2, 3]. The essence of this combination is alternating the work of these methods. The Chebyshev method reduces errors of the solution $\vec{\boldsymbol{x}}$ of the system (1) for high eigenvalues of the matrix [$\boldsymbol{A}$]. The minimal residual method reduces errors of the solution corresponding with small eigenvalues of the matrix [$\boldsymbol{A}$]. As soon as the minimal residual method loses stability, the error norm, i.e. the norm of the residuum:

$$\overrightarrow{\boldsymbol{res}} = [\boldsymbol{A}] \cdot \vec{\boldsymbol{x}} - \vec{\boldsymbol{b}} \tag{2}$$

is enlarged.

Then the stable Chebyshev method that reduces errors associated with the upper half of the spectrum of the matrix [$\boldsymbol{A}$] is executed [4]. The greatest eigenvalue of λ_{max} is usually easy to estimate, e.g. using the Gershgorin theorem [5], or by adopting any norm of the matrix [$\boldsymbol{A}$] corresponding to the vector norm.

It is assumed that the Chebyshev method is intended to reduce errors of a solution corresponding to the eigenvalues from the range of

$$\left[\lambda_{max}, \frac{1}{2}\lambda_{max}\right].$$

The alternative use of Chebyshev methods and the minimal residual method [3, 4] always allows to obtain a solution of the symmetrical system of Equations (1).

The essence of the proposal included in this article is to replace the Chebyshev method by a direct solution (i.e. not iterative). This step resets the errors associated with the upper part of the spectrum of the matrix [$\boldsymbol{A}$] in a single execution. Further reduction of residuum will be performed by, also previously initiated, the iterative minimal residual method.

A part of the solution $\vec{\boldsymbol{x}}$ associated with smaller eigenvalues of the spectrum of the matrix [$\boldsymbol{A}$] will be improved with this iterative method. The ratio of the maximum eigenvalue to the minimum eigenvalue of this spectrum part will be lower than in full spectrum of the matrix [$\boldsymbol{A}$]. This means better conditioning of the minimal residual method and a much lower number of iterations needed.

2. The finite element method equations for the systems with magnetically coupled windings

The magnetic field is expressed by a vector potential

$$\vec{\boldsymbol{A}} = \sum_i \vec{\boldsymbol{N}}_{\boldsymbol{i}} \cdot A_i \ ,$$

where $\vec{N}_i$ represents the edge basis functions. Scalar potential is expressed by nodal basis functions N_i as

$$\varphi = \sum_i N_i \cdot \varphi_i$$

The current density of the j-th winding with the current i, i.e. $\vec{\boldsymbol{J}}_j$ is expressed by the vector introduced by $\vec{\boldsymbol{T}}_j$ as $\vec{\boldsymbol{J}}_j = \overrightarrow{\text{rot}}(\vec{\boldsymbol{T}}_j) \cdot i_j$ [1, 6, 9]. The vector $\vec{\boldsymbol{T}}_j$ is stretched on a j-th winding. By its means, one can write the magnetic flux coupled with j-th winding:

$$\Psi_j = \int_V \vec{\boldsymbol{T}}_j \cdot \vec{\boldsymbol{B}} \, \mathrm{d}V = \int_V \vec{\boldsymbol{T}}_j \cdot \overrightarrow{\text{rot}}\left(\vec{\boldsymbol{A}}\right) \mathrm{d}V \ , \tag{3}$$

where $\vec{\boldsymbol{B}}$ is the magnetic induction.

Voltage equations for windings can be written (after integrating) as:

$$\Psi_j + L_{\sigma j} i_j + R_j \int_0^t i \mathrm{d}t = \int_0^t u_j \mathrm{d}t \ ; j = 1,2,\ldots f \ , \tag{4}$$

where $L_{\sigma j}$ is the leakage inductance of the j-th winding, R_j is its resistance, u_j is the supplying voltage, and f is a number of phases (of windings).

In 2D calculations, leakage inductance of the winding $L_{\sigma j}$ should include the end-winding and mains leakage inductance. With the use of implicit methods of solving equations, $L_{\sigma j} + R_j / 2\mathrm{d}t$ should be considered as leakage inductance, where $\mathrm{d}t$ is the integration step. In 3D calculations, the end-windings inductance is not included because it is included directly by the finite element method. With v the inverse of magnetic permeability and with γ electrical conductivity of metal sheets are determined. Applying the Galerkin weak formulation [1, 9] a set of equations of the finite element method for systems with magnetically coupled windings can be written [1, 6, 9] as:

$$\begin{bmatrix} \begin{bmatrix} v[\boldsymbol{R}] & 0 & 0 \\ 0 & v[\boldsymbol{R}] + \gamma \dfrac{\mathrm{d}}{\mathrm{d}t}[\boldsymbol{C}] & \gamma \dfrac{\mathrm{d}}{\mathrm{d}t}[\boldsymbol{D}] \\ 0 & \gamma \dfrac{\mathrm{d}}{\mathrm{d}t}[\boldsymbol{D}]^t & \gamma \dfrac{\mathrm{d}}{\mathrm{d}t}[\boldsymbol{G}] \end{bmatrix} & \begin{matrix} [-\boldsymbol{T}_0] \\ \\ [\boldsymbol{L}_\sigma] \end{matrix} \\ [\boldsymbol{T}_0]^t & \end{bmatrix} \begin{bmatrix} \begin{bmatrix} \boldsymbol{X}_1 = \vec{\boldsymbol{A}}_{\gamma=0} \\ \boldsymbol{X}_1 = \vec{\boldsymbol{A}}_{\gamma>0} \\ \boldsymbol{X}_2 = \varphi_{\gamma>0} \end{bmatrix} \\ \boldsymbol{X}_3 = \begin{matrix} i_1 \\ i_2 \\ \vdots \\ i_f \end{matrix} \end{bmatrix} = \begin{bmatrix} [\mathbf{P}_1] \\ \left[\int_0^t u_j \mathrm{d}t\right] = [\mathbf{P}_2] \end{bmatrix}, \tag{5}$$

where:

$$[\boldsymbol{R}]_{ij} = \iiint_V \overrightarrow{\mathrm{rot}}\,\vec{\boldsymbol{N}}_i \cdot \overrightarrow{\mathrm{rot}}\,\vec{\boldsymbol{N}}_j \,\mathrm{d}V\,, \qquad [\boldsymbol{G}]_{ij} = \iiint_V \overrightarrow{\mathrm{grad}}N_i \cdot \overrightarrow{\mathrm{grad}}N_j \,\mathrm{d}V\,,$$

$$[\boldsymbol{C}]_{ij} = \iiint_V \vec{\boldsymbol{N}}_i \cdot \vec{\boldsymbol{N}}_j \,\mathrm{d}V\,, \qquad [\boldsymbol{D}]_{ij} = \iiint_V \vec{\boldsymbol{N}}_i \cdot \overrightarrow{\mathrm{grad}}N_j \,\mathrm{d}V\,,$$

$$[\boldsymbol{T}_0]_{ij} = \iiint_V \overrightarrow{\mathrm{rot}}\,\vec{\boldsymbol{N}}_i \cdot \vec{\boldsymbol{T}}_j \,\mathrm{d}V\,,$$

where: i is the line number, j is the number of windings, and t is the matrix transposition.

In conductive areas, where the electrical conductivity $\gamma \neq 0$ the scalar potentials φ are unknowns.

Partial skew-symmetry is related to winding currents, that act as a vector of unknowns $[\boldsymbol{X}_3]$. This is confirmed by Maxwell's equations:

$$\overrightarrow{\mathrm{rot}}\,\vec{\boldsymbol{H}} = \vec{\boldsymbol{J}};\ \overrightarrow{\mathrm{rot}}\,\vec{\boldsymbol{E}} = \frac{-\partial \vec{\boldsymbol{B}}}{\partial t}\,. \tag{6}$$

The resulting Equation (5) with a sparse matrix, due to the large size, should be solved by iterative methods. The symmetry of the matrix radically quickens the solution of iterative methods. It is therefore necessary to bring the system (5) to a symmetrical form [1].

The system of Equations (5) can be written as:

$$\begin{bmatrix} \boldsymbol{M} & -\boldsymbol{T}_0 \\ \boldsymbol{T}_0^t & \boldsymbol{L}_\sigma \end{bmatrix} \cdot \begin{bmatrix} \boldsymbol{X}_{12} \\ \boldsymbol{X}_3 \end{bmatrix} = \begin{bmatrix} \boldsymbol{P}_1 \\ \boldsymbol{P}_2 \end{bmatrix}, \quad \text{where} \quad [\boldsymbol{X}_{12}] = \begin{bmatrix} \boldsymbol{X}_1 \\ \boldsymbol{X}_2 \end{bmatrix}. \tag{7}$$

By reducing the unknowns $[\boldsymbol{X}_3]$ from the system, it can be reduced to a symmetrical form of:

$$[\boldsymbol{M} + \boldsymbol{T}_0 \cdot \boldsymbol{L}_\sigma^{-1} \cdot \boldsymbol{T}_0^t] \cdot [\boldsymbol{X}_{12}] = [\boldsymbol{P}_1 + \boldsymbol{T}_0 \cdot \boldsymbol{L}_\sigma^{-1} \cdot \boldsymbol{P}_2] = [\boldsymbol{P}] \tag{8}$$

and

$$[\boldsymbol{X}_3] = \boldsymbol{L}_\sigma^{-1}\left[\boldsymbol{P}_2 - \boldsymbol{T}_0^t \cdot [\boldsymbol{X}_{12}]\right]. \tag{9}$$

The system of Equations (8) is symmetrical, because the $[\boldsymbol{L}_\sigma]$ matrix is symmetrical. The main matrix of the system includes components created by the finite element method introduced by the matrix $[\boldsymbol{M}]$. It also includes the components associated with $[\boldsymbol{L}_\sigma]^{-1}$ that have high values. Therefore, this matrix spectrum is wide. The ratio of the highest to the lowest eigenvalue, i.e. the condition number is large. This implies a large number of iterations at which the stability of the solution may be lost. It is possible, however, to extract earlier the solution's components associated with large eigenvalues. They are introduced into the system (8) by the element $[\boldsymbol{L}_\sigma]^{-1}$. For this purpose, a direct method is used. It solves a system of small dimensions, because the $[\boldsymbol{L}_\sigma]$ matrix has a size equal to the f number of windings.

This direct method replaces the previously described Chebyshev iterations. This method is the essence of the presented article.

Other components of the solution, corresponding to smaller eigenvalues, are obtained by iterative methods, e.g. by the minimal residual method. They are much faster after the elimi-

nation of the components corresponding to large eigenvalues. They work in a smaller range of the spectrum, so conditioning is much better. Despite a series of additional operations related therein and large dimension of the issue, iterative calculations can be carried out using the sparse matrix technique.

3. Improvement of the matrix condition number of the system with magnetically coupled windings

The reduction of matrix spectrum of the magnetic system will be exemplified by the system solved with circuital methods. The principle of the transformation is the same as for a system solved with the finite element method (5). However, due to smaller dimensions of the equations it is easier to observe the results of transformations. The tested system is shown in Fig. 1.

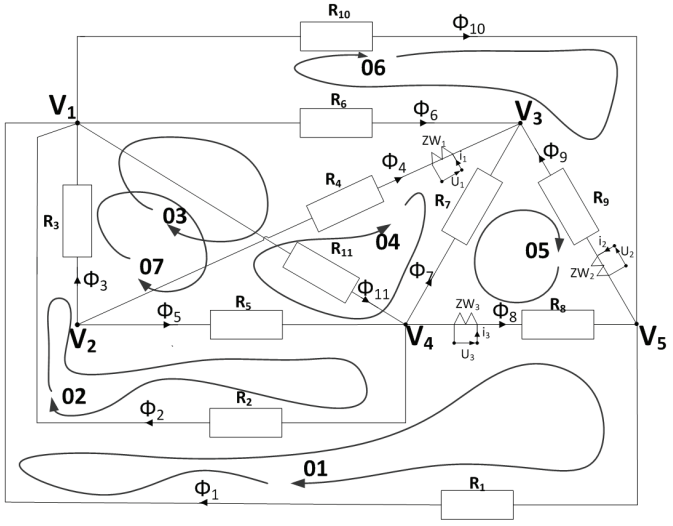

Fig. 1. System with three magnetically coupled windings ($g = 11$, $s = 7$, $r = 5$)

An exemplary system has $g = 11$ magnetic cores with the Φ_{gi} magnetic fluxes, ($i = 1 : 11$). Magnetic reluctance (resistance) of cores is marked by R_i, ($i = 1 : 11$).

The magnetic system has $r = 5$ nodes with magnetic potentials V_i, ($i = 1 : 5$). This means that the system of equations has $s = g - (r - 1) = 7$ independent loops (degrees of freedom). It will be solved by the loop flux method.

The loop fluxes Φ_{oi} ($i = 1 : 7$) are introduced. The loops are indicated in Fig. 1 as O_i, ($i = 1 : 7$). Connections of cores are described by the connection matrix ***pol***($s = 7$, $g = 11$). From the fluxes of loops Φ_O one can obtain fluxes in the branches Φ_g.

$$[\boldsymbol{\Phi}_g] = [\boldsymbol{pol}]^t \cdot [\boldsymbol{\Phi}_O], \tag{10}$$

where the connection matrix [***pol***] is:

$$[\boldsymbol{pol}] = \begin{bmatrix} 1 & -1 & 0 & 0 & 0 & 0 & 0 & 1 & 0 & 0 & 0 \\ 0 & 1 & -1 & 0 & 1 & 0 & 0 & 0 & 0 & 0 & 0 \\ 0 & 0 & 1 & -1 & 0 & 1 & 0 & 0 & 0 & 0 & 0 \\ 0 & 0 & 0 & 1 & -1 & 0 & -1 & 0 & 0 & 0 & 0 \\ 0 & 0 & 0 & 0 & 0 & 0 & 1 & -1 & -1 & 0 & 0 \\ 0 & 0 & 0 & 0 & 0 & -1 & 0 & 0 & 1 & 1 & 0 \\ 0 & 0 & 1 & 0 & -1 & 0 & 0 & 0 & 0 & 0 & 1 \end{bmatrix}. \tag{11}$$

Magnetic reluctances of cores form a square matrix of the values established on the diagonal are:

$$\operatorname{diag}(\boldsymbol{R}_g) = [2.706 \;\; 2.408 \;\; 1.036 \;\; 2.011 \;\; 17.84 \;\; 3.383 \;\; 1.934 \;\; 2.586 \;\; 1.497 \;\; 2.806 \;\; 1.789]. \tag{12}$$

On the magnetic cores with numbers 4, 9 and 8 windings were placed with the number of coils of respectively $zw_1 = 2$, $zw_2 = 1$, $zw_3 = 4$. Therefore magnetomotive forces can be written as: $\Theta_4 = zw_1 \cdot i_1$, $\Theta_9 = zw_2 \cdot i_2$, $\Theta_8 = zw_3 \cdot i_3$, where i_1, i_2, i_3 are the winding currents. The remaining cores have specific electric loading equal to zero. Creating a winding number matrix [***Zw***] with dimension$(g \times f)$ is:

$$[\boldsymbol{Zw}] = \begin{bmatrix} 0 & 0 & 0 & zw_1 & 0 & 0 & 0 & 0 & 0 & 0 & 0 \\ 0 & 0 & 0 & 0 & 0 & 0 & 0 & 0 & zw_2 & 0 & 0 \\ 0 & 0 & 0 & 0 & 0 & 0 & 0 & zw_3 & 0 & 0 & 0 \end{bmatrix}^t. \tag{13}$$

The magnetic voltages on cores can be written as:

$$[\boldsymbol{E}_g] = [\boldsymbol{R}_g] \cdot [\boldsymbol{\Phi}_g] - [\boldsymbol{Zw}] \cdot [\boldsymbol{i}], \tag{14}$$

where $[\boldsymbol{i}] = [\, i_1 \,,\; i_2 \,,\; i_3 \,]^t$ and i_1, i_2, i_3 are the currents flowing through the windings.

The equations of magnetic tensions of the circuit can be written as:

$$[\boldsymbol{pol}] \cdot [\boldsymbol{E}_g] = [0] \tag{15}$$

At the same time, voltage equations for windings (equivalent to Equation [4]) can be written (after integrating) as:

$$[\boldsymbol{L}_\sigma] \cdot [\boldsymbol{i}] + [\boldsymbol{Zw}]^t \cdot [\boldsymbol{\Phi}_g] = \begin{bmatrix} \int u_1 \, \mathrm{d}t \\ \int u_2 \, \mathrm{d}t \\ \int u_3 \, \mathrm{d}t \end{bmatrix} = [\boldsymbol{E}_C], \tag{16}$$

To Equations (14) and (16) we incorporate Equation (10) that expresses the branch fluxes

$[\Phi_g]$ through the loop fluxes $[\Phi_o]$. Then, from the Equation (16) we calculate currents $[\boldsymbol{i}]$ and insert them into the Equation (14). What we get from Equation (15) is:

$$\begin{aligned}\left\{[\boldsymbol{pol}]\cdot[\boldsymbol{R_g}]\cdot[\boldsymbol{pol}]^t+[\boldsymbol{pol}]\cdot[\boldsymbol{Zw}]\cdot[\boldsymbol{L_\sigma}]^{-1}\cdot[\boldsymbol{Zw}]^t\cdot[\boldsymbol{pol}]^t\right\}[\boldsymbol{\Phi_o}]=\\ =[\boldsymbol{pol}]\cdot[\boldsymbol{Zw}]\cdot[\boldsymbol{L_\sigma}]^{-1}\cdot[\boldsymbol{E_C}]=[\boldsymbol{P}]\ldots\end{aligned} \tag{17}$$

and:

$$[\boldsymbol{i}]=[\boldsymbol{L_\sigma}]^{-1}\cdot\left\{[\boldsymbol{E_C}]-[\boldsymbol{Zw}]^t\cdot[\boldsymbol{pol}]^t\cdot[\boldsymbol{\Phi_o}]\right\}. \tag{18}$$

Equations (17) and (18) are equivalent to Equations (8) and (9). Equation (17) as well as (8) have a symmetric matrix, obtained after reduction of the vector of currents $[\boldsymbol{i}]$.

Further considerations will be carried out with the denotations from the Equations (8) and (9), that correspond to equations (17, 18):

$$\begin{aligned}[\boldsymbol{M}]&=[\boldsymbol{pol}]\cdot[\boldsymbol{R_g}]\cdot[\boldsymbol{pol}]^t,\\ [\boldsymbol{T_0}]&=[\boldsymbol{pol}]\cdot[\boldsymbol{Zw}].\end{aligned} \tag{19}$$

The matrix $[\boldsymbol{T_0}]$ has dimensions $s\times f$ ($s=7$, $f=3$). The dimension s is the number of independent loops from the system in Fig. 1. At the same time it is the number of unknowns of the loop flux method $[x]=[\Phi_o]$. When calculating with the finite elements method there is a very large number of unknowns in this method, i.e. $[\boldsymbol{X}_{12}]$ from the Equation (7). It should be noted that the columns of the matrix $[\boldsymbol{T_0}]$ from equations (5, 7) and (19) are not always independent from each other, i.e. they are not always mutually orthogonal. Using the Gram-Schmidt method of orthogonalization [2, 4] one can achieve mutual orthogonality of matrix columns $[\boldsymbol{T_0}]$.

$$[\boldsymbol{T_0}]=[\boldsymbol{w}]\cdot[\boldsymbol{p}],\ \text{while}\ [\boldsymbol{w}]^t\cdot[\boldsymbol{w}]=[\boldsymbol{I}]_f. \tag{20}$$

The matrix $[w]$ includes $f=3$ mutually orthogonal columns. The matrix $[p]$ is a permutation matrix with $f\times f$ dimensions, and $[\boldsymbol{I}]_f$ is the identity matrix.

The main matrix of the system (17) can be written as:

$$[\boldsymbol{mgl}]=[\boldsymbol{M}]+[\boldsymbol{w}]\cdot[\boldsymbol{p}]\cdot[\boldsymbol{L_\sigma}]^{-1}\cdot[\boldsymbol{p}]^t\cdot[\boldsymbol{w}]^t. \tag{21}$$

We introduce a denotation:

$$[\lambda]=[\mathbf{p}]\cdot[\mathbf{L}_\sigma]^{-1}\cdot[\mathbf{p}]^t, \tag{22}$$

i.e.

$$[\mathbf{mgl}]=[\mathbf{M}]+[\mathbf{w}]\cdot[\lambda]\cdot[\mathbf{w}]^t. \tag{23}$$

The matrix $[\boldsymbol{L_\sigma}]$ has on its diagonal leakage inductance of windings, which were adopted as:

$$\operatorname{diag}(\boldsymbol{L}_{\boldsymbol{\sigma}}) = [0.004 \quad 0.0018 \quad 0.0013]\,. \tag{24}$$

One can compare the eigenvalues of the loop flux matrix [***M***] and the main matrix [***mgl***] of the system (17) (arranged in rows):

$$\begin{aligned} [\boldsymbol{M}] &\rightarrow [0.69783 \quad 1.6748 \quad 4.7887 \quad 5.7198 \quad 9.6157 \quad 11.387 \quad 57.683] \\ [\boldsymbol{mgl}] &\rightarrow [0.75934 \quad 2.0638 \quad 6.2271 \quad 49.228 \quad 822.86 \quad 2016.3 \quad 24294] \end{aligned}. \tag{25}$$

It can be seen that the ratio of the largest eigenvalue to the smallest one i.e. the condition number has been enlarged in the matrix [***mgl***], after the introduction of windings and leakage inductance [$\boldsymbol{L}_{\boldsymbol{\sigma}}$] into the system:

$$82.66 = \frac{57.684}{0.69783} \rightarrow 31994 = \frac{24294}{0.75934}\,. \tag{26}$$

This implies a huge inconvenience in iterative calculations and threatens their stability. This occurs despite the fact, that the matrix [***mgl***] is symmetric. The element which caused the deterioration of conditioning [$\boldsymbol{\lambda}$] is related to vectors which are columns of the matrix [***w***]. To improve the condition number, one must separate the elements of the solution [x] = [Φ_o] of the system (17), associated with these vectors contained in the columns of the matrix [***w***]. This is the essence of the method presented in this article.

Therefore, we assume that the solution [x] = [Φ] of the system (17) can be written as:

$$[\boldsymbol{x}] = [\boldsymbol{w}] \cdot [\boldsymbol{x}_0] + [\boldsymbol{y}]\,. \tag{27}$$

We assume that the first part of the solution [***w***] · [$\boldsymbol{x}_0$] belongs to the subspace created by vectors, which are columns in the matrix [***w***]. These vectors create the vector space Ω_1. It has a small dimension $f = 3$. The entire space which dimension is $s = 7$, is denoted as Ω. It contains the solution [***x***]. We assume that the part of the solution, denoted as [***y***] is orthogonal to the subspace Ω_1 and belongs to the subspace $\Omega_2 = \Omega \setminus \Omega_1$:

$$[\boldsymbol{w}]^t \cdot [\boldsymbol{y}] = [\boldsymbol{0}]_{\boldsymbol{f=3}}\,. \tag{28}$$

For further calculations we assume that the vector [P] of the right side of the Equation (17) is:

$$[\boldsymbol{P}] = [33010 \quad 9.5717 \quad -5995.1 \quad 6008 \quad -51149 \quad 18154 \quad 9.1574]^t\,. \tag{29}$$

In order to calculate the vector [$\boldsymbol{x}_0$] from the formula (27) we substitute the solution [***x***] from the formula (27) into Equation (17) and multiply the resulting equation from the left side by [***w***]^t.

$$\left\{[\boldsymbol{w}]^t \cdot [\boldsymbol{M}] \cdot [\boldsymbol{w}] + [\boldsymbol{\lambda}]\right\} \cdot [\boldsymbol{x}_0] = [\boldsymbol{w}]^t \cdot [\boldsymbol{P}] - [\boldsymbol{w}]^t \cdot [\boldsymbol{M}] \cdot [\boldsymbol{y}]\,. \tag{30}$$

Denoting:

$$[\boldsymbol{M}_0] = [\boldsymbol{w}]^t \cdot [\boldsymbol{M}] \cdot [\boldsymbol{w}] + [\boldsymbol{\lambda}]\,, \tag{31}$$

we have:

$$[\boldsymbol{x_0}] = \underbrace{[\boldsymbol{M_0}]^{-1} \cdot [\boldsymbol{w}]^t \cdot [\boldsymbol{P}]}_{[x00]} - \underbrace{[\boldsymbol{M_0}]^{-1} \cdot [\boldsymbol{w}]^t \cdot [\boldsymbol{M}]}_{[y00]} \cdot [\boldsymbol{y}]. \tag{32}$$

Due to the size of the vector $[\boldsymbol{x}_0]$ equal to $f = 3$, the above calculation is fast and carried out by the non-iterative method (direct). The vector $[\boldsymbol{x}_0]$ from the formula (32) is substituted to the formula (27), on $[\boldsymbol{x}]$, and then to the Equation (17). The purpose is to calculate the vector $[\boldsymbol{y}]$. This way we obtain:

$$\begin{aligned} &\left\{[\boldsymbol{M}]+[\boldsymbol{w}]\cdot[\boldsymbol{\lambda}]\cdot[\boldsymbol{w}]^t-([\boldsymbol{M}]\cdot[\boldsymbol{w}])\cdot[\boldsymbol{M_0}]^{-1}\cdot\left([\boldsymbol{w}]^t\cdot[\boldsymbol{M}]\right)-[\boldsymbol{w}]\cdot[\boldsymbol{\lambda}]\cdot[\boldsymbol{M_0}]^{-1}\cdot\right. \\ &\left.\cdot\left([\boldsymbol{w}]^t\cdot[\boldsymbol{M}]\right)\right\}\cdot[\boldsymbol{y}]=[\boldsymbol{P}]-[\boldsymbol{mgl}]\cdot[\boldsymbol{w}]\cdot[\boldsymbol{M_0}]^{-1}\cdot[\boldsymbol{w}]^t\cdot[\boldsymbol{P}] \quad \Leftrightarrow \quad [\boldsymbol{mac}]\cdot[\boldsymbol{y}]=[\boldsymbol{b}] \end{aligned} \tag{33}$$

This is a linear Equation (1). Due to its large dimensions as for the finite element method, it should be solved by iterative methods. In the case of the finite element method, the calculation of the residue $\overrightarrow{\boldsymbol{res}}$ from the formula (2) for this equation involves operations on sparse matrices which are multiplied by vectors. Therefore, it is fast.

The example considered in Fig. 1 has small dimensions. Therefore one can compare the results of the presented method and direct calculations.

The results of direct calculations $[\boldsymbol{x}] = [\Phi_o]$ from the Equation (17) are applied to calculate the vector $[\boldsymbol{y}]$ by separating from $[\boldsymbol{x}]$ the components that belong to the subspace Ω_2. In order to do this, the solution $[\boldsymbol{x}]$ should be multiplied by the matrix $[\boldsymbol{U}]$.

$$[\boldsymbol{U}] = \mathrm{eye}(s) - [\boldsymbol{w}]\cdot[\boldsymbol{w}]^t; \quad [\boldsymbol{y}] = [\boldsymbol{U}]\cdot[\boldsymbol{x}], \tag{34}$$

where $\mathrm{eye}(s)$ is the identity matrix of dimensions $s = 7$. The vector $[\boldsymbol{y}]$ calculated in this way is used for comparison with the vector $[\boldsymbol{y}]$ calculated from Equation (33). Similarly, knowing $[\boldsymbol{y}]$ one can calculate $[\boldsymbol{x}_o]$ with (32).

It can be compared with the results $[\boldsymbol{x}]$ of a directly solved Equation (17) by means of the multiplication:

$$[\boldsymbol{x_0}] = [\boldsymbol{w}]^t \cdot [\boldsymbol{x}]. \tag{35}$$

Such verification is only possible thanks to small dimensions of the example considered in Fig. 1.

The matrix $[\boldsymbol{mac}]$ of the equation system (33) is not symmetrical. The missing element $[\boldsymbol{dod}]$ of its symmetrization is the transposition of the last component of the matrix $[\boldsymbol{mac}]$ in the formula (33):

$$[\boldsymbol{dod}] = -[\boldsymbol{M}]\cdot[\boldsymbol{w}]\cdot[\boldsymbol{M_0}]^{-1}\cdot[\lambda]\cdot[\boldsymbol{w}]^t. \tag{36}$$

In the Equation (33) this element is multiplied by a vector of unknowns $[\boldsymbol{y}]$. Due to the assumption (28), the vector $[\boldsymbol{y}]$ belongs to the subspace Ω_2. In the same way also:

$$[\boldsymbol{dod}]\cdot[\boldsymbol{y}] = [0]_{\boldsymbol{S}=7}. \tag{37}$$

Therefore, an additional element of [***dod***] does not contribute to the residuum $\overrightarrow{\boldsymbol{res}}$ (2) of the system of Equations (33) and therefore may be abandoned. After abandoning the element [***dod***], despite the asymmetry, the iterative methods can be used, e.g. the minimal residual method, suitable for symmetrical systems. This accelerates calculation process considerably.

The right side [***b***] of the system (33) also belongs to the subspace Ω_2. It can be seen after multiplying the left side by $[\boldsymbol{w}]^t$:

$$[\boldsymbol{w}]^t \cdot [\boldsymbol{b}] = [\boldsymbol{w}]^t \cdot [\boldsymbol{P}] - \underbrace{[\boldsymbol{w}]^t \cdot [\boldsymbol{mgl}] \cdot [\boldsymbol{w}]}_{[\boldsymbol{M}_0]} \cdot [\boldsymbol{M}_0]^{-1} \cdot [\boldsymbol{w}]^t \cdot [\boldsymbol{P}] = [0]_f \ . \tag{38}$$

Taking into account Equations (23) and (31) we obtain a confirmation of the formula (38).

During the iterative process of solving the system of Equations (33), both the solution [***y***] and the vector of residuals (2) should belong to the subspace Ω_2, thus should be orthogonal to the vector-columns of the matrix [***w***]. However, due to rounding errors, there may occur components that belong to the subspace Ω_1. These errors will increase, because when calculating the residuum (2) they are multiplied by large eigenvalues of the matrix [***mac***], that correspond to the subspace Ω_1.

They can cause a loss of stability of the minimal residual method, which manifests itself in a normal increase of the residue during iteration. In order to counteract, these components must be removed during iteration. For this purpose, the substitution by means of the matrix $[\boldsymbol{U}]$ from the formula (34) should be performed during iteration:

$$[\boldsymbol{y}] := [\boldsymbol{U}] \cdot [\boldsymbol{y}]. \tag{39}$$

Removing these components corresponds to the Chebyshev iterative method, carried out on error vectors corresponding to large eigenvalues. This was previously described as the combination of the Chebyshev method and the minimal residual method. However, it is much easier and faster.

In order to prove the assumption (28) of the vector [***y***] belonging to the space Ω_2, one must prove that the solution of the system (33) has this property.

For this purpose, we multiply the left side of the equation (33) by $[\boldsymbol{w}]^t$. We use the Equations (38) and (31). We also use mutual orthogonality of the matrix [***w***] columns (20).

$$[\mathbf{w}]^t \cdot ([\mathbf{mac}] \cdot [\mathbf{y}]) = [\mathbf{w}]^t \cdot [\mathbf{b}] \ \Rightarrow \ [\lambda] \cdot \left([\mathbf{w}]^t \cdot [\mathbf{y}]\right) = [\mathbf{0}]_f \ \Rightarrow \ \text{equation (28)} \ . \tag{40}$$

The matrix [***mac***] of the system of Equations (33) is asymmetric. This does not prevent the use of iterative methods designed for symmetric systems to solve this system. This is because the solution $[\boldsymbol{y}]$ of this system belongs to the subspace Ω_2, and the symmetry defect [***dod***] (36) of this matrix [***mac***] relates to the subspace Ω_1. The subspace Ω_1 is disjoint with the subspace Ω_2. These dependences can be presented by placing values and eigenvectors of these matrices in Tables 1 and 2.

As illustrated in Tables 1 and 2, the matrix [***mac***] is taken from the Equation (33), the supplementary matrix to the symmetry [***dod***] is taken from the formula (36). When comparing both tables it can be seen that the subspace Ω_2, to which the solution [***y***] of the system (33)

belongs, is identical for each matrix. They contain the same eigenvalues and corresponding (placed in columns under the eigenvalues) eigenvectors. The condition number of the system (33) for calculations [***y***] in subspace Ω_2 amounts 49.232/0.75934 = 65. The subspace Ω_1, created by vectors that are the columns of the matrix [***w***] from the Equation (20) for both the matrix of Table 1 and 2 has slightly different eigenvalues and eigenvectors. But in both cases it is the same subspace Ω_1, obtained as $\Omega_1 = \Omega \setminus \Omega_2$.

Table 1. Eigenvalues (in the first row) and, below them in the columns, eigenvectors of asymmetrical matrix [***mac***] from the system of Equations (33)

Ω_2				Ω_1		
0.75934	2.0638	6.2271	49.232	815.33	2000	24285
−0.33253	−0.016104	0.47169	0.0013036	0.42165	−1.6865e-04	−0.69871
−0.47931	0.51316	−0.32214	0.63495	−0.0013169	0.006042	6.9107e-05
−0.4682	−0.25424	−0.33787	−0.31937	0.001261	0.70431	−2.7257e-05
−0.4682	−0.25424	−0.33787	−0.31937	0.001261	−0.70984	−2.7257e-05
−0.33253	−0.016104	0.47169	0.0013036	0.39294	−1.6865e-04	0.71522
−0.33253	−0.016104	0.47169	0.0013036	−0.81719	−1.6865e-04	−0.016606
−0.010494	0.77886	0.020925	−0.62677	7.9325e-05	−0.0060384	1.7218e-07

Table 2. Eigenvalues (in first row) and, below them in the columns, eigenvectors of symmetrical matrix [***mac***] + [***dod***]

Ω_2				Ω_1		
0.75934	2.0638	6.2271	49.232	807.86	1984	24275
0.33253	−0.016104	−0.47169	0.0013036	0.42251	−9.1128e-04	0.69868
0.47931	0.51316	0.32214	0.63495	4.336e-16	−4.1949e-17	2.0375e-17
0.4682	−0.25424	0.33787	−0.31937	0.0014722	0.70711	3.1981e-05
0.4682	−0.25424	0.33787	−0.31937	−0.0014722	−0.70711	−3.1981e-05
0.33253	−0.016104	−0.47169	0.0013036	0.39382	−7.876e-04	−0.71524
0.33253	−0.016104	0.47169	0.0013036	−0.81633	0.0016989	0.016563
0.010494	0.77886	−0.020925	−0.62677	−7.9445e-18	−6.4153e-19	2.3809e-20

The scheme shown in Fig. 1, has small dimensions of the system of Equations (33), so direct methods should rather be used to solve it. The equations of type (33) obtained from the finite element method, however, have large dimensions and must be solved with the use of iterative methods, operating in the subspace Ω_2.

4. Conclusions

Systems with magnetically coupled windings solved with the finite element method have an ill-conditioned skew-symmetric matrix [13]. The method proposed in the article is based on

direct solving of a system with large eigenvalues of the problem. In this way the spectrum decreases (spectrum of eigenvalues), to the remaining components of the solution. This simplifies and accelerates the iterative process of obtaining the remaining components of the solution. A condition number understood as the ratio of the largest and smallest eigenvalues for the iterative method is therefore significantly improved. This is particularly important with a very large number of unknowns of the problem.

The proposed method was exemplified with the magnetic circuit with windings, solved by a circuital method. Due to small dimensions one could observe numerical effects of individual steps of the algorithm.

The application of the presented algorithm in the finite element method was performed in [6-8, 14]. The 3-column autotransformer with five windings on each column was investigated. Mono-harmonic calculations were performed for the given pulsations on complex numbers. An autotransformer impedance matrix was created. Having found eigenvalues and eigenvectors, the autotransformer inductance was identified [6-8].

It should be underlined that in space Ω_1, solved with direct methods, there are not only the effects of the leakage inductance (including inductance in end winding connections in 2D calculations), of external connections $[\boldsymbol{L}_\sigma]$, but also magnetic fluxes, calculated with the finite element method. They seem to be "selected" using vectors-columns of the matrix $[\boldsymbol{w}]$. It is evidenced by the formula (31) of matrix $[\boldsymbol{M}_0]$. Those chosen, additional components are equal to $[\boldsymbol{w}]^t \cdot [\boldsymbol{M}] \cdot [\boldsymbol{w}]$.

References

[1] Demenko A., Wojciechowski R., Sykulski J., *2-D versus 3-D electromagnetic field modeling in electromechanical energy converters*, IEEE Transactions on Magnetics, vol. 50, no. 2, pp. 897-900 (2014).

[2] Saad Y., *Iterative Methods for Sparse Linear Systems, Second Edition*, Society for Industrial and Applied Mathematics (2003).

[3] Traub J.F., Woźniakowski H., *On the Optimal Solution of Large Linear Systems*, Department of Computer Science Columbia University (1982).

[4] Higham N.J., *Accuracy and Stability of Numerical Algorithms, Second Edition*, Society for Industrial and Applied Mathematics (2002).

[5] Saad Y., *Numerical Methods for Large Eigenvalues Problems*, Second Edition, Society for Industrial and Applied Mathematics (2011).

[6] Gołębiowski M., *The effect of the leakage inductance auto-transformers, which supply a multi-pulse rectifier systems on the network current distortion factor (dissertation in Polish)*, PhD Thesis, The Faculty of Electrical and Computer Engineering, Rzeszów University of Technology, Rzeszów (2010).

[7] Gołębiowski M., Mazur D., *Calculating the main and leakage inductance matrix of the 3-column 15-winding autotransformer*, Archives of Electrical Engineering, vol. 60, no. 3, pp. 215-222 (2011).

[8] Gołębiowski M., Mazur D., *Measurement and calculation of 3-column 15-winding autotransformer*, Archives of Electrical Engineering, vol. 60, no. 3, pp. 223-230 (2011).

[9] Jin J.M., *The Finite Element Method in Electromagnetics, 3rd Edition*, Wiley-IEEE Press (2014).

[10] Tomczuk B., Koteras D., Waindok A., *3D Field Calculations of the Modular Transformer Heating under High Frequency Operation*, Proceedings of the XIX International Conference on the Computation of Electromagnetic Fields, Budapest, Hungary (2013).

[11] Gołębiowski M., Gołębiowski L., Mazur D., *Voltages in the Shaft of the Induction Motor in 3D FEM Formulation*, IEEE International Symposium on Diagnostics for Electric Machines, Power Electronics and Drives, Valencia, Spain, pp. 142-145 (2007).
[12] Choi S.C.T., *Minimal Residual Methods for Complex Symmetric, Skew Symmetric and Skew Hermitian Systems*, arXiv: 1304.6782v2 [cs.MS] (2014).
[13] Nowak L., *Field Models of Transients in Electromechanical Converters (in Polish)*, Poznan University of Technology Publishing House (1999).
[14] Berhausen S., Paszek S., *Use of the finite element method for parameter estimation of the circuit model of a high power synchronous generator*, Bulletin of the Polish Academy of Science, vol. 63, no. 3, pp. 575-582 (2015).

ARCHIVES OF ELECTRICAL ENGINEERING VOL. 66(2), pp. 339-350 (2017)

DOI 10.1515/aee-2017-0025

Implementation of mathematical model of thermal behavior of electronic components for lifetime estimation based on multi-level simulation

MICHAL FRIVALDSKY, MICHAL PRIDALA, PETER DRGONA

Faculty of electrical engineering, Department of Mechatronics and Electronics
University of Zilina
Univerzitna 1, 010 26, Zilina, Slovakia
e-mail: Michal.frivaldsky@fel.uniza.sk

(Received: 20.09.2016, revised: 25.01.2017)

Abstract: The main purpose of the paper is the proposal of multi-level simulation, suited for the evaluation of the lifetime of critical electronic devices (electrolytic capacitors). The aim of this issue is to imagine about the expected operation of complex and expensive power electronic systems, when the failure of the most critical component occurs. For that reason, various operational conditions and various physical influences must be considered (e.g. mechanical, humidity, electrical, heat stress), where nonlinearities are naturally introduced. Verification of the proposal is given, whereby the life-time estimation of an electrolytic capacitor operated in a DC-DC converter during various operational conditions is shown. At this point electrical and heat stress is considered for lifetime influence. First, the current state in the field of mathematical modeling of the lifetime for electrolytic capacitors, considering main phenomena is introduced. Next, individual sub-models for multi-level simulation purposes are developed, including a thermal simulation model and electrical simulation model. Several complexities of individual models are mutually compared in order to evaluate their accuracy and suitability for further use. Proper simulation tools have been mutually linked and data transfer was secured, in order to have the possibility of investigation of a lifetime depend on the changes of various variables.

Key words: electrolytic capacitor, lifetime model, lifetime estimation, system-level simulation

1. Introduction

The paper deals with the proposal of multi-level simulation, suited for the evaluation of the lifetime of critical electronic devices (electrolytic capacitors). Verification of the proposal is given, whereby the life-time estimation of an electrolytic capacitor operated in a DC-DC converter during various operational conditions is shown. The paper describes multi-level simula-

tion design, as well as possible practical application areas. Proposal for target application (DC-DC converters) is initially considered. At first the individual simulation modules are presented. Consequently necessary settings for simulation data exchange between individual modules are described together with the description of relevant physical phenomena. Finally verification of the proposed multi-level simulation system is evaluated, whereby the life-time estimation of an electrolytic capacitor operated in a DC-DC converter during various operational conditions is being shown.

2. Life-time estimation model (*LT* estimation methodology)

For determination of expected the lifetime of an electrolytic capacitor during various operation conditions, it is necessary to consider each physical phenomenon, which directly influence component's behavior (1).

$$T = L_0 \cdot K_T \cdot K_R \cdot K_V \,, \tag{1}$$

where: L_0, K_T, K_R, and K_V are the factors which are influencing the lifetime of a capacitor based on various changes of variables, i.e., L_0 is the lifetime at nominal ripple and upper category temperature (values from datasheet), K_T is the temperature factor (ambient temperature), K_R is the ripple current factor (causing self-heating), K_V is the voltage factor (operating voltage).

Individual variables are defined below.

A temperature factor: the lifetime of elcaps follows the industry wide-well established "10-Kelvin rule" from Arrhenius:

$$K_T = 2^{\frac{T_0 - T_a}{10K}} \,, \tag{2}$$

where: T_0 is the upper category temperature (datasheet value of maximal allowable capacitor temperature), T_a is the ambient temperature in the application

A ripple current: this factor estimates the impact of the applied ripple current on the self-heating and thus on the lifetime.

$$K_R = K_i^{A\frac{\Delta T_0}{10K}} \,, \tag{3}$$

$$A = 1 - \left(\frac{I_a}{I_0}\right)^2 \,, \tag{4}$$

where: I_a is the ripple current in the application (within actual operation of the system), I_0 is the nominal ripple current at upper category temperature (datasheet value), ΔT_0 is the core temperature increase (typ. 5EK for 105EC capacitor temperature class and 10EK for 85EC capacitor temperature class), K_i is the empirical safety factor defined as:

$$T_0 = 105\text{EC}, \quad I > I_0;\ K_i = 4, \quad I \le I_0;\ K_i = 2,$$

$$T_0 = 85°\text{C}, \quad K_i = 2.$$

Voltage factor:

$$K_V = \left(\frac{U_a}{U_r}\right)^{-n}, \tag{5}$$

where: U_r is the rated voltage, U_a is actual operating voltage, n is the exponent, defined as:

$$0.5 \le \left(\frac{U_a}{U_r}\right) \le 0.8 \rightarrow n = 3,$$

$$0.8 \le \left(\frac{U_a}{U_r}\right) \le 1 \rightarrow n = 5.$$

The final form of the lifetime estimation model of the electrolytic capacitor is:

$$LT = L_0 \cdot 2^{\frac{T_0 - T_a}{10K}} \cdot K_i^{A\frac{\Delta T_0}{10K}} \cdot \left(\frac{U_a}{U_r}\right)^{-n}. \tag{6}$$

This approach has been obtained from [5]. As was already mentioned, based on (6) it is clear, that an *LT* estimation model is dependent on electro-thermal processes, which are valid during system operation. It is possible to calculate the lifetime based on (6) from the estimated/ measured values of relevant variables from the system operation. Anyway it is better to think about implementation of the lifetime model into simulation tools and within pre-construction stage to evaluate the expected system behavior. Thus it is possible to significantly optimize the system. This methodology is further described within this paper.

3. Life-time estimation model (simulation interface)

During operation of any electronic system, various physical phenomena influence system behavior. Practically it is very difficult to experimentally determine the impact of these physical processes due to the necessity of long-running measurements, or due to the requirements on special measuring equipment (testing chambers etc.).

A possible way to determine how to investigate previously described issues is a multi-level simulation design, where various electrical and non-electrical processes can be considered (Fig. 1 – right).

It is well known that the electrolytic capacitors act as most critical components when we talking about a lifetime. Proper operational conditions (electrical, thermal, etc…) can contribute to extension of these parameters. The proposed system (Fig. 1 – right) enables to investigate/or define proper operational characteristic in order to determine/ or define the expected component lifetime.

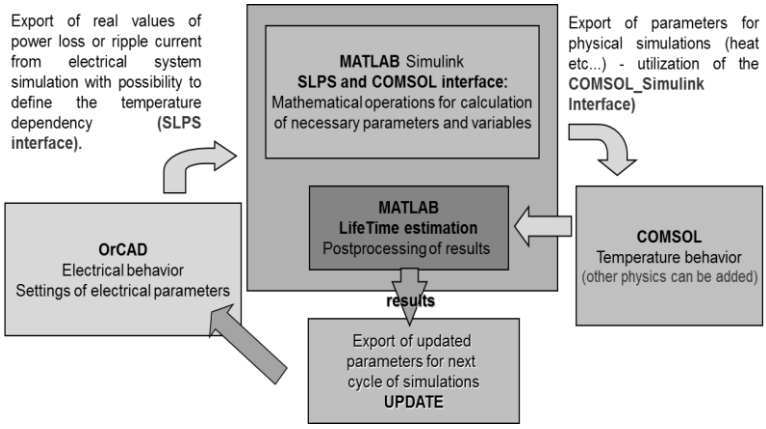

Fig. 1. Proposal for multi-level simulation with consideration of various physical phenomena

For the design of the electrical systems, we decided to use sub-packages from the OrCAD 16.6 software.

Capture/analog or mixed A/D – a schematic editor with a high number of integrated electro physical electrical models:

– Pspice A/D – a simulation substructure of OrCAD that models real electrical behaviour of a circuit. It is possible to simulate the mix of analog and digital devices.

For design of multiphysics models we used COMSOL. The advantages of this software:

– CAD import module for simulation of more complex geometries,
– predefined equations for nonlinear problems (e.g. thermal, magnetic, ambient, mechanical).

For control of co-simulations and for data analysis, we decided to use Matlab:

– m-file – post processing of results, evaluation of convergence, determination of optimal parameter settings.

It is necessary to develop individual models for each simulation module. In the next chapters of this paper, we describe the development process of thermal and electrical modelling of an electrolytic capacitor, including the most necessary dependencies that occur during system operation and are relevant to (6).

4. Capacitor thermal model – model's complexity within internal structure

The internal structure of an electrolytic capacitor consists of several turns of sandwich structure layers with various material properties (Fig. 2). For development of a lifetime estimation model based on multilevel simulation, we decided to investigate a real physical sample of an electrolytic capacitor – Nichicon CE 105EC, series GU (K). The determination of thickness of several layers has been done with the use of a biological light microscope (micrometer

calibration grid) and simultaneously with the use of a dial indicator. Based on the measured values we have deduced the average values of the thicknesses.

For the approximate estimation of the specific values of electrical parameters, i.e. electrical conductivity, we have examined several literary and scientific publications, based on which we were able to estimate conductivity values for electrolyte, that was the main problem in determination of material properties [6].

The layers of the core form a structure that consists of interconnected very thin blocks within the same area, but with different thickness of individual layers. This approach is similar to the one which was done during the PCB thermal modeling of DC-DC converter, during the previous task (Thermal resistances of a block in 3D for "*x*", "*y*", and "*z*" were determined by an averaging method).

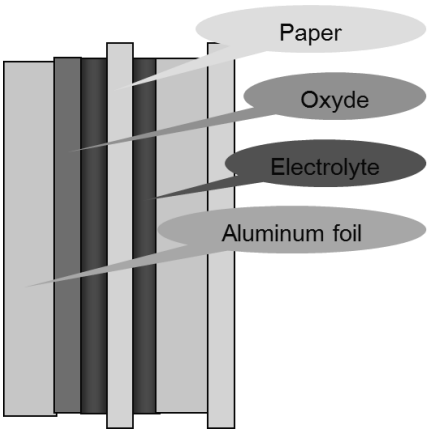

Layer	Material	Width [mm]	Conductivity [S/m]
Anode	Al	0.0001	3.77 e+7
Dielectric	Al_2O_3	0.00001	1.00 e-14
Electrolyte	PC	0.00001	1.00 e-10
Isolation	Paper	0.00005	1.00 e-14
Electrolyte	PC	0.00001	1.00 e-10
Cathode	Al	0.0001	3.77 e+7
Isolation	Paper	0.00005	1.00 e-14

Fig. 2. One turn of electrolytic capacitor with material properties of individual layers

There are several possible ways, in which a thermal simulation model can be designed, while complexity and accuracy are main factors that must be considered for a multi-level simulation approach. Modelling of a capacitor core is, therefore, the most important issue. Next, various approaches for capacitor's core thermal modelling will be shown.

Structural thermal model

A structured model consists of 90 turns, whereby one turn consists of 7 layers in a sandwich structure in a given order (Fig. 3). This model was done just in 2-D interpretation because of the reduction of computation time during verification processes (3-D interpretation would need a powerful computation machine).

The geometrical model of a structural thermal model consists of meticulously ordered layers of an internal structure of the investigated sample (Fig. 3). The number of turns is equal to 90, cause that the final width of 2D core is equal to 19.5 mm, with a height of 100 mm. This approach is principally very time consuming, but on the other hand, very high accuracy can be achieved due to close proximity to a physical sample.

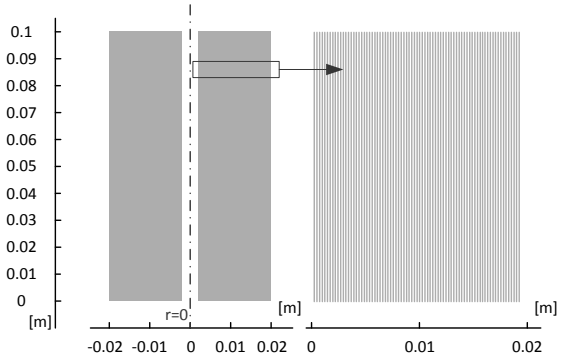

Fig. 3. Structural model of electrolytic capacitor core

Coil thermal model

A coil model is based on the approximation of thermal resistance in the axial and radial direction of one turn (7 layers), whereby value of thermal conductivity is consequently dependent on the number of turn [7]. The axial element of electrical resistance of individual turns in order $j \in (1; n)$ is given by (7) and the radial element is defined by (8):

$$R_a(j) = \frac{L}{\sigma_a S(j)}, \tag{7}$$

$$R_r(j) = \frac{1n\dfrac{r_j}{R_{r-1}}}{2\pi L \sigma_r(j)}, \tag{8}$$

where: σ_a, σ_r represent the axial and radial electric conductivity of individual layers, $S(j)$ is the area of the layer, $r(j)$ is the diameter of the turn in given order, L is the length of the electrolytic capacitor core (height of capacitor).

Fig. 4 shows dependency of axial and radial element of electric conductivity in dependency on the number of turn of capacitor core, which was derived with the use of (7) and (8) respectively.

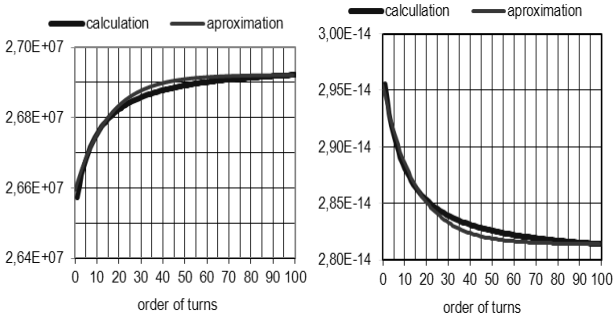

Fig. 4. Dependency of electrical conductivities σ_a and σ_r (S/m) on a number of turns of a capacitor core

At this point, it must be said that for the coil thermal model of a capacitor, the electrical conductivity is introduced as a tensor of 2nd degree. This must be accepted during OrCAD electrical simulations. The core of the electrolytic capacitor is made of anisotropic material which depends on the *x*, *y* and *z*-axes. The approximated value have been taken from the previous analysis (Fig. 4)

$$\sigma_x = 2.81399.10^{-14} + 1.5 \cdot 10^{-15} \cdot e^{\frac{-0.00258+radius}{0.00195}},$$

$$\sigma_y = 2.81399.10^{-14} + 1.5 \cdot 10^{-15} \cdot e^{\frac{-0.00258+radius}{0.00195}},$$

$$\sigma_x = 2692181 - 349772 \cdot e^{\frac{-0.00258+radius}{0.00195}},$$

$$radius = \sqrt{x^2 + y^2}.$$

Sandwich model

As was said, the layers of a capacitor core form a structure which consists of intercomnected, very thin blocks within the same area, but with different thickness of individual layers (Fig. 2). This approach is similar to the one where multilayer PCB is considered and modelled for thermal simulations [8]. Thermal resistances of a block in 3D space for „*x*“, „*y*“, and „*z*“, in that case were determined by an averaging method.

For the structure in Fig. 2, it is possible to define average thermal conductivities in a radial and axial direction with the use of (9), (10). A sandwich model contains just one substance with different conductivity in an axial and radial direction.

$$k_r(j) = \frac{\sum_{i=1}^{n} w_i}{\sum_{i=1}^{n} \frac{w_i}{k_i}}, \tag{9}$$

$$k_a(j) = \frac{\sum_{i=1}^{n} w_i . k_i}{\sum_{i=1}^{n} w_i}, \tag{10}$$

where: k_r is the averaged thermal conductivity in a radial direction, k_a is the averaged thermal conductivity in a axial direction, w_i is the width/thickness of the *i*-th layer, k_i is the thermal conductivity of the *i*-th layer.

Within the definition of subdomains, there are two radial parts (in *x* and *y* direction) and one axial part (in *z* direction). This approach is much simpler than precise modeling of a structural model (Fig. 3) and less computation time shall be required. However, the results might be worse compared to structural and coil thermal models.

The aim of development of three different approaches for capacitor's core thermal simulation model was:

1) Confirmation of theory that averaged models compared to a structured model are accurately enough for further use.
2) Investigation of computation time during 3-D heat transfer simulations with averaged models for *LT* estimation purposes.
3) Finding possibilities of reduction of computation time because of use in more complex Life-Time estimation methodology-simulations.

Figs. 5-6 show the simulation results from the investigation of thermal behavior of the capacitor core (we have considered an EPCOS capacitor with the product ID B43511A5158M), when a ripple of the current, flowing through the core is being changed. The simulation was done for different values of the ripple, while two approaches of the simulation model were compared – an averaged non-structural model (Fig. 2) and a structural model (Fig. 3). Zero on the *x*-axis is representing the middle point of the capacitor, and the maximum on the right side of *x*-axis represents the side of the capacitor.

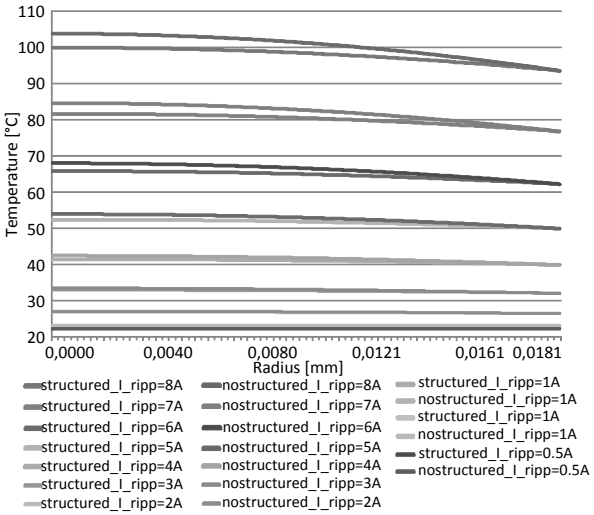

Fig. 5. Summary from simulation comparison between structural and averaged model for various value of ripple current

It can be seen, that the temperature difference between the structural and averaged model (sandwich model) becomes higher with the increase of the value of the current ripple. The highest error is observed in the proximity of the core. Even for higher values of the ripple current, the relative error is below 5%, which is a target of most of precise simulation models, when comparing to experimental measurements [9].

The target of this point was the confirmation of physical abilities of averaged nonstructural models, because these models are simpler and require much less computation power and computation time for heat transfer simulations. The main point for this evaluation was heat distribution in the core of the capacitor, which has a layered structure. From the previous results it can be seen, that physical interpretation of a nonstructural model shows good accordance with the value of I ripple = 8 A, at which a relative error is 4% (this result is valid for the

centre of the core). We decided to provide this experiment in order to facilitate the acceptance of the results, which will be obtained during a lifetime estimation process with nonstructural models of capacitors.

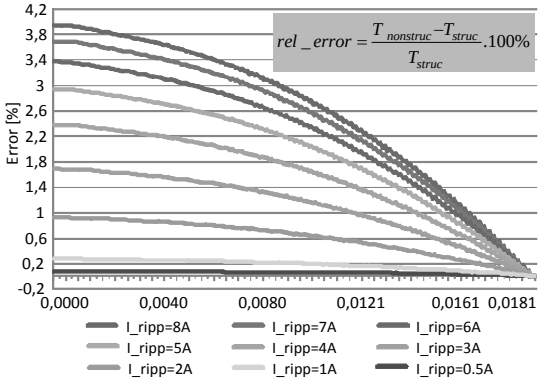

Fig. 6. Relative error from simulation experiments of heat distribution for various current ripple

5. Capacitor electrical model – ESR nonlinearity

It is well known that temperature dependency of ESR influences the lifetime of capacitors. The main problem during initial circuit modelling was the development of an electrical model of the investigated capacitor's ESR that will be temperature dependent. Standard libraries in OrCAD do not have such a model, therefore it was necessary to develop a personal model. For this purpose, and after many attempts the optimal way, how to design the electrical model of ESR with temperature dependency was found out – the use of ABM (Analog Behavioral model) modeling.

The main advantage of the proposed approach is that it is possible to calculate the values of temperatures almost during the computational process of system level simulation (the temperature of ESR is defined as the temperature of the core of the investigated capacitor sample), whereby the capacitor heat transfer behavior is computed – simulated in COMSOL and consequently actual values are exported into OrCAD Capture. A temperature-dependent resistor (or thermistor) can be modeled with help of a look-up table, or an expression can be used to describe how the resistance varies with temperature. The denominator in the expression in Fig. 7 is used to describe common thermistors. The T_{val} variable in the expression is the simulation temperature, in Celsius. This is then converted to Kelvin by adding 273.15. This step is necessary to avoid a divide by zero problem in the denominator, when T = 0EC [10, 11].

With the use of ABM modelling it is possible to design various electrical devices (inductors, LEDs, diodes...), together with possibility of entering the values during computational/simulation process.

The temperature dependency of transistors is already included in factory models of OrCAD Capture, whereby their interface for the external definition of actual values is already done, so this simplifies future tasks.

The main electrical parameters of a power test circuit are:

Input voltage = 240 Vdc, output voltage = 400 Vdc, output power = 1 kW, switching frequency = 100 kHz.

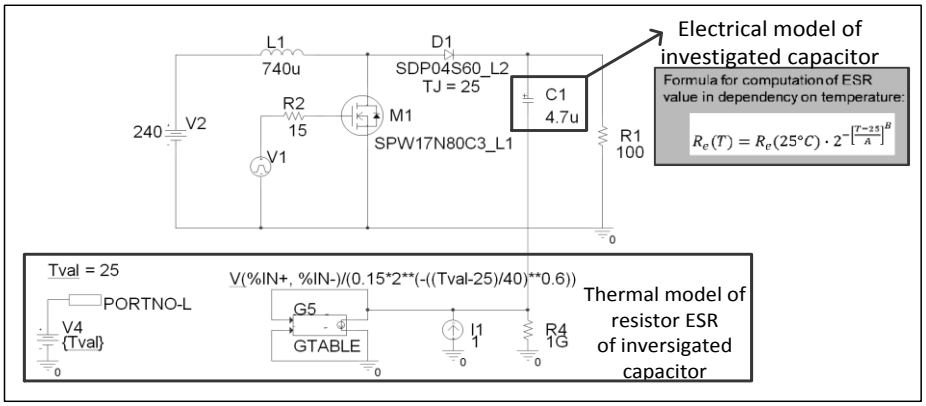

Fig. 7. Implementation of capacitor's ESR temperature nonlinearity into electrical model of capacitor

6. Implementation and results

We have designed multi-level simulation for the determination of a lifetime of an electrolytic capacitor in a DC-DC converter (Fig. 8). The simulation model considers these physical phenomena relevant for lifetime estimation:

– Electrical – with given parameters of voltage stress, current ripple stress and with the possibility of define nonlinear component behavior (e.g. temperature dependence of capacitor's ESR).
– Thermal – with given parameters like ambient temperature, air velocity and with a variable parameter like component temperature (electrical dependence).

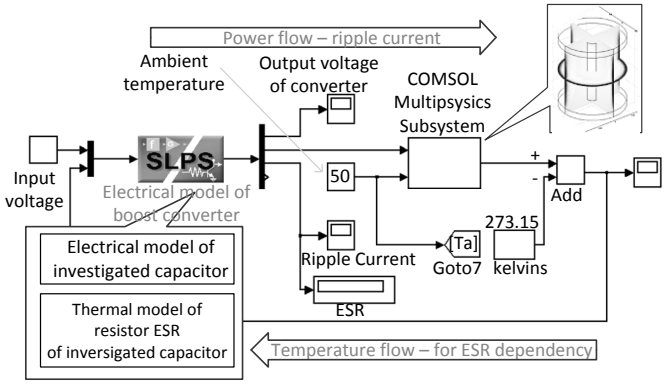

Fig. 8. Proposed multi-level simulation model for lifetime estimation with consideration of various physical phenomena

In order to provide precise multi-level simulation, it is required to design precise simulation models for selected modules. Therefore a very accurate thermal simulation model was developed in COMSOL, and consequently implemented into the circuit simulator of SLPS interface (Matlab – OrCAD).

The simulation results from Fig. 8 are shown in Fig. 9. After several runs of simulations, during which critical operational parameters vary, the lifetime dependence on given parameters can be plotted. It must be mentioned here, that this dependency considers other sub-dependencies, like nonlinearity of an ESR capacitor, temperature dependency of the capacitor core, current ripple dependency etc. Estimation of *LT* was done considering Eq. (6).

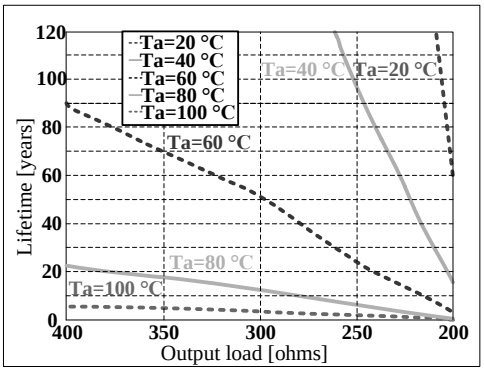

Fig. 9. Estimated lifetime for investigated capacitor in dependency on ambient temperature and output load of converter

The proposed algorithm is also able to determine operating conditions, within which the chosen lifetime of components shall be fulfilled. For example, if we want to have *LT* operating from 15 to 25 years, then the operation of the capacitor must be relevant to operation a conditions, which are defined in Fig. 10.

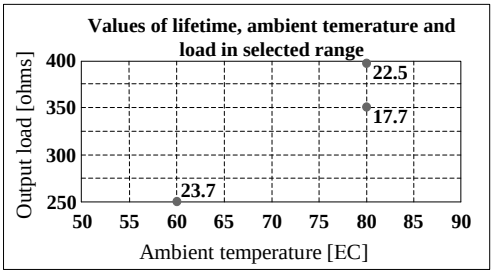

Fig. 10. The estimated lifetime of the investigated capacitor depending on ambient temperature and output load of a converter

7. Conclusion

At this point we would like to conclude, that design of multi-level simulation can be helpful in the case of complex and expensive electrical systems investigation, where experimental

testing of various physical phenomena is very time-consuming, or costly. The chosen methodology considers the precise and accurate simulation sub-models of the selected component – an electrolytic capacitor. Complexity of such sub-models cannot be high due to acceptable requirements on computational time. Therefore more variations of a thermal model were designed in order to investigate the relative error of simplified models. Temperature is the most critical parameter which is influencing a lifetime and operation of capacitors. It is necessary to consider nonlinear thermal dependency of parasitic elements during the simulations. We found a possible solution in the way of utilization of analog behavioral modelling. Also other variables must be considered, e.g. humidity, mechanical stress, etc. This will be implemented within the proposed methodology and will be a future task of this work.

Acknowledgements
The authors wish to thank VEGA, the Slovak Grant Agency, for project no. 1/0558/14 – "Research of methodology for optimization of lifetime of critical components in perspective electronic appliances through the use of system level simulation".

References

[1] Varde P.V., *Physics-of-Failure Based Approach for Predicting Life and Reliability of Electronics Components*, Barc Newsletter, vol. 313 (2010).
[2] Gasperi M.L., *A Method for Predicting the Expected Life of Bus Capacitors*, IEEE Industry Application Society, Annual Meeting, Lousiana, New Orleans, USA (1997).
[3] Bâzu M., Gălăteanu L., Ilian V.E., Vârşescu D., *Lifetime prediction for components with scarce data: The "worst case" approach*, IEEE 17th International Symposium for Design and Technology in Electronic Packaging (SIITME), Timisoara, Romania, pp. 309-312 (2011).
[4] Nicolics J., Mundlein M., Hanreich G., Zluc A., Stahr A., Franz M., *Thermal Analysis of Multilayer Printed Circuit Boards with Embedded Carbon Black-Polymer Resistors*, 30th International Spring Seminar on Electronics Technology (ISSE), Cluj-Napoca, Romania, pp. 46-52 (2007).
[5] Albertsen A., *Electrolytic capacitor lifetime estimation*, Jianghai Europe GmbH (2010).
[6] Mirsky G., *Determining end of life, ESR, and lifetime calculations for electrolytic capacitors at higher temperatures*, EDN (2008).
[7] Frivaldsky M., Cuntala J., Spanik P., *Simple and accurate thermal simulation model of supercapacitor suitable for development of module solutions*, International journal of thermal sciences, vol. 84, pp. 34-47 (2014).
[8] Pspice SLPS Interface Users Guide Ver. 2.5, Cybernet Systems CO., LTD (2004).
[9] Hruska K., Kindl V., Pechanek R., *Design and FEM analyses of an electrically excited automotive synchronous motor*, Proceedings of Power Electronics and Motion Control Conference (EPE/PEMC), Novi Sad, Serbia, pp. LS2e.2-1 - LS2e.2-7 (2012).
[10] Grman L., Hrasko M., Kuchta J., *Single phase PWM rectifier in traction application*, Journal of Electrical Engineering, vol. 62, pp. 206-212 (2011).
[11] Park K.H., Yi K.H., *Cost-effective power system with an electronic double layer capacitor for reducing the standby power consumption of consumer electronic devices*, Journal of power Electronics, vol. 13, pp. 329-338 (2013).

ARCHIVES OF ELECTRICAL ENGINEERING VOL. 66(2), pp. 351-360 (2017)

DOI 10.1515/aee-2017-0026

Influence of the mechanical fatigue progress on the magnetic properties of electrical steel sheets

JAN KARTHAUS[1], SIMON STEENTJES[1], DANIEL GRÖBEL[2], KOLJA ANDREAS[2], MARION MERKLEIN[2], KAY HAMEYER[1]

[1]*RWTH Aachen University, Institute of Electrical Machines*
Schinkelstr. 4, 52062 Aachen, Germany
e-mail: jan.karthaus@iem.rwth-aachen.de

[2]*FAU Erlangen-Nürnberg, Institute of Manufacturing Technology*
Egerlandstr. 11-13, 91058 Erlangen, Germany

(Received: 23.09.2016, revised: 18.01.2017)

Abstract: The purpose of this paper is to study the variation of the magnetic properties of non-oriented electrical steel sheets with the fatigue state during cyclic mechanical loading. The obtained results are central to the design of variable drives such as traction drives in electric vehicles in which varying mechanical loads, e.g. in the rotor core (centrifugal forces), alter the magnetic properties. Specimens of non-oriented electrical steel are subject to a cyclically varying mechanical tensile stress with different stress amplitudes and number of cycles. The specimens are characterised magnetically at different fatigue states for different magnetic flux densities and magnetising frequencies. The measurements show a variation in magnetic properties depending on the number of cycles and stress magnitude which can be explained by changes in the material structure due to a beginning mechanical fatigue process. The studied effect is critical for the estimation of the impact of mechanical material fatigue on the operational behaviour of electrical machines. Particularly in electrical machines with a higher speed where the rotor is stressed by high centrifugal forces, material fatigue occurs and can lead to deterioration of the rotor's stack lamination.

Key words: Cyclic mechanical stress, electrical machines, electrical steel sheets, magnetic properties, material fatigue

1. Introduction

The effect of static mechanical stresses is in the focus of recent research. Due to the Villari effect, magnetic hysteresis curves of electrical steel sheets are sheared while loaded by mechanical stress [1]. The shear of the hysteresis curves leads to a higher energy demand and thus to increased iron losses [2]. Due to a variation in the material lattice caused by mechanical stress, the magnetic properties alter. These effects can be observed for mechanical stress within the elastic and plastic region [1, 3].

In electrical machines, mechanical stress appears with static and periodic or cyclic behaviour. Particularly the consequences of static mechanical stress on the iron losses of electrical machines are in the focus of current research [4] as well as the modelling of the magneto-mechanical effect [5].

In contrast to the effect of static mechanical stress, the influence of cyclic mechanical stress on the magnetic properties of electrical steel sheet is less studied. Cyclic mechanical stress is caused by a fluctuation of centrifugal forces which are dependent on the speed of the rotor. Furthermore, periodic electromagnetic forces on the rotor surface or stator teeth are the reason for cyclic mechanical stress. Electrical steel packages fatigue mechanically dependent on the number of cycles and the magnitude of the stress. Material fatigue deteriorates the structure of a material starting by a generation of dislocations which then creates micro cracks. At the final state, a dominant crack occurs that leads to total material failure. Fatigue appears already for cyclic mechanical stress amplitudes below yield strength and is dependent on the number of cycles and load amplitude. The fatigue behaviour is also influenced by the geometry of the studied material. In the area around notches such as corners, exaggerated mechanical stresses are induced and lead to a faster material fatigue degradation. Due to the strong interdependence between the material's microstructure and the magnetic properties, fatigue causes a persistent variation in the magnetic properties which is reported in [6-8].

During operational life of constructions or machines, the cyclic mechanical loading of steel parts can lead to an accumulation of fatigue damage. In order to avoid that the fatigue damage process ends in a sudden fracture or significant change in the machine's operating characteristics due to alterations of magnetic properties, it is vital to assess the material degradation. Particularly, this effect can influence the magnetic flux path or the iron losses after a certain time of operation in rotating electrical machines.

In this paper, the influence of the mechanical fatigue progress on the extrinsic magnetic properties (coercivity, remanence, specific losses) of a non-oriented electrical steel sheet for the uniaxial case is studied. At several interruptions of the cyclic load, the magnetic properties are measured using a standard single-sheet-tester (SST). The results show a variation in the magnetic properties depending on the number of cycles and the level of mechanical stress.

2. Cyclic stress

Cyclic mechanical loading of a specimen causes material fatigue that can result in failure at stress levels below the static tensile strength of the material [9]. This material degradation process is caused by a movement and agglomeration of dislocations followed by nucleation and growth of micro cracks. Micro cracks emanate from stress sensitive notches on the surface of the specimen or from inclusions in the material volume which are both a result of the manufacturing process [10]. With ongoing stress exposure, the cracks proceed to enlarge due to repeated plastic flow at the crack edges whereby the crack front evolves perpendicular to the direction of the principal stress vector. Finally, the crack sizes reach critical values that lead to

a rapid weakening of the material and ultimately to an instable residual fracture of the specimen [9].

Table 1. Mechanical properties of M250-35A

Description	Symbol	Value
Yield Strength	σ_y	361 MPa
Young's modulus	E	210 GPa
Tensile strength	σ_{TS}	471 MPa

A widely-used method to characterise the fatigue behaviour of steels is the Wöhler (*s-N*) approach which relates the number of cycles to failure to the fatigue stress [11]. In order to determine the fatigue strength for different zones of load cycles, specimens are stressed with constant stress or strain values until failure occurs. Typical values of cycle numbers range from $N = [1, 104]$ for low cycle fatigue, $N = [104, 107]$ for high cycle fatigue and $N > 107$ for endurance fatigue [11].

2.1. Investigated material

To analyse the effect of cyclic stress on the magnetic properties of electrical steel sheet, sheets of type M250-35A cut by a CO2-laser are used. Due to the used cutting method, material deterioration at the cutting edges can be expected. In this study, this effect is neglected because each specimen has the same amount of material deterioration due to cutting. Examining the determined stress-strain curve of the studied material, the mechanical data of the material is collected in Table 1. Only specimens in rolling direction are studied. The shape of the specimens to apply cyclic loads is shown in Fig. 1b.

2.2. Cyclic load

To analyse the variation of the magnetic properties due to fatigue evolution, specimens are loaded at different stress levels and different numbers of cycles using the hydraulic testing machine HA250 (Zwick). The hydraulic driven machine enables to test flat specimens by means of an application of cyclic uniaxial loads with a frequency of 20 Hz. The specimen design is orientated on the recommendations of the norm [12]. An influence of the testing frequency on the fatigue behaviour or the magnetic properties will be investigated in further studies. However, adjustments have to be made in order to fulfil the requirements of the clamping conditions and the magnetic measurement system (Fig. 1a). With the objective to provide constant conditions for every parameter setting, the specimens are not tested as single sheets, but as packages of six specimens. To ensure the same load for every sheet, the machining of the final geometry is conducted in packages of six sheets as well.

For this study, a cyclic tensile load following a sinusoidal-shaped curve is used. To avoid compressive stresses on the specimen, the pre-load has a minimum value of $\sigma_{min} = 1.6$ MPa. In contrast to conventional fatigue tests, no cracking of the specimen is intended here. Hence, the maximum stress is determined to 70% of the static tensile strength. To provide sufficient data points, three stress levels are chosen which amount to 0.23 σ_y (83 MPa), 0.46 σ_y (165 MPa)

and 0.69 σ_y (249 MPa). Furthermore, to enable insights into the development of the magnetic properties in respect to the cycle number with sufficient resolution, six different values ranging from 10 000 to 500 000 cycles are studied for stress levels of 83 MPa and 165 MPa. For a load of 249 MPa, only cycle numbers of up to 100 000 are utilized since cracking of the specimen is expected for higher values.

Table 2. Stress levels and corresponding number of cycles performed

Stress level σ_{max}	**Number of cycles** N
83 MPa	500 000 / 250 000 / 100 000 / 50 000 / 25 000 / 10 000
165 MPa	500 000 / 250 000 / 100 000 / 50 000 / 25 000 / 10 000
249 MPa	100 000 / 50 000 / 25 000 / 10 000

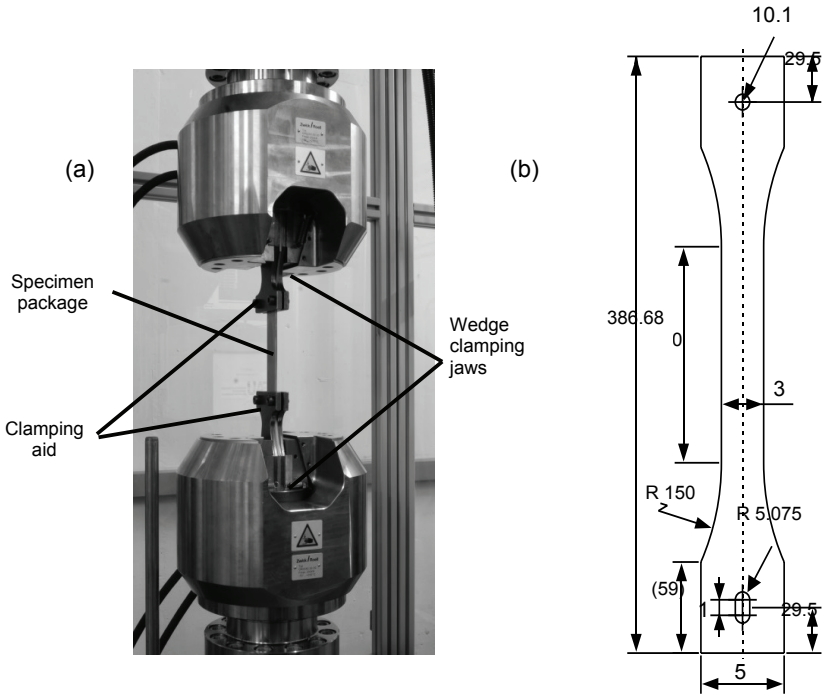

Fig. 1. Experimental setup (a) and geometric properties of the specimen (b)

A detailed overview of the experimental design is depicted in Table 2.

3. Magnetic measurements

3.1. Experimental setup

Four specimens of each load state (Table 2) are stressed in a cyclic way. Due to the required sample width of 120 mm of the magnetic testing setup, which is described below, the

central parts of four specimens that were loaded mechanically are cut, merged and fixed by a non-magnetic adhesive tape to a sample with a width of 120 mm to fit into the used SST (Fig. 2).

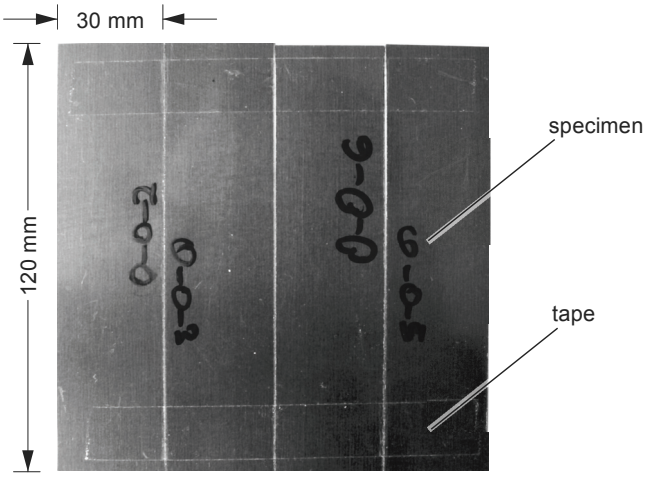

Fig. 2. Merged specimen with tape

For each stress level and number of cycles, one of the expanded specimens is measured magnetically by a standard SST constructed for samples with a width and length of 120 mm. The usage of the expanded specimens reduces the discrepancy of the results of the fatigue experiments (Fig. 6).

The SST is incorporated into a computer-aided setup in accordance with the international standard [13]. The samples are characterised using controlled sinusoidal magnetic flux density with a form factor error of less than 1 % in the frequency range from quasi-static to 1 kHz.

3.2. Results

Regarding the variations in the hysteresis curves depending on the fatigue state under a constant stress level (Fig. 3), a shear in the hysteresis curves which results in a small increase of coercivity and a decrease of remanence polarisation is observed. It is apparent that for an increasing number of load cycles, the amount of magnetic field strength to reach the same magnetic polarisation increases as well. This is valid both for low and high magnetising frequencies (Fig. 3).

An influence of the stress level is also apparent for a constant number of load cycles (Fig. 4). While for the stress levels up to 165 MPa, the shear of the hysteresis curves is insignificantly small, the variation for higher stress levels is obvious. This behaviour can be explained by a larger variation in the microstructure at higher mechanical stresses.

Fig. 5 depicts the trend of the different magnetic properties such as coercive field, remanence polarisation and specific losses for various stress levels depending on the number of cycles for two operating points (f = 50 Hz, J_{max} = 1.5 T and f = 400 Hz, J_{max} = 1.5 T).

The behaviour of the magnetic properties can be separated into three stages which can also be found in the literature [14, 16]:

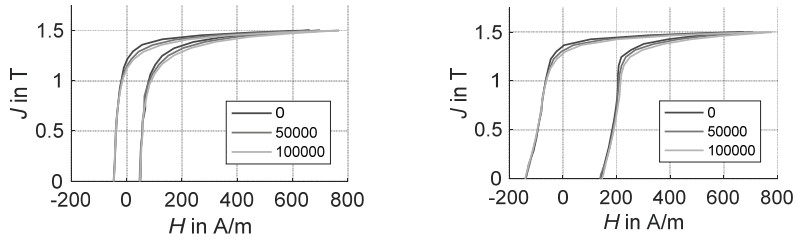

(a) f = 50 Hz and J_{max} = 1.5 T (b) f = 400 Hz and J_{max} = 1.5 T

Fig. 3. Hysteresis curves of stressed samples depending on the number of load cycles N for σ_{max} = 249 MPa

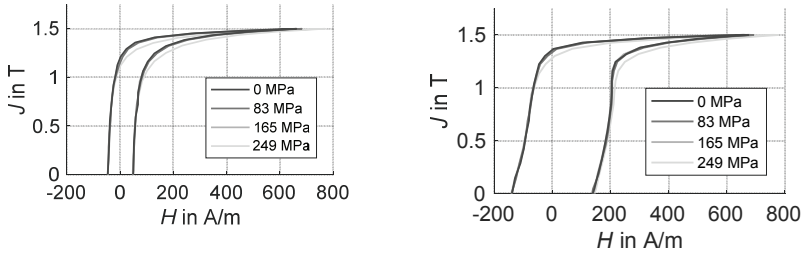

(a) f = 50 Hz and J_{max} = 1.5 T (b) f = 400 Hz and J_{max} = 1.5 T

Fig. 4. Hysteresis curves of stressed samples depending on the mechanical stress level σ_{max} for N = 100 000

During the first percent of the fatigue life-time, the dislocation density increases which is indicated by an increase of coercivity, i.e. fatigue hardening occurs. This behaviour is observable for all studied stress stages. The occurrence of fatigue hardening is typical for heat-treated materials [14]. At the same time, the remanence polarisation is decreasing. At this stage, an increase of losses, i.e. increase of coercivity and decrease of remanence, is apparent, seemingly due to the negative effect of an increase of the dislocation density inside the material.

In the next stage, between 100 000 and 250 000 cycles, the magnetic properties remained almost unchanged for stress levels of 83 MPa and 165 MPa. Because of the more progressed fatigue process for 249 MPa, this behaviour is not observable for this stress level. At this stage, the number of dislocations stays almost constant which results in the constant magnetic properties. The existing dislocations tend to move to the surface of the specimen [14].

In the last stage, the magnetic properties are altered significantly. Due to the fatigue progress, micro cracks are formed and propagate within the material before creating a final crack and failure of the material.

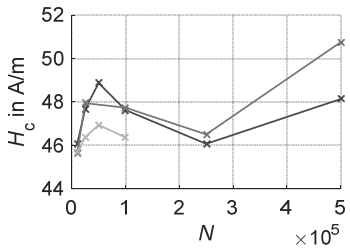

(a) Coercive field for $f = 50$ Hz and $J_{max} = 1.5$ T

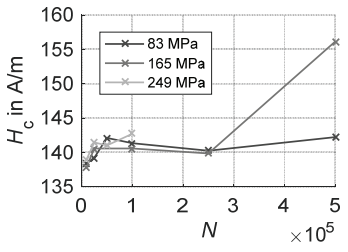

(b) Coercive field for $f = 400$ Hz and $J_{max} = 1.5$ T

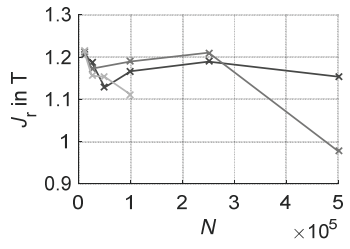

(c) Remanence polarisation for $f = 50$ Hz and $J_{max} = 1.5$ T

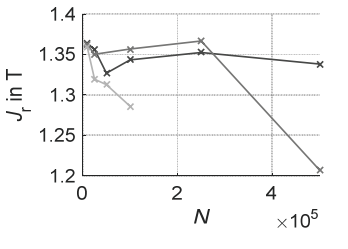

(d) Remanence polarisation for $f = 400$ Hz and $J_{max} = 1.5$ T

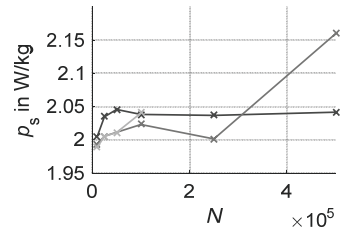

(e) Specific losses for $f = 50$ Hz and $J_{max} = 1.5$ T

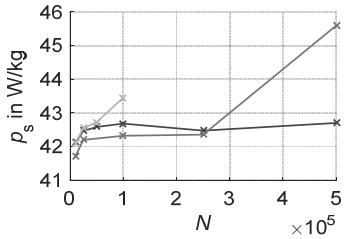

(f) Specific losses for $f = 400$ Hz and $J_{max} = 1.5$ T

Fig. 5. Coercive field, remanence polarisation and specific losses at different stress levels depending on the number of load cycles at various operating points

The magnetic properties are strongly depending on the crack size [15]. It is apparent that for a higher stress level, the final fatigue state is reached for a smaller number of cycles while for a low stress level, the final fatigue stage is not reached yet, observing the small variation in magnetic properties for 83 MPa.

Although the variation of the magnetic properties is only a few percent, a clear trend is observable validated by different magnetising frequencies. Compared to the influence of static stress on the magnetic properties, the influence of cyclic stress is seemingly low.

Fig. 6 depicts the mean values and corresponding standard deviations for each measurement of the six original specimens for one stress level and number of cycles at one magnetic operating point. Due to the fact that the mechanical cyclic load is subject to statistical uncertainties, a wide variation for each measurement can be observed. Another reason is the small width of the specimen (30 mm) which is crucial for the SST which requires samples

with a width of 120 mm. Nevertheless, a clear trend is observable which is validated by the more exact measurements with the merged sample of 120 mm as well.

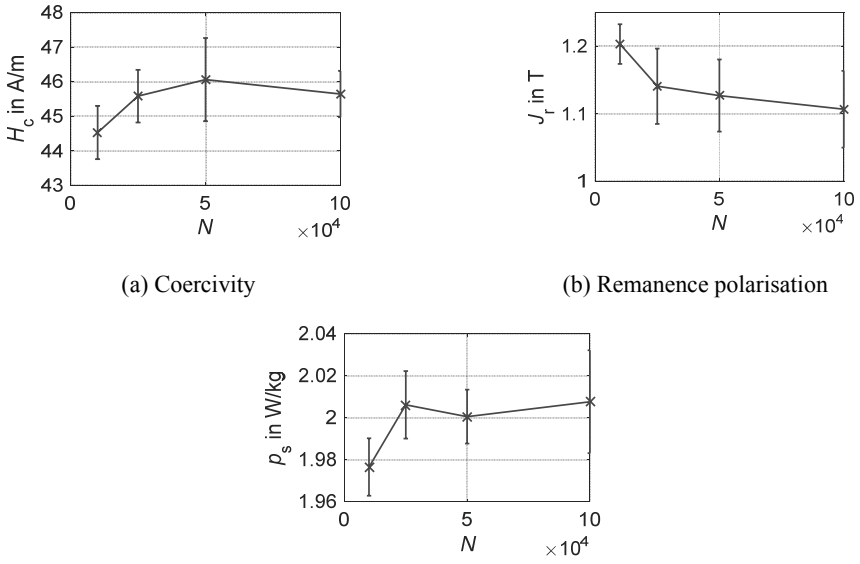

(a) Coercivity

(b) Remanence polarisation

(c) Specific losses

Fig. 6. Mean value (x) and standard deviation of the measurement of the magnetic properties for original samples for $J = 1.5$ T, $f = 50$ Hz and $\sigma_{max} = 249$ MPa

According to this study, the fatigue-depending behaviour of the magnetic properties of electrical steel sheet cannot be neglected. In particular, in the first percentage of the fatigue progress to 100 000 load cycles, a large variation in magnetic properties is observed. The effect on the hysteresis curves and the iron losses can lead to different machine behaviour after a certain time of operation, depending on the cyclic load which affects the stack laminations. For example, fatigue can be induced by centrifugal forces that cause mechanical stress within the stack lamination or by electromagnetic forces causing mechanical stress in stator teeth and rotor edge. Regarding the rotor of an electrical machine with higher speeds (e.g. traction drives of electric vehicles), mechanical tensile stresses up to the yield strength of the steel sheet material, e.g. 320 MPa can occur. Examining the results of this study, the magnetic properties of the areas with high mechanical stresses are altered more intensively. Even though rotors of electrical machines are not loaded with a large number of cycles which initialise cracks, there is a large variation in magnetic properties for low number of cycles.

As a result of this study, it is evidenced that the influence on the magnetic properties of non-oriented electrical steel sheet is depending on the number of load cycles and stress level. Since the fatigue process is more intensive for mechanical stress levels closer to the yield strength of the material, i.e. the final failure occurs after a smaller number of cycles, the deterioration of magnetic properties is larger in the area of high mechanical stresses. For example, in permanent-magnet synchronous machines with a higher speed, the rotor stiffness

is influenced by the position and geometry of the magnet pockets. Operating the machine with cyclic speeds, thin bridges and notches lead to high mechanical stresses and material fatigue in the materials. As a consequence, the magnetic properties alter due to static stress and cyclic stress. Furthermore, mechanical fatigue can produce changes in the microstructure which lead to micro cracks and component failure. Additional influences such as the mechanical stress due to electromagnetic forces or the mechanical stress induced by cutting and punching of the electrical steel sheets can lead to an accelerated fatigue progress.

4. Conclusions

In this paper, the effect of cyclic stress on the magnetic properties of electrical steel sheet is studied. The relation between magnetic properties and fatigue state is presented. Particularly, for a small number of load cycles, the variation in the magnetic properties is higher when compared to a high number of cycles. The stress level also shows an influence on the intensity of variation at larger mechanical load.

In this study, three typical fatigue states have been identified and explained by changes in the microstructure and occurrence of micro cracks within the electrical steel sheet. The results of fatigue-depending magnetic measurements of different steel materials of other authors support the observed results [14, 16]. Compared to the influence of static mechanical stress, the influence of cyclic stress is low. The influence of the superposition of cyclic and static stress on the magnetic properties has to be analysed.

The study will be continued for a smaller number of cycles ($N < 10\ 000$) because the results show a large variation in magnetic properties in the first fatigue state. The used measurement approach, combining cyclically-loaded specimens and a standardised magnetic SST lead to appropriate measurement results which is comparable to other measurement techniques such as presented in [17].

This study is done by rectangular specimens loaded in a uniaxial way and magnetic measurements collinear to the rolling direction. Neither the influence multiaxial loadings nor rotating magnetic fields are covered within this study. Further investigations with different measurement equipment such as a rotating SST and notched specimens will be performed. For additional studies, a higher number of specimens will be used to provide trends with a higher statistical value.

Depending on the state of an electrical machine's operational life and its cyclic mechanical loads, the magnetic properties are altered in a noticeable way, i.e. the iron losses and coercive field are increased while the remanence polarisation is decreased. Particularly for a number of cycles up to 100 000, the largest variation in properties is overserved. For example, the total iron losses increase about 4% when compared to the initial state at 400 Hz. For the operational life of electrical machines, it can be assumed that the overall efficiency and the machine's behaviour due to a variation in the magnetic flux path may be changed.

Acknowledgements
This work is originated as part of the research training group GRK 1856 by the Deutsche Forschungsgesellschaft (DFG).

References

[1] Leuning N., Steentjes S., Schulte M., Bleck W., Hameyer K., *Effect of elastic and plastic tensile mechanical loading on the magnetic properties of NGO electrical steel*, Journal of Magnetism and Magnetic Materials, vol. 417, pp. 42-48 (2016).
[2] Permiakov V., Dupré L., Pulnikov A., Melkebeek J., *Loss separation and parameters for hysteresis modelling under compressive and tensile stresses*, Journal of Magnetism and Magnetic Materials, vol. 272-276, pp. E553-E554 (2004).
[3] Hug E., *Evolution of the magnetic domain structure of oriented 3% SiFe sheets with plastic strains*, Journal of Materials Science, vol. 30, no. 17, pp. 4417-4424 (1995).
[4] Singh D., Rasilo P., Martin F., Belahcen A., Arkkio A., *Effect of Mechanical Stress on Excess Loss of Electrical Steel Sheets*, IEEE Transactions on Magnetics, vol. 51, no. 11, pp. 1-4 (2015).
[5] Vanoost D., Steentjes S., Peuteman J., Gielen G., de Gersem H., Pissoort D., Hameyer K., *Magnetic hysteresis at the domain scale of a multi-scale material model for magneto-elastic behaviour*, Journal of Magnetism and Magnetic Materials, vol. 414, pp. 168-179 (2016).
[6] Devine M.K., Jiles D.C., Hariharan S., *Effects of cyclic stress on the magnetic hysteresis parameters of polycrystalline iron*, Journal of Magnetism and Magnetic Materials, vol. 104-107, pp. 377-378 (1992).
[7] Bozorth R.M., *Ferromagnetism*, IEEE Press; Wiley-Interscience (1993).
[8] Gilanyi A., Morishita K., Sukegawa T., Uesaka M., Miya K., *Magnetic nondestructive evaluation of fatigue damage of ferromagnetic steels for nuclear fusion energy systems*, Fusion Engineering and Design, vol. 42, no. 1-4, pp. 485-491 (1998).
[9] Radaj D., *Ermüdungsfestigkeit: Grundlagen für Leichtbau, Maschinen- und Stahlbau*, Springer Verlag (1995).
[10] Murakami Y., Kodama S., Konuma S., *Quantitative evaluation of effects of non-metallic inclusions on fatigue strength of high strength steels. I: Basic fatigue mechanism and evaluation of correlation between the fatigue fracture stress and the size and location of non-metallic inclusions*, International Journal of Fatigue, vol. 11, no. 5, pp. 291-298 (1989).
[11] *Testing of materials; fatigue test (Woehlertest); definitions, symbols, execution, evaluation*, DIN 50100:1978-02 (1978).
[12] *Metallic materials – Tensile testing – Part 1: Method of test at room temperature* (ISO 6892-1:2009), DIN EN ISO 6892-1:2009-12 (2009).
[13] *Magnetic materials – Part 3: Methods of measurement of the magnetic properties of electrical steel strip and sheet by means of a single sheet tester* (IEC 60404-3:1992 + A1:2002 + A2:2009), DIN IEC 60404-3:2010-05 (2010).
[14] Lo C.C., Tang F., Jiles D.C., Biner S.B., *Evaluation of fatigue damage using a magnetic measurement technique*, IEEE Transactions on Magnetics, vol. 35, no. 5, pp. 3977-3979 (1999).
[15] Bi Y., Jiles D.C., *Dependence of Magnetic Properties on Crack Size in Steels*, IEEE Transactions on Magnetics, vol. 34, no. 4, pp. 2021-2023 (1998).
[16] Devine M.K., Kaminski D.A., Sipahi L.B., Jiles D.C., *Detection of Fatigue in Structural Steels by Magnetic Property Measurements*, Journal of Materials Engineering and Performance, vol. 1, no. 2, pp. 249-253 (1992).
[17] Jiles D.C., Hariharan S., Devine M.K., *Magnescope: a portable magnetic inspection system for evaluation of steel structures and components*, IEEE Transactions on Magnetics, vol. 26, no. 5, pp. 2577-2579 (1990).

ARCHIVES OF ELECTRICAL ENGINEERING VOL. 66(2), pp. 361-369 (2017)

DOI 10.1515/aee-2017-0027

The impact of electromagnetic radiation on the degradation of magnetic ferrofluids

MAREK PAVLÍK[1], LUKÁŠ KRUŽELÁK[1], MIROSLAV MIKITA[1], MICHAL ŠPES[1], SAMUEL BUCKO[1], LUKÁŠ LISOŇ[1], MICHAL KOSTEREC[1], ĽUBOMÍR BEŇA[1], PAVOL LIPTAI[2]

[1]*TUKE FEI, Department of Electric Power Engineering*
Mäsiarska 74, 042 00 Košice, Slovakia

[2]*TUKE SjF, Department of process and environmental engineering,*
Letna 9, 04200 Kosice, Slovakia

e-mail: {marek.pavlik, lukas.kruzelak, miroslav.mikita, michal.spes, samuel.bucko, lukas.lison, michal.kosterec, lubomir.bena, pavol.liptai}@tuke.sk

(Received: 02.08.2016, revised: 28.01.2017)

Abstract: This article deals with magnetic nano-fluids, which are the part of transformer oil ITO 100 and their behavior is influenced by a permanent magnetic field. We performed an IRC analysis in the time domain on the three different samples. Measurements were made before and after radiation of an electromagnetic field. The main objective was to examine changes in the properties of the samples due to the influence of the electromagnetic field. The measurements depend on the orientation of the external magnetic field. This behavior occurs especially during the structuring of the nanoparticles in the sample exposed to the magnetic field. These processes change the polarization of the liquid because the nanoparticles concentration is contained in the fluid.

Key words: ferrofluids, electromagnetic radiation, oxidation stability, transformer oil

1. Introduction

The condition of the insulation is an essential aspect for the operational reliability of power transformers, generators, cables and other high voltage equipment. The power transformer is expensive and vital equipment in the transmission and distribution grid and its life is predominantly determined by the condition of the insulation system. During its operation, this system is continuously subjected to thermal, electrical and chemical stresses etc. [1, 5].

Electrical insulation and the heat transfer are important properties of the liquids used in the transformers. New liquids, e.g. silicone or esters, are used in the special-purpose transformers. These liquids such as seed-oil-based ones are more environmentally friendly, but absorb more moisture. Actually, a large majority of the transformers have their insulation systems consisting of the cellulose paper and the mineral oil. The mineral oil has good oxidation stability and a poor moisture absorbing property due to inhibitors, but his disadvantage rests in the low

thermal conductivity and this factor has an influence on the thermal loading property of the device [2, 4]. From the chemical point of view, the mineral oil is a mixture of the naphthenic, paraffinic and aromatic hydrocarbons. A fire point of mineral oil is approximately 160°C, which is lower than the fire point of ester – approximately 300°C [3]. It was provided by comparison of the mineral oil with the vegetable oil. When compared to vegetable oils, permittivity measured for the new mineral oil was $\varepsilon_r = 2.9$. New environmentally friendly products and limited petroleum resources are an impulse for many researchers to replace mineral oils by vegetable oils or to improve the thermal and insulating properties of mineral oils. For the improvement of the cooling and isolation properties, the transformer based magnetic nano-fluid (MN) was proposed and tested. Ferrofluid [8] is one of such MNs.

The ferrofluids exhibit special properties that make them suitable for many technical and medical applications. Some of these properties are determined by the particular physics of small-sized magnetic nanoparticles [18]. Therefore, it is important to search for better methods and theories describing the physical behavior of these liquids, and in particular, induced structuring of magnetic particles [12, 15].

Many physical properties of the magnetic fluids observed while influenced by the magnetic field reveal, that clusters of constituent magnetic particles exist, which results in various anisotropic properties [16]. Therefore, an understanding of the clustering phenomena in magnetic fluids is important when explaining the physical properties of magnetic fluids while being subjected to the external electromagnetic field [11, 14].

These ferrofluids consist of the carrier fluid (transformer oil), nanoparticles and a hydrophobic single layer of oleic acid as a surfactant. The surfactant has a role of covering the nanoparticles and it prevents their contact from each other, thus the creation of clusters. Magnetite (Fe_3O_4) was used as nanoparticles. The creation procedure was developed in the article [7]. To estimate the effective electric permittivity of MN ε_{MF} the Maxwell-Garnett formula was used for a mixture with spherical inclusions [8].

$$\varepsilon_{MF} = \varepsilon_{ITO} + 3\varphi\varepsilon_{ITO}\frac{\varepsilon_{NP} - \varepsilon_{ITO}}{\varepsilon_{NP} + 2\varepsilon_{ITO} - \varphi(\varepsilon_{NP} - \varepsilon_{ITO})}. \tag{1}$$

where: ε_{ITO} and ε_{NP} are the electric permittivity of the transformer oil and nanoparticles of magnetite. The φ is a solid volume fraction of magnetite nanoparticles [17].

In the article [9], EMR is exactly used for thorough dispersion of nanoparticles while producing ferrofluid with a carrier fluid (ester). After the thermal aging of the samples, it is proved that the surfactant degrades and the particles start to agglutinate into the clusters [10, 15]. In the case of insulating liquids this phenomenon is undesirable because of polarizability and the resultant breakdown of dielectric material that has a destructive impact on the transformer [13, 19].

This fact is a motivation for this article, where the impact of EMC radiation on the ferrofluid and potential partial breakdown of the nanopartical clusters are observed. This phenomenon may partially revitalise or accelerate degradation of the ferrofluid. The revitalization is observed by the time domain spectroscopy (polarization and depolarization current) [10, 16-17].

2. General knowledge about the experimental method

With time domain spectroscopy, it is possible to investigate the slow polarization processes. It is a way of measuring the polarization and depolarization of currents (PDC) with a DC voltage step [6].

The electric field is generated by an external voltage $u(t)$ and it is applied on the dielectric material. The current through the dielectric material can be expressed as (2)

$$i(t) = C_0\left[\frac{\sigma}{\varepsilon_0}u(t) + \varepsilon_r\frac{\mathrm{d}u(t)}{\mathrm{d}t} + \frac{\mathrm{d}}{\mathrm{d}t}\int_0^t f(t-\tau)u(\tau)\,\mathrm{d}\tau\right], \tag{2}$$

where, C_0 is the geometrical capacitance of the dielectric material, $u(t)$ is the step voltage, σ is the DC conductivity of the dielectric material, τ is the time constant, $\varepsilon_0 = 8.852\cdot10^{-12}$ F/m is the permittivity of a vacuum, ε_r is the relative permittivity of the dielectric material and $f(t)$ is the response function of the dielectric material [9].

As a result of the influence of the DC electrical field on the insulation, is the electric current influenced with conductive processes. This effect is characterized by leakage of the current and polarization processes, which are characterized by absorption of the current that flows through dielectric. Charging current $i_n(t)$ flowing through the dielectric is expressed by the formula:

$$i_n(t) = i_c(t) + i_a(t) + i_v, \tag{3}$$

where: $i_c(t)$ is the capacitive component of the current, $i_a(t)$ is the absorption component of the current, $i_v$iis the conductive component of the current.

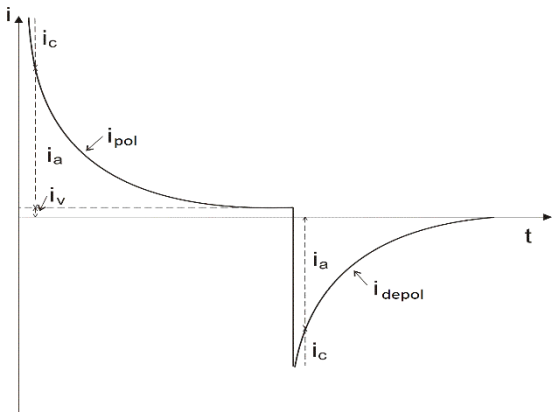

Fig. 1. Time course of the charging and discharging currents [4]

The total current $i(t)$ flowing through the dielectric can be expressed as the sum of all elementary relaxation currents. It exponentially decreases over time and is determined as:

$$i(t) = \frac{U}{R} + \sum_{i=1}^{n} I_{mi} \exp(\frac{-t}{\tau_i}), \tag{4}$$

where: U is the applied direct voltage, R is the insulation resistance over ∞ time, I_{mi} is the amplitude of the i-th elementary current, τ_i is the time constant of the i-th elementary current, n is the number of elementary currents [11].

3. Realization of experiment

The electric power transformers are sometimes placed in the vicinity of transmitters for mobile communications and their radiation can affect these transformers. By using the conventional transformer oil the electromagnetic radiation has no effect. Power engineering develops new and better insulation materials, such as magnetic fluid, that is one of them. In the future, magnetic fluids could replace the transformer oil. Our aim was to determine whether high frequency of electromagnetic field radiation had any influence on the magnetic fluids. Therefore, we have chosen a frequency of 900 MHz since it is used by mobile operators.

The aim of the measurement was to determine the impact of the electromagnetic field on magnetic ferrofluids at room temperature (20°C) without the influence of an external electromagnetic field. For the measurement, the KEITHLEY K617 device was used with a measuring voltage of 100 V intended for measurements of charging and discharging currents. The measuring devices and the circuit configuration is shown in Fig. 2.

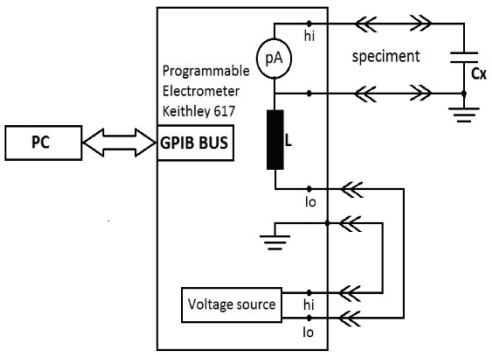

Fig. 2. Circuit configuration for measurement

Used measuring devices are very susceptible to electromagnetic interference (EMI). For that reason, measurements were carried out in the non-reflective EMC chamber, which prevents against permeability of EMI from the environment. Three selected samples of magnetic fluids were submitted to PDC analysis, while the charging and discharging currents were measured. The measurements were automated by the Agilent VEE software. The measured values were recorded during the measurements. The magnetic fluid has been drawn up in concentrations that are expressed using magnetization. A manufacturer doesn't define the volu-

metric representation of particles in magnetic fluid and defines only the size of magnetization of individual samples. The labeled samples were called Gauss 10, Gauss 25 and Gauss 50 and the concentration of particles in the individual magnetic fluids did not exceed 5%. The container, which is shown in Fig. 3 and which was used for measurements, contains the system of flat electrodes.

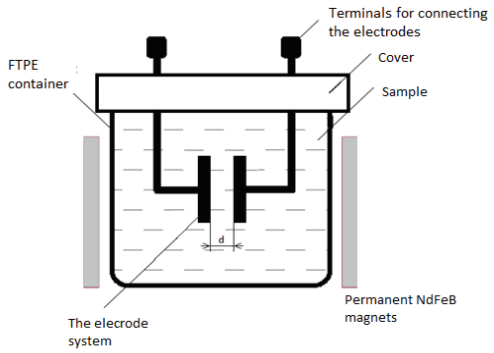

Fig. 3. Preparation for measurement of samples

The used container should have a volume of approximately 75 ml with the two circular electrodes. The diameter of each electrode was 20 mm and the distance between the electrodes was 1 mm.

Afterwards, we have measured individual samples which were exposed to the electromagnetic field. Each measurement was repeated for comparison of the results.

The samples were placed in a non-reflective EMC chamber because of exterior influences. The antenna was connected with Analog Signal Generator Agilent MXG N5183A. The power amplifier was connected to an analog signal generator. Radiation power of electromagnetic field was set at 30 W at a frequency of 900 MHz. All samples were irradiated during 100 hours.

The measurements of the individual samples were repeated three times. The resulting values of charging and discharging currents were averaged.

4. Evaluation of measured results

At processed results, there can be seen that the curve of charging currents is slightly deformed. The size of the bending depends on the percentage of magnetic particles in the magnetic fluid. These anomalies are probably caused by dielectrophoresis.

For the sample GAUSS 10, the anomalies are much smaller than for the other samples. This is due to the fact, that concentration of magnetic particles is lower in this particular sample and therefore it creates less chains which has a great influence on the charging current of the samples.

When comparing the charging currents of irradiated and non-irradiated samples, it is clear that the irradiated sample shows more anomalies than the non-irradiated sample. Increased

occurrence of these anomalies is likely to be caused by irradiation of the samples. This radiation has an influence on the magnetic particles contained in the magnetic fluid.

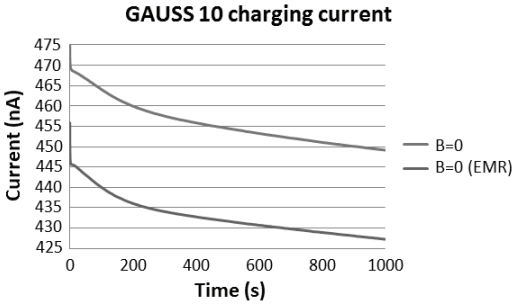

Fig. 4. The graphic dependence of the charging current on the time, the sample GAUSS 10 before the influence of electromagnetic radiation (EMR) and after the influence of EMR

This electromagnetic radiation has a high frequency and power. The magnetic particles under the influence of an electromagnetic field are heated and these overheated magnetic particles release the chains of surfactant. These surfactants deteriorating the properties of the magnetic fluid.

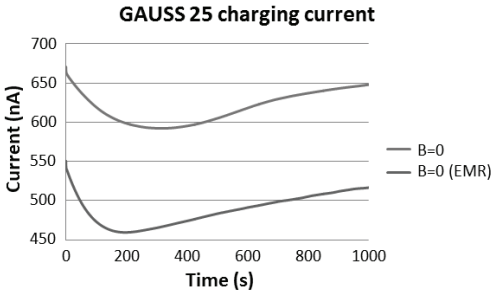

Fig. 5. The graphic dependence of the charging current on the time, the sample GAUSS 25 before the influence of EMR and after the influence of EMR

The volumetric representation of magnetic particles is much greater in the samples GAUSS 50 and GAUSS 25 than in the sample GAUSS 10 and the volume of surfactants is greater, too.

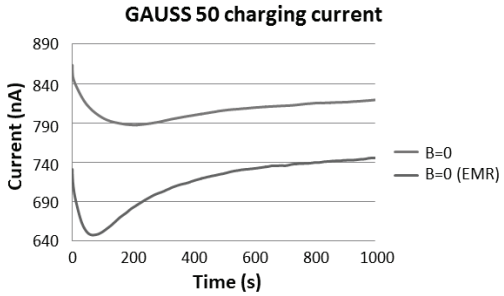

Fig. 6. The graphic dependence of the charging current on the time, the sample GAUSS 50 before the influence of EMR and after the influence of EMR

From graphic results of discharging currents in the individual samples, it can be seen that the discharging in the sample GAUSS 10 is much steeper than in the samples GAUSS 25 and GAUSS 50. These differences are caused by chains that were formed while charging of the samples. These chains create a stable structure, causing that the depolarization of the samples was carried out slowly. This phenomenon is more noticeable in the samples GAUSS 25 and GAUSS 50, which is associated with the greater volumetric representation of the magnetic particles.

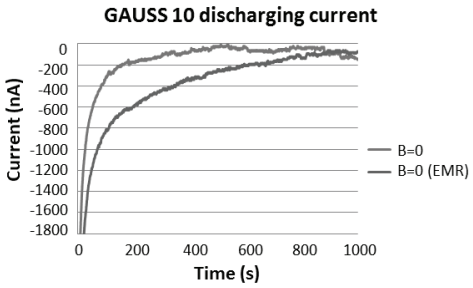

Fig. 7. The graphic dependence of the discharging current on the time, the sample GAUSS 10 before the influence of EMR and after the influence of EMR

When comparing the same samples before irradiation and after irradiation of the electromagnetic field, we can see the change in discharge characteristics of the current. The most significant change is observed in the sample GAUSS 10, this radiation has an impact on the magnetic particles, as well.

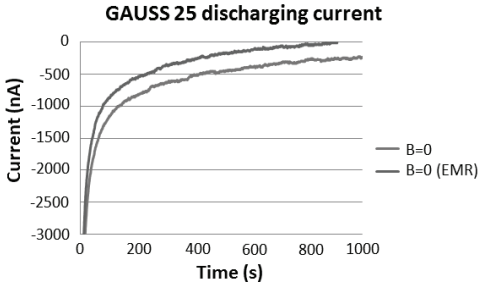

Fig. 8. The graphic dependence of the discharging current on the time, the sample GAUSS 25 before the influence of EMR and after the influence of EMR

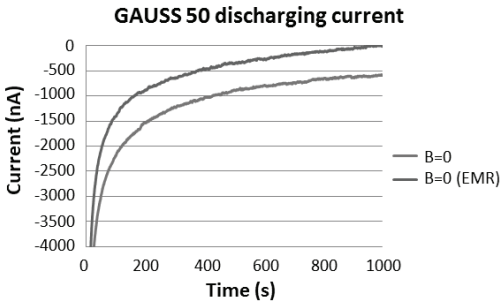

Fig. 9. The graphic dependence of the discharging current on the time, the sample GAUSS 50 before the influence of EMR and after the influence of EMR

As mentioned, under the influence of an electromagnetic field, the magnetic particles are heated up, that causes that weaker bond between the surfactant and the magnetic particles was disrupted. Increasing release of the amount of surfactant molecules in the magnetic fluid, caused deterioration of dielectric properties of the magnetic fluids.

The minor differences are observed in the irradiated and non-irradiated sample for samples GAUSS 25 and GAUSS 50, which are associated with the clusters formation of magnetic particles.

5. Conclusion

The main objective of this paper was to investigate whether electromagnetic radiation has an influence on the degradation of parameters of the magnetic fluids. In this experiment, three samples of magnetic fluids were used. To determine the state of liquid, PDC analyses were executed in the time domain. Individual samples were measured before and after the influence of an electromagnetic field. The results were graphically processed and compared. Experiments showed that electromagnetic radiation at a frequency of 900 MHz and power of 30 W had a negative influence on the magnetic fluids. Since power transformers generate electromagnetic fields with a frequency of 50 Hz, it would be advisable to verify experimentally the influence of the electromagnetic radiation at a frequency of 50 Hz.

Acknowledgements
This work was supported by grant award FEI no. FEI-2015-6, The impact of electromagnetic fields on the properties of materials.

References

[1] Wolny S., Adamowicz A., Lepich M., *Influence of temperature and moisture level in paper oil insulation on the parameters of the Cole-Cole model*, IEEE Transactions on Power delivery, vol. 29, no. 1, pp. 246-250 (2014).
[2] Cimbala R., Kurimský J., Kolcunová I., *Determination of thermal ageing influence on rotating machine insulation system using dielectric spectroscopy*, Przegląd Elektrotechniczny, vol. 87, no. 8, pp. 176-179 (2011).
[3] Dolník B., *Electromagnetic compatibility*, TU of Košice (in Slovak), monography, pp. 36-64 (2013).
[4] Timko M., Marton K., Király J., Cimbala R. et al., *Magneto-dielectric properties of transformer oil based magnetic fluids in the frequency range up to 2 MHz*, Magnetohydrodynamics, vol. 48, no. 2, pp. 427-434 (2012).
[5] Zbojovský J., Mészáros A., Medveď D., *Simulation of electromagnetic fields propagation through the various materials*, Proceedings of 15th International Scientific Conference on Electric Power Engineering (EPE), Brno, Czech Republic, pp. 257-260 (2014).
[6] Bica D., *Preparation of magnetic fluids for various applications*, Romanian Reports in Physics, vol. 47, pp. 265-272 (1995).
[7] Medveď D., Kanálik M., *Addressing arrangement of the electromagnetic field in the vicinity of electric power lines*, Elektroenergetika (in Slovak), vol. 8, no. 2, pp: 9-12 (2015).

[8] Liptai P., Lukáčová K., *The electromagnetic fields near a microwave oven – measurement and analysis*, Annals of Faculty Engineering Hunedoara – International Journal of Engineering, vol. 14, no. 1, pp. 83-86 (2016).
[9] Du Y., Mamishev A.V., Lesieutre B.C., Zahn M., Kang S.H., *Moisture solubility for differently conditioned transformer oils*, IEEE Transactions on Dielectrics and Electrical Insulation, vol. 8, no. 5, pp. 805-811 (2001).
[10] Petráš J., Balogh J., Džmura J., *Overvoltage protection in high-frequency technology*, Proceedings of 13th International Scientific Conference on Electric Power Engineering (EPE) (in Czech), Brno, Czech Republic, pp. 893-897 (2012).
[11] Zbojovský J. et al., *Effect of shielding materials for electromagnetic field distribution*, Proceedings of 7th International Scientific Symposium on Electrical Power Engineering (in Slovak), Stará Lesná, Slovak Republic, pp: 439-442 (2013).
[12] Cimbala R., Kolcunová I., Dedinska L., Cackova V., *Thermal dependency of dielectric properties of liquid insulating materials*, Proceedings of 11th International Scientific Conference on Electric Power Engineering (EPE), Brno, Czech Republic, pp. 743-747 (2010).
[13] Kanálik M., Kolcun M., *Computation of harmonic flows in three-phase systems*, Acta Electrotechnica et Informatica, vol. 7, no. 3, pp. 41-45 (2007).
[14] Liptai P., *Measurement methodology and evaluation of high-frequency electromagnetic fields of base stations of mobile operators in populated areas Ukraine – EU*, Modern Technology, Business and Law (in Slovak), pp. 306-309, (2016).
[15] Pavlík M., Kolcunová I., Dolník B., Kurimský J., Mészáros A., Medveď D., Kolcun M., Zbojovský J., *Measuring of dependence of shielding effectiveness of wet materials on the frequency of electromagnetic field in the high frequency range*, Acta Electrotechnica et Informatica, vol. 13, no. 3, pp. 12-16 (2013).
[16] Medveď D., Hirka O., *Impact of electromagnetic fields in residential areas*, Elektroenergetika, vol. 9, no. 2, pp. 13-16 (2016).
[17] Zbojovský J., Mészáros A., Kurimský P., *Modelling the high frequency electromagnetic field propagation through the polystyrene*, Proceedings of 8th International Scientific Symposium on Electrical Power Engineering, Stará Lesná, Slovak Republic, pp. 556-559 (2015).
[18] Marton K., Tomčo L., Cimbala R. et al., *Magnetic fluid in ionizing electric field*, Journal of Electrostatics, vol. 71, no. 3, pp. 467-470 (2013).
[19] Rajnak M., Timko M., Kopcansky P., Paulovicova K et al., *Structure and viscosity of a transformer oil-based ferrofluid under an external electric field*, Journal of Magnetism and Magnetic Materials 2016, doi: 10.1016/j.jmmm.2016.10.008

ARCHIVES OF ELECTRICAL ENGINEERING VOL. 66(2), pp. 371-382 (2017)

DOI 10.1515/aee-2017-0028

A modelling of AC voltage stabilizer based on a hybrid transformer with matrix converter

PAWEŁ SZCZEŚNIAK

Institute of Electrical Engineering, University of Zielona Góra
Licealna 9, 65-417 Zielona Góra, Poland
e-mail: P.Szczesniak@iee.uz.zgora.pl

(Received: 12.08.2016, revised: 27.01.2017)

Abstract: This article presents a study of an AC voltage stabilizer based on a three-phase hybrid transformer combined with a matrix converter. The proposed solution is used to control AC voltage amplitude and phase shift. By adjustment of these voltage parameters we can reduce the effects of overvoltage, voltage dips or lamp flicker. Such negative phenomena are very significant, particularly from the perspective of the final consumer and sensitive loads connected to the power network. Often the voltage in the power system can be adjusted using a mechanical or thyristor controlled regulator, which in a stepwise manner switches the taps of the electromagnetic transformer. The method for obtaining continuous control of the voltage magnitude and phase shift with the use of a conventional transformer with two output windings and a matrix converter is presented in this paper. The operating principles, mathematical model and properties of the proposed voltage stabilizers are discussed in this paper. The main part of the article will be devoted to the mathematical model which is based on an averaged equation. Computer simulation results are presented and compared with the results of a mathematical study.

Key words: AC voltage stabilizer, averaged model, hybrid transformer, matrix converter

1. Introduction

Electric Power Quality (EPQ) is a term that refers to the maintenance of a near sinusoidal waveform of power distribution bus voltages and currents at rated magnitude and frequency. Moreover, modern systems in industrial plants are based on high-tech equipment for increased productivity and this requires high quality electrical power. In addition, poor quality electricity can also cause damage to domestic electronic equipment, which more often than not now has miniature and large-scale integration of electronic circuits. Voltage sags are among the most significant power quality problems impacting on sensitive industrial and home equipment. Power quality standards define and classify voltage disturbances [1, 2]. A large number of scientific papers are also dedicated to the issue of voltage disturbances in the power grid [3, 4]. Power quality problems occur due to various types of electrical disturbances. Most of the EPQ disturbances impact on amplitude or frequency or on both. Voltage sags and interruptions are common phenomena resulting from network faults and dynamic load changes.

Voltage sags are rms/magnitude reductions in the AC voltage for a duration ranging from a half-cycle to several dozen seconds.

In modern power systems, operators should prevent the causes and mitigate the effects of voltage distortion. The best possible solution for customers might be the installation of mitigation equipment for voltage disturbances. There are many solutions for power systems. The most common devices are tap changers (mechanical or solid-state) in electromagnetic transformers [5, 6]. The second most common group consists of power electronic devices, which continuously stabilize the voltage at the point of common coupling (PCC) [7, 8]. Such solutions are often called Custom Power Devices (CPD). There are two main methods for compensation of voltage-disturbances in power systems using power electronics devices: current oriented parallel devices (STATCOM-static synchronous compensator, SVC-static VAR compensator); and voltage oriented series devices (DVR-Dynamic Voltage Restorer) [9, 10]. In this article only series compensation systems will be considered. The Dynamic Voltage Restorer (DVR) is one of the most efficient CPDs used to compensate fast voltage sags and overvoltages at PCC [9]. The DVR devices inject a voltage of the required magnitude, phase angle and frequency in series with the load. In this way the DVR maintains the set amplitude and waveform for the voltage at the load, even when the source voltage is distorted or unbalanced [7].

The concept of a hybrid transformer (HT) is defined as a combination of a classical electro-magnetic transformer with a power electronics converter. The literature describes a few concepts of HT with shunt connected converters, series connected converters and a combination of series and shunt connected converters [11-13]. The conception of the HT presented in this paper is based on a structure with a series connected converter. In the proposed HT the matrix converter (MC) is used [14, 15]. Generally, the three-phase MC is a single-stage converter with an array of nine bi-directional switches. In order to ensure good performance, the MC should have a LC source filter to minimize the high frequency current distortion. The MC is a power device without a DC energy storage element. The DC energy storage element used in classical frequency converters with a voltage source inverter (VSI) is the main factor increasing size, weight and cost of the converter [15, 16]. Furthermore, this energy storage in the form of electrolytic capacitors is the most frequently damaged element in operational service. Elimination of the DC energy magazine will increase the reliability of the proposed voltage compensator.

A preliminary study of the properties of the proposed MC based HT is presented in [12], where the idealized properties are shown. In addition, several similar solutions of AC voltage controllers for compensation of overvoltage and voltage sags (also based on the HT) are proposed in [10, 11, 13, 17-21]. In the HT solution proposed in [11, 17] the PWM AC/AC matrix and matrix-reactance choppers are used [15]. The proposed choppers are employed for adjustment of the RMS value of the output voltages, excluding the possibility of output voltage phase shift adjustment. Using the HT with the matrix converter we obtain the possibility to control both the amplitude (or RMS value) and phase shift of the HT output voltages. This additional degree of regulation offers new possibilities for the application of the proposed solution, as previously shown in [12].

The main purpose of this paper is to describe the basic operations, based on the averaged mathematical model [22, 23] and simulation investigation, of the proposed HT with a space vector modulated (SVM) matrix converter. The simulation and theoretical results will be analysed and compared. In addition, the paper presents an application of the proposed HT to voltage sag compensation at the PCC in balanced and unbalanced conditions.

2. Principles of the proposed solution

As illustrated in Fig. 1, the proposed hybrid transformer consists of two main units: a three-phase matrix converter [14] and a conventional transformer. The transformer has two taps for each of the output phases. The first tap (a_1, a_2, a_3-the names of first taps in each phase) is connected with the corresponding matrix converter input filter terminal (L_F, C_F). Both the primary and secondary windings a_1, a_2, a_3 are in star-connections (Fig. 1). Subsequent secondary windings (b_1, b_2, b_3-the names of second taps in each phase) are connected in series with the corresponding MC output terminals. The voltage turn ratios of the windings a_1, a_2, a_3 and b_1, b_2, b_3 are equal to $n_a = 4/3$ and $n_b = 2/3$, respectively. The voltage gains have been adopted from the previous publications presenting HTs with AC choppers [11, 17]. It is possible to use other transformer turn ratios, as will be mentioned in the summary. The HT output voltage is the sum or result of the MC output voltage and output voltage of windings b_1, b_2, b_3. In order to extract the fundamental component of the MC output voltage, a low-pass L_L, C_L output filter is employed.

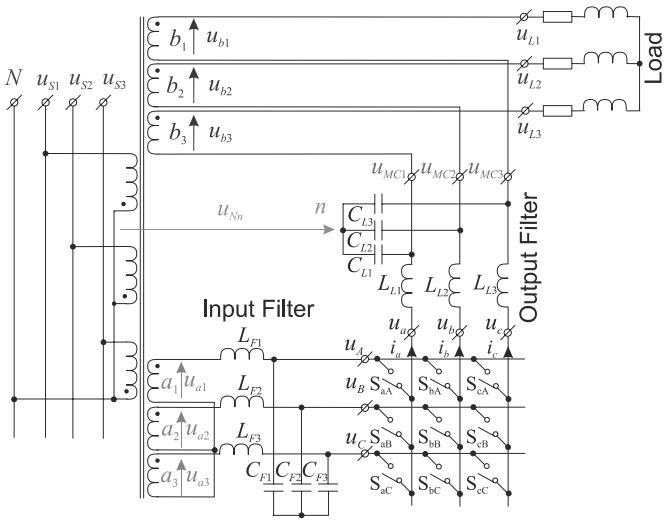

Fig. 1. Proposed hybrid transformer with MC and passive load

The MC output voltage is adjusted using voltage gain q and the voltage phase shift φ_L. The maximum HT output voltage is achieved when the MC output voltages (u_{MC1}, u_{MC2}, u_{MC3} are

voltages at the output of L_L, C_L filter) have the same phase as voltages u_{b1}, u_{b2}, u_{b3}. If the source voltages are given as follows:

$$\begin{bmatrix} u_{S1} \\ u_{S2} \\ u_{S3} \end{bmatrix} = \begin{bmatrix} U_S \sin(\omega t + \varphi_S) \\ U_S \sin(\omega t + 2/3\pi + \varphi_S) \\ U_S \sin(\omega t - 2/3\pi + \varphi_S) \end{bmatrix}, \tag{1}$$

then the HT output voltages (for an ideal transformer without LC filters) are described by Eq. (2), where U_S, U_L represent the amplitude of the input and HT output voltage, respectively, φ_S, φ_L, φ represent the phase shift of the input voltage, MC output voltage and HT output voltage, respectively. To determine the exact HT voltage transmittance, it is necessary to describe a mathematical model that takes into account the parameters of components used in the LC filters and the MC modulation strategy.

$$\begin{bmatrix} u_{L1} \\ u_{L2} \\ u_{L3} \end{bmatrix} = \begin{bmatrix} U_S \sin(\omega t + \varphi_S + \varphi_L) n_a q + U_S \sin(\omega t + \varphi_S) n_b \\ U_S \sin(\omega t + 2/3\pi + \varphi_S + \varphi_L) n_a q + U_S \sin(\omega t + 2/3\pi + \varphi_S) n_b \\ U_S \sin(\omega t - 2/3\pi + \varphi_S + \varphi_L) n_a q + U_S \sin(\omega t - 2/3\pi + \varphi_S) n_b \end{bmatrix} = \begin{bmatrix} U_L \sin(\omega t + \varphi) \\ U_L \sin(\omega t + 2/3\pi + \varphi) \\ U_L \sin(\omega t - 2/3\pi + \varphi) \end{bmatrix}. \tag{2}$$

The Space Vector Modulation (SVM) technique is the most frequently used modulation strategy for MC applications [14, 22]. The instantaneous space vector representation of load voltages ($\underline{u}_{OL}$) and source currents ($\underline{i}_S$) in the MC is presented as follows:

$$\underline{u}_{OL} = \frac{2}{3}\left(u_{ab} + e^{-j2\pi/3} u_{bc} + e^{j2\pi/3} u_{ca}\right) = u_{OL} e^{j\alpha_{OL}(t)}, \quad \underline{i}_S = \frac{2}{3}\left(i_A + e^{-j2\pi/3} i_B + e^{j2\pi/3} i_C\right) = i_S e^{j\beta_i(t)}. \tag{3}$$

The SVM method for the MC has been described many times in various publications (e.g., [14, 22]). In this article there will be indicated only the basic formulas, useful for creating mathematical models. The reference space-vectors $\underline{u}_{OL}$ and $\underline{i}_S$ are constructed by selecting four basic "nonzero vectors" and one "zero vector", used during the appropriate time intervals within the switching period T_{Seq}. The required modulation duty cycles for the corresponding "nonzero vectors" are given by Eqs. (4) [22]:

$$\begin{gathered} d_{\mathrm{I}} = (-1)^{S_0+S_i+1} \frac{2q\cos(\alpha_0 - \pi/3)\cos(\beta_i - \pi/3)}{\sqrt{3}\cos\varphi_i}, \quad d_{\mathrm{II}} = (-1)^{S_0+S_i} \frac{2q\cos(\alpha_0 - \pi/3)\cos(\beta_i + \pi/3)}{\sqrt{3}\cos\varphi_i}, \\ d_{\mathrm{III}} = (-1)^{S_0+S_i} \frac{2q\cos(\alpha_0 + \pi/3)\cos(\beta_i - \pi/3)}{\sqrt{3}\cos\varphi_i}, \quad d_{\mathrm{IV}} = (-1)^{S_0+S_i+1} \frac{2q\cos(\alpha_0 + \pi/3)\cos(\beta_i + \pi/3)}{\sqrt{3}\cos\varphi_i}, \end{gathered} \tag{4}$$

where: φ_i is the input displacement angle, α_0 and β_i are the position angles of the output voltage and input current vectors, respectively, measured from the bisecting line of the corresponding sectors of the complex coordinate system, which are limited as follows: $-\pi/6 < \alpha_0 < \pi/6$, $-\pi/6 < \beta_i < \pi/6$. The disadvantage of the MC is its limited voltage gain, which for the SVM is equal to $q_{\max} = \sqrt{3/2} \approx 0.866$.

Knowing the maximum voltage gain of the MC and voltage turn ratios of the transformer windings n_a and n_b, it is possible to determine the idealized expressions for the maximum and minimum HT output voltage [12]. The maximum HT output voltage for $n_a = 4/3$, $n_b = 2/3$ and an MC with SVM is defined by Eq. (5), whereas the minimum for the MC output voltage phase shift equals 180 deg, and is defined by Eq. (6). The relations between voltage phasors for $\underline{U}_L = \underline{U}_{L\max}$, $\underline{U}_L = \underline{U}_{L\min}$ and $\underline{U}_{L\max} < \underline{U}_L < \underline{U}_{L\min}$ for $\varphi_L \neq 0$, are shown in Fig. 2. The voltage adjustment range is limited by a circle, as shown in Fig. 2. It shows that in the proposed solution it is possible to compensate both voltage sags and overvoltage with the ability to control the phase shift of the output voltage.

$$U_{L\max} = U_S n_a q_{\max} + U_S n_b = U_S \frac{4}{3}\frac{\sqrt{3}}{2} + U_s \frac{2}{3} \approx 1.82 U_S \,, \tag{5}$$

$$U_{L\min} = -U_S \frac{4}{3}\frac{\sqrt{3}}{2} + U_s \frac{2}{3} \approx -0.49 U_S \,. \tag{6}$$

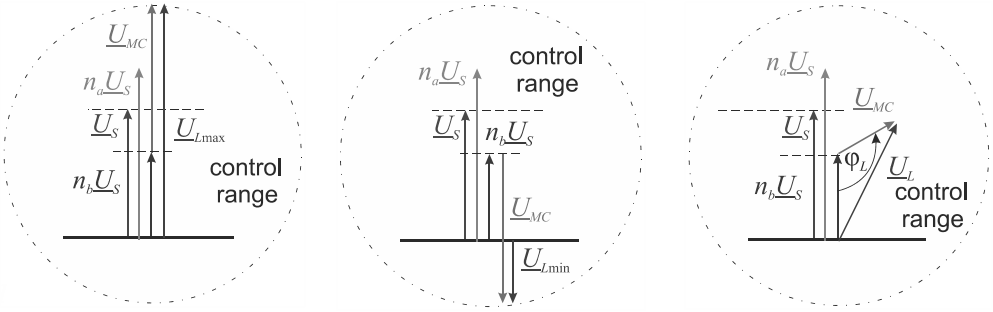

(a) (b) (c)

Fig. 2. HT voltage phasors for $n_a = 4/3$ and $n_b = 2/3$ and SVM: $U_L = U_{L\max}$ for $\varphi_L = 0°$ and $q_{\max} = 0.866$ (a); $U_L = U_{L\min}$ for $\varphi_L = 180°$ and $q_{\max} = 0.866$ (b); $U_{L\max} < U_L < U_{L\min}$ for $\varphi_L \neq 0°$ and $q_{\max} < 0.866$ (c)

The mathematical description and characteristics presented above are defined in the idealized case, without influence of the LC filter and transformer parameters. For a precise depiction the properties of the analyzed system require a detailed mathematical model, which will be shown in the next section. The main problem in providing a detailed mathematical description of the analyzed HT is the inclusion of the modulation pattern of the MC switches. The proposed modelling process will be based on the state-space average model [22, 23].

3. Modelling theory

The presented mathematical model is based on the state-space equations for the averaged variables which are described by (7) [22].

$$\frac{\mathrm{d}\bar{\boldsymbol{x}}}{\mathrm{d}t} = \boldsymbol{A}(d)\bar{\boldsymbol{x}} + \boldsymbol{B}(d), \tag{7}$$

where: $\bar{\boldsymbol{x}}$ is the vector of the averaged state variables, $\boldsymbol{A}(d)$ is the averaged state matrix, $\boldsymbol{B}(d)$ is the averaged input matrix. This model is created by averaging of state variables in the sequence period T_{Seq} for all switch combinations of the analysed converter. The elementary averaged models for each switch combination are defined for the relative duty cycles $d_k = t_k/T_{Seq}$, as is shown in Eq. (8), where $\boldsymbol{x}$ represents the vectors of the state variables; $\boldsymbol{A}_k(t)$ and $\boldsymbol{B}_k(t)$ are the state matrix and input matrix for k–th switch configuration respectively. The state-space average Eq. (9) for an MC can be represented by 27 elementary averaged models:

$$\frac{\mathrm{d}\boldsymbol{x}}{\mathrm{d}t} = \boldsymbol{A}_k(t)\boldsymbol{x} + \boldsymbol{B}_k(t), \tag{8}$$

$$\frac{\mathrm{d}\bar{\boldsymbol{x}}}{\mathrm{d}t} = \boldsymbol{A}(d,t)\bar{\boldsymbol{x}} + \boldsymbol{B}(d,t), \tag{9}$$

where:

$$\sum_{k=1}^{27} d_k = 1, \quad \boldsymbol{A}(d,t) = \sum_{k=1}^{27} d_k \boldsymbol{A}_k(d,t), \quad \boldsymbol{B}(d,t) = \sum_{k=1}^{27} d_k \boldsymbol{B}_k(d,t).$$

The coefficient d_k is the degree of occurrence of all the possible configurations, and depends on the switch modulation strategy. In an SVM MC only 21 switch configurations are used; 18-active, and 3-zero [22]. Furthermore, the pulse duty factors d_k for MCs are a time variable, therefore the presented model is a time-varying one [23]. Using the transformation matrix $\boldsymbol{K}$ (10) we obtain the time-invariant model in the d-q rotating frame. Because the HT output voltage frequency is equal to the supply voltage frequency, then $\boldsymbol{K}$ is defined only for the supply voltage frequency, unlike MC models operating as a frequency converter [22, 23].

$$\boldsymbol{K} = \begin{bmatrix} \boldsymbol{K}_S & \dots & 0 \\ \vdots & \ddots & \vdots \\ 0 & \dots & \boldsymbol{K}_S \end{bmatrix}, \quad \boldsymbol{K}_S = \sqrt{\frac{2}{3}} \begin{bmatrix} \cos(\omega t) & \sin(\omega t) & 1/\sqrt{2} \\ \cos(\omega t - 2\pi/3) & \sin(\omega t - 2\pi/3) & 1/\sqrt{2} \\ \cos(\omega t + 2\pi/3) & \sin(\omega t + 2\pi/3) & 1/\sqrt{2} \end{bmatrix}. \tag{10}$$

On the assumption of symmetry of HT components, we obtain the final version (11) of the averaged models.

$$\frac{\mathrm{d}\boldsymbol{Y}}{\mathrm{d}t} = (\boldsymbol{A} - \boldsymbol{\Omega})\boldsymbol{Y} + \boldsymbol{B}, \tag{11}$$

where:

$$\bar{\boldsymbol{x}} = \boldsymbol{K}\boldsymbol{Y}, \quad \boldsymbol{\Omega} = \begin{bmatrix} \boldsymbol{\Omega}_S & \cdots & 0 \\ \vdots & \ddots & \vdots \\ 0 & \cdots & \boldsymbol{\Omega}_S \end{bmatrix}, \quad \boldsymbol{\Omega}_S = \begin{bmatrix} 0 & \omega & 0 \\ -\omega & 0 & 0 \\ 0 & 0 & 0 \end{bmatrix}.$$

The solution of Eq. (11) for general conditions and for the steady state is described by (12) and (13) respectively [23], where $\boldsymbol{Y}_0$ represents the initial values of state variables, and $\boldsymbol{I}$ is the unit matrix.

$$\bar{\boldsymbol{x}} = \boldsymbol{K}\boldsymbol{e}^{(\boldsymbol{A}-\boldsymbol{\Omega})t}\boldsymbol{Y}_0 + \boldsymbol{K}(\boldsymbol{A}-\boldsymbol{\Omega})^{-1}\left(\boldsymbol{e}^{(\boldsymbol{A}-\boldsymbol{\Omega})t} - \boldsymbol{I}\right)\boldsymbol{B}\,, \tag{12}$$

$$\bar{\boldsymbol{x}} = -\boldsymbol{K}(\boldsymbol{A}-\boldsymbol{\Omega})^{-1}\boldsymbol{B}\,. \tag{13}$$

The proposed model of the HT should take into account the MC switch modulation strategy. For the SVM of MC switches what should additionally be taken into account is the offset voltage u_{Nn} (Fig. 1) [22]. Description of averaged state equations is connected with the calculation of the averaged pulse duty factor for each MC switch S_{jK}, which is described by (14).

$$\begin{bmatrix}\bar{u}_a\\ \bar{u}_b\\ \bar{u}_c\end{bmatrix} = \begin{bmatrix}d_{aA} & d_{aB} & d_{aC}\\ d_{bA} & d_{bB} & d_{bC}\\ d_{cA} & d_{cB} & d_{cC}\end{bmatrix}\begin{bmatrix}\bar{u}_A\\ \bar{u}_B\\ \bar{u}_C\end{bmatrix} = \boldsymbol{D}\bar{\boldsymbol{u}}_{ABC}\,,\quad \begin{bmatrix}\bar{i}_A\\ \bar{i}_B\\ \bar{i}_C\end{bmatrix} = \begin{bmatrix}d_{aA} & d_{bA} & d_{cA}\\ d_{aB} & d_{bB} & d_{cB}\\ d_{aC} & d_{bC} & d_{cC}\end{bmatrix}\begin{bmatrix}\bar{i}_a\\ \bar{i}_b\\ \bar{i}_c\end{bmatrix} = \boldsymbol{D}^T\bar{\boldsymbol{i}}_{abc}\,. \tag{14}$$

The SVM of an MC is described in many publications, e.g., [14, 22], thus switching relations and vector definitions are not shown in this paper. All names of voltage and current vectors, presented later in this article, are compatible with the names presented in the article [22]. In order to determine the voltage u_{Nn}, consider the switching sequence in the sectors $S_i = 1$ and $S_O = 1$. The switch configurations are as follows: +9, –7, –3, +1, and matrix switches are switched-on successively by a related time scheme:

$$|d_{\mathrm{I}}| \rightarrow |d_{\mathrm{II}}| \rightarrow |d_{\mathrm{III}}| \rightarrow |d_{\mathrm{IV}}|\,. \tag{15}$$

Then, the transformation matrix $\boldsymbol{D}$ (14) is determined as follows:

$$\boldsymbol{D} = \boldsymbol{D}_{(+9)}|d_{\mathrm{I}}| + \boldsymbol{D}_{(-7)}|d_{\mathrm{II}}| + \boldsymbol{D}_{(-3)}|d_{\mathrm{III}}| + \boldsymbol{D}_{(+1)}|d_{\mathrm{IV}}| = \begin{bmatrix}|d_{\mathrm{I}}|+|d_{\mathrm{II}}|+|d_{\mathrm{III}}|+|d_{\mathrm{IV}}| & 0 & 0\\ |d_{\mathrm{I}}|+|d_{\mathrm{II}}| & |d_{\mathrm{IV}}| & |d_{\mathrm{III}}|\\ 0 & |d_{\mathrm{II}}|+|d_{\mathrm{IV}}| & |d_{\mathrm{I}}|+|d_{\mathrm{III}}|\end{bmatrix}. \tag{16}$$

The same procedure is given for the other sectors with combined S_i and S_O. Offset voltage u_{Nn} in the averaged model of the MC with SVM is described by (17) and (18).

$$\bar{u}_N = \frac{\left(\bar{u}_a + \bar{u}_b + \bar{u}_c\right)}{3}\,, \tag{17}$$

$$\bar{u}_N = \frac{(d_{aA}+d_{bA}+d_{cA})\bar{u}_A + (d_{aB}+d_{bB}+d_{cB})\bar{u}_B + (d_{aC}+d_{bC}+d_{cC})\bar{u}_C}{3} = s_1\bar{u}_A + s_2\bar{u}_B + s_3\bar{u}_C\,, \tag{18}$$

where:

$$s_1 = \frac{d_{aA}+d_{bA}+d_{cA}}{3}, s_2 = \frac{d_{aB}+d_{bB}+d_{cB}}{3}, s_3 = \frac{d_{aC}+d_{bC}+d_{cC}}{3}\,.$$

Taking into account expressions (14) – (18), the final state–space averaging Eq. (9) of the HT with the SVM MC are described by (19).

$$\begin{bmatrix} \frac{d\bar{i}_{S1}}{dt} \\ \frac{d\bar{i}_{S2}}{dt} \\ \frac{d\bar{i}_{S3}}{dt} \\ \frac{d\bar{i}_{LS1}}{dt} \\ \frac{d\bar{i}_{LS2}}{dt} \\ \frac{d\bar{i}_{LS3}}{dt} \\ \frac{d\bar{u}_{CF1}}{dt} \\ \frac{d\bar{u}_{CF2}}{dt} \\ \frac{d\bar{u}_{CF3}}{dt} \\ \frac{d\bar{u}_{L1}}{dt} \\ \frac{d\bar{u}_{L2}}{dt} \\ \frac{d\bar{u}_{L3}}{dt} \end{bmatrix} = \begin{bmatrix} -\frac{R_{LF1}}{L_{F1}} & 0 & 0 & 0 & 0 & 0 & -\frac{1}{L_{F1}} & 0 & 0 & 0 & 0 & 0 \\ 0 & -\frac{R_{LF2}}{L_{F2}} & 0 & 0 & 0 & 0 & 0 & -\frac{1}{L_{F2}} & 0 & 0 & 0 & 0 \\ 0 & 0 & -\frac{R_{LF3}}{L_{F3}} & 0 & 0 & 0 & 0 & 0 & -\frac{1}{L_{F3}} & 0 & 0 & 0 \\ 0 & 0 & 0 & -\frac{R_{L1}}{L_{L1}} & 0 & 0 & \frac{d_{aA}-s_1}{L_{L1}} & \frac{d_{aB}-s_2}{L_{L1}} & \frac{d_{aC}-s_3}{L_{L1}} & \frac{-1}{L_{L1}} & 0 & 0 \\ 0 & 0 & 0 & 0 & -\frac{R_{LL2}}{L_{L2}} & 0 & \frac{d_{bA}-s_1}{L_{L2}} & \frac{d_{bB}-s_2}{L_{L2}} & \frac{d_{bC}-s_3}{L_{L2}} & 0 & \frac{-1}{L_{L2}} & 0 \\ 0 & 0 & 0 & 0 & 0 & -\frac{R_{LL3}}{L_{L3}} & \frac{d_{cA}-s_1}{L_{L3}} & \frac{d_{cB}-s_2}{L_{L3}} & \frac{d_{cC}-s_3}{L_{L3}} & 0 & 0 & \frac{-1}{L_{L3}} \\ \frac{1}{C_{F1}} & 0 & 0 & -\frac{d_{aA}}{C_{F1}} & -\frac{d_{bA}}{C_{F1}} & -\frac{d_{cA}}{C_{F1}} & 0 & 0 & 0 & 0 & 0 & 0 \\ 0 & \frac{1}{C_{F2}} & 0 & -\frac{d_{aB}}{C_{F2}} & -\frac{d_{bB}}{C_{F2}} & -\frac{d_{cB}}{C_{F2}} & 0 & 0 & 0 & 0 & 0 & 0 \\ 0 & 0 & \frac{1}{C_{F3}} & -\frac{d_{aC}}{C_{F3}} & -\frac{d_{bC}}{C_{F3}} & -\frac{d_{cC}}{C_{F3}} & 0 & 0 & 0 & 0 & 0 & 0 \\ 0 & 0 & 0 & \frac{1}{C_{L1}} & 0 & 0 & 0 & 0 & 0 & \frac{-1}{R_{L1}C_{L1}} & 0 & 0 \\ 0 & 0 & 0 & 0 & \frac{1}{C_{L2}} & 0 & 0 & 0 & 0 & 0 & \frac{-1}{R_{L2}C_{L2}} & 0 \\ 0 & 0 & 0 & 0 & 0 & \frac{1}{C_{L3}} & 0 & 0 & 0 & 0 & 0 & \frac{-1}{R_{L3}C_{L3}} \end{bmatrix} \begin{bmatrix} \bar{i}_{S1} \\ \bar{i}_{S2} \\ \bar{i}_{S3} \\ \bar{i}_{LL1} \\ \bar{i}_{LL2} \\ \bar{i}_{LL3} \\ \bar{u}_{CF1} \\ \bar{u}_{CF2} \\ \bar{u}_{CF3} \\ \bar{u}_{L1} \\ \bar{u}_{L2} \\ \bar{u}_{L3} \end{bmatrix} + \begin{bmatrix} \frac{n_a u_{S1}}{L_{F1}} \\ \frac{n_a u_{S2}}{L_{F2}} \\ \frac{n_a u_{S3}}{L_{F3}} \\ 0 \\ 0 \\ 0 \\ 0 \\ 0 \\ 0 \\ \frac{-n_b u_{S1}}{R_{L1}C_{L1}} \\ \frac{-n_b u_{S2}}{R_{L2}C_{L2}} \\ \frac{-n_b u_{S3}}{R_{L3}C_{L3}} \end{bmatrix} \quad (19)$$

4. Validation of HT averaged model

Static characteristics obtained from the mathematical model (19) are presented in Fig. 3. The voltage gain K_U as a function of the setting of the MC output voltage phase shift φ_L for different MC voltage gains q is show in Fig. 3a. The adjustment range of the amplitude of the HT output voltage is shown with 3D characteristics in Fig. 3b. As can be seen from these characteristics, it is possible to obtain the amplitude of output voltage U_L equal to the amplitude of source voltage U_S, with and without a phase shift between source and output voltages. It should also be noted that it is possible to obtain an output voltage equal to zero for $q = 0.5$ and φ_L approximately equal to 220°. Then, the matrix converter output voltage is shifted by 180° relative to the voltage u_b of the transformer secondary winding and has the same amplitude. An output voltage in antiphase to the mains voltage it also achieved.

The general function of the HT is compensation of AC voltage sags and overvoltage. Thus, the HT works as a power transformer with a dynamic voltage restorer (DVR) function. Examples of AC voltage stabilization during a 70% source voltage sag and 120% source overvoltage, using the HT with the MC are presented in Fig. 4a. As can be seen in the presented time waveforms (Fig. 4a), the moments of start and end of the voltage sag or overvoltage are almost imperceptible, because both amplitude and phase shift δ are compensated. A large number of voltage sags in the power network are single-phase or unbalanced sags, resulting from a single-phase short circuit to ground, a two-phase short circuit or a two-phase short circuit to ground [3, 4]. The analysis of this type of compensation requires a complex form of

power converter switch modulation strategy. Fig. 4b shows the simulation results of unbalanced sag compensation using the proposed HT. Before and during the disturbance the output voltages have constant amplitude, but there can be seen some deformation in the shape of the output voltages – low harmonic distortion [24]. In addition, simulation time waveforms of voltages in the system for unbalanced and nonlinear loads are shown in Fig. 6. For unbalanced load (Fig. 6a), the HT allows compensation of voltage sag and overvoltage with a similar accuracy as for a symmetrical load (Fig. 5a). It should be noted that, for non-linear loads there is considerable distortion of the output voltage (Fig. 6). All the presented simulation waveforms were obtained in an open control loop, since the main aim of this article was to describe the basic properties of the HT. Using a closed control loop a reduction in output voltage distortion is to be expected.

All theoretical and simulation studies have been done using the following parameters: source voltage 230 V/50 Hz, input and output filter inductance and their resistances $L_F = L_L$ = 1 mH/0.01 Ω, input and output filter capacitance $C_F = C_L = 20$ μF, switching frequency $f_{Seq} = 5$ kHz and simulation step $T_p = 1$ μs. It should be noted that in the simulation investigation idealized bidirectional switches are used. None of the commutation strategies of bidirectional switches that are commonly used in MCs ([14, 25]) are used in the simulation model. Different commutation strategies in an MC are used to provide the correct current switching pattern for bidirectional switches and to eliminate distortion in the voltage and current waveforms, which occurs when the "dead time" between two control signals is used [25].

The proposed solution of an HT with an MC has some drawbacks, related to the connections of the HT to the same system in which there is a grid fault. Because the system has no energy storage element, the HT needs a minimum network voltage to work properly and it may not be able to compensate very deep sags [16].

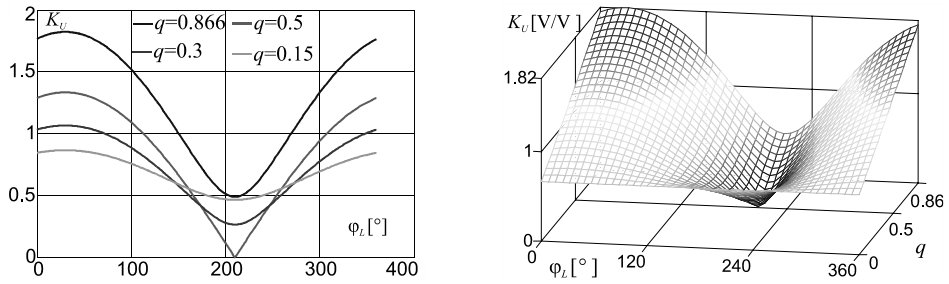

Fig. 3. Voltage gain K_U of HT as a function of: output voltage phase shift φ_L for different MC setting voltage gains q (a), output voltage phase shift φ_L and MC voltage gain q (b)

Fig. 6 compares the simulation results obtained in Matlab Simulink software for the presented HT and the resulting averaged models in transient states. To provide a meaningful comparison of the simulation model and the averaged model, the corresponding time waveforms of output voltage u_{L2}, obtained from both models are juxtaposed in one graph. The corresponding results from both models agree very well with and validate the accuracy of the averaged

model versus the simulation model. Both results demonstrate good correlation, which confirms the usefulness of the analytical averaged method used in the analysis of the HT properties.

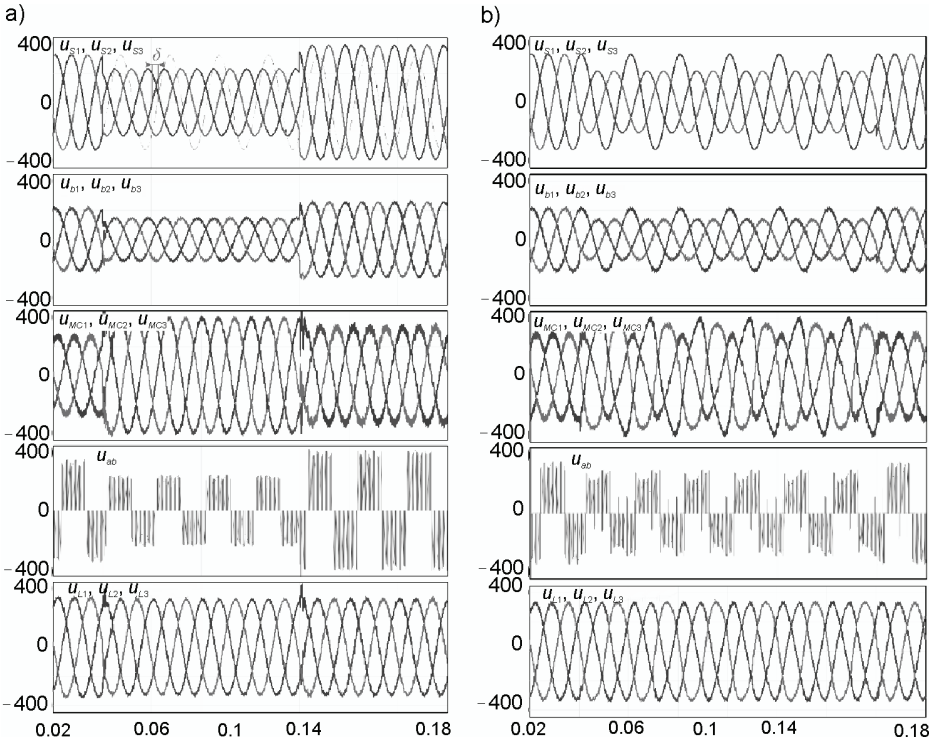

Fig. 4. Simulation results of HT with MC as a voltage compensator: voltage time waveforms during balanced 70% source voltage sag, and 120% source overvoltage (a); voltage time waveforms during 65% unbalanced source voltage sag, which are the result of two-phase short circuit to ground (b)

5. Conclusions

This paper has presented a study of the properties and a mathematical averaged model of a three-phase hybrid transformer with a matrix converter. The electrical circuit scheme and its operational conditions have been described. Furthermore, a detailed mathematical model based on average equations for an MC with SVM has also been presented. The proposed HT is able to compensate voltage sags and overvoltage, as shown in the simulation investigation. Compensation of both amplitude and resulting voltage phase shift, even for asymmetrical deformations, is possible in the analyzed system.

It should be emphasized that such a system may already be easily implemented to protect consumers in a power range equal to a few kVA. The next step of the research will focus on experimental applications in closed loop control, and define a compensation range of voltage sag and overvoltage.

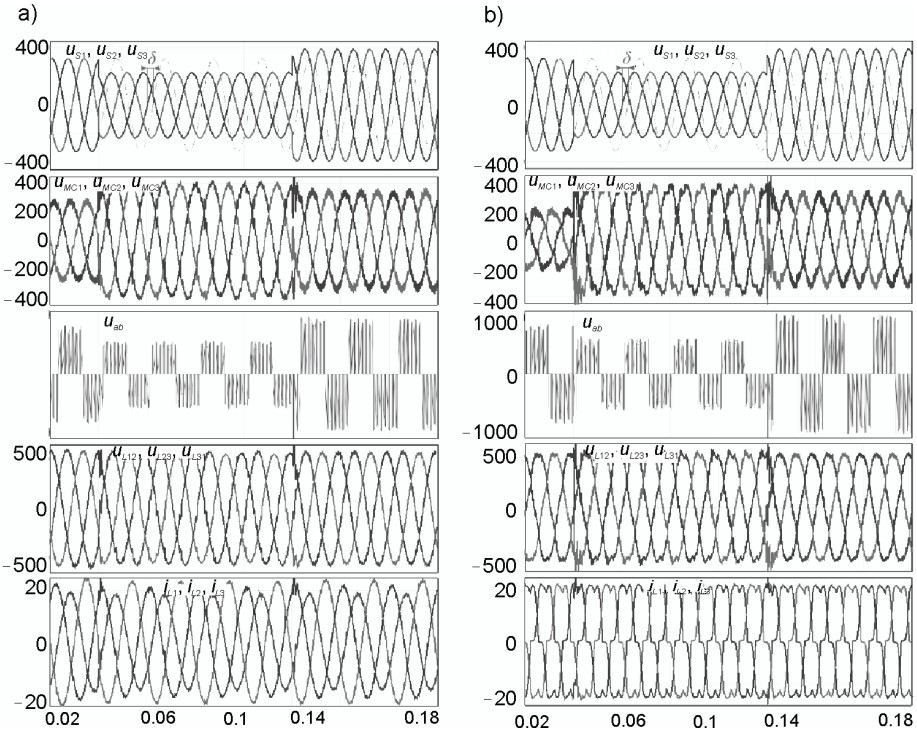

Fig. 5. Simulation results of HT with MC as a voltage compensator during balanced 70% source voltage sag, and 120% source overvoltage, for unbalanced load (a), for nonlinear load (b)

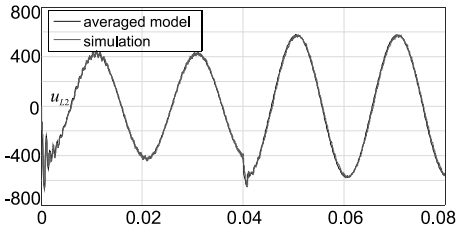

Fig. 6. Comparison of HT simulation and average models – time waveforms of output voltage u_{L2}, obtained during simulation process and average modelling

Acknowledgements

The research was carried out within the scope of the project funded by the "National Science Centre, Poland" under the reference number 2015/19/D/ST7/01371.

References

[1] EN 50160, *Voltage characteristics of electricity supplied by public distribution systems* (2007).
[2] IEEE Standard 1159, *Recommended practice for monitoring electric power quality* (2009).
[3] Mahela O., Shaik A.G., Gupta N., *A critical review of detection and classification of power quality events*, Renewable & Sustainable Energy Reviews, vol. 41, pp. 495-505 (2015).
[4] Jurado F., Saenz J.R., *Detecting transient voltage stability and voltage sag*, COMPEL, The International Journal for Computation and Mathematics in Electrical and Electronic Engineering, vol. 23, no. 2, pp. 392-409 (2004).

[5] Ekström R., Thomas K., Leijon M., *Fast solid-state on-load tap change using two current-controlled voltage-source inverters*, IET Power Electronics, vol. 7, no. 10, pp. 2610-2617 (2014).
[6] Choi J-H., Moon S-I., *The dead band control of LTC transformer at distribution substation*, IEEE Transactions on Power Systems, vol. 24, no. 1, pp. 319-326 (2009).
[7] Nielsen J.G., Blaabjerg F., *A Detailed comparison of system topologies for dynamic voltage restorers*, IEEE Transactions on Industrial Applications, vol. 41, no. 5, pp. 1272-1280 (2005).
[8] Torres A.P., Roncero-Sánchez P., del Toro García X., Batlle V.F., *Generalized proportional-integral controller for dynamic voltage restorers*, COMPEL, The International Journal for Computation and Mathematics in Electrical and Electronic Engineering, vol. 31, no. 6, pp.1964-1984 (2012).
[9] Benysek G., *Improvement in the quality of delivery of electrical energy using PE systems*, Springer (2007).
[10] Kaniewski J. Szcześniak P., Jarnut M., Benysek G., *Hybrid Voltage Sag/Swell Compensators: A Review of Hybrid AC/AC Converters*, IEEE Industrial Electronics Magazine, vol. 9, no. 4, pp. 37-48 (2015).
[11] Kaniewski J., Fedyczak Z., Benysek G., *AC voltage sag/swell compensator based on three-phase hybrid transformer with buck-boost matrix-reactance chopper*, IEEE Transactions on Industrial Electronics, vol. 61, no. 8, pp. 3835-3846 (2014).
[12] Szcześniak P., Kaniweski J., *Hybrid transformer with matrix converter*, IEEE Transactions on Power Delivery, vol. 31, no. 3, pp. 1388-1396 (2016).
[13] Burkard J., Biela J., *Evaluation of topologies and optimal design of a hybrid distribution transformer*, European Conference on Power Electronics and Applications, EPE'15 ECCE Europe, Geneva, Switzerland, pp. 1-10 (2015).
[14] Rodriguez J., Rivera M., Kolar J.W., Wheeler P.W., *A review of control and modulation methods for matrix converters*, IEEE Transactions on Industrial Electronics, vol. 59, no. 1, pp. 58-70 (2012).
[15] Szcześniak P., Kaniewski J., Jarnut M., *AC-AC power electronic converters without DC energy storage: a review*, Energy Conversion and Management, vol. 92, pp. 483-497 (2015).
[16] Szcześniak P., Kaniewski J., *Power electronics converters without DC energy storage in the future electrical power network*, Electric Power Systems Research, vol. 129, pp. 194-207 (2015).
[17] Kaniewski J., Fedyczak Z. Szcześniak P., *Three-phase hybrid transformer using matrix-chopper as an interface between two AC voltage sources*, Archives of Electrical Engineering, vol. 63, no. 2, pp. 197-210 (2014).
[18] Montero-Hernandez O.C., Enjeti P.N., *Application of a boost AC/AC converter to compensate for voltage sags in electric power distribution systems*, Power Electronics Specialists Conference PESC 2000, Galway, Ireland, pp. 470-475 (2000).
[19] Aeoliza E.C., Enjeti N.P., Moran L.A., Montero-Hernandez O.C., Kim S., *Analysis and design of a novel voltage sag compensator for critical loads in electrical power distribution systems*, IEEE Transactions on Industrial Applications, vol. 39, no. 4, pp. 1143-1150 (2003).
[20] Choi N., Li Y., *Modeling and analysis of ac line conditioner based on three-phase PWM Ćuk ac-ac converter*, Annual Conference of the IEEE Industrial Electronics Society, IECON'04, Busan, Korea, pp. 1646-1651 (2004).
[21] Minh-Khai N., Young-Cheol L., Joon-Ho C., *Single-phase Z-source based voltage sag/swell compensator*, Applied Power Electronics Conference and Exposition, APEC'13, Long Beach, USA, pp. 3138-3142 (2013).
[22] Szcześniak P., *A static and dynamic model of a space vector modulated matrix-reactance frequency converter*, Electric Power Systems Research, vol. 108, pp. 82-92 (2014).
[23] Korotyeyev. I,Y., Fedyczak Z., *Steady and transient states modelling methods of matrix-reactance frequency converter with buck-boost topology*, COMPEL, The International Journal for Computation and Mathematics in Electrical and Electronic, vol. 28, no. 3, pp. 626-638 (2009).
[24] Lozano J.M., Ramirez J.M., Correa R.E., *A novel dynamic voltage restorer based on matrix converters*, Modern Electric Power Systems, MEPS'10, Wroclaw, Poland, pp. 1-7 (2010).
[25] Wheeler P.W., Rodriguez J, Clare J.C., Empringham L., Weinstejn A., *Matrix converters: a technology review*, IEEE Transactions on Industrial Electronics, vol. 49, no. 2, pp.276-288 (2002).

ARCHIVES OF ELECTRICAL ENGINEERING VOL. 66(2), pp. 383-396 (2017)

DOI 10.1515/aee-2017-0029

Influence of the rotor eccentricity on the torque of a cage induction machine

BISHAL SILWAL[1], PAAVO RASILO[1, 2], ANOUAR BELAHCEN[1], ANTERO ARKKIO[1]

[1]*Department of Electrical Engineering and Automation, Aalto University*
P.O. Box 13000, FI-00076 AALTO, Finland

[2]*Department of Electrical Engineering, Tampere University of Technology*
P.O. Box 692, FI-33101, Tampere, Finland
email: bishal.silwal@aalto.fi

(Received: 12.08.2016, revised: 08.02.2017)

Abstract: The non-uniform air gap in an electrical machine caused by rotor eccentricity creates an asymmetrical flux-density distribution in the air gap. This can affect the nominal torque produced by the machine. Eccentricity also produces forces that act on the rotor which may also have an effect on the torque. Thus, it is important to know how the torque of the machine behaves. In this paper, the torque of a cage induction machine is studied when the machine has dynamic eccentricity. The study is performed using the finite element method and a magnetic vector potential formulation. The torque is calculated by the method of energy balance. The harmonic components of the torque are also analyzed. The results show that the machine under eccentricity does not exhibit the same torque as a normal healthy machine. The harmonic components around the first principal slot harmonic is most affected.

Key words: cage induction machine, dynamic eccentricity, electromagnetic torque, energy balance, finite element method, harmonics

1. Introduction

The rotor of a radial flux electrical machine is ideally supposed to be concentric with the stator which may not be always true. The rotor may be shifted from the center point or it may also be whirling around the center point in a circular path at a certain frequency and with a small radius, as shown in Fig. 1. Conventionally, there are two types of eccentricity. Static eccentricity corresponds to the situation where the rotor is just shifted from the center point but does not make any whirling motion. In dynamic eccentricity, the shifted rotor also makes a whirling motion, i.e. the center point of the rotor rotates around the center point of the stator at a certain frequency and with a certain radius. Rigorous studies have been already done in the past to study the eccentricity in a cage induction machine, and the forces caused by it [1-3]. However, most of the literature focuses on an eccentric cage induction machine and the

forces and vibrations related to it. The unbalanced magnetic pull due to rotor eccentricity has also been a topic of investigation in the past [4-6]. The analytical models have been validated by experimental investigations.

However, very few publications regarding the study of the behavior of the torque in the case of an eccentric machine were found. The electromagnetic torque of an electrical machine is very important since it is used to convert the electrical power into mechanical power to the shaft of the machine. The torque in eccentric switched reluctance machines was studied in [7]. [8] presents a study on a similar problem in the same type of machine. A brief discussion about the difference in the torque behavior of a healthy machine and an eccentric machine can be found in [9]. An analytical study of a similar problem for an induction machine has been done in [10]. Some studies have also been done for the induction machine under mixed eccentricity, which is a case when the machine has both static and dynamic eccentricities simultaneously. For instance, [11] presents the analysis of stator current under mixed eccentricity and also explains the influence of the load variations on different harmonic components induced in the current spectrum due to the eccentricity. [12] employs the stator current spectrum for the diagnosis of the mixed rotor eccentricity and also presents the effect of mixed eccentricity on the time variation of the torque. [13] briefly compares the peak value of the instantneous torque in the torque of an induction motor for a healthy case and cases with static, dynamic and mixed eccentricities but the results presented are not comprehensive enough to have a concrete conclusion. In this paper, we comprehensively investigate the effect of the dynamic rotor eccentricity on the electromagnetic torque of a cage induction machine numerically, using finite element analysis. The analysis will be based on the average torque, time variation of the torque and the harmonic components in the torque waveform.

The torque calculation using the finite element method (FEM) is very common, especially while designing an electrical machine and a handful of publications can be found about computing the torque. There are methods based on the magnetic coenergy [14] and stored energy [15] but typically the Maxwell stress tensor method [16] and Coulomb's method based on the principle of virtual work [17] are used for the numerical computation of torque. However, these methods do not ensure an accurate torque estimate in the case of an eccentric machine. When the torque is integrated over the elements in the air gap of the machine, the radius of integration is important. Generally, the radius of integration is taken by considering the geometrical center point of the stator as the center, which, in the case of an eccentric machine, is not true. This has been explained figuratively in [18].

In this paper, the method of energy balance has been used to compute the torque. This method is found to be accurate and insensitive to the type of mesh used in the air gap of the machine. Recently, a study compared the energy balance method and Coulomb's virtual work method based on the type of discretization used in the air gap [19]. The average torque calculated from Coulomb's virtual work method is dependent on the density of the mesh and the shape of the elements. It has also been seen to be affected by the uniformity of the mesh. In the case of dynamic eccentricity, the finite element modeling of whirling makes the non-uniformity of the airgap inevitable in the air gap. Therefore, the use of energy balance method to compute the torque ensures a better accuracy.

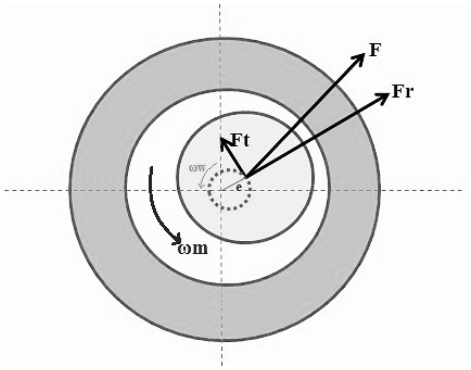

Fig. 1. Forces due to eccentricity. F_r and F_t are the radial and the tangential components of the force, respectively

2. Method of analysis

2.1 Time-stepping finite element method

The magnetic field in the cross section of the machine is calculated by using two-dimensional finite element analysis. The time-stepping method is based on the $\boldsymbol{A} - \Phi$ formulation where $\boldsymbol{A}$ is the magnetic vector potential and Φ is the reduced electric scalar potential. The Maxwell field equations in the quasi-static state together with the constitutive material equations lead to the following equation to be solved in the cross-sectional geometry of the machine.

$$\nabla \times (\upsilon \nabla \times \boldsymbol{A}) = -\sigma \left(\frac{\delta \boldsymbol{A}}{\delta t} - \nabla \Phi \right), \tag{1}$$

where: υ is the reluctivity and σ is the conductivity of the material. One period of the fundamental frequency is divided into 800 time steps and second order triangular elements are used for the study. The whole mesh has 4290 elements and 8677 nodes. Part of the mesh showing the air gap region is shown in Fig. 2. The magnetic field in the machine is assumed to be two-dimensional. The three dimensional end winding fields are modeled approximately by adding the end-winding impedances to the circuit equations of the windings. Trapezoidal rule is used for time integrations. The nonlinearity of the materials is taken into account by using a single valued magnetization curve. The details of the method have been presented in [20].

The movement of the rotor is taken into consideration by the moving-band technique. The center position of the rotor is forced to move along a circular path at a constant speed to model the dynamic eccentricity. In addition, the rotor was rotated at its mechanical angular speed around its geometrical center.

An analytical derivation predicts that the eccentric rotor motion induces two eccentricity harmonics in the air-gap flux density [1, 21]. When expressed in the stator frame of reference, they are:

$$B_{p+1} = \hat{B}_{p+1} \cos\left[(p+1)\phi - (\omega_s + \omega_w)t + \alpha_{p+1}\right],$$
$$B_{p-1} = \hat{B}_{p-1} \cos\left[(p-1)\phi - (\omega_s - \omega_w)t + \alpha_{p-1}\right], \tag{2}$$

where: $\hat{B}$ is the peak value of flux density, p is the number of pole pairs, ω_s is the supply frequency and ω_w is the whirling frequency. These eccentricity harmonics together with the fundamental flux density create an asymmetrical flux-density distribution which causes the forces that act on the rotor.

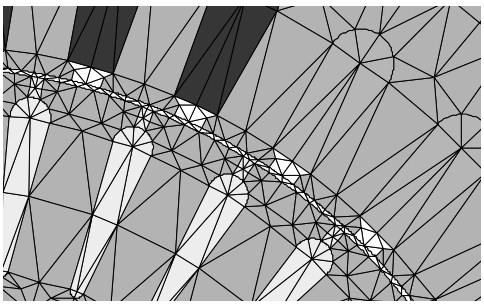

Fig. 2. Mesh used in the simulation

2.2 Energy balance method

The primary focus of this study is the torque and its harmonic components. In this paper, the torque is calculated by the method based on the energy balance of the machine. In this method, if the angular speed of the rotor is constant, the power balance of the machine can be integrated for a certain period of time to obtain the average torque over the time interval. The expression for the torque computed from this method is given by:

$$T^a = \frac{P^a_{\text{in}} - P^a_{\text{loss}} - \dfrac{\Delta W_t}{\Delta t} - P^a_{\text{whirl}}}{\omega^a_m}, \tag{3}$$

where: P_{in} is the input power, P_{loss} is the electromagnetic loss, W_f is the energy of the electromagnetic field, P_{whirl} is the power produced by the tangential component of the force and the velocity vector of whirling, ω_m is the mechanical angular speed of the rotor and the superscript ^{a} denotes the average value. The whirling power, P_{whirl}, gets either added to or subtracted from the system depending on the direction of the force. This power becomes significant under eccentricity operation and therefore it has to be taken into consideration when the power balance is used to calculate the force. But since the torque corresponding to this power is very small, we can neglect it in the present study.

In the present study, the stator winding has been modeled as a filamentary winding without eddy currents. The input power to the machine is calculated using the currents and the flux linkages of the stator phases

$$P_{\text{in}}^{\text{a}} = \frac{\Delta W_{\text{in}}}{\Delta t} = \frac{1}{\Delta t}\sum_{k=1}^{m}\int_{\Psi_{ki}}^{\Psi_{kf}} i_k \,\mathrm{d}\Psi_k \,, \tag{4}$$

where: i_k is the current of phase k, ψ_{ki} and ψ_{kf} are the flux linkages of phase k at the beginning and end of the period Δt, respectively. m is the number of phases.

P_{loss} is obtained as:

$$P_{\text{loss}}^{\text{a}} = \frac{\Delta W_{\text{loss}}}{\Delta t} = \frac{1}{\Delta t}\int_{V}\int_{t_0}^{t_0+\Delta t}\left(-E\cdot\frac{\partial \mathbf{A}}{\partial t}\right)\mathrm{d}t\,\mathrm{d}V \,, \tag{5}$$

$$= \frac{1}{\Delta t}\int_{V}\int_{t_0}^{t_0+\Delta t}\sigma\left(\frac{\partial \mathbf{A}}{\partial t} - \frac{u}{l}\mathbf{e}\right)\cdot\frac{\partial \mathbf{A}}{\partial t}\mathrm{d}t\,\mathrm{d}V \tag{6}$$

where: V is the volume of the solution region, E is the electric field strength, u is the electric scalar potential and l is the length of the machine. In the simulations, the core materials have been treated as non-conducting, and thus the core losses are not included in the present study.

The change in the magnetic field energy W_f over the period of time is calculated from the magnetization curves of the materials and flux densities B_0 and B_t at the beginning and the end of the period.

$$\Delta W_f = \int_{V}\int_{B_0}^{B_t} \boldsymbol{H}\cdot\mathrm{d}\boldsymbol{B}\,\mathrm{d}V \,. \tag{7}$$

If one is interested in the instantaneous torque, Δt in Eq. (4) can be equal to the length of one time step. For an average torque in the steady state of the machine, the time interval Δt should be chosen to be an integer multiple of the fundamental period of the machine. The time derivatives are approximated by first order difference ratios and the time integrals in Eqs (4-7) are summed up time-step by time-step. Over one time step, the input energy and the energy consumed by the resistive loss in the rotor cage are respectively,

$$\Delta W_{\text{in}} = \sum_{n=1}^{m}\left[\beta i_{n,k+1} + (1-\beta)i_{n,k}\right]\left(\Psi_{n,k+1}\Psi_{n,k}\right), \tag{8}$$

$$\Delta W_{rt} = \int_{V}\sigma\left\{\begin{bmatrix}\dfrac{\boldsymbol{A}_{k+1}-\boldsymbol{A}_k}{\Delta t}\\ \dfrac{-1}{l}\left[\beta u_{k+1} + (1-\beta)u_k\right]\boldsymbol{e}_z\end{bmatrix}\cdot\left(\boldsymbol{A}_{k+1}-\boldsymbol{A}_k\right)\right\}\mathrm{d}V \,. \tag{9}$$

where $\beta = 0.5$ for the trapezoidal rule.

3. Results and discussion

A 4-pole 15 kW cage induction machine, the parameters of which are given in Table 1, is used as a test machine in this study. The method of analysis for the calculation of the eccentricity forces has been validated earlier by modeling and measuring this machine [1]. A part of the geometrical cross-section of the machine along with the calculated magnetic flux density distribution is shown in Fig. 3. The eccentric rotor, displaced from its center position can be clearly seen from the figure. The force produced by the eccentricity is directed towards the shortest air gap. The magnetic flux density is also higher in that region, as can be seen from the figure.

Table 1. Parameters of the test machine

Parameter name	**Value**
Number of poles	4
Connection	Delta
Rated voltage [V]	380
Supply frequency	50
Rated current [A]	31
Rated power [kW]	15

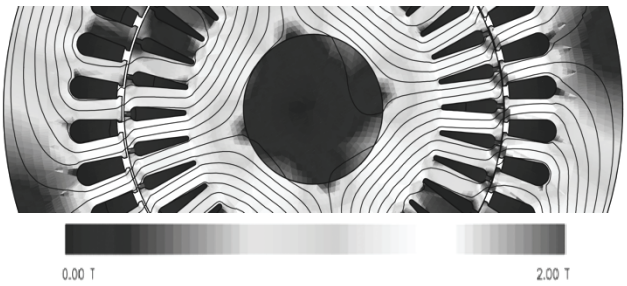

Fig. 3. Flux density distribution in the cross-section of an eccentric machine

Many simulations were performed by varying the whirling radius in each simulation. Initially the torque computed from the energy balance method is compared with that computed from the Coulomb's method for different types of mesh used in the air gap. For this purpose, the air gap of the machine was discretized with single, double and triple layers of elements. For a single layer mesh, both the torque computation and the movement of the rotor is done using the same band of elements. But for the double and triple layer mesh, the band of elements used for the torque computation and the movement of the rotor may be the same or different. In this way, altogether 14 different combinations of the number of layers, and the bands used for the torque computation and the rotor movement were used for comparison and the result is shown in Fig. 4. The eccentricity in this case was 33% and the machine was rotated at its rated speed. The average torque computed from Coulomb's method varies with

the variation in the type of mesh. However, the energy balance method gives an average torque almost independent from such variations. Therefore, the energy balance method seems more accurate and has been further used to compute the torque in this paper.

Fig. 5 shows the average torque of the machine as a function of the whirling radius. All the simulations were performed at the rated slip of the machine, which is 3.2%. It is clear from the results that an electrical machine under eccentricity does not exhibit the same torque as a healthy machine. The results show an increase in the torque of the machine with increasing eccentricity. The results at 0% relative eccentricity refer to a concentric healthy machine.

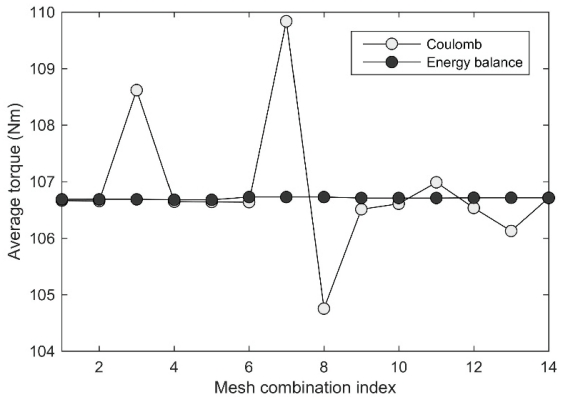

Fig. 4. Average torque calculated with different types of mesh in the air gap. Mesh index notation: *XYZ*, *X* = number of layers, *Y* = movement layer, and *Z* = torque computation layer;1 = 111, 2 = 211, 3 = 212, 4 = 221, 5 = 222, 6 = 311, 7 = 312, 8 = 313, 9 = 321, 10 = 322, 11 = 323, 12 = 331, 13 = 332, and 14 = 333

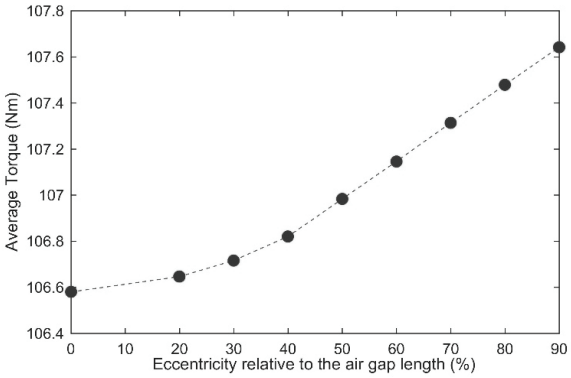

Fig. 5. Average torque as a function of the whirling radius

In addition to the average torque, the influence of the eccentricity on the harmonic contents in the torque is analyzed. The time variation of the torque is shown in Fig. 6. Since the energy balance method gives only the average torque over an interval of time, the time variation was obtained by using a period of integration equal to the time step size used in the simulations.

The time-axis of the figure has been zoomed-in to clearly see the time variation of the torque at different eccentricity levels. An increased distortion in the torque waveform with the increase in relative eccentricity can be witnessed from the figure.

The harmonic components of the torque are computed using fast Fourier transform (FFT). The harmonic distortions of the torque waveform for different relative eccentricities are shown in Table 2. Fig. 7 shows the frequency spectrum of the torque for a healthy machine and Fig. 8 shows the frequency spectrums of the torque for the machine with dynamic eccentricity. The figures show the frequency range of 200-2000 Hz because the harmonic components having considerably larger amplitude, other than the fundamental component are seen to occur in this frequency range. For a healthy machine, some of the largest torque components are found to be at 300 Hz and 1700 Hz. In the case of dynamic eccentricity, the 870 Hz component becomes significant and the behavior of this component is quite interesting as the results show a drastic increase in the amplitude of this component with the increase in the eccentricity. The 600 Hz component also shows similar behavior with the increase in eccentricity.

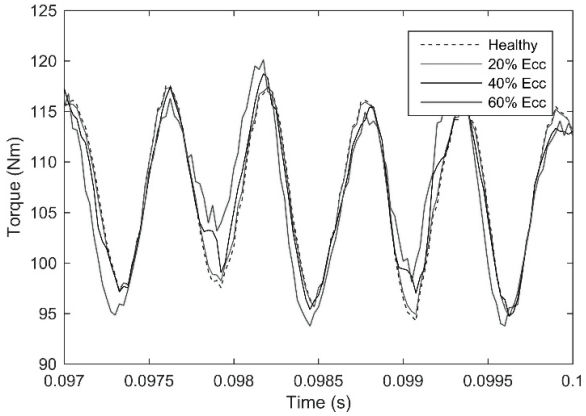

Fig. 6. Time variation of the torque at different eccentricity levels

Table 2. Harmonic distortion in torque

Relative eccentricity [%]	**Distortion [%]**
0	38.05
20	38.22
30	38.59
40	39.77
50	42.19
60	46.01
70	49.87
80	54.36
90	61.26

Among other larger harmonics, the 300 Hz component also shows a slight increase in the amplitude, but it is very small compared to the increase in the 870 Hz component. The higher order harmonic around 1700 Hz has a slightly reduced amplitude with increasing eccentricity.

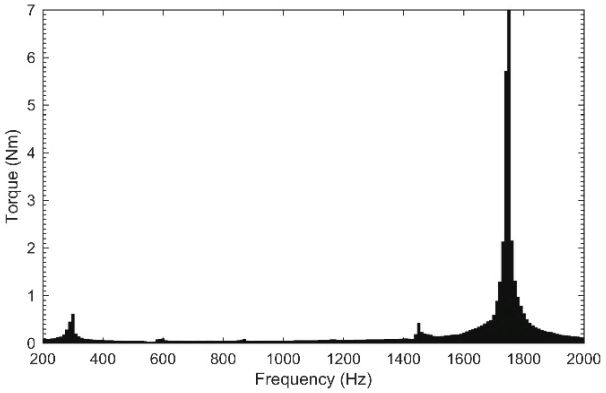

Fig. 7. Frequency spectrum of the torque for a healthy machine

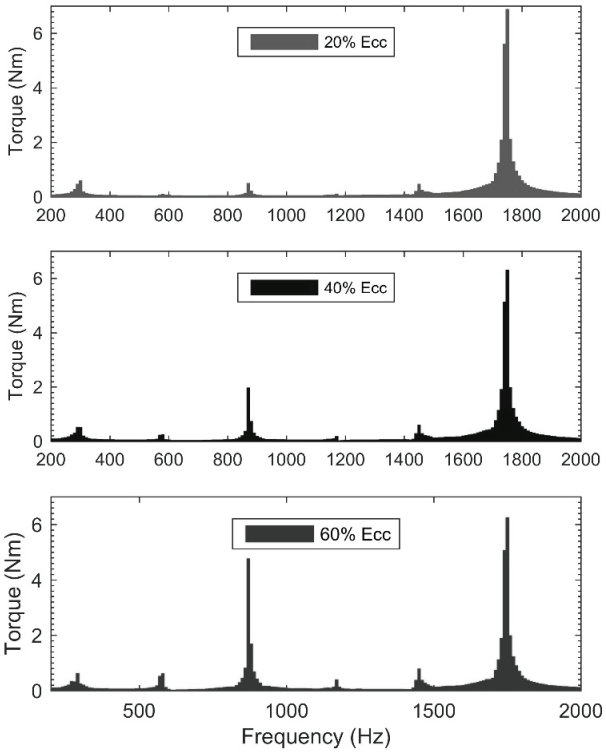

Fig. 8. Frequency spectrums of the torque in case of dynamic eccentricity

The origin of the harmonic components of the torque can be found in the harmonics of the stator current. Therefore, to investigate further, the harmonic components in the stator current are studied. Fig. 9 shows the waveform of the line currents in the stator windings, simulated at the rated load, for a healthy machine. The frequency spectrum of the line current i_a is shown in Fig. 10. The frequency of the principal slot harmonic (*PSH*) for the type of machine under study can be estimated from

$$PHS = f_s + k \times Q_r \times (1 - s) \times \frac{f_s}{p}, \tag{10}$$

where: f_s is the supply frequency, Q_r is the number of rotor slots, s is the slip, p is the number of pole pairs and k = 1, 2, 3, etc. At the rated slip, the *PSH* should occur around 872.8 Hz. For the *PSH* to be seen in the current spectrum, the pole pair number $Q_r \pm np$, where n is the harmonic order, should be equal to the pole pair number of the space harmonics produced by the stator winding [22]. The machine under study is a cage induction machine with the number of rotor slots (Q_r) = 34. In a healthy machine, this number of rotor slots does not give a *PSH* and therefore it does not appear in the current spectrum shown in Fig. 10. However, the rotor slot harmonics exist and can be seen around 1695.6 Hz.

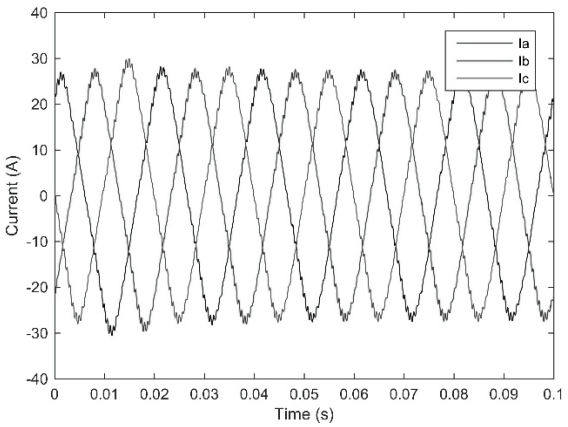

Fig. 9. Waveform for three-phase line currents, for a healthy machine

When the machine is under dynamic eccentricity, the harmonics corresponding to $nf_s \pm 2f_w$ appear in the spectrum, where n is the harmonic order in the supply and f_w is the whirling frequency. Although, the *PSH* does not appear in the healthy machine, $PSH \pm 2f_w$ components exist in the eccentric case, and it can be seen from Fig. 11 that these components show a significant increase in their amplitude with the increase in the eccentricity. This explains the drastic increase in the torque component around 870 Hz. However, the eccentricity harmonics corresponding to the second order PSH do not show much change in their amplitudes, the result of which is also seen in the spectrum of the torque shown in Fig. 8. Nonetheless, some other harmonics around 600 Hz are also slightly affected by the eccentricity, which is in turn also seen in the torque spectrum.

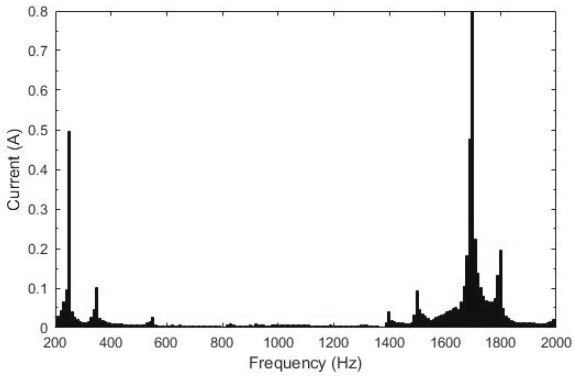

Fig. 10. Frequency spectrum of the stator line current i_a healthy machine

For additional assessment of the torque in the machine with dynamic eccentricity, the machine was simulated at a quarter load, half load and full load. Table 3 shows the average torques computed for each case. Fig. 12 shows the differences between the torques of an eccentric motor and a non-eccentric motor for each case of loading, with different values of eccentricity. The results show how the difference between the torques of a healthy machine and an eccentric machine increases with eccentricity in different loading conditions.

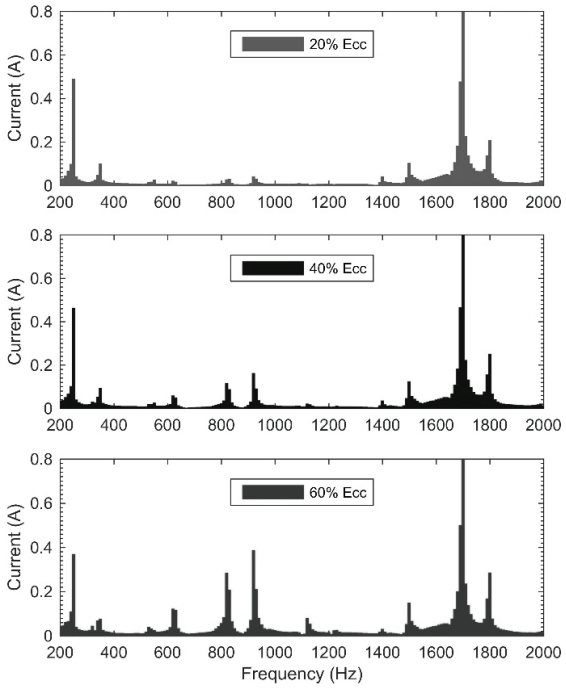

Fig. 11. Waveform for three-phase current in the stator winding, with dynamic eccentricity

Table 3. Average torque values for different loading cases with different values of eccentricity [Nm]

Eccentricity [%]	Quarter load	Half load	Full load
0	28.6606	56.1111	106.5773
20	28.7081	56.1860	106.6427
40	28.8341	56.4089	106.8095
60	29.0121	56.7683	107.1187
80	29.1843	57.2064	107.4045

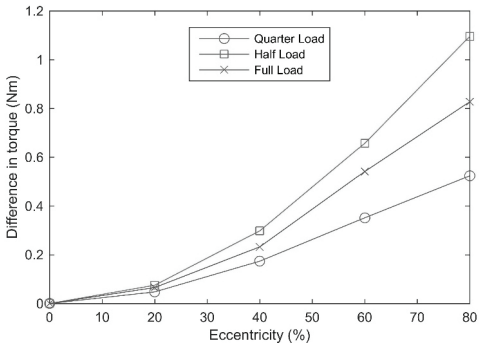

Fig. 12. Difference between the torque of an eccentric motor and a non-eccentric motor with different cases of loading

4. Comparison with measurements

A comparison between the simulated and the measured torque spectrums has been done for the case of static eccentricity. The measurement system consists of a 15 kW cage induction machine as a test machine, suspended with four horizontal arms connected to the frame of the machine in both the drive and the non-drive ends. The machine is equipped with active magnetic bearings used to create eccentricity and the whirling motion of the rotor. Four piezoelectric force sensors are placed vertically beneath the horizontal arms, which measure the vertical forces. The force sensors measure the dynamic force components only. The torque is extracted from the force. The harmonic components of the torque are obtained by performing an FFT for the torque signal. More details about the measurement set-up and the measurement process can be found in [23].

Fig. 13 shows the measured spectrum of the torque together with those obtained from the simulations. A locked rotor condition with a sinusoidal supply of 25 V was used both in the measurement and simulations. Fig. 13(a) shows a comparison for a healthy case and Fig. 13(b) shows that for 22% and 33% static eccentricity. The additional harmonics introduced in the eccentric case can be clearly observed from the figure. However, the simulation does not seem to yield similar results. This could possibly be for the reason that at 25 V, the machine is still linear in the simulations. Using higher voltage in the simulation yields the harmonics which are not visible for 25 V. This has also been explained in [23].

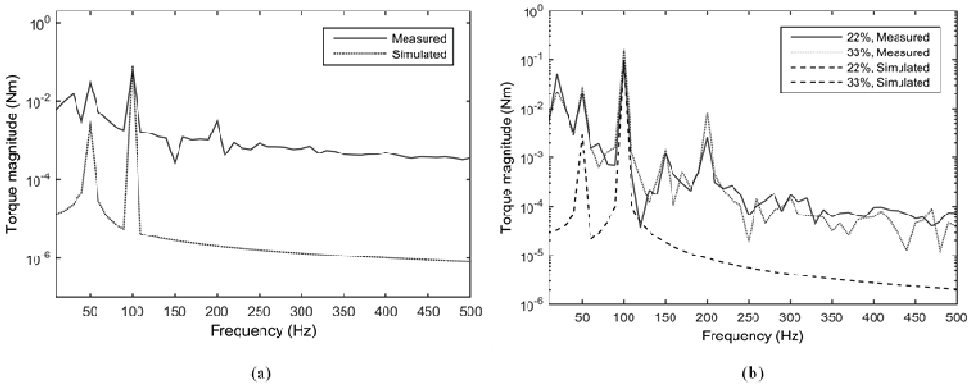

Fig. 13. Comparison between simulation and measurement: (a) healthy case; (b) static eccentricity case

5. Conclusion

The torque of a cage induction machine with a dynamic eccentric rotor has been studied. The finite element analysis is used for the study. Initial comparison between the Coulomb's virtual work method and the energy balance method showed the energy balance method to be more accurate, especially when the meshing in the air gap is considered. The investigation of torque revealed that the torque of an eccentric motor is relatively larger compared to the normal healthy machine. The torque harmonics were also investigated and the harmonic component with frequency close to the *PSH* was found to have significant increase with the increasing eccentricity. Other larger harmonics were slightly affected. The additional torque might play an important role to induce torsional vibrations in the case when two machines are coupled and one of them becomes eccentric due to some practical problem, for instance, bearing breakdown or misalignment. The knowledge of the behavior of the harmonic components can also be applied for the detection of faults related to the eccentricity. To validate the simulations, the torque spectrums of the machine with static eccentricity obtained from both measurements and simulations were compared. The additional harmonics due to the static eccentricity were observed in the measurements.

References

[1] Arkkio A., Antila M., Pokki K., Simon A., Lantto E., *Electromagnetic force on a whirling cage rotor*, IEE Proceedings on Electric Power Applications, vol. 147, n. 5, pp. 353-360 (2000).

[2] Tenhunen A., Benedetti T., Holopainen T.P., Arkkio A., *Electromagnetic forces in cage induction motors with rotor eccentricity*, International Electric Machines and Drives Conference 2003, vol. 3, pp. 1616-1622 (2003).

[3] Arkkio A., Nepal B.R., Sinervo A., *Electromechanical interaction in a synchronous reluctance machine*, SPEEDAM 2010, pp. 501-506 (2010).

[4] Dorrell D.G., Smith A.C., *Calculation of UMP in induction motors with series or parallel winding connections*, IEEE Transactions on Energy Conversion, vol. 9, no. 2, pp. 304-310 (1994).

[5] Smith A.C., Dorrell D.G., *Calculation and measurement of unbalanced magnetic pull in cage induction motors with eccentric rotors, I. Analytical model*, IEE Proceedings on Electric Power Applications, vol. 143, no. 3, pp.193-201 (1996).
[6] Dorrell D.G., Smith A.C., *Calculation and measurement of unbalanced magnetic pull in cage induction motors with eccentric rotors. II. Experimental investigation*, IEE Proceedings on Electric Power Applications, vol. 143, no. 3, pp. 202-210 (1996).
[7] Dorrell D.G., Chindurza I., Cossar C., *Effects of rotor eccentricity on torque in switched reluctance Machines*, IEEE Transactions on Magnetics, vol.41, no. 10, pp. 3961-3963 (2005).
[8] Sheth N.K., Rajagopal K.R., *Effects of nonuniform airgap on the torque characteristics of a switched reluctance motor*, IEEE Transactions on Magnetics, vol. 40, no. 4, pp. 2032-2034 (2004).
[9] Belahcen A., Arkkio A., *Computation of additional losses due to rotor eccentricity in electrical machines*, IEE Proceedings on Electric Power Applications, vol. 4, no. 4, pp. 259-266 (2009).
[10] Dorrell D.G., *The influence of rotor eccentricity on the output torque of cage induction motors*, International Conference on Electrical Machines, Paris, vol. 1, pp. 35-40 (1994).
[11] Faiz J., Ebrahimi B.M., Akin B., Toliyat H.A., *Dynamic analysis of mixed eccentricity signatures at various operating points and scrutiny of related indices for induction motors*, IET Proceedings on Electric Power Applications, vol. 4, no. 1, pp. 1-16 (2010).
[12] Faiz J., Ebrahimi B.M., Akin B., Toliyat H.A., *Finite-Element Transient Analysis of Induction Motors Under Mixed Eccentricity Fault*, IEEE Transactions on Magnetics, vol. 44, no. 1, pp. 66-74 (2008).
[13] Polat A., Ertuğrul Y.D., Ergene L.T., *Static, dynamic and mixed eccentricity of induction motor*, IEEE 10th International Symposium on Diagnostics for Electrical Machines, Power Electronics and Drives (SDEMPED), pp. 284-288 (2015).
[14] Sadowski N., Lefevre Y., Lajoie-Mazenc M., Cros, J., *Finite element torque calculation in electrical machines while considering the movement*, IEEE Transactions on Magnetics, vol. 28, no. 2, pp. 1410-1413 (1992).
[15] Marinescu M., Marinescu N., *Numerical computation of torques in permanent magnet motors by Maxwell stresses and energy method*, IEEE Transactions on Magnetics, vol. 24, no. 1, pp. 463-466 (1988).
[16] Reichert K., Freundl H., Vogt W., *The calculation of forces and torques within numerical magnetic field calculation methods*, Proceedings of COMPUMAG. Oxford, 31 March – 2 April 1976, Rutherford Laboratory, pp. 64-73 (1976).
[17] Coulomb J.L., *A methodology for the determination of global electromechanical quantities from a finite element analysis and its application to the evaluation of magnetic forces, torques and stiffness*, IEEE Transactions on Magnetics, vol. 19, no. 6, pp. 2514-2519 (1983).
[18] Silwal B., Rasilo P., Perkkiö L., Hannukainen A., Eirola T., Arkkio A., *Numerical analysis of the power balance of an electrical machine with rotor eccentricity*, IEEE Transactions on Magnetics, vol. 52, no. 3, pp. 1-4 (2016).
[19] Silwal B., Rasilo P., Perkkiö L., Oksman M., Hannukainen A., Eirola T., Arkkio A., *Computation of torque of an electrical machine with different types of finite element mesh in the air gap*, IEEE Transactions on Magnetics, vol. 1, no. 6, pp. 1-9 (2014).
[20] Arkkio A., *Analysis of induction motors based on the numerical solution of the magnetic field and circuit equations*, Acta Polytechnica Scandinavica (1987).
[21] Früchtenicht J., Jordan H., Seinsch H.O., *Exzentnzitätsfelder als ursache von laufinstablilitäten bei asynchron-machinen. Parts 1 and 2*, Archiv für Electrotechnik (in German), vol. 65, pp. 271-292 (1982).
[22] Nandi S., Bharadwaj R.M., Toliyat H.A., Parlos A.G., *Performance analysis of a three phase induction motor under mixed eccentricity condition*, IEEE Transactions on Energy Conversion, vol. 17, no. 3, pp. 392-399 (2002).
[23] Silwal B., Rasilo P., Haavisto A., Belahcen A., Arkkio A., *Measurement of torque harmonics of a cage induction machine under rotor eccentricity*, In Proceedings of International Conference on Electrical Machines and Systems, Pattaya, pp. 98-102 (2015).

ARCHIVES OF ELECTRICAL ENGINEERING VOL. 66(2), pp. 397-408 (2017)

DOI 10.1515/aee-2017-0030

The model of double-cage induction motor for the analysis of thermal fields in transient operations

JAN MRÓZ

Rzeszow University of Technology
janmroz@prz.edu.pl

(Received: 28.09.2016, revised: 11.02.2017)

Abstract: Emergency motor switch-on happens occasionally while operating a double-squirrel-cage motor at full supply voltage with the rotor blocked (e.g., in coal mills). After releasing the blockage, the by now heated motor is started up again. However, the mechanical stress caused by the increased temperature poses considerable hazards to the squirrel-cage winding. This paper presents a double-cage induction motor model for analysis of thermal fields in transient operation. The thermal field for the rotor of a double-squirrel-cage motor of soldered or cast structure, operating in the conditions described, has been calculated in the present paper using a thermal network method. Measurement results have been presented for the double-squirrel-cage winding temperature for a soldered cage construction in the blocked rotor state.

Key words: AC motors, heating, induction motors, squirrel cage motors, temperature rise

1. Introduction

As stated in prior research [l, 2], while starting up the deep-bar and double-squirrel-cage motors with soldered rotors, the squirrel-cage winding is the component most vulnerable to damage. The method of starting motors through an immediate connection to the rated supply voltage is widely used; however, the risk to the squirrel-cage, resulting from thermal and electro-dynamical action of starting currents, is greatest here. Such phenomena become of extreme importance during the prolonged start-up. Fig. 1 presents a damaged squirrel-cage winding in the end region of the starting cage in a medium-power squirrel-cage motor.

Thermal problems while starting up squirrel-cage motors are referenced in a relatively large number of studies; however, in most cases, the reference is made to deep-bar motors started up with either an immediate connection to a full supply voltage [1] or with a blocked rotor [3]. The heat issues surrounding double-squirrel-cage motors operating in such conditions are represented only in a small number of publications [4]. This paper presents a double-cage motor model with a cast structure rotor and a soldered cage to analyse the thermal field of the rotor in selected, severe operating conditions. Cases in which the motor can be switched on with blocked rotor (mill motor) have been investigated. In such cases, the motor operates

for several seconds and is switched off. After releasing the blockage, the motor is started up again.

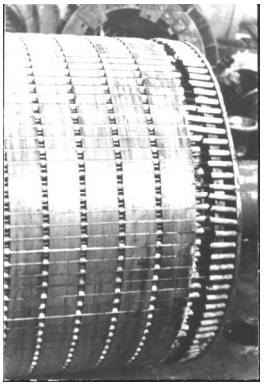

Fig. 1. Damaged end region of the starting cage in a medium-power squirrel-cage motor

2. Calculating the thermal field of a double-squirrel-cage rotor

The studied operating states of a double-squirrel-cage-motor are accompanied by considerable variations in the motor thermal field. To analyse such variations, the algorithm presented in Fig. 2 has been adapted.

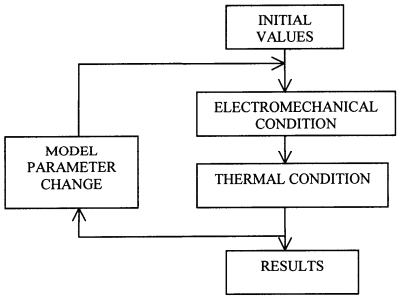

Fig. 2. Algorithm for calculating the rotor thermal field

Once the initial temperature values have been assigned, the electromechanical condition is calculated. As the aperiodic components of the starting current – because of its short persistence compared to that of a prolonged start up – have minor influence on the winding temperature, their actions can be neglected [2]. Moreover, they have little influence on the starting time, as positive oscillations, present at the beginning of the start up, reduce its duration, whereas negative ones prolong it. Consequently, the starting time is almost the same as that calculated from torque static characteristics. Furthermore, it is assumed that the start up takes place in a quasi-static manner, which allows the utilisation of speed sequences and rms current values in winding for calculating the static torque load characteristics and temperature. In each

stage of calculations, the change (including the temperature) of resistances present in the equivalent motor circuit diagram is taken into consideration.

By determining the motor thermal field in the first step, it becomes possible to change the model parameters, including resistance (effect of the temperature) and reactance (effect of the saturation) of the motor. The software I have designed additionally allows to carry out calculations that take into account changes of bar dimensions (affecting the slot clearance) and changes of material constants due to changes of temperature. The changing slot clearance influences the heat exchange conditions. This option was not used for calculations presented in this paper.

Changing the model parameters is required to initiate the next calculation stage, which is accomplished by repeating the step previously described. In this way, the relationship is considered between the transient electromechanical condition and the transient thermal condition with the accuracy of a single time step. The calculations are completed when the condition defining selected electromechanical state is met (such as the end of start up or when constant speed has been reached).

Prior research [2] has proven that for start up states, the heating of stator components can be examined regardless of the rotor heating because even in prolonged start up conditions, the heat exchange between the rotor and the stator, the body shape, and the ventilating system are of minor importance. Therefore, no heat exchange between stator and rotor is assumed. However, the heat from both rotor and stator surface is transferred to cooling air. Fig. 3 shows the related heat transfer coefficients α. Due to the symmetry of construction and load distribution in the double-squirrel-cage motor, the analysed area has been confined in the peripheral direction, as far as the middle of the rotor slot pitch to half of the rotor length. In the radial direction, the analysed area extends from the inner surface of the rotor yoke to the external surface of the rotor pack. Fig. 3 presents part of the double-squirrel-cage rotor with separate end rings of soldered construction (on the left) and a cast cage (on the right).

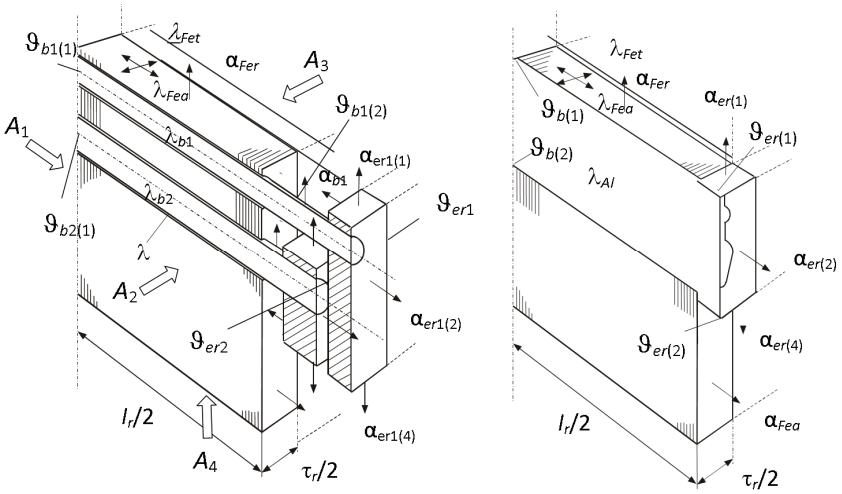

Fig. 3. Diagram of the double-squirrel-cage rotor with separate end rings (on the left), a cast cage (on the right)

For the cast cage, the end rings come in immediate contact with the rotor core. The symbol α with subscripts denotes the heat transfer coefficient of individual components. The symbol λ with respective subscripts is used to denote coefficients of thermal conductivity of respective rotor parts. The symbol l_r denotes the length of the rotor core. The symbol τ_r denotes the rotor slot pitch.

To calculate the thermal field of the motor, the thermal network method, created by means of the control volume method, has been utilised [5]. This method involves the division of the object examined into components of any shapes (determined control volumes) and drawing up energy balances for them, which allows the study of heat exchange issues in the areas with complex shapes. It is assumed that the heat capacity of a component focuses on a single node that lies in the component centre of gravity. The fulfilment of the energy balances in separated control volumes allows us to determine, with great accuracy, the temperature distribution and the heat flux density. This method provides obvious physical interpretations, and it involves a larger number of equations than the boundary elements method. However, the matrix is banded and symmetric, which considerably simplifies the solution.

The equation of transient heat conductivity in the area containing inner sources of heat of volume density q_V is as follows [5]:

$$c\rho\frac{\partial\vartheta}{\partial t} = -\mathrm{div}\mathbf{q} + q_V\,, \tag{1}$$

where: c is the specific heat, $\mathbf{q}$ is the heat flux density vector, ϑ is the temperature, and ρ is the density. The heat does not flow through planes A_1, A_2, and A_3 (Fig. 3), as they are symmetry planes. The boundary condition of the second type is present:

$$\lambda\frac{\partial\vartheta}{\partial \mathrm{n}} = q_A = 0\,, \tag{2}$$

where: q_A is the surface density of the heat flux and λ is the coefficient of thermal conductivity.

In the inner surface of the rotor yoke (plane A_4 in Fig. 3), which is considerably distant from the essential heat sources, the constant temperature has been assumed and the boundary condition of the first type is present:

$$\vartheta = \vartheta_a\,, \tag{3}$$

where: ϑ_a is the ambient temperature.

From other surfaces, the heat is transferred with heat transfer coefficients α in Fig. 3, where the boundary condition of the third type occurs:

$$\lambda\frac{\partial\vartheta}{\partial \mathrm{n}} = \alpha(\vartheta_A - \vartheta)\,, \tag{4}$$

where: ϑ_A is the fluid temperature. Having integrated Eq. (1) for volume V_i, based on the Green-Gauss-Ostrogradski theorem for a single element, the following is obtained:

$$\int_{V_i} c\rho \frac{\partial \vartheta}{\partial t} \mathrm{d}V = -\int_{A_i} \boldsymbol{n} \cdot \boldsymbol{q} \mathrm{d}A + \int_{V_i} q_V \mathrm{d}V \,, \tag{5}$$

where: $\boldsymbol{n}$ is the vector normal to area A.

Individual terms of Eq. (5) can be presented as follows:

$$\int_{V_i} c\rho \frac{\partial \vartheta}{\partial t} \mathrm{d}V \approx V_i \rho_i c_i \frac{\mathrm{d}\vartheta_i}{\mathrm{d}t} \,, \tag{6}$$

$$-\int_{A_i} \boldsymbol{n} \cdot \boldsymbol{q} \mathrm{d}A = \sum_j Q_{ji} + Q_{Ai} \,, \tag{7}$$

$$\int_{V_i} q_V \mathrm{d}V = V_i q_{Vi} \,, \tag{8}$$

where: Q_{Ai} is the heat flux flowing to the node i from the external surface and Q_{ji} is the heat flux flowing from node j to node i. Bear in mind in Eq. (7):

$$Q_{ji} = \frac{1}{R_{thij}} (\vartheta_j - \vartheta_i) \,, \tag{9}$$

$$Q_{Ai} = \frac{1}{R_{thAi}} (\vartheta_{Ai} - \vartheta_i) \,, \tag{10}$$

and for any element i, the energy balance can be expressed in the following form:

$$\sum_j \frac{1}{R_{thij}} \vartheta_j + \frac{1}{R_{thAi}} \vartheta_{Ai} - \left(\frac{1}{R_{thAi}} + \sum_j \frac{1}{R_{thij}} \right) \vartheta_i + V_i \, q_{Vi} = V_i \, c_i \, \rho_i \frac{\mathrm{d}\vartheta_i}{\mathrm{d}t} \,, \tag{11}$$

where: $i = 1, 2, \ldots n_n$, n_n is the number of elements in which the area in question was divided, R_{thAi} is the thermal resistance from the heat transferred from the external surface of the element i, and R_{thij} is the thermal resistance for heat flowing from the node j to the node i. The summation in Eq. (11) is carried out for all j that are neighbouring element i. For the boundary condition of the first type, ϑ_{Ai} is the known boundary temperature of element i. For the boundary condition of the third type, ϑ_{Ai} is the temperature of the fluid beside element i.

The general form of the dependence that allows calculation of the thermal resistance values results directly from the heat conductivity Fourier law:

$$R_{thij} = \int_{x_i}^{x_j} \frac{\mathrm{d}x}{\lambda_{ij}(x) A(x)} \,, \tag{12}$$

where: x_i, x_j are the coordinates of the nodes i, j, respectively, and $A(x)$ is the surface area perpendicular to the integration path, along the line which joins the nodes.

Thermal resistance is related to heat transfer and can be obtained from the dependence:

$$R_{thAi} = \frac{1}{\alpha_i A_i}, \tag{13}$$

where: α_i is the heat transfer coefficient and A_i is the surface area of element i.

The resulting system of ordinary differential equations shown in Eq. (11) describes the transient thermal field in the area in question. For the zero boundary condition of the second type $R_{thAi} \to \infty$.

Within the rotor core, the volume density of heat sources is the quotient of the iron loss P_{Fer} and its volume V_{Fer}:

$$q_{VFei} = \frac{P_{Fer}}{V_{Fer}}, \tag{14}$$

Within the bar and ring area of the soldered squirrel cages the volume density of heat sources is:

$$q_{Vi} = J_i^2 \rho_{Ri}, \tag{15}$$

where: J_i is the current density in the element i and ρ_{Ri} is the resistivity of the material of element i. For the relatively large width end rings located far from the core, it can be assumed that the current density is of uniform nature, or if otherwise, the density distribution in ring section should be taken into consideration. By assuming uniform density, underrated temperature values are obtained in some areas of the end ring.

Concerning the motor with a cast squirrel-cage, the rotor impedance and current density distribution can be calculated with the conductor element method [6]. The method assumes that the bar fitted into the slot is composed of insulated conductors, the sections of which are matched to individual sections of the slot that are then joined together outside the core. The current displacement effect is neglected separately in each conductor. Fig. 4 shows the division of the rotor bar into pa modules. The equivalent circuit of the k module is presented in Fig. 5.

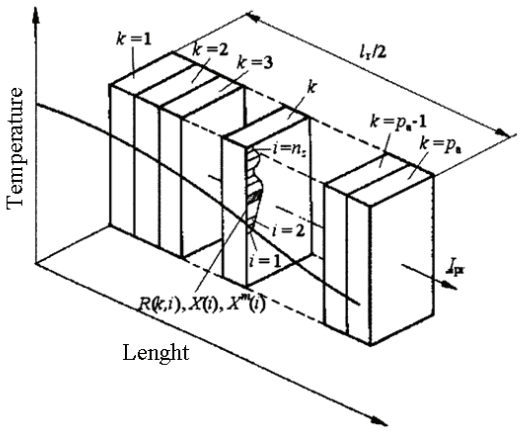

Fig. 4. Modules in the rotor bar

By connecting the circuits (obtained for each of the p_a modules) in series from Fig. 5, the equivalent circuit diagram for the entire bar is obtained, which is included in the whole equivalent circuit of the motor. Calculating the currents based on the equivalent diagram is done according to the algorithm presented in [6].

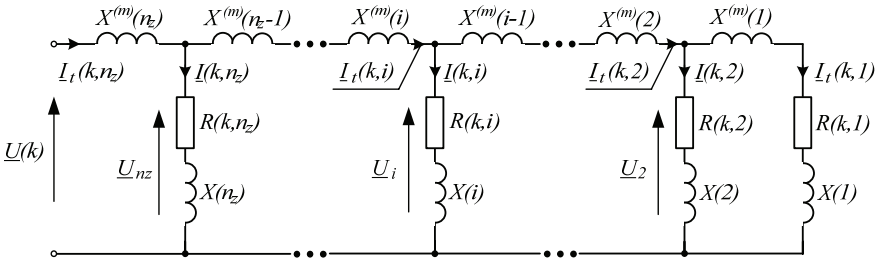

Fig. 5. Equivalent circuit of module k

The distribution of current density upwards in the bar in each module will be different because of the expected temperature changes along the motor axis, as shown in Fig. 4. The current density in component i of module k is expressed in the dependence:

$$J(k,i)=\frac{6\,I(k,i)\,N_s\,k_{ws}}{A_i\,Q_r\,k_{sq}}, \tag{16}$$

where: $I(k, i)$ is the rms current $I(k, i)$ (Fig. 5), $k_{s\,q}$ is the skew factor, $k_{w\,s}$ is the stator winding coefficient, Q_r is the number of rotor slots, and N_s is the number of serial coils in stator phase winding. Hence the volume density of heat sources in component i of module k can be written as:

$$q_{Vi}=J^2(k,i)\rho_R\left[1+\alpha_{thR}\,\Delta\vartheta(k,i)\right], \tag{17}$$

where: $\Delta\vartheta(k,i)$ is the temperature increase of element i in module k above the ambient temperature, α_{thR} is the temperature coefficient of resistance increase, ρ_R is the resistivity of the material in ambient temperature.

Homogenous current density in the end ring is given as:

$$J_{\mathrm{er}}=\frac{6\,I_t(1,n_z)\,N_s\,k_{ws}}{2\,A_{er}\,Q_r\,k_{sq}\sin\dfrac{\pi\,p}{Q_r}}, \tag{18}$$

where: $I_t(1,n_z)$ is the rms total bar current $\underline{I}_t(1,n_z)$, $A_{e\,r}$ is the surface area of the end ring, p is the pole number. It is also assumed that the resistance change of individual ring components has no effect on the distribution of current density within the end ring. Good adhesion of cast bars to the sheet pack causes the cross-currents to occur, which are then contained in the pack, leading to the reduction of the ring current. That effect was not taken into consideration.

3. Measurement and calculation results

Calculations of motor heating are done on the following sequence: switch on with the rotor blocked – switch off to cool down – start up. The calculations were performed using programs created by the author by means of Matlab software.

The calculations were performed on both a double-cage motor type SZDC196Ex with 320 kW, 6000 V, and $p = 3$ with a soldered squirrel-cage and on a cast cage type SCgx280M4 with 200 kW, 380 V, and $p = 2$. The measurements and calculations of the cage winding temperature supplied with a blocked rotor have been taken for the motor type SGR315M4 with 200 kW, 1000 V, and a rated speed of 1479 r/min, with a soldered cage. Table 1 shows the chosen parameters of the examined motors.

Table 1. Chosen parameters of the motors

Parameter	SZDC196Ex (Motor A)	SCgx280M4 (Motor B)	SCR315M4 (Motor C)
Rated power, kW	320	200	200
Rated voltage, V	6000	380	1000
Rated frequency, Hz	50	50	50
Pole pair number	3	2	2
Air gap, mm	1.6	0.9	1.2
Stator diameter, m	0.888/0.600	0.470/0.308	0.520/0.334
Rotor diameter, m	0.597/0.369	0.306/0.105	0.3316/0.130
Core length, m	0.56	0.31	0.35
Number of stator/rotor slots	72/58	48/38	48/38
Class of insulation	F	F	F
Ratio of coil span to pole pitch	10/12	10/12	10/12
Number of stator-winding turns per coil	240	44	56
Stator-winding resistance, Ω	0.6479	0.0307	0.0369

The duration of blocked rotor mode has been selected so that the maximum admissible cage temperature can be reached. The non-voltage interval has been selected to allow cooling of the hottest component of the cage to one third of the maximum admissible temperature. For squirrel cages with bars, the admissible temperature is approx. 350°C and 250°C for the cast cage [2]. After cooling, the motor was started up. It has been assumed that during the entire start up phase, the motor is subjected to constant torque that equals the maximum rated torque of the motor. The moment of inertia in both cases is selected to prevent thermal risks to the squirrel-cage. Fig. 6 presents the temperature changes calculated in selected locations (according to Fig. 3) of the motor (Motor B) with a cast cage, in the analysed operating mode. In Fig. 7, these form soldered cages (Motor A) are presented. Fig. 8 shows the thermal field in the slot axis of the motor with a cast cage (Motor B) in the all phases of the process calculated, i.e., operating mode with a blocked rotor, the non-voltage interval and the start up of the heated motor. The temperature of the starting cage of the motor with a soldered squirrel-cage (Motor A) varies as shown in Fig. 9.

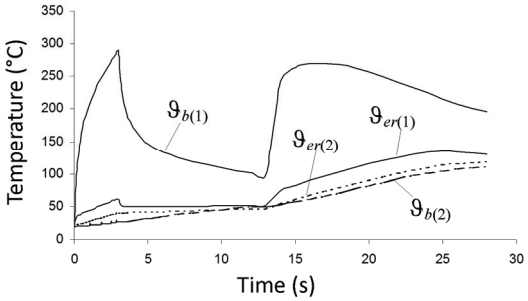

Fig. 6. Temperature changes in individual locations of the cast cage during motor blockage (3 s), non-voltage interval (10 s), and start up (15 s) (marking as in Fig. 3)

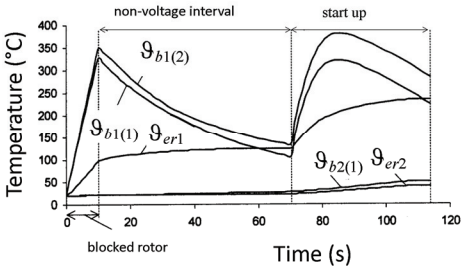

Fig. 7. Temperature changes in individual locations of the soldered cage during motor A blockage (10 s), non-voltage interval (60 s), and start up (45 s) (marking as in Fig. 3)

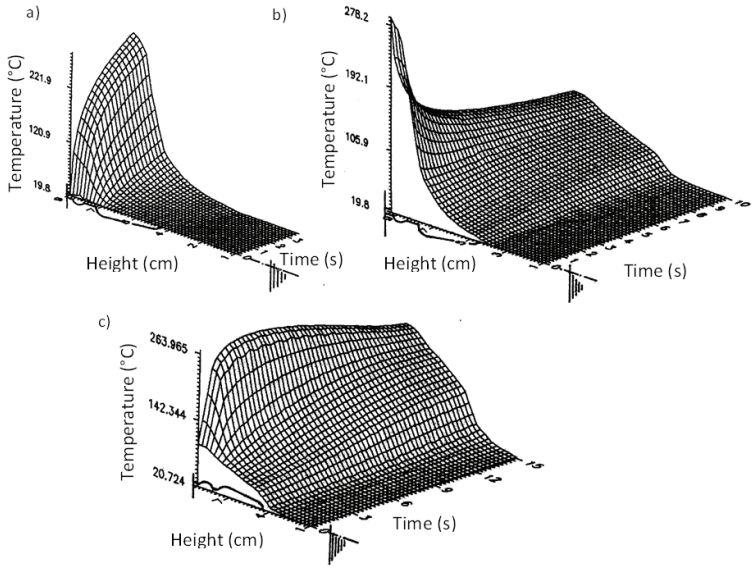

Fig. 8. Temperature changes in the slot axis in the motor with a cast cage (Motor B): a) while powered on with a blocked rotor; b) during cool down phase; c) during the start up phase

In the case of the motor with a bar cage (Motor A), the relationship between the times with a blocked rotor until the non-voltage interval, and until the start up (taking into consideration the above assumptions) is 10 : 60 : 40 (Fig. 7). For the motor with a cast cage (Motor B), the relation is 3 : 10 : 15 (Fig. 6). It can be concluded that the motor with the cast cage is less

resistant to operating with a blocked rotor than the one with the bar cage. Accelerated heating of the cast cage in the top of the slot is a result of the strong current displacement. One should note that the lower winding parts in the slot reach considerably lower temperatures (Fig. 6).

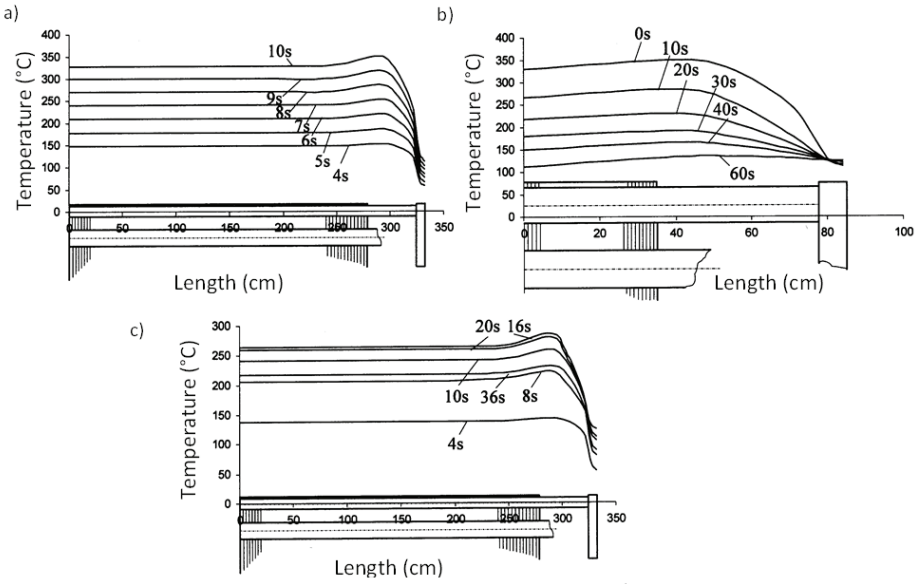

Fig. 9. Temperature distribution in the starting cage bar (Motor A): a) with power on with a blocked rotor; b) during cool down phase; c) during motor A start up

The time relations presented indicate that very hot parts of the cast cage cool down very quickly compared to the bar cage. Giving up the heat from the starting bars of the soldered cage to the rotor pack is difficult (slot clearance) and takes place mainly in the axial direction (towards the end rings), proven by the increase in the ring temperature ϑ_{er1} during the non-voltage interval (Fig. 7). The heat from the hottest parts of the cast cage is additionally given up towards the slot bottom, and the temperature of components located there increases during the non-voltage interval (Fig. 6 and Fig. 8). The heated motor with the bar cage is capable of performing considerably longer start ups than that of the one with the cast cage. When the temperature of the hottest cage components in the operating mode in question reaches its limiting value, the temperature of the stator winding is far below the upper limit [2].

The measurements of cage winding temperature have been taken for the motor type SGR315M4 with a soldered cage (Motor C) with a rated power of 200 kW, supply voltage of 1000 V, with the rotor blocked. The ambient temperature during measurements was $\vartheta_a = 30.5°C$, and the temperature inside the motor as read from thermocouples was $\vartheta_0 = 27°C$. The temperatures for the starting cage bar, the end region ($\vartheta_{b1(2)}$ in Fig. 3), and the end ring (ϑ_{er1} in Fig. 3) were recorded while the motor was supplied with 968 V for 5 s.

Fig. 10 presents the measured and calculated temperature changes in the starting cage bar and ring in points $\vartheta_{b1(2)}$ and ϑ_{er1} marked in Fig. 3 and in analogous points placed in the neighbouring slot pitch.

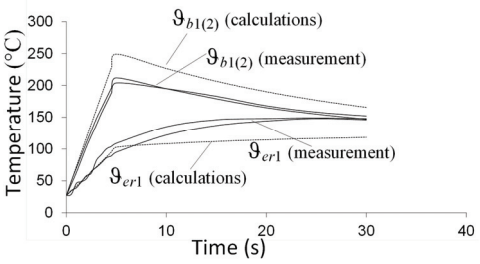

Fig. 10. Measured and calculated temperature changes in the starting cage bar (Motor C – see Table 1)

From the results presented in Fig. 10 it can be concluded that the differences between the calculated and measured values do not exceed 17%. Several basic sources of such differences can be identified: inaccuracies resulting from thermocouples inertia and calibration of recording equipment, errors in determining the model parameters (heat transfer coefficients, slot clearance, etc.), inaccuracies in calculation sources of loos, asymmetry of rotor currents resulting from differences in positioning of the rotor slots in relation to the stator, and uneven adhesion of individual bars to slot walls.

4. Conclusions

The need to operate motors with a blocked rotor emerges occasionally (e.g., when the mechanical coal miner or coal mill is fully charged). Prolonged start ups resulting from large inertia pose serious risks to motor performance. Winding overheating and the occurrence of mechanical stress, resulting from increased temperature as a result of prolonged start up, also poses serious risk to the motor squirrel-cage. In the operating conditions referred to herein, the electromagnetic, thermal, and mechanical states are correlated.

Determining thermal fields in the winding of a double-squirrel-cage rotor is of great importance in those states because this is when there is a risk of shortening the life of the cage winding, as the stator temperature does not exceed the maximum values [2]. By using the double-squirrel-cage soldered winding, large values of starting torques are achieved; this is, however, at the cost of non-uniform heating of the cage, along with the tendency of the cage bars to overheat. Compared to a motor with a soldered cage, a motor with a cast cage is less resistant to operation with a blocked rotor or prolonged start up. However, the faster cooling of the winding compared to the bar cage is an advantage while operating the motor with frequent shorter start ups.

Carrying out experimental research on high-power motors involves a range of logistic operations as it usually has to be carried out in industrial conditions. It generates a high cost, which explains why a relatively small number of publications is currently being devoted to

experimental research on heating problems in high-power squirrel cage induction motors [7-10]. This type of research is generally limited to steady-state operations.

The model can also be used by the motor user to establish the maximum admissible start up time, the operating time with blocked rotor, the length of the interval between the subsequent start ups, and the admissible number of start ups, as numerous systems protecting the motor from faulty start up require estimation of such settings.

The theoretical solutions presented herein have been verified only partially by the measurements described. The results obtained indicate that there is a particular need to examine the observed effects related to double-squirrel-cage motors. Thermal aspects of difficult start ups are of primary importance in terms of drive reliability because, regardless of the chosen start up method, unfavourable deformations occur to the heated cage components, which are then accompanied by detrimental mechanical stress. Due to this fact the design of a double squirrel cage induction motor is still being perfected [11].

References

[1] Chan C.C., Yan L., Chen P., Wang Z., Chau K.T., *Analysis of electromagnetic and thermal fields for induction motors during starting*, IEEE Transactions on Energy Conversion, vol. 9, no. 1, pp. 53-60 (1994).

[2] Mróz J., *The analysis of coupled electromechanical and thermal problems in transient states of double-cage induction motor*, Oficyna Wydawnicza Politechniki Rzeszowskiej (in Polish), Rzeszów (2013).

[3] Feyzi M.R., Parker A.M., *Heating in deep-bar rotor cage*, IEE Proceedings – Electric Power Applications, vol. 144, no. 4, pp. 271-276 (1997).

[4] Runge B., *Berchnung der Stillstandserwarmung explosionsgeschutzter Asynchronmotoren mittels dreidimensionaler Finite-Elemente-Methode und Zeitschrittrechnung*, Electrical Engineering, vol. 79, no. 3, pp. 179-191 (1996).

[5] Taler J., Duda P., *Solving straight and reverse problems of heat conduction*, WNT (in Polish), Warszawa (2003).

[6] Śliwiński T., *Methods of calculating induction motors*, Analysis (in Polish), PWN, Warszawa, vol. 1 (2008).

[7] Krok R., *Influence of work environment on thermal state of electric mine motors*, Archives of Electrical Engineering, vol. 60, no. 3, pp. 357-370 (2011).

[8] Al'Akayshee Q., Staton D.A., *1150 hp motor design, electromagnetic and thermal analysis*, ICEM-15-th International conference on electrical machines, Bruges, Belgium (2002).

[9] Dymond J.H., Ong R., Stranges N., *Instrumentation, Testing, and Analysis of Electric Machine Rotor Steady-State Heating*, IEEE Transactions on Industry Applications, vol. 38, no. 6, pp. 1661-1667 (2002).

[10] Zhang Y., Ruan J., Huang T., Yang X., Zhu H., Yang G., *Calculation of Temperature Rise in Air-cooled Induction Motors Through 3-D Coupled Electromagnetic Fluid-Dynamical and Thermal Finite-Element Analysis*, IEEE Transactions on Magnetics, vol. 48, no. 2, pp. 1047-1050 (2012).

[11] Poprawski W., Wolnik T., *Innovative design of double squirrel cage induction motor for high start frequency operation,* Maszyny Elektryczne – Zeszyty Problemowe (in Polish), vol. 111, no. 3, pp. 41-44 (2016).

ARCHIVES OF ELECTRICAL ENGINEERING VOL. 66(2), pp. 409-422 (2017)

DOI 10.1515/aee-2017-0031

The novel control method of switched reluctance generator

PIOTR BOGUSZ

Rzeszow University of Technology
Faculty of Electrical and Computer Engineering
Wincentego Pola 2, 35-959 Rzeszów, Poland
e-mail: pbogu@prz.edu.pl

(Received: 04.02.2017, revised: 19.04.2017)

Abstract: In the paper, a novel control method of a switched reluctance generator was discussed. The presented control method allows a rotor rotating at high speed to enter the continuous-conduction mode which causes an increase of generated output power. A control function of the presented method was given as well as simulation and laboratory tests.

Key words: switched reluctance generator, electric vehicle, current control, low speed, high speed

1. Introduction

The intensified development of the automotive industry causes that the research on development of travelling comfort, safety improvement and also the decrease of fuel consumption of vehicles and thereby increase of their range on a single tank are being conducted. In the last twenty years, the intensified research is also being conducted on the development of vehicles with an electric drive system due to the development of power electronics systems, control systems as well as the technology of electrochemical accumulators production [1-3]. When an electric motor is used in an electric drive vehicle, the efficiency of electric energy conversion into mechanical energy (during motoring operation) is just as important as conversion of mechanical energy into electric energy (during generating operation). Modern electric drives are supplied with converter systems. Switched reluctance machines are tested, among others, in drives of electric vehicles [4-5]. They are characterized by a simple structure, wide speed range and a high reliability. Unlike drives with combustion engines, merits of electric drives include a bidirectional conversion of energy (electric energy into mechanical energy and mechanical energy into electric energy). Additionally, electric energy can be easily stored in electrochemical accumulators and supercapacitors [6]. The aim of the paper is to present the

novel control strategy of a SRM in generating operation which allows for the increase of output power and to present results of simulation and laboratory tests.

2. Mathematical model of SRM

The equations of mathematical model which takes into account nonlinearity of a magnetic circuit can be written down in the following form:

$$\boldsymbol{u} = \boldsymbol{R}\,\boldsymbol{i} + \frac{\mathrm{d}}{\mathrm{d}t}[\boldsymbol{\psi}(\theta, \boldsymbol{i})], \tag{1}$$

$$J\frac{\mathrm{d}\omega}{\mathrm{d}t} + D\omega + T_L = T_e, \tag{2}$$

$$\frac{\mathrm{d}\theta}{\mathrm{d}t} = \omega, \tag{3}$$

$$T_e = \frac{\partial W^*(\theta, \boldsymbol{i})}{\partial \theta}, \tag{4}$$

where vectors of voltages $\boldsymbol{u}$, currents $\boldsymbol{i}$, flux-linkages $\boldsymbol{\psi}(\theta, \boldsymbol{i})$ and the matrix of resistances $\boldsymbol{R}$ are defined as: $\boldsymbol{u} = [u_1, ..., u_N]^T$, $\boldsymbol{i} = [i_1, ..., i_N]^T$, $\boldsymbol{\psi}(\theta, \boldsymbol{i}) = [\psi_1(\theta, i_1, ..., i_N), ..., \psi_N(\theta, i_1, ..., i_N)]^T$, $\boldsymbol{R} = \mathrm{diag}(R_1, ..., R_N)$. Moreover, the following symbols are used in the equations: ω – the angular velocity of a rotor, J – the moment of inertia, D – the coefficient of viscous friction, θ – the rotor position, T_L – the load torque, T_e – the electromagnetic torque, $W^*(\theta, i)$ – the co-energy.

3. The subject of research

The subject of simulation and laboratory tests is a four-phase 8/6 switched reluctance machine which geometry was shown in Fig. 1. In Table 1, basic parameters of the tested machine were listed.

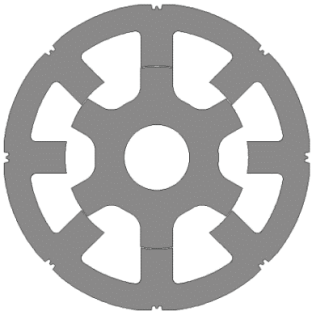

Fig. 1. SRM 8/6: a cross-section

Table 1. Basic parameters of the SRM

Machine type	SRM
Number of phases	4
Number of stator/rotor poles	8/6
Rated supply voltage	48 V
Rated power	3.3 kW
Rated speed	4500 rpm
Maximum phase current	130 A

It was assumed that the rotor and stator are made from anisotropic M530-50A sheet. The B-H curve of the used sheet was implemented in a resource base of FEM software. The calculations for various currents and rotor position were made based on the loaded data and flux-current-angle and torque-current-angle characteristics were determined. The machine was supplied with a classic H-type half-bridge [7]. The schematic diagram of the motor supply system was shown in Fig. 2. A lead-acid battery of 48 V rated voltage was used as a voltage source.

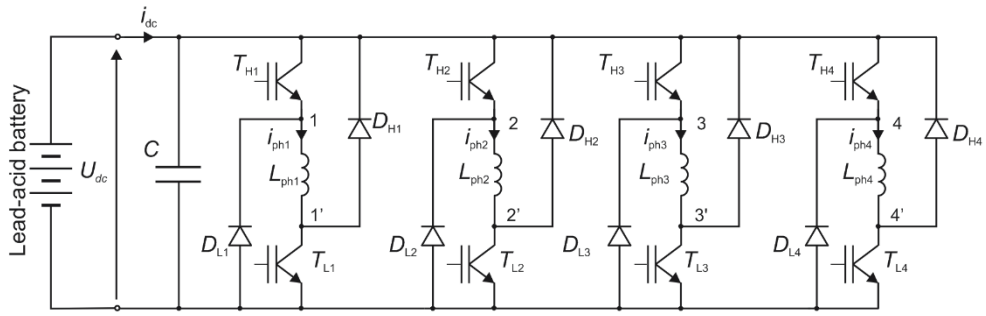

Fig. 2. A schematic diagram of the SRM supply system

4. Control methods of Switched Reluctance Generator

4.1. Generator Classical Current Control (GCCC)

In electric and hybrid vehicles, an electric machine which operates as a generator is the main system of energy recovery during braking. A control of braking operation of an electric machine allows changing of a braking torque of a vehicle according to the actual position of brake and accelerator pedals. The possibility of mechanical energy conversion into electric energy is limited by both electric machine parameters and parameters of energy storage systems like electrochemical accumulators or hybrid systems (accumulator-supercapacitor) [6]. In classic structures of switched reluctance machines, a current in phases is unidirectional. The energy recovery to supply a source can be obtained during descending the region of a phase inductance when phase voltages are negative. A braking torque of a machine can be changed through proper regulation of phase currents [7-8]. The regulation of phase currents can be

realized by using current controllers or by changing the turn-on angle (θ_{on}) and turn-off angle (θ_{off}) but without using current controllers [7]. In [9], authors present the current control algorithm of a switched reluctance generator (SRG) which minimizes output current (I_{dc}) ripples with simultaneous maximizing of efficiency based on previously registered data. The comparison of SRG properties under discontinuous-conduction mode (DCM) and under continuous-conduction mode (CCM) was presented in [10].

Current regulation is possible when the back-electromotive force (back-EMF) is lower than the dc-link voltage U_{dc}. Such a situation was shown in Fig. 3a. In this case, the current controller is able to maintain the current on the defined level. However, when the back-EMF is higher than the dc-link voltage, the current regulation is not possible. The transistors are switched-off (at point $\theta^{i}_{off\,(k)}$) by the current controller when the phase current reaches a reference value (I_{ref}) which causes the negative voltage on the phase $-U_{dc}$ until the current falls to zero. In this case, the drive changes operation into the single-pulse mode. Waveforms of the current, voltage and self-inductance of the phase were presented in Fig. 3b.

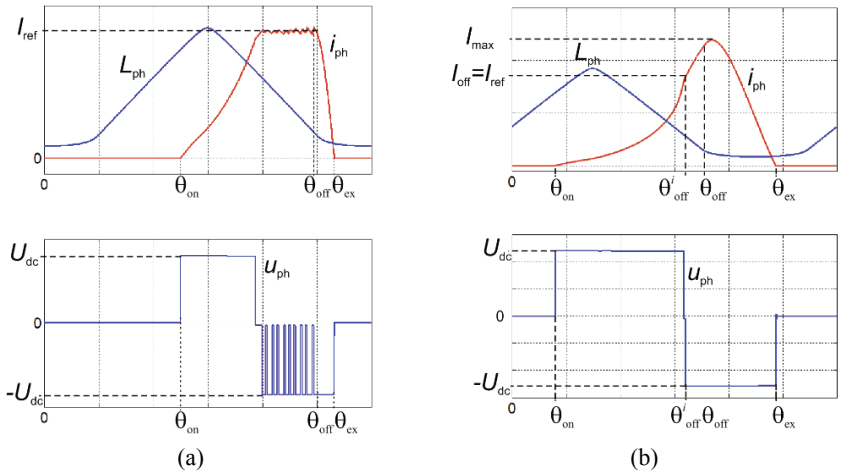

Fig. 3. Waveforms of self-inductance (L_{ph}), current (i_{ph}) and phase voltage (u_{ph}) under the current control (a); under the single-pulse mode (b)

In the following part of the paper, phase currents were marked according to Fig. 4 as: $i_{ph\,(k-1)}$ – the outgoing current, $i_{ph\,(k)}$ – the present current and $i_{ph\,(k+1)}$ – the incoming current.

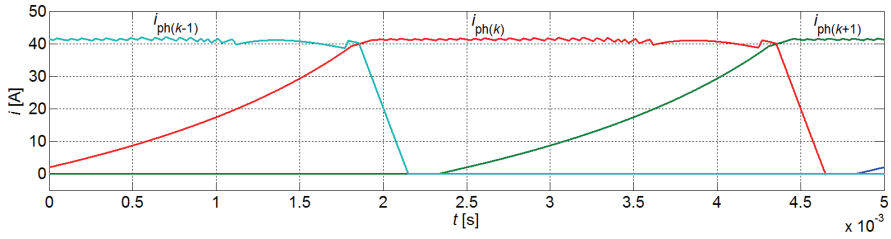

Fig. 4. Designations of phase currents: outgoing $i_{ph\,(k-1)}$, present $i_{ph\,(k)}$ and incoming $i_{ph\,(k+1)}$

A control function of a current controller in the whole range of the classic current control GCCC can be described as follows:

$$S_{(k)}^{\mathrm{GCCC}} = \begin{cases} f_{(k)} & \theta_{\mathrm{on}(k)} \le \theta_{(k)} < \theta_{\mathrm{off}(k)} \\ -1 & \theta_{\mathrm{off(k)}} \le \theta_{(k)} < \theta_{\mathrm{ex}(k)} \end{cases}, \tag{5}$$

where the function $f_{(k)}$ can be written as:

$$f_{(k)} = \begin{cases} -1 & if\,(i_{\mathrm{ph}(k)} \ge I_{\mathrm{ref}} + \Delta i) \\ 0 & if\,(I_{\mathrm{ref}} - \Delta i < i_{\mathrm{ph}(k)} < I_{\mathrm{ref}} + \Delta i) \\ 1 & if\,(i_{\mathrm{ph}(k)} \le I_{\mathrm{ref}} - \Delta i) \end{cases} \tag{6}$$

and angles θ_{on} and θ_{off} are turn-on and turn-off angles of the present phase (k), and Δi is a range of current hysteresis.

4.2. Generator dependent current control (GDCC)

In the paper, the novel function of a current regulation in a generating operation of the SRM, in which the current controller in the outgoing phase (k-1) depends on the current controller in the present phase (k), was proposed. In a conduction period $<\theta_{\mathrm{on}(k)}, \theta_{\mathrm{off}(k)}>$, phase currents controllers operate in the same way like in the GCCC control. It was proposed that instead of the constant value –1, the control function of current of the outgoing phase $f_{(k-1)}$ during the current decay period should be dependent on the current controller of the present phase $f_{(k)}$. The proposed method was called the generator dependent current control (GDCC). For the proposed control strategy, a shape of a phase current alters according to a working point of the machine. The operation of the SRM can be divided according to a shape of a phase current into:

– the current-control mode,
– the single-pulse mode,
– the continuous-conduction mode.

A control function of the current controller can be written as follows:

$$S_{(k)}^{\mathrm{GDCC}} = \begin{cases} f_{(k)} & \theta_{\mathrm{on}(k)} \le \theta_{(\mathrm{k})} < \theta_{\mathrm{off}(k)} \\ f_{\mathrm{decay}(k)} & \theta_{\mathrm{off}(k)} \le \theta_{(\mathrm{k})} \le \theta_{\mathrm{ex}(k)} \end{cases}, \tag{7}$$

where:

$$f_{\mathrm{decay}(k)} = \begin{cases} 0 & if\,(f_{(k-1)} = -1) \\ -1 & if\,(f_{(k-1)} \ne -1) \end{cases}, \tag{8}$$

where the function $f_{(k-1)}$ is analogical to the function $f_{(k)}$ in Equation (6). Waveforms of phase currents and voltages under the control according to the function (7) were shown in Fig. 5.

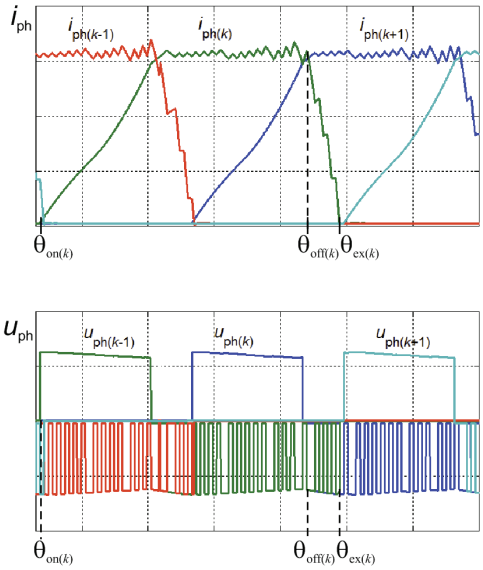

Fig. 5. Waveforms of phase currents (i_{ph}) and phase voltages (u_{ph}) under the current-control mode

For the single-pulse mode, a control function of the current controller is similar to (7), but an operating period is different. This function can be written as follows:

$$S_{(k)}^{GDCC} = \begin{cases} f_{(k)} & \theta_{on(k)} \le \theta_{(k)} < \theta_{off(k)}^{i} \\ f_{decay(k)} & \theta_{off(k)}^{i} \le \theta_{(k)} < \theta_{ex(k)} \end{cases}, \tag{9}$$

where the turn-off angle $\theta^{i}_{off(k)}$ depends on the value of the reference current I_{ref}. The angle $\theta_{off(k)}$ should be greater than $\theta^{i}_{off(k)}$ to generate proper operation of the current controller (Fig. 6). When the current controller in the outgoing phase depends on the current controller in the present phase then a final stage of current falling in the outgoing phase occurs in the zero-volt state and falling time of the current increases. Such a situation causes that the motor enters the continuous-conduction mode much earlier than under the GCCC control (Fig. 7). Therefore, higher output power can be obtained in the same working point compared to the GCCC control. Previous publications have reported that a transition into the continuous-conduction mode occurs without the zero-volt state [11-14].

The current controller operation under the continuous-conduction mode can be described by the function:

$$S_{(k)}^{GDCC} = \begin{cases} f_{(k)} & \theta_{on(k)} \le \theta_{(k)} \le \theta_{off(k)} \\ f_{decay(k)} & \theta_{off(k)} < \theta_{(k)} \le \theta_{Ioff(k+1)} \\ 0 & \theta_{Ioff(k+1)} \le \theta_{(k)} \le \theta_{on(k)} + \alpha_r \end{cases}, \tag{10}$$

where α_r is the rotor pole-pitch.

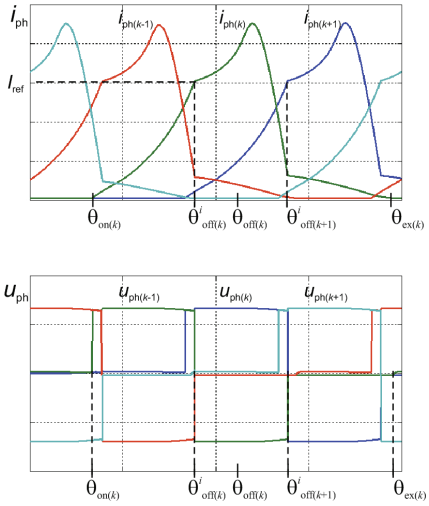

Fig. 6. Waveforms of phase currents (i_{ph}) and phase voltages (u_{ph}) under the single-pulse mode

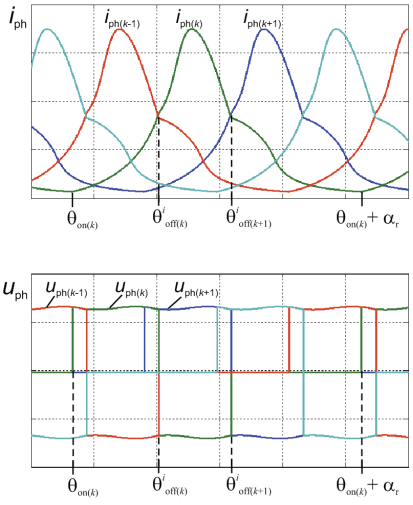

Fig. 7. Waveforms of phase currents (i_{ph}) and phase voltages (u_{ph}) under the continuous-conduction mode

5. Simulation tests

5.1. The simulation model

The simulation model of a SRM was built in the Matlab/Simulink environment [15]. The simulation model was realized based on Equations (1)-(4) and flux-current-angle and torque-current-angle characteristics which were calculated by means of FEM software. A detailed description of the simulation model was presented in [3]. Waveforms of currents, voltages and torque under the GCCC control and under the proposed GDCC control were registered. The simulation tests were made at low and high speeds. It was assumed that the SRM is supplied from a DC voltage source with a voltage of 54 V. The MOSFET transistors were used due to a low operating voltage of the SRM drive.

5.2. GCCC control

The control function described in Equation (7) was implemented in all phases of the SRM simulation model. Fig. 8 shows waveforms of the currents ($i_{ph1} - i_{ph4}$), phase voltages ($u_{ph1} - u_{ph4}$), source current (i_{dc}) and motor torque (T_e) at a speed of n = 2000 rpm and a reference current of I_{ref} = 37.5 A. As it can be seen in Fig. 8, obtained waveforms have characteristic shape for generating operation of the SRM.

Once the rotor reaches the angle θ_{off}, the current in the phase decays due to the negative value of the voltage $-U_{dc}$. Fig. 8b shows tristate operation of the current controller. The back-EMF increases with the increase of a phase current and/or speed.

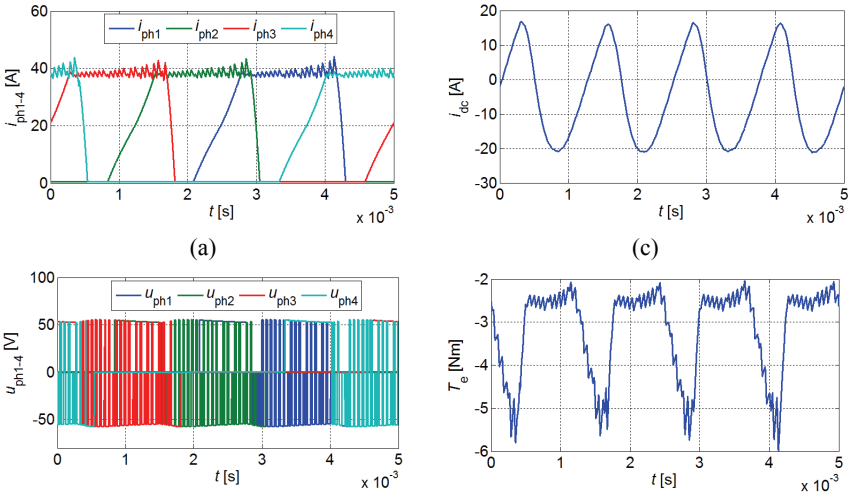

Fig. 8. Waveforms of phase currents (a); phase voltages (b); source current (c) and electromagnetic torque (d) under the GCCC control

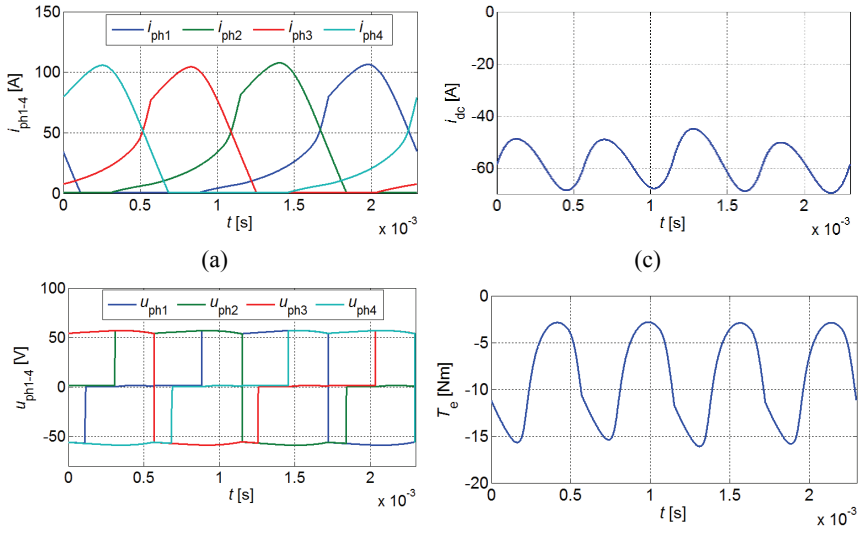

Fig. 9. Waveforms of phase currents (a); phase voltages (b); source current (c) and electromagnetic torque (d) under the single-pulse mode with a GCCC controller

In the GCCC control, it is not possible to maintain current at the defined value when the back-EMF is higher than U_{dc} and then the current controller changes the turn-off angle. Waveforms for the above-mentioned working point were shown in Fig. 9. They were determined at a speed of n = 4350 rpm and I_{ref} = 37.5 A.

5.3. GDCC control

The simulation tests for the GDCC control were conducted at a speed of $n = 2000$ rpm and a reference current of $I_{ref} = 37.5$ A. Fig. 10 shows waveforms of the phase currents (i_{ph1}-i_{ph4}), phase voltages (u_{ph1}-u_{ph4}), source current (i_{dc}) and motor torque (T_e). It can be seen in Fig. 10a that the current decays slower than under the GCCC control (Fig. 8a). It results from a dependence of the current controller of the outgoing phase on the controller of the present phase.

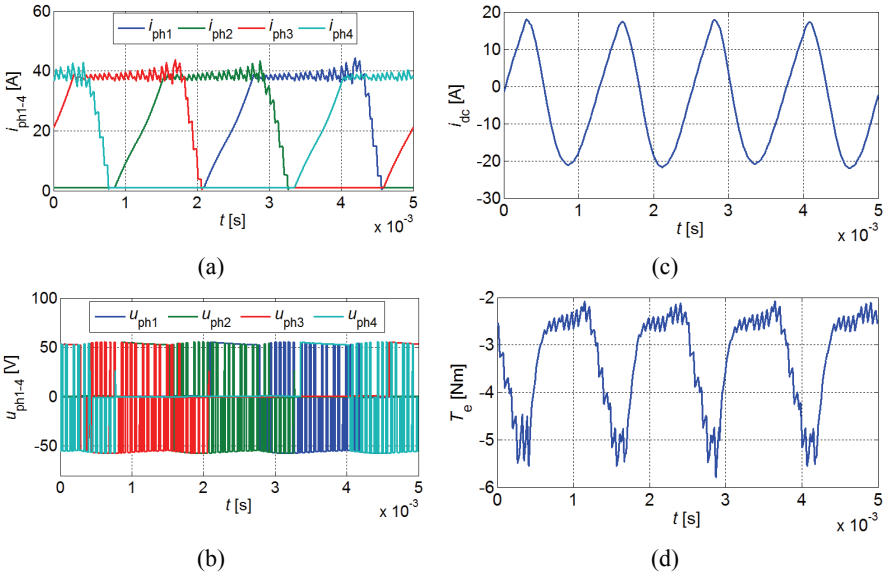

Fig. 10. Waveforms of phase currents (a); phase voltages (b); source current (c) and electromagnetic torque (d) under the GDCC control

Fig. 11 shows waveforms of the phase currents (Fig. 11a), phase voltages (Fig. 11b), source current (Fig. 11c) and electromagnetic torque (Fig. 11d) under the continuous-conduction mode at a speed of $n = 4350$ rpm and a reference current of $I_{ref} = 80$ A. An increase of speed causes an increase of the back-EMF and an increase of the maximum values of phase currents.

It can be seen in Fig. 11a that the phase current conduction is continuous not discontinuous. It results from the operation of the GDCC current controllers at high instantaneous values of the back-EMF.

6. Laboratory tests

The laboratory tests were conducted on the experimental setup which consists of a SRM (with details listed in Table 1) and the commutator DC machine with a power of 4.7 kW. The machines were coupled with a planetary gear and a HBM T22 torque meter.

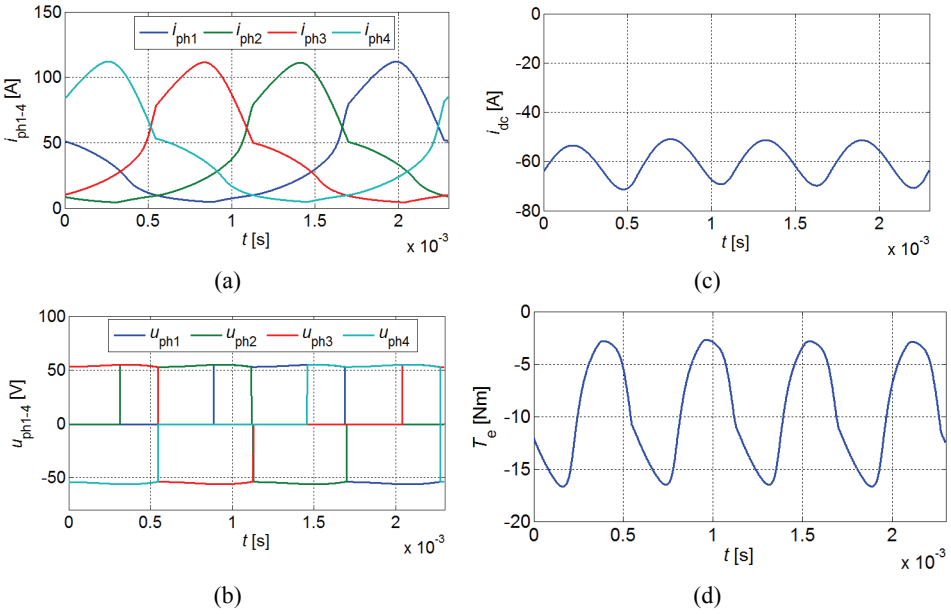

Fig. 11. Waveforms of phase currents (a); phase voltages (b); source current (c) and electromagnetic torque (d) under the continuous mode with a GDCC controller

The DC machine was supplied from a thyristor controller „Mentor”. The SRM was controlled by the dSPACE's DS1103 card. A lead-acid battery of 48 V rated voltage and a programmable load (connected in parallel with the accumulator) which operated in the constant voltage mode were used as a load of the SRM. The voltage limit was set to 54 V. The programmable load was used to make results independent of a battery charge status.

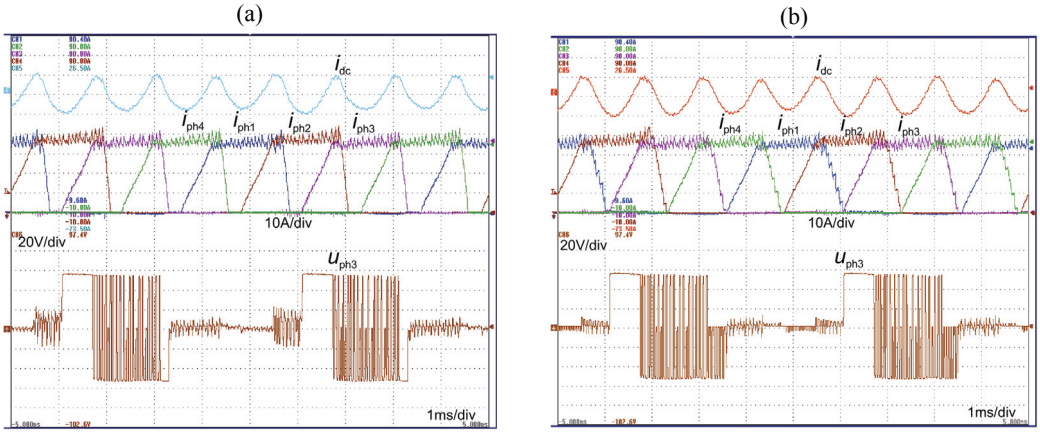

Fig. 12. Waveforms of phase currents, source current and phase voltage at n = 2000 rpm, I_{ref} = 37.5 A, U_{dc} = 54 V – under: the GCCC (a); the GDCC (b)

Figs. 12 and 13 show oscillograms of the phase currents and phase voltage under the GCCC control and the GDCC control at a speed of $n = 2000$ rpm and a reference current of $I_{ref} = 37.5$ A (Fig. 12) and at a speed of $n = 4350$ rpm and a reference current $I_{ref} = 80$ A (Fig. 13). The oscillograms were registered by a DL850 Yokogawa multi-channel scope recorder. It can be seen in Fig. 13 that duration of the negative voltage is longer under the GCCC control than under the GDCC control.

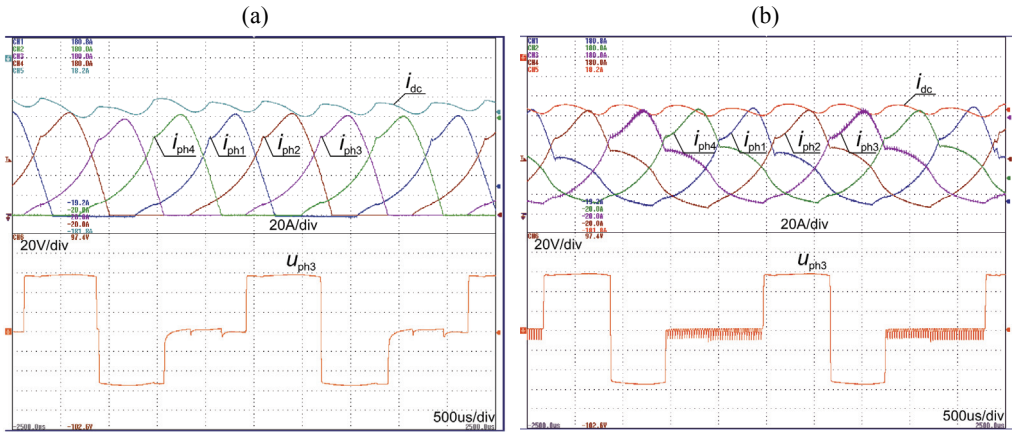

Fig. 13. Waveforms of phase currents, source current and phase voltage at $n = 4350$ rpm, $I_{ref} = 80$ A, $U_{dc} = 54$ V – under the GCCC (a); the GDCC (b),

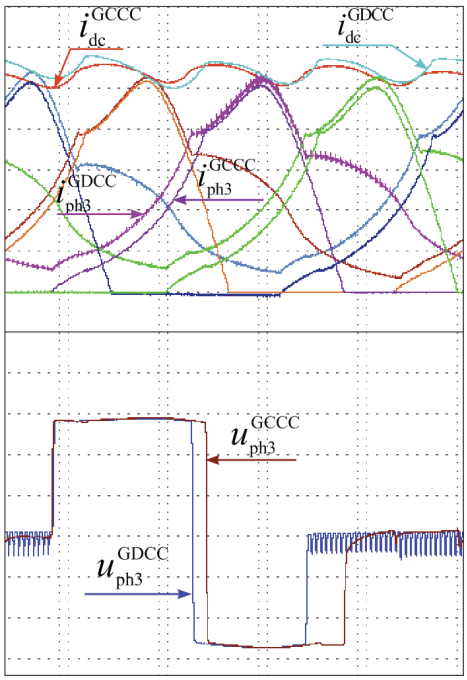

Fig. 14. A comparison of waveforms under the GCCC and the GDCC control

However, under the GDCC controller it acts earlier than under the GCCC because a phase current reaches earlier the reference value. In the initial stage of the negative voltage appearance, the inductance change of the phase in the function of rotor position is much bigger than in the moment of phase voltage changing from $-U_{dc}$ to zero (Fig. 5b).

It causes that the amount of generated energy is higher under the GDCC control than under the GCCC control. Fig. 14 shows a comparison of the waveforms of the phase currents, phase voltages and source current for the same operating conditions which were shown in the oscillograms in Fig. 13. The maximum value of phase currents was limited during tests to 120 A due to the maximum permissible currents of controller elements.

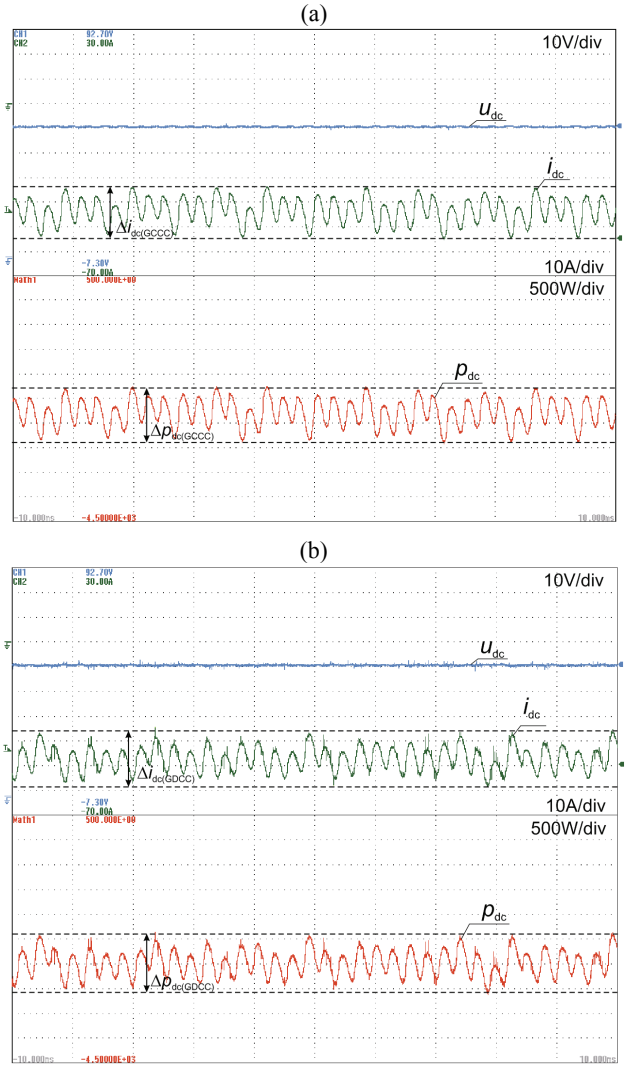

Fig. 15. Waveforms of voltage u_{dc}, current i_{dc} and output power p_{dc} under the GCCC (a) and the GDCC (b)

Fig. 15 shows waveforms of the voltage u_{dc}, current i_{dc} and output power p_{dc} under the GCCC (Fig. 15a) and the GDCC (Fig. 15b) at a speed of $n = 4500$ rpm and a reference current of $I_{ref} = 75$ A. A range of voltage change of a battery is almost unnoticeable. As it can be seen, a range of output current (i_{dc}) change is about $\Delta i_{dc\,(GCCC)} = 21.2$ A under the GCCC and $\Delta i_{dc\,(GDCC)} = 24.4$ A under the GDCC. It considerably affects the output power ripples. A range of instantaneous power change at batteries voltage $U_{dc} = 60$ V was equal to $\Delta p_{dc\,(GCCC)} = 1272$ W under the GCCC and $\Delta p_{dc\,(GCCC)} = 1464$ W under the GDCC. It should be noted that under the GCCC the average output power at this working point was equal to $P_{GCCC} = 2330$ W and under the GDCC it was equal to $P_{GDCC} = 2520$ W.

Fig. 16 shows a dependence of the SRG efficiency in the function of output power and the graph of power losses in windings under the GCCC and the GDCC control. By comparing both graphs, it can be seen that despite increasing of winding losses under the GDCC control, the resultant efficiency is almost the same in both cases. It can be seen in Fig. 16a that for the reference current higher than 50 A ($I_{ref} > 50$ A) the difference in output power between the GCCC and the GDCC control increases.

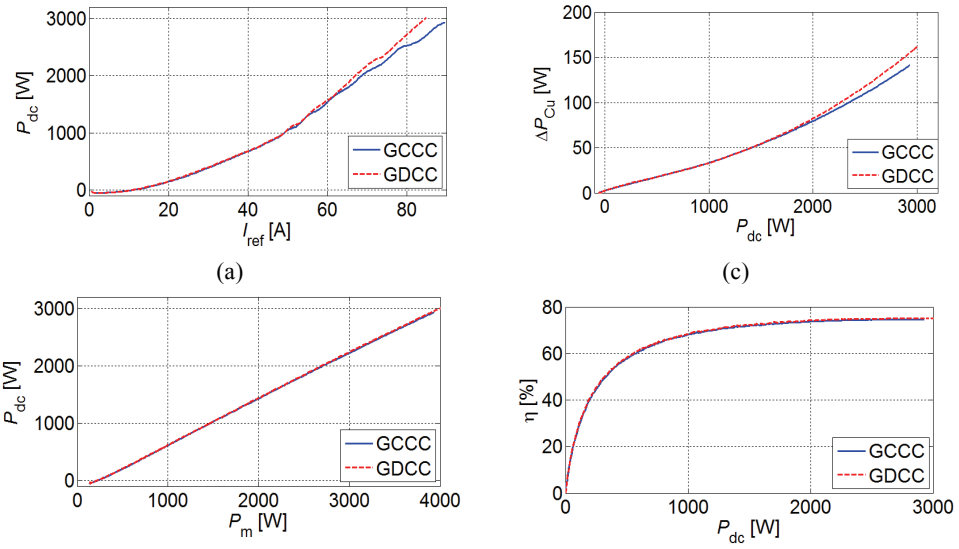

Fig. 16. Graphs of output power P_{dc} in the function of reference current I_{ref} (a); output power P_{dc} in the function of mechanical power P_m (b); copper losses ΔP_{Cu} in the function of output power P_{dc} (c); drive efficiency η in generating operation in the function of output power P_{dc} (d) under the GCCC and the GDCC control

7. Conclusions

In the paper, the novel control strategy of a SRM called the generator dependent current control (GDCC), in which operation of the current controller of the outgoing phase depends on

the operation of the controller in the incoming phase, was proposed. Such a solution in comparison to the classic current controller (GCCC):

- does not change motor performance under the current control,
- causes that an increase in output power is noticeable as early as half way through the tested range of output power i.e. when phase currents enter continuous conduction mode,
- does not change the efficiency of a machine with a control system.

In general, thanks to the capability of obtaining a higher output power under the continuous-conduction mode, the proposed control method proved advantageous over the GCCC control method. For this reason, the use of an SRM in drives of electric and hybrid vehicles is more profitable. Unfortunately, a high current and output power ripples occur under the GCCC and the GDCC control without any filter systems.

References

[1] Gasbaoui B., Abdelkader Ch., Adellah L., *Multi-input multi-output fuzzy logic controller for utility electric vehicle*, Archives of Electrical Engineering, vol. 60, no. 3, pp. 239-256 (2011).

[2] Adamczyk D., Wilk A., Michna M., *Model of the double-rotor induction motor in terms of electromagnetic differential*, Archives of Electrical Engineering, vol. 65, no. 4, pp. 761-772 (2016).

[3] Bogusz P., *A switched reluctance motor control method limiting the maximum dc source current in the low-speed range*, Bulletin of the Polish Academy of Sciences Technical Sciences, vol. 64, no. 1, pp. 197-206 (2016).

[4] Chiba A., Takeno M., Hoshi N., Takemoto M., Ogasawara S., Rahman, M.A., *Consideration of Number of Series Turns in Switched-Reluctance Traction Motor Competitive to HEV IPMSM*, IEEE Transactions on Industry Applications, vol. 48, no. 6, pp. 2333-2340 (2012).

[5] Faiz J., Moayed-Zadeh K., *Design of switched reluctance machine for starter/generator of hybrid electric vehicle*, Electric Power Systems Research no. 75, Elsevier, pp. 153-160 (2005).

[6] Baoming G., de Almeida A.T., Ferreira F.J.T.E., *Supercapacitor-based optimum switched reluctance drive for advanced electric vehicles*, in IEEE International Conference on Electrical Machines and Systems, vol. 1, pp. 822-827 (2005), DOI: 10.1109/ICEMS.2005.202652.

[7] Miller T.J.E., *Electronic Control of switched reluctance machines*, Newnes (2001).

[8] Kosmatin P., Miljavec D., Vončina D., *A novel control strategy for the switched reluctance generator*, Przegląd Elektrotechniczny, vol. 88, no. 7a, pp. 49-53 (2012).

[9] Sikder Ch., Husain I., Sozer Y., *Switched Reluctance Generator Control for Optimal Power Generation With Current Regulation*, IEEE Transactions on Industry Applications, vol. 50, no. 1, pp. 307-316 (2014).

[10] Hannoun H., Hilairet M., Marchand C., *Experimental Validation of a Switched Reluctance Machine Operating in Continuous-Conduction Mode*, IEEE Transactions on Vehicular Technology, vol. 60, no. 4, pp. 1453-1460 (2011).

[11] Nuwantha F., *Control of Switched Reluctance Generators in Continuous Conduction Mode*, IEEE Energy Conversion Congress and Exposition (ECCE), pp. 1360-1365 (2014), DOI: 10.1109/ECCE.2014.6953576.

[12] Vujičić V.P., Ćalasan M.P., *Simple Sensorless Control for High-Speed Operation of Switched Reluctance Generator*, IEEE Transactions on Energy Conversion, vol. 31, no. 4, pp. 1325-1335 (2016).

[13] Korkosz M., Mazur D., *Operation of the switched reluctance motor at continuous conduction of phase current*, IEEE Mediterranean Electrotechnical Conference - MELECON 2006, pp. 1166-1169 (2006), DOI: 10.1109/MELCON.2006.1653308.

[14] Korkosz M., Bogusz P., Pilecki M., *The impact of parameter control on the characteristics of switched reluctance motor designed for small electric vehicle drive*, Selected Problems of Electrical Engineering and Electronics (WZEE), pp. 1-4 (2015), DOI: 10.1109/WZEE.2015.7394044.

[15] *Matlab/Simulink R2012a- User's Guide*, Mathworks (2012).

ARCHIVES OF ELECTRICAL ENGINEERING VOL. 66(2), pp. 423-432 (2017)

DOI 10.1515/aee-2017-0032

Scaling-based prediction of magnetic anisotropy in grain-oriented steels

MARIUSZ NAJGEBAUER

Faculty of Electrical Engineering
Czestochowa University of Technology
e-mail: mariusz.najgebauer@gmail.com

(Received: 28.02.2017, revised: 27.04.2017)

Abstract: The paper presents the scaling-based approach to analysis and prediction of magnetic anisotropy in grain-oriented steels. Results of the anisotropy scaling indicate the existence of two universality classes. The hybrid approach to prediction of magnetic anisotropy, combining the scaling analysis with the ODFs method, is proposed. This approach is examined in prediction of angular dependencies of magnetic induction as well as magnetization curves for the 111-35S5 steel. It is shown that it is possible to predict anisotropy of magnetic properties based on measurements in three arbitrary directions for $\phi = 0°$, 60° and 90°. The relatively small errors between predicted and measured values of magnetic induction are obtained.

Key words: grain-oriented steels, magnetic anisotropy, ODFs method, scaling analysis

1. Introduction

Electrical steels are still the basic magnetic materials used as magnetic cores in electrical machines such as motors, generators and transformers. There are two groups of electrical steels: non-oriented and grain-oriented ones. Typical non-oriented steels are 0.35-0.8 mm thick with 0-3% silicon content, while grain-oriented steels are 0.23-0.35 mm with 2.9-3.2% silicon content. Non-oriented steels are usually considered as isotropic materials, with the same magnetic properties in any direction. Grain-oriented steels exhibit strong anisotropy of magnetic properties, created by many rolling and re-crystallization production steps [1-7]. In fact, non-oriented steels may reveal a significant level of anisotropy [2, 8], which can affect the efficiency of electrical devices. For this reason, the anisotropy of magnetic properties is – apart from peak induction and power loss – one of the most important parameters determining material usefulness for magnetic circuits of electrical machines.

There are many models describing an anisotropy phenomenon in magnetic materials. However, the models used in practical computations should allow one to predict magnetic anisotropy based on input data (e.g. measurements) obtained for selected directions, which reduces troublesome sample preparations and measurements for intermediate directions. This require-

ment is met by the phenomenological models based on the coenergy concept as well as the theory of Orientation Distribution Functions (ODFs).

The coenergy-based model of magnetic anisotropy have been proposed by Péra [9] and developed by Biró [10] and Chwastek [11, 12]. This description is given by the ellipse-like equation:

$$\left(\frac{\boldsymbol{B}\cdot\boldsymbol{e}_1}{B_1(H)}\right)^n+\left(\frac{\boldsymbol{B}\cdot\boldsymbol{e}_2}{B_2(H)}\right)^n=1, \tag{1}$$

where: $\boldsymbol{B}$ is a magnetic induction vector, $\boldsymbol{e}_{1,2}$ are unit vectors in the rolling and the transverse direction, $B_{1,2}(H)$ describes magnetization curve in these directions and n is a model exponent.

The original elliptical model (for $n=2$) does not provide satisfactory results for the direction of the worst magnetic properties. In the case of $n \approx 1.4$, Eq. (1) takes the form more appropriate for the description of magnetic anisotropy in all directions [10-12].

The coenergy-based model allows one to predict magnetization curves for any direction using measurements carried out for the rolling and the transverse direction, which are often provided by steel manufacturers. However, this method may cause some problems in numerical implementations.

Another approach to the anisotropy modeling is based on the theory of Orientation Distribution Functions (ODFs), which allows one to correlate magnetic properties and the crystallographic texture of the sample. This approach has been developed by Bunge [13, 14] and advanced by de Campos [15, 16]. Recently, Chwastek examined this method for grain-oriented electrical steels [17, 18]. In general, the ODFs method allows one to describe the anisotropy of magnetic properties (such as magnetization, coercivity or power loss) using the three first ODFs coefficients

$$A = A_0 + A_1\cos 2\phi + A_2\cos 4\phi, \tag{2}$$

where: $A_{0,1,2}$ are the ODFs coefficients given by the following expressions:

$$\begin{aligned} A_0 &= 0.25\cdot\left[A(0°)+A(90°)+2A(45°)\right],\\ A_1 &= 0.5\cdot\left[A(0°)-A(90°)\right],\\ A_0 &= 0.25\cdot\left[A(0°)+A(90°)-2A(45°)\right]. \end{aligned} \tag{3}$$

It results from (2) and (3), that measurements of the magnetic property carried out in the three arbitrary directions ($\phi = 0°$, 45° and 90°) are sufficient to predict values of this property for intermediate directions. It should be noted that the value of the ODFs coefficients vary depending on the excitation [17]. Thus, even though the ODFs method provides satisfactory results of the magnetic anisotropy prediction, it requires measurements in the three directions carried out for each level of the excitation.

The paper presents a hybrid approach to prediction of magnetic anisotropy, combining the scaling analysis with the ODFs method. The proposed approach should result in further simplification of anisotropy prediction due to using universal values of the ODFs coefficients. This approach will be examined for the grain-oriented steel.

2. Samples and measurements

Samples for measurements were prepared from the grain-oriented steel grade 111-35S5, produced by Stalprodukt S.A., Bochnia. The samples had a shape of stripes (305 ± 0.5 mm long, 30 ± 0.2 mm wide and 0.35 mm thick) and were cut from the steel sheet at a different angle to the rolling direction, i.e. for $\phi = 0°$, 15°, 30°, 45°, 60°, 75° and 90°. Measurements were carried out using the 25 cm Epstein frame according to the international standard IEC 60404-2:1996-03, Part 2: *Methods of measurement of the magnetic properties of electrical steel sheet and strip by means of an Epstein frame*. Angular dependencies of magnetic induction for different level of magnetic field strength are depicted in Fig. 1. The measurements indicate a strong anisotropy of magnetic properties of the examined steel. For $H > 200$ A/m, the worst magnetic properties are observed for the angle close to $\phi = 55°$, what is determined by the Goss texture of grain-oriented steels [5-7, 12, 17, 19-21]. It should be noted that the angular dependence of magnetic induction for $H = 100$ A/m has a different trajectory compared to the other dependencies – the worst direction of magnetic properties is for $\phi = 90°$. Similar results were reported in [21-25]. This effect may result from the change of the magnetization mechanism for magnetic field strength of about 200 A/m. For $H < 200$ A/m the domain-wall translation is responsible for the magnetization process, while in the case of $H > 200$ A/m the rotation of magnetization vectors is the main magnetization mechanism [17].

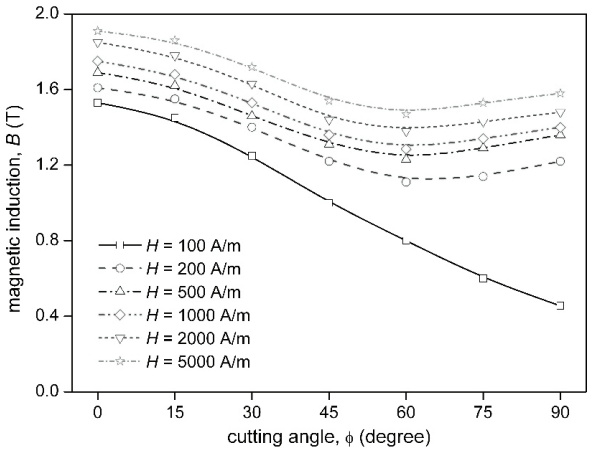

Fig. 1. Magnetic induction versus the cutting angle for the 111-35S5 steel

3. Scaling analysis of magnetic anisotropy

In modern physics, the scaling theory is applied usually in the analysis of critical behavior and phase transitions [26-29]. The scaling analysis is also used in materials science, including the study of magnetic material properties such as power loss [30-34], coercivity [35-37], magnetic viscosity [38-40] or hysteresis loops [41-45].

Referring to the scaling theory as well as the measurements (see Fig. 1), it is proposed to describe the anisotropy of magnetic properties by a functional relationship of a cutting angle ϕ and magnetic field strength H

$$B = f(\phi, H). \tag{4}$$

The relationship (4) is assumed to be a generalized homogenous function, which is defined as:

$$\lambda^x B = f(\lambda^y \phi, \lambda^z H), \tag{5}$$

where: λ is a scaling coefficient and x, y, z are any numbers [28, 29]. For $\lambda = H^{-1/z}$, the relationship (5) is transformed as follows:

$$H^{-x/z} B = f(H^{-x/z}\phi, 1), \tag{6}$$

$$\frac{B}{H^{\psi}} = F\left(\frac{\phi}{H^{\varphi}}\right), \tag{7}$$

and finally the scaled form of (4) is obtained

$$B_H = F(\phi_H), \tag{8}$$

where: B_H and ϕ_H are magnetic induction and a cutting angle scaled with respect to H, ψ and φ are scaling exponents and $F(\phi_H) = f(\phi_H, 1)$ denotes a so-called scaling function. In the previous studies, a scaling function was usually represented by Maclaurin series [30-37].

In the considered study, the scaling function $F(\phi_H)$ is supposed to be represented by the following series:

$$B_H = B_0 + B_1 \cos 2\phi_H + B_2 \cos 4\phi_H + B_3 \cos 6\phi_H + \ldots, \tag{9}$$

which results from the angular dependence of the magnetic properties anisotropy. Referring to the ODFs methods (2), only the three first coefficients of (9) may be taken into account. Thus, in further computations the reduced expression describing scaled magnetic induction will be examined

$$B_H = B_0 + B_1 \cos 2\phi_H + B_2 \cos 4\phi_H . \tag{10}$$

4. Results and discussion

4.1. Scaling of magnetic anisotropy

The measured dependencies of magnetic induction B versus the cutting angle ϕ were scaled in respect to magnetic field strength H according to (10). The scaling coefficients ψ, φ and $B_{0\text{-}2}$ were estimated using the least square method in such a way that allowed collapsing of

measurement data onto a single dependency. Only in the case of data collapse, the coefficient values may be considered as universal. The scaling of magnetic induction measurements for the examined study is presented in Fig. 2. It can be observed that data points for $H = 100$ A/m are not collapsed and diverge significantly from the data collapse curve. It suggests that the measurements at low magnetic field strength (about 100 A/m) belong to one universality class, while the other measurements – to another universality class. The existence of different universality classes were reported previously in analysis of power loss in La-containing alloys [33] and minor hysteresis loops in Finmet type cores [45].

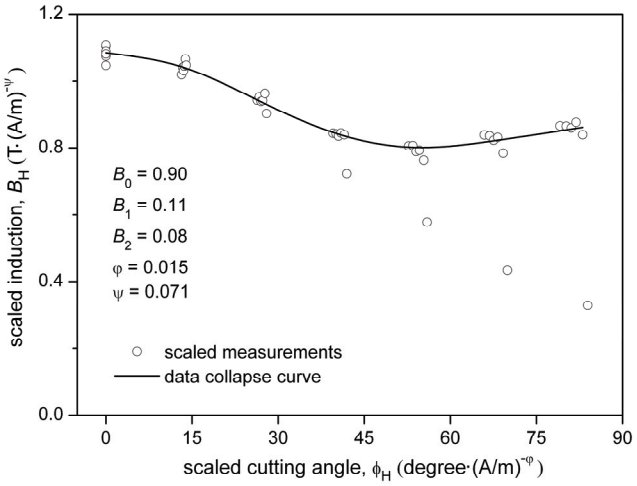

Fig. 2. Scaling and data collapse of the magnetic anisotropy for the 111-35S5 steel

Referring to the scaling theory, each class of universality should be characterized by the specific set of coefficients. Thus, values of the coefficients ψ, φ and $B_{0\text{-}2}$ can be considered as universal in the measurement range $H = 200 \div 5000$ A/m. Concluding, the presented results confirm the validity of scaling procedures in the analysis of magnetic anisotropy.

4.2. Prediction of magnetic anisotropy

The proposed scaling should allow one to prediction the anisotropy of magnetic properties, including such levels of magnetic field strength H or cutting angles ϕ, which haven't been used in estimation of the scaling coefficients. This assumption was verified in two case studies, concerning the prediction of:

1) Angular dependencies of magnetic induction at various levels of magnetic field strength,
2) Magnetization curves at various cutting angles.

In the first case study, scaling coefficients were estimated from the angular dependencies of magnetic induction, measured for all cutting angles and selected levels of magnetic field strength, i.e. $H_{min} = 200$ A/m and $H_{max} = 5000$ A/m. The angular dependencies of magnetic induction were then predicted for intermediate levels of magnetic field strength using (10), transformed to the following form:

$$B = H^{\Psi} \cdot \left(B_0 + B_1 \cos 2\frac{\phi}{H^{\varphi}} + B_2 \cos 4\frac{\phi}{H^{\varphi}} \right). \tag{11}$$

The prediction results for H = 500, 1000 and 2000 A/m are depicted in Fig. 3. The relative errors between the measured and predicted values of magnetic induction did not exceed 5%. The error values are presented in Table 1.

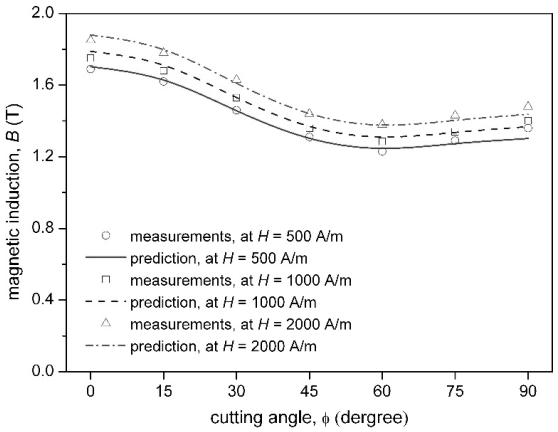

Fig. 3. Prediction of magnetic induction versus the cutting angle for the 111-35S5 steel

Table 1. Prediction errors for the case study 1

Cutting angle ϕ (degree)	**0**	**15**	**30**	**45**	**60**	**75**	**90**
Errors (%) at H = 500 A/m	0.77	0.49	0.24	0.50	1.41	1.35	4.26
Errors (%) at H = 1000 A/m	2.25	1.83	0.09	0.77	1.99	0.27	2.29
Errors (%) at H = 2000 A/m	1.61	1.00	1.23	0.06	0.22	1.86	2.91

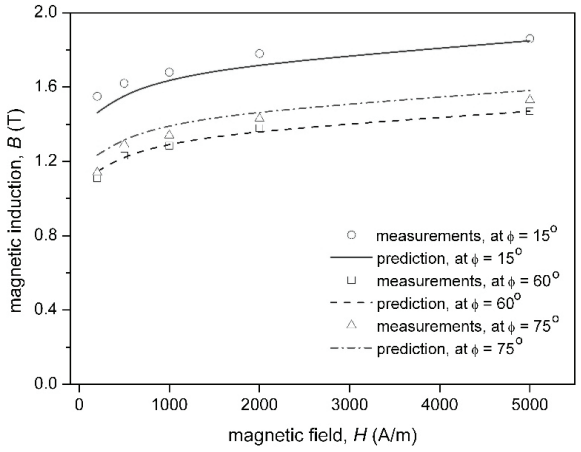

Fig. 4. Prediction of magnetization curves for the 111-35S5 steel

In the second case study, the scaling coefficients were estimated according to the ODFs method, i.e. from measurements for cutting angles $\phi = 0°$, 60° and 90°. The cutting angle $\phi = 60°$ was chosen instead of $\phi = 45°$ (the ODFs method), because it represented the direction of worst magnetic properties. The magnetization curves, predicted for chosen cutting angles, are depicted in Fig. 4, while corresponding relative errors are presented in Table 2. The prediction errors in this case study did not exceed 6%.

Table 2. Prediction errors for the case study 2

Magnetic field H (A/m)	**200**	**500**	**1000**	**2000**	**5000**
Errors (%) at $\phi = 15°$	5.70	3.53	2.15	2.86	0.61
Errors (%) at $\phi = 60°$	3.24	0.05	0.99	0.78	0.01
Errors (%) at $\phi = 75°$	2.79	1.48	0.59	0.01	0.03

Values of the scaling coefficients, estimated from different measurement ranges, are presented in Table 3. These are comparable in all considered studies except the scaling exponent φ, whose value depends on the measurement range. This issue will be the subject of further research.

Table 3. Estimated values of scaling coefficients

Measurements	B_0	B_1	B_2	φ	ψ
Full range	0.90	0.11	0.08	0.015	0.071
Reduced range (case study 1)	0.90	0.13	0.07	0.004	0.071
Reduced range (case study 2)	0.86	0.10	0.09	−0.010	0.074

The results presented in this section confirm that the scaling-based method allows one to predict the magnetic anisotropy in a wide range of magnetic field strength or cutting angles, with relatively low errors. Moreover, the proposed method generates universal values of the coefficients $B_{0\text{-}2}$, whereas in the case of the ODFs method – the coefficients $A_{0\text{-}2}$ should be estimated separately for each level of magnetic field strength.

5. Conclusions

In the paper, the use of scaling analysis in description of magnetic anisotropy in electrical steels has been proposed. This approach was examined for the grain-oriented steel 111-35S5. The angular dependencies of magnetic induction for $H = 200 \div 5000$ A/m were collapsed onto a single curve, while a significant divergence of measurements for $H = 100$ A/m was observed. For this reason, the existence of two universality classes was postulated. Estimated values of the scaling coefficients could be considered as universal only in the limited range of magnetic field strength $H = 200 \div 5000$ A/m. Nevertheless, the presented results confirmed the validity of scaling procedures in the analysis of magnetic anisotropy.

The hybrid method for magnetic anisotropy prediction, combining the scaling analysis with the ODFs method, was proposed. This approach was verified in two case studies, concerning prediction of angular dependencies of magnetic induction as well as magnetization curves for various cutting angles. It was shown that it is possible to predict anisotropy of magnetic properties based on measurements for three arbitrary angles $\phi = 0°$, 90° and 60°, corresponding to rolling, transverse and worst magnetic properties direction, respectively. The relatively small errors of the scaling-based prediction of magnetic anisotropy were obtained. The proposed method generates coefficients, which have universal values for a wide range of magnetic field strength. In contrast, the coefficients in the ODFs method should be estimated separately for each level of magnetic field strength. For this reason, the scaling-based prediction of magnetic anisotropy should be considered as a simpler and more universal method, compared to the ODFs one.

In future research, the proposed method will be examined in the analysis of magnetic anisotropy in the range of low magnetic field strength ($H < 200$ A/m) in order to investigate its scaling behavior.

Acknowledgements

The author would like to thank Professor Jan Szczygłowski for providing measurements of angular magnetic properties as well as a useful, inspiring and motivating discussion. The author is also grateful to Professor Krzysztof Chwastek for his comments pertaining to magnetic anisotropy.

References

[1] Fiorillo F., *Anisotropy and magnetization process in soft magnets: Principles, experiments, applications*, Journal of Magnetism and Magnetic Materials, vol. 304, pp. 139-144 (2006).

[2] Tumański S., *Investigations of the anisotropic behaviour of SiFe steel*, Journal of Magnetism and Magnetic Materials, vol. 254-255, pp. 50-53 (2003).

[3] Soiński M., Bak Z., Bargiel P., *Anisotropy of magnetic properties in thin electrical sheets*, IEEE Transactions on Magnetics, vol. 26, no. 6, pp. 3076-3079 (1990).

[4] Soiński M., Moses A.J., *Anisotropy of iron-based soft magnetic materials (Chapter 4)*, Handbook of magnetic materials, vol. 8, North-Holland Elsevier, pp. 325-414 (1995).

[5] Fryskowski B., *Experimental evaluation of magnetic anisotropy in electrical steel sheets*, Journal of Magnetism and Magnetic Materials, vol. 320, pp. 515-552 (2008).

[6] Emura M., de Campos M.F., Landgraf F.J.G., Teixeira J.C., *Angular dependence of magnetic properties of 2% silicon electrical steel*, Journal of Magnetism and Magnetic Materials, vols. 226-230, pp. 1524-1526 (2001).

[7] Mazgaj W., Warzecha A., *Influence of electrical steel sheet textures on their magnetization curves*, Archives of Electrical Engineering, vol. 62, no. 3, pp. 425-437 (2013).

[8] Najgebauer M., Szczygłowski J., Kapłon A., *Soft magnetic materials for energy-efficient electric motors*, the 12th Conference on Selected Problems of Electrical Engineering and Electronics (WZEE2015), Kielce, Poland, pp. 1-4 (2015).

[9] Péra T., Ossart F., Waeckerlé Th., *Numerical representation for anisotropic materials based on coenergy modeling*, Journal of Applied Physics, vol. 73, no. 10, pp. 6784-6786 (1993).

[10] Biró O., Ausserhofer S., Preis K., Chen Y., *A modified elliptic model of anisotropy in nonlinear magnetic materials*, Proceedings of 8th International Symposium on Electric and Magnetic Field (EMF'2009), Mondovi, Italy, pp. 25-26 (2009).

[11] Chwastek K., Najgebauer M., Szczygłowski J., Wilczyński W., *Modelling the influence of anisotropy on magnetic properties in grain-oriented steels*, Przegląd Elektrotechniczny, vol. 87, no. 3, pp. 126-128 (2011).
[12] Chwastek K., *Anisotropic properties of non-oriented steel sheets*, IET Electronic Power Applications, vol. 7, no. 7, pp. 575-579 (2013).
[13] Bunge H.J., *Texture analysis in materials science: mathematical methods*, Butterworth (1982).
[14] Bunge H.J., *The basic concepts of texture investigation in polycrystalline materials*, Steel Research, vol. 62, no. 12, pp. 530-541 (1991).
[15] de Campos M.F., *Anisotropy of steel sheets and consequence for Epstein test*, Proceeding of XVIII IMEKO World Congress "Metrology for a Sustainable Development", Rio de Janeiro, Brazil, p. 6 (2006).
[16] Yonamine T., de Campos M.F., Castro N.A., Landgraf F.J.G., *Modeling magnetic polarization J_{50} by different methods*, Journal of Magnetism and Magnetic Materials, vol. 304, pp. e589-e592 (2006).
[17] Chwastek K., Baghel A., De Campos M., Kulkarni S.V., Szczygłowski J., *A Description for the Anisotropy of Magnetic Properties of Grain-oriented Steels*, IEEE Transactions on Magnetics, vol. 51, no. 12, pp. 6000905.1-5 (2015).
[18] Chwastek K., Baghel A.P.S., Wodzyński A., Kulkarni S.V., *Anisotropic properties of electrical steels*, 6th International Conference on Computational Problems of Electrical Engineering (CPEE), Lviv, Ukraine, pp. 21-23 (2015).
[19] Cornut B., Kedous-Lebouc A., Waeckerlé Th., *From metallurgy to modelling electrical steels: a multiple approach to their behaviour and used based on physics and experimental investigations*, Journal of Magnetism and Magnetic Materials, vol. 160, pp. 102-108 (1996).
[20] Pluta W., *Angular properties of specific total loss components under axial magnetization in grain-oriented electrical steel*, IEEE Transactions on Magnetics, vol. 52, issue 4, no. 6300912 (2016).
[21] Paltanea G., Paltanea V., Gavrila H., Popovici D., Ionescu G., *Magnetic anisotropy in grain oriented steels cut through mechanical punching and electro-erosion technologies*, AIP Conference Proceedings, vol. 1809, pp. 020041.1-6 (2017).
[22] Fiorillo F., Dupré L.R., Appino C., Rietto A.M., *Comprehensive model of magnetization curve, hysteresis loops, and losses in any direction in grain-oriented Fe-Si*, IEEE Transactions on Magnetics, vol. 38, no. 3, 1467-1475 (2002).
[23] Fiorillo F., Appino C., Beatrice C., Garsia F., *Magnetization process under generically directed field in GO Fe–(3 wt%)Si laminations*, Journal of Magnetism and Magnetic Materials, vols. 242-245, pp. 257-260 (2002).
[24] Tumański S., *Handbook of magnetic measurements*, CRC Press (2011).
[25] Tumański S., *Investigations of two-dimensional properties of selected electrical steel samples by means of the Epstein method*, 7th Workshop on 2D Measurements, Lüdenscheid, Germany, pp. 151-157 (2002).
[26] Widom B., *Equation of state in the neighbourhood of the critical point*, Journal of Chemical Physics, vol. 43, pp. 3898-3905 (1965).
[27] Stanley H.E. *Introduction to phase transitions and critical phenomena*, Clarendon Press (1971).
[28] Klamut J., Durczewski K., Sznajd J., *Introduction to the physics of phase transition*, Zakład Narodowy im. Ossolińskich (in Polish), Wrocław (1978).
[29] Stanley H.E., *Scaling, universality and renormalization: three pillars of modern critical phenomena*, Reviews of Modern Physics, vol. 71, no. 2, pp. S358-S366 (1999).
[30] Sokalski K., Szczygłowski J., Najgebauer M., Wilczyński W., *Losses scaling in soft magnetic materials*, COMPEL: The International Journal for Computation and Mathematics in Electrical and Electronic Engineering, vol. 26, no. 3, pp. 640-649 (2007).
[31] Najgebauer M., *Scaling theory and its chosen applications in electromagnetism*, Przegląd Elektrotechiczny, vol. 84, no. 12, pp. 213-216 (2008).
[32] Najgebauer M., *Application of fractional scaling in modelling of magnetic power losses*, Acta Physica Polonica A, vol. 128, pp. 107-110 (2015).

[33] Gozdur R., Najgebauer M., *Measurements and scaling analysis of power losses in La-containing alloys*, Journal of Electrical Engineering, vol. 66, no. 7/s, pp. 37-40 (2015).
[34] Najgebauer M., *Scaling-based analysis and modelling of power losses in amorphous and nanocrystalline alloys*, Acta Physica Polonica A, vol. 131, no. 5, pp. 1125-1127 (2017).
[35] Najgebauer M., *The concept of scaling analysis in describing the properties of soft magnets*, Solid State Phenomena, vol. 220-221, pp. 646-651 (2015).
[36] Najgebauer M., Sokalski K., Szczygłowski J., *The modified scaling procedure in coercivity modelling*, Archives of Electrical Engineering, vol. 64, no. 3, pp. 351-359 (2015).
[37] Najgebauer M., *Fractional scaling of magnetic coercivity in electrical steels*, Acta Physica Polonica A, vol. 131, no. 4, pp. 633-635 (2017).
[38] Mayergoyz I.D., Adly A.A., Korman C., Huang M., Krafft C., *Scaling and data collapse in magnetic viscosity*, Journal of Applied Physics, vol. 85, pp. 4358-4360 (1999).
[39] Mayergoyz I.D., Adly A.A., Huang M.W., Krafft C., *Scaling and data collapse in magnetic viscosity (creep) of superconductors*, IEEE Transactions on Magnetics, vol. 36, no. 5, pp. 3208-3210 (2000).
[40] Adedoyin A., Andrei P., *Data collapse and viscosity in three-dimensional magnetic hysteresis modeling*, IEEE Transactions on Magnetics, vol. 44, no. 11, pp. 3165-3168 (2008).
[41] Takahashi S., Kobayashi S., Shishido T., *A scaling power-law relation in magnetic minor hysteresis loops in Fe and Ni metals*, Journal of Physics: Condensed Matter, vol. 20, pp. 035217/1-035217/6 (2008).
[42] Kobayashi S., Kikuchi N., Takahashi S., Kikuchi H., Kamada Y., *Scaling analysis of minor hysteresis loops in ferromagnets with large uniaxial anisotropy*, Journal of Magnetism and Magnetic Materials, vol. 322, no. 9-12, pp. 1515-1518 (2010).
[43] Kobayashi S., Tsukidate S., Kamada Y., Kikuchi H., Ohtani T., *Investigation of scaling laws in frequency-dependent minor hysteresis loops for ferromagnetic steels*, Journal of Magnetism and Magnetic Materials, vol. 324, no. 2, pp. 215-221 (2012).
[44] Kobayashi S., Takahashi S., Ishibashi Y., *Hysteresis scaling behavior in a remanent magnetization state*, IEEE Transactions on Magnetics, vol. 48, no. 4, pp. 3165-3168 (2012).
[45] Varga L.K., Kováč J., *Minor loop scaling rules for Finemet type soft magnetic cores*, Acta Physica Polonica A, vol. 126, pp. 156-157 (2014).

ARCHIVES OF ELECTRICAL ENGINEERING VOL. 66(2), pp. 433-446 (2017)

DOI 10.1515/aee-2017-0033

Surface Impedance Boundary Conditions applied to solving nonlinear electrodynamic systems

STANISŁAW PAWŁOWSKI, JOLANTA PLEWAKO

The Faculty of Electrical and Computer Engineering
Rzeszow University of Technology
Wincentego Pola 2, 35-959 Rzeszów, Poland
e-mail: {spawlo/jplewako}@prz.edu.pl

(Received: 28.03.2017, revised: 05.05.2017)

Abstract: The paper presents a method for solving electromagnetic field problems by applying impedance boundary conditions for systems including conducting bodies of nonlinear magnetic properties in an excited harmonic field. Three types of impedance boundary conditions were derived. A procedure for computing surface impedance based on the transfer matrix is proposed. This procedure has been tested by comparing computational results to calculations where time function distortions were considered, and to the experimental data.

Key words: nonlinear electrodynamics, Surface Impedance Boundary Conditions, harmonic fields, quasi-stationary fields, skin effect

1. Introduction

Surface Impedance Boundary Conditions (SIBC) have been successfully applied to solving electrodynamic problems for complex geometry systems (see e.g. [1-7], more extensive references on this subject can be found in [3]). SIBC are to be applied to systems where skin effect occurs. It is related to tangential components of the electric $\boldsymbol{E}$ and magnetic field $\boldsymbol{H}$ on the conducting surface being mutually normal, and their ratio, so called surface impedance, to be constant. Such dependencies allow to split electromagnetic field distribution calculations into separate, unrelated problems that can be formulated separately for each specific area of the system under consideration.

The basic requirements for effective SIBC application include electromagnetic penetration depth to be small in comparison to the curvature radius of the interface, and the field function to be only slightly variable along the tangents to these surfaces. Such conditions are easily satisfied in electromagnetic systems of high frequencies (e.g. radio frequencies). The skin effect is strongly pronounced there. Low frequency systems (e.g. power-line frequencies) may prove fairly compliant and eligible for SIBC application [4-7] – as well.

Commonly SIBC are developed for systems of linear and homogenous medium that is of constant electromagnetic parameters. Nevertheless, such an assumption does not provide prerequisites for developing SIBC [1]. Wherever analysed systems cover either inhomogeneous, or non-linear areas, it is still necessary to modify SIBC and the methodology for computing specific parameters, as presented in chapter 3 of this paper.

A general method for solving nonlinear, quasi-stationary problems of 3D electrodynamics with SIBC was proposed [8, 9, 11]. It is based on Fundamental Solutions Method (FSM). Magnetic field distribution is found iteratively as self-consistent distribution of the magnetic field at magnetically active surfaces (i.e. ferromagnetic) of magnetic permeability determined from the given magnetisation curve $\mu = \mu(H)$. Introductory numerical experiments performed for model problems confirmed the method to be correct and fairly convergent. However, only a simplified determination of SIBC parameters was assumed, specifically, while developing the formulas an assumption on linearity was made, and only a properly modified, local value for magnetic permeability based on the magnetisation curve were substituted into. Obviously, such an approach disregards e.g. the magnetic permeability dependence on the distance from the conductor surface, which may significantly contribute to errors. Therefore, the next step was to develop a more precise procedure for determining local surface impedance values [11].

The procedure made use of the transfer matrix concept and applied it to compute electromagnetic field distribution in the layer structures [10]. The skin area beneath the conductor surface divided into discreet elements, within which a constant (invariant in time) value, as of the magnetisation curve, for the magnetic permeability is assumed. It means that under a harmonic excitation field, the induced field functions are harmonic as well. Under such an assumption, the analysis of electrodynamic systems is much facilitated. It allows to disregard time dependence by introducing Maxwell equations in their complex form. Still, the problem arises how to determine a substitute magnetic permeability for particular elements of the skin layer. In this paper, the procedure reported elsewhere [11] has been completed by adding two methods for averaging the value of magnetic permeability.

Moreover, a way of considering an approximated magnetic hysteresis by applying a complex value for the magnetic permeability has been proposed [13, 14]. A series of numerical tests have been performed. Results have been compared both to the simulation results where field function distortions due to time dependences were included, and to the experimental results presented elsewhere [14].

2. Surface Impedance Boundary Conditions

2.1. A linear approach

As it was stated in the Introduction, SIBC are applicable where skin effect occurs, i.e. where the electromagnetic field penetrates not too deeply into the areas located under the conductive surface. It can be assumed that, for cases where such areas are significantly greater in size than the substitute field penetration depth (massive conductor cases), their internal electromagnetic field is limited to a thin layer under the surface, which is called a skin layer. The basic differential operations in such areas are presented in the Appendix.

By applying these formulas and as long as the assumption that all s_1, s_2 derivatives of the electromagnetic field components are negligible in comparison with their respective s_3 derivatives holds, a general relationship between the intensities of the electric and magnetic field at the conductor-dielectric boundary surface can be expressed as [1-3]:

$$\boldsymbol{n}\times\boldsymbol{E} = Z_c\boldsymbol{n}\times(\boldsymbol{n}\times\boldsymbol{H}), \tag{1}$$

where Z_c denotes surface impedance, $\boldsymbol{n}$ – stands for the unit vector perpendicular to the interface.

This relationship is called a surface impedance boundary condition (SIBC) and it means that both the electric $\boldsymbol{E}_t$ and magnetic $\boldsymbol{H}_t$ field components tangent to the boundary surface are mutually normal, and the ratio of their magnitudes:

$$Z_c = \frac{\boldsymbol{E}_t}{\boldsymbol{H}_t} \tag{2}$$

depends solely on the local properties of the adjacent areas, i.e. their electromagnetic parameters, and on the field frequency.

In the homogenous media of linear properties the surface impedance can be expressed by the formula [1-3]:

$$Z_c = \sqrt{\frac{\mathrm{j}\omega\mu}{\gamma+\mathrm{j}\omega\varepsilon}}, \tag{3}$$

where: μ, ε, γ and ω stand for magnetic permeability, permittivity, electric conductivity, and pulsation, respectively.

It shall be underlined here that neither homogeneity, nor linearity of the electromagnetic parameters of the areas, provides the necessary assumption while applying the condition (1) [3]. Nonetheless, dependence (3) does not hold for nonlinear media and the local Z_c magnitude should be then determined numerically. In chapter 3 a numerical procedure for determining Z_c for magnetically nonlinear media is provided. It is based on the transfer matrix approach.

Practical arrangements for applying SIBC numerically in a form (1) may prove troublesome, as all the components for $\boldsymbol{E}$ and $\boldsymbol{H}$ fields must be computed simultaneously. Fortunately, other more convenient SIBC formulation can be found, where parameters related to material properties and field frequency other than Z_c occur.

Below, three other SIBC representations for which fields need to be harmonic and quasi-stationary (i.e. for which the Maxwell displacement current is negligible) and conductive areas linear are presented [2-4, 8, 11]:

$$\boldsymbol{J} = \alpha\,\boldsymbol{n}\times\boldsymbol{H}, \tag{4}$$

$$\frac{\partial H_n}{\partial n} = -\beta H_n, \tag{5}$$

$$\overline{=}\Delta V_m = \beta\frac{\partial V_m}{\partial n}, \tag{6}$$

where: $\boldsymbol{J}$ stands for current density at the interface, V_m is the magnetic potential ($\boldsymbol{H} = -\,\mathbf{grad}\,V_m$), H_n – normal component of magnetic field, $\underline{\underline{\Delta}}$ – surface Laplacian (see (A10)),

$$\alpha = \sqrt{\mathrm{j}\omega\gamma\mu}\,, \tag{7}$$

$$\beta = \mu_0\sqrt{\frac{\mathrm{j}\omega\gamma}{\mu}}\,. \tag{8}$$

Though the above relationships result from condition (1), stable material parameters are assumed for their derivation. In the chapter that follows analogous dependencies are derived for SIBC in the nonlinear (applicable also to non-homogenous) systems.

2.2. Condition (4) for nonlinear systems

Due to $\boldsymbol{E}_t$ and $\boldsymbol{H}_t$ components being mutually normal, and from (2) it can be concluded that (1) can be rewritten in the form:

$$\boldsymbol{E}_t = Z_c\boldsymbol{n}\times\boldsymbol{H}\,. \tag{9}$$

Additionally, as the condition on the continuity for the tangent components of both electric and magnetic fields holds, clearly this dependence is correct on both sides of the interface, i.e. on the dielectric and conductor side alike. On the conductor side, i.e. within the skin layer, the normal component of the electric field does not occur [1], hence

$$\boldsymbol{E} = \boldsymbol{E}_t\,. \tag{10}$$

With the differential Ohm's law taken into consideration

$$\boldsymbol{J} = \gamma\,\boldsymbol{E} \tag{11}$$

and (20) (9) we arrive at

$$\boldsymbol{J} = \gamma\,Z_c\boldsymbol{n}\times\boldsymbol{H}\,. \tag{12}$$

By comparing (23) (12) to (15) (4) it may be concluded that the condition has taken on the form which is identical to the one for the linear case, as long as

$$\alpha = \gamma\,Z_c\,. \tag{13}$$

2.3. Condition (5) for nonlinear systems

Let us assumed that all the field components are sinusoidal functions of time. Though such an assumption does not hold for systems including media of nonlinear properties, the error due to such a simplification can be acceptable in electrodynamics. Comparisons of the computational data performed under such an assumption with computations where time dependent distortions in the time field function were taken into account confirmed this supposition. The conclusion was also supported with comparison of the experimental data [12] presented in chapter 4.

To obtain the sought relationships let us consider a certain neighbourhood of any point P within the thin layer area including the dielectric - conductor boundary surface (Fig. A1). The

thickness of this sector is assumed to be equal to 2η and to be large enough to include entire skin layer of the conducting area; it means that for $s_3 > \eta$ the field is negligible. Within the coordinate system s_1, s_2, s_3 introduced in the Appendix we have $\boldsymbol{n} = [0,0,1]$. By denoting

$$\boldsymbol{E} = [E_1, E_2, E_3], \quad \boldsymbol{H} = [H_1, H_2, H_3] \tag{14}$$

and making use of (9)

$$E_1 = Z_c H_2, \qquad E_2 = -Z_c H_1 . \tag{15}$$

Within the dielectric sector of the concerned area, as based on Faraday's law

$$\mathbf{rot}\,\boldsymbol{E} = -\mathrm{j}\omega\mu_0 \boldsymbol{H} . \tag{16}$$

By decomposing from (A8) the third component $\mathbf{rot}\boldsymbol{E}$

$$\frac{1}{h_1 h_2}\left(\frac{\partial}{\partial s_1}(h_2 E_2) - \frac{\partial}{\partial s_2}(h_1 E_1)\right) = -j\omega\mu_0 H_3 . \tag{17}$$

By substituting the dependence (15) to (17), with a few simple operations and applying (A9) and (A11)

$$Z_c \overline{\overline{\mathrm{div}}}\,\boldsymbol{H} + \boldsymbol{H} \cdot \overline{\overline{\mathbf{grad}}}\, Z_c = \mathrm{j}\omega\mu_0 H_3 . \tag{18}$$

According to (A7) and (A11)

$$\overline{\overline{\mathrm{div}}}\,\boldsymbol{H} = \mathrm{div}\,\boldsymbol{H} - \frac{\partial H_3}{\partial s_3} \tag{19}$$

and as $\mathrm{div}\,\boldsymbol{H} = 0$ for the dielectric area, so

$$\frac{\partial H_3}{\partial s_3} = -\frac{\mathrm{j}\omega}{Z_c} H_3 + \frac{1}{Z_c} \boldsymbol{H} \cdot \overline{\overline{\mathbf{grad}}}\, Z_c . \tag{20}$$

As s_3 represents the component normal to the boundary surface, finally

$$\frac{\partial H_n}{\partial n} = -\beta H_n + \frac{1}{Z_c} \boldsymbol{H} \cdot \overline{\overline{\mathbf{grad}}}\, Z_c , \tag{21}$$

where

$$\beta = \frac{\mathrm{j}\omega\mu_0}{Z_c} . \tag{22}$$

Relation (21) is a generalised SIBC (5) under the simplified assumptions for the electromagnetic field to be harmonic and quasi-stationary.

2.4. Condition (6) within a nonlinear approach

For quasi-stationary fields, within the dielectric part of the considered system a scalar magnetic potential can be introduced:

$$\boldsymbol{H} = -\mathbf{grad} V_m , \tag{23}$$

that satisfies Laplace's equation

$$\Delta V_m = 0 . \tag{24}$$

By substituting (23) to (20)

$$-\frac{\partial^2 V_m}{\partial s_3^2} = -\beta \frac{\partial V_m}{\partial s_3} - \frac{1}{Z_c} \mathbf{grad} V_m \cdot \overline{\overline{\mathbf{grad}}} Z_c \tag{25}$$

and on the base of (A6), (A10) and (24) observing that

$$\frac{\partial^2 V_m}{\partial s_3^2} = -\overline{\overline{\Delta}} V_m , \tag{26}$$

we arrive at the sought generalisation of SIBC for the scalar magnetic potential, namely

$$\overline{\overline{\Delta}} V_m = -\beta \frac{\partial V_m}{\partial n} - \frac{1}{Z_c} \overline{\overline{\mathbf{grad}}} V_m \cdot \overline{\overline{\mathbf{grad}}} Z_c , \tag{27}$$

with β derived as in formula (22) (33).

3. Procedure for computing surface impedance

Applying SIBC formulas (1), (12), (21), and (27) to solving electromagnetic field problems in systems including conducting areas of nonlinear magnetic properties the surface impedance Z_c distribution at the boundary surfaces for these areas is required to be known. However, local magnitude of Z_c is known to depend on the magnetic permeability, which in turn depends on the magnetic field intensity. Therefore, the procedures for determining Z_c and computing field distribution need to be interrelated. A transfer matrix method based concept for numerical procedure to compute surface impedance was presented elsewhere [10, 11]. Further in this chapter a brief summary of it, completed with some significant supplements is provided.

Accordingly to the assumptions made earlier, within the conducting sector of the system under consideration the area where electromagnetic field occurs is limited to the skin layer beneath the boundary surface (see Fig. 1). The relation $\mu = \mu(H)$ for this area is assumed to be known. The relationship is assumed to be unique, though μ can be also a complex value, which allows to incorporate an approximated magnetic hysteresis effect [12, 13].

The first step of the proposed procedure is discretization by dividing of the skin layer on the surfaces being parallel and perpendicular to the interface, into small volume elements $\Omega_{i,j,k}$, as shown in Fig. 1. Magnetic permeability within the element is assumed to be constant (the

distribution of magnetic permeability is approximated by the step function). It shall be noticed here that under the assumption made earlier, the field is variable, and consequently also magnetic permeability variations are much more pronounced along the normal direction than along the directions tangent to the surface, and thus the elements width d_k, (compare Fig. 1) shall be respectively smaller than their dimensions along the directions s_1, s_2.

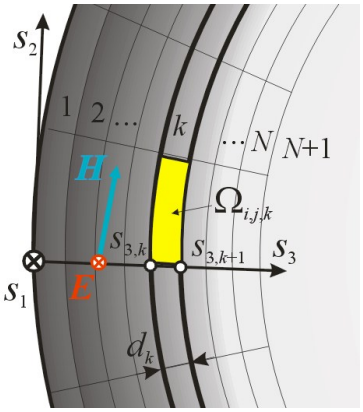

Fig. 1. Skin layer area – illustrated method for computing surface impedance; i, j, k means numbering indices in directions s_1, s_2, s_3 (respectively)

With no limitations to the generality of the considerations it can be assumed that within the selected element axis s_1 is parallel to the vector $\boldsymbol{E}$, thus

$$\boldsymbol{E} = [E_1, 0, 0], \qquad \boldsymbol{H} = [0, H_2, H_3]. \tag{28}$$

With such assumptions, the electromagnetic field components in the element $\Omega_{i,j,k}$ (see Fig. 1) can be approximated with the functions listed below (to further simplify the notation, indexes i, j are ignored).

$$E_{1,k} = E^{+}_{1,k}(s_1, s_2)e^{-\alpha_k(s_3 - s_{3,k})} + E^{-}_{1,k}(s_1, s_2)e^{\alpha_k(s_3 - s_{3,k})}, \tag{29}$$

$$H_{2,k} = H^{+}_{2,k}(s_1, s_2)e^{-\alpha_k(s_3 - s_{3,k})} + H^{-}_{2,k}(s_1, s_2)e^{\alpha_k(s_3 - s_{3,k})}, \tag{30}$$

$$H_{3,k} = H^{+}_{3,k}(s_1, s_2)e^{-\alpha_k(s_3 - s_{3,k})} + H^{-}_{3,k}(s_1, s_2)e^{\alpha_k(s_3 - s_{3,k})}, \tag{31}$$

where $s_{3,k}$ denotes the initial coordinate of the k^{th} sector (compare Fig. 1),

$$\alpha_k = \sqrt{\mathrm{j}\omega\gamma\mu_{i,j,k}}\ ,\ \mu_k$$

is substitute magnetic permeability of Ω_k element. To further simplify the notation, indexes i, j are ignored.

According to Faraday's law the following relations are obtained

$$\frac{E^{+}_{1k}}{H^{+}_{2k}} = -\frac{E^{-}_{1k}}{H^{-}_{2k}} = Z_k = \sqrt{\frac{\mathrm{j}\omega\mu_k}{\gamma}}, \tag{32}$$

$$H_{3k}^{+} = \frac{1}{\mathrm{j}\omega\mu_k}\left(\frac{\partial E_{1k}^{+}}{\partial s_2} - \frac{\partial E_{2k}^{+}}{\partial s_1}\right), \tag{33}$$

$$H_{3k}^{-} = \frac{1}{\mathrm{j}\omega\mu_k}\left(\frac{\partial E_{1k}^{-}}{\partial s_2} - \frac{\partial E_{2k}^{-}}{\partial s_1}\right). \tag{34}$$

Due to continuity conditions for the tangent components of the electric and magnetic fields, $\boldsymbol{E}$ and $\boldsymbol{H}$, respectively at the boundary between the sectors k and $k + 1$, it can be shown that [10, 11]

$$\begin{bmatrix} E_{k+1}^{+} \\ E_{k+1}^{-} \end{bmatrix} = \boldsymbol{M}_k \begin{bmatrix} E_{k}^{+} \\ E_{k}^{-} \end{bmatrix}, \tag{35}$$

where

$$\mathbf{M}_k = \frac{1}{2}\begin{bmatrix} (1+\lambda_k)e^{-\alpha_k d_k} & (1-\lambda_k)e^{\alpha_k d_k} \\ (1-\lambda_k)e^{-\alpha_k d_k} & (1+\lambda_k)e^{\alpha_k d_k} \end{bmatrix}, \tag{36}$$

$$\lambda_k = \frac{Z_{k+1}}{Z_k}. \tag{37}$$

The relation between the electric field amplitude in the first layer and beyond the last one, i.e. within the area $k = n + 1$ – (see Fig. 1) can be written as:

$$\begin{bmatrix} E_{1,n+1}^{+} \\ E_{1,n+1}^{-} \end{bmatrix} = \boldsymbol{P} \begin{bmatrix} E_{1,1}^{+} \\ E_{1,1}^{-} \end{bmatrix}, \tag{38}$$

where

$$\boldsymbol{P} = \boldsymbol{M}_n \boldsymbol{M}_{n-1} \,..\, \boldsymbol{M}_1 = \begin{bmatrix} p_{11} & p_{12} \\ p_{21} & p_{22} \end{bmatrix} \tag{39}$$

is the transfer matrix for the entire skin layer. By neglecting within the $n + 1$ area the wave incident onto the coordinate s_3, then with (32) and (39) it is obtained [11]:

$$\left.\frac{E_{1,1}}{H_{2,1}}\right|_{s_3=0} = Z_c = Z_1 \frac{p_{22} - p_{21}}{p_{22} + p_{21}}. \tag{40}$$

According to the description provided above the procedure for computing Z_c comes down to computing the $\boldsymbol{P}$ matrix, which is a simple product of 2nd rank matrices (see formula (39)). Still, for nonlinear cases $\boldsymbol{M}_k$ matrix elements cannot be directly computed, as it is necessary to know

local magnetic permeability μ_k values, which are dependent on the magnetic field distribution to be computed. Therefore, the concerned procedure has to be linked with another procedure (e.g. FEM, BEM, FSM – see [8, 9, 11]) for computing the electromagnetic field distribution within the dielectric area under the SIBC condition set at the boundary surfaces. Such a concept as well as the results of introductory numerical tests were reported elsewhere [8, 9, 11]. It consists in iterative finding electromagnetic field distribution that is self-consistent with the surface impedance distribution at the conducting sectors surfaces of the considered system. At each iteration step a linear problem is solved. That allows to compute approximately the field distribution, and based on that, to determine Z_c distribution required for the next step of computations.

The very procedure for computing local Z_c magnitudes is also of iterative nature. At each iteration matrices $\boldsymbol{M}_k$ are computed according to formula (36) for μ_k values computed in the preceding iteration. Then the field distribution within the skin layer is computed from formulas (29) – (31), and in turn μ_k magnitudes for the next iteration are computed from $\mu = \mu(H)$ relation. The process is repeated until the magnetic field distribution within the skin layer is consistent with the magnetic permeability distribution (i.e. in each element Ω_k the dependence between μ_k and H follows the magnetisation curve with the acceptable accuracy). The iteration starts with constant values for μ_k.

It is crucial to find the values for μ_k in the skin layer elements. As instantaneous magnitude for absolute value of magnetic field intensity varies in time, instantaneous values for magnetic permeability can be also significantly variable, though to simplify the problem μ_k is treated as invariable in time. Thus, a problem arises how to set the appropriate value for μ_k. Three approaches to determine μ_k seem most natural, namely

– directly from the magnetisation curve based on the magnetic field amplitude

$$\mu_k = \mu(H_m), \tag{41}$$

where H_m corresponds to the magnetic field amplitude in the central point of the k^{th} element of the skin layer,

– by averaging the $\mu = \mu(H)$ function

$$\mu_k = \frac{1}{H_m}\int_0^{H_m} \mu(H)\mathrm{d}H, \tag{42}$$

– by averaging over time

$$\mu_k = \frac{2}{T}\int_0^{T/2} \mu(H_m \sin\omega t)\mathrm{d}t = \frac{1}{\pi}\int_0^{\pi} \mu(H_m \sin\varphi)\mathrm{d}\varphi. \tag{43}$$

The next chapter deals with numerical experiments where all the above approaches to determine μ_k values were taken into consideration.

4. Verification of the method

Introductory numerical test results for the provided method for determining surface impedance were presented elsewhere [11]. The procedure was found to converge effectively. After a few iterations the magnetic field distribution was found convergent with the magnetic permeability distribution within the skin layer. However, due to assumed simplification, as well as with regard to the options applicable while determining μ_k values, a comparison of the results to computations where distortions from the time dependencies had been considered, as well as to experimental measurements would prove essential. Such results were reported in another paper [12] where the problem of finding electromagnetic field distribution within the conductive half-space of nonlinear magnetic properties was considered. Though the magnetic hysteresis effect had not been taken into account there, the distortions from the time dependencies were considered. The finite difference method computations allowed to determine such relations as active power losses as a function of magnetic field intensity on the boundary surface. The results were also set against experimental measurements. It shall be highlighted that unit power loss can be directly related to the surface impedance with

$$P = \frac{1}{2}\mathrm{Re}\left(Z_c\right)H_0^2, \tag{44}$$

where H_0 stands for the magnetic field strength at the boundary surface. In Fig. 2 curves denoted as 1, 2, 3 are reproduced from [12]. Discrepancies between the experimental curve no 1 and the computed one (no 3) were attributed to hysteresis losses not considered in the computations.

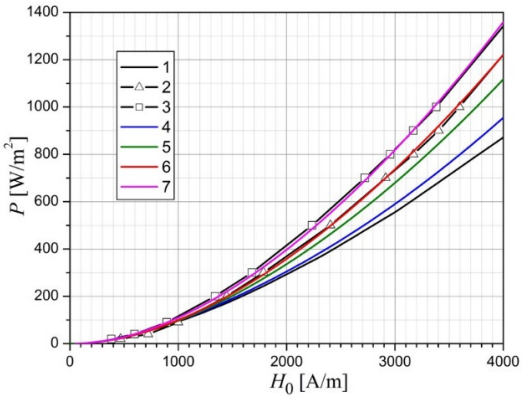

Fig. 2. Unit power losses in the conductive half-space; 1 is a curve where constant magnetic permeability was assumed (as reported by [12]), 2 is a computation curve where time function distortion were considered (as reported by [12]), 3 is the measurement curve (as reported by [12]), 4, 5, 6 are computation curves where time function distortion were disregarded and obtained for formulas (41), (42), (43), respectively, 7 is the curve for applied formula (42) with a complex magnetic permeability for ψ = 14 degrees (compare (45))

The remaining curves in Fig. 2 represent the results obtained with the computation procedure for determining surface impedance provided hereby with the formula (44). Curves no 4, 5, and 6 represent various approaches to selecting the substitute magnetic permeability (formulas (41)-(43)). A computation curve reported in [12] was closely followed by our curve for which average magnetic permeability was applied according to the formula (42) (curve no 5).

The hysteresis losses can be incorporated by applying a complex magnetic permeability [13, 14], i.e. the hysteresis curve approximated with an elliptical curve as follows:

$$\underline{\mu} = \mu e^{j\psi} . \tag{45}$$

As the paper [12] does not provide the hysteresis loop for the material for which experimental measurements had been performed, it was not possible to fully verify our method applicability to this case. Nevertheless, we managed to test compatibility of the measurement curve no 1 with our results, and prove it to be the highest for the approach where averaging magnetic permeability followed formula (42) with $\psi = 14$ degrees (curve no 7).

5. Summary

A method for solving electromagnetic field problems by applying impedance boundary conditions is presented in the paper for systems including conducting bodies of nonlinear magnetic properties in an excited harmonic field. Nonlinear properties of the conducting areas cause the real field time functions to depart from their clear sinusoidal patterns, which increases difficulty of solving. We have proposed a method where a simplified assumption is made for the distortions from proper time functions to be disregarded. The resulting error could fall within the range acceptable for typical technical systems in electrodynamics. An obvious advantage such an assumption brings is applicability of time independent Maxwell equations for complex fields.

With the assumption made valid, three types of impedance boundary conditions were derived (see formulas (12), (21), (27)) which provided generalised SIBC in linear systems. To apply them surface impedance distribution is to be known at the conductor – dielectric boundary surfaces of the system under consideration. Therefore, a procedure for computing this quantity based on the transfer matrix is proposed. The proposed procedure has been tested by comparing computational results to computations where time function distortions were considered, and to the measurements data reported elsewhere [12].

Based on the performed comparison the following conclusions were drawn:

– Accuracy of the presented procedure is highly dependent on the option for determining substitute magnetic permeability for the skin layer elements of the system (see the differences between the curves 4, 5, and 6 in Fig. 2).

– By applying averaged magnetic permeability according to formula (42) high compatibility with the results with distortions from time dependencies considered was reached.

– By applying a complex magnetic permeability, high compatibility with the measurements was achieved.

Nevertheless, it should be noted here that scarcity of the comparative material prevents us from announcing conclusions as final. Comparison of results obtained for the provided method with detailed experimental results for various types of magnetic materials would prove particularly useful.

Appendix. Differential operations within thin-layer areas

In this chapter formulas for basic differential operations within thin-layer areas are presented. The thin-layer area of a width of 2η contains all the points whose distance to the specific surface S is either equal to η, or smaller (Fig. A1). It is assumed, that η is significantly smaller than the curvature radius of the surface S at each of its points.

Then, at the surface S an orthogonal coordinate system s_1, s_2 is introduced. Any P point of the thin layer area can be defined with s_1, s_2 coordinates of its orthogonal projection to the surface S and s_3 coordinate, which is the distance from point P to the considered surface (see Fig. A1).

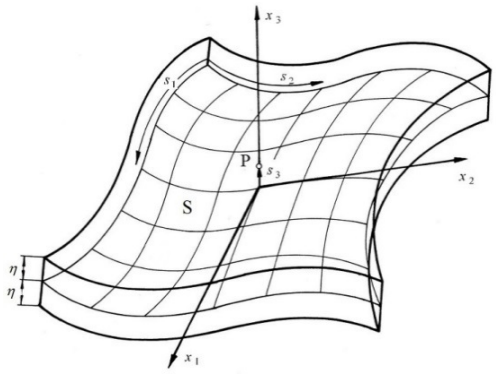

Fig. A1. A thin-layer area

Lamé coefficients for any curvilinear coordinate system s_1, s_2, s_3 can be expressed with the formula [15]

$$h_i = \sqrt{\sum_{j=1}^{3}\left(\frac{\partial x_j}{\partial s_i}\right)}, \quad i = 1, 2, 3, \tag{A1}$$

where

$$x_i = x_i(s_1, s_2, s_3) \tag{A2}$$

are the interrelations between coordinate s_i and any Cartesian coordinate system x_1, x_2, x_3. The magnitudes h_i, as the lengths of certain vectors, namely the ones tangent to the appropriate coordinate lines, are not dependent on any selected Cartesian system.

To determine Lamé coefficients for the coordinate system defined above let us consider a small thin layer sector within the neighbourhood of any point P. The Cartesian coordinate system x_i is selected to make x_1 and x_2 axes tangent to the surface S, and x_3 axes to cross the P point (see Fig. A1). It can be then safely assumed that within the concerned sector coordinates x_1 and x_2 are practically independent of the coordinate s_3, i.e. the depth at which point P is located, hence

$$x_1 = x_1(s_1, s_2), \qquad x_2 = x_2(s_1, s_2), \qquad x_3 = s_3, \tag{A3}$$

which when substituted with (1) allows to arrive at

$$h_1 = h_1(s_1, s_2), \qquad h_2 = h_2(s_1, s_2), \qquad h_3 = s_3. \tag{A4}$$

By considering general relations determining basic differential operations for any scalar field φ and a vector field $\boldsymbol{V}$ in the orthogonal curvilinear coordinate system [15], and by applying (A4):

$$\mathbf{grad}\varphi = \left[\frac{1}{h_1}\frac{\partial\varphi}{\partial s_1}, \frac{1}{h_2}\frac{\partial\varphi}{\partial s_2}, \frac{\partial\varphi}{\partial s_3}\right], \tag{A5}$$

$$\Delta\varphi = \frac{1}{h_1 h_2}\left(\frac{\partial}{\partial s_1}\left(\frac{h_2}{h_1}\frac{\partial\varphi}{\partial s_1}\right) + \frac{\partial}{\partial s_2}\left(\frac{h_1}{h_2}\frac{\partial\varphi}{\partial s_2}\right)\right) + \frac{\partial^2\varphi}{\partial {s_3}^2}, \tag{A6}$$

$$\mathrm{div}\boldsymbol{V} = \frac{1}{h_1 h_2}\left(\frac{\partial}{\partial s_1}(h_2 V_1) + \frac{\partial}{\partial s_2}(h_1 V_2)\right) + \frac{\partial V_3}{\partial s_3}, \tag{A7}$$

$$\mathbf{rot}\boldsymbol{V} = \left[\frac{1}{h_2}\frac{\partial V_3}{\partial s_2} - \frac{\partial V_2}{\partial s_3}, \quad \frac{\partial V_1}{\partial s_3} - \frac{1}{h_1}\frac{\partial V_3}{\partial s_1}, \quad \frac{1}{h_1 h_2}\left(\frac{\partial}{\partial s_1}(h_2 V_2) + \frac{\partial}{\partial s_2}(h_1 V_1)\right)\right]. \tag{A8}$$

As point P has been freely selected, the relations [A5-A8] for the coordinate system under consideration are correct within the entire thin layer sector.

The following surface differential operators are used in the paper:

– surface gradient

$$\overline{\overline{\mathbf{grad}}}\varphi = \left[\frac{1}{h_1}\frac{\partial\varphi}{\partial s_1}, \frac{1}{h_2}\frac{\partial\varphi}{\partial s_2}, 0\right], \tag{A9}$$

– surface Laplacian

$$\overline{\overline{\Delta}}\varphi = \frac{1}{h_1 h_2}\left(\frac{\partial}{\partial s_1}\left(\frac{h_2}{h_1}\frac{\partial\varphi}{\partial s_1}\right) + \frac{\partial}{\partial s_2}\left(\frac{h_1}{h_2}\frac{\partial\varphi}{\partial s_2}\right)\right), \tag{A10}$$

– surface divergence

$$\overline{\overline{\mathrm{div}}}\boldsymbol{V} = \frac{1}{h_1 h_2}\left(\frac{\partial}{\partial s_1}(h_2 V_1) + \frac{\partial}{\partial s_2}(h_1 V_2)\right). \tag{A11}$$

References

[1] Leontovich M.A., *On the approximate boundary conditions for the electromagnetic field on the surface of well conducting bodies*, Investigations of Radio Waves, Academy of Sciences of USSR, Moscow (1948).

[2] Senior T.B.A., Volakis J.L., *Approximate Boundary Conditions in Electromagnetics*, The Institution of Electrical Engineers, London (1995).

[3] Yuferev S., Ida N., *Surface Impedance Boundary Conditions. A comprehensive approach*, CRC Press (2010).

[4] Kaźmierski M., Pawłowski S., *Practical application of integral equations for calculation of transformer leakage field*, Archives of Electrical Engineering, vol. 45, no. 3, pp. 251-261 (1996).
[5] Lin L., Xiang C., *Losses Calculation in Transformer Tie Plate Using the Finite Element Method*, IEEE Transactions on Magnetics, vol. 34, no. 5 (1998).
[6] Higuchi Y., Koizumi M., *Integral Equation Method with Surface Impedance Model for 3D Eddy Current Analysis in Transformers*, IEEE Transactions on Magnetics, vol. 36, no. 4 (2000).
[7] Pawłowski S., *Analysis of Leakage Field in Power Transformers with Use of Boundary-Iterative Method*, WSEAS Transactions on Circuits and Systems, vol. 11, no. 4, pp. 1620-1627 (2005).
[8] Apanasewicz S., Pawłowski S., Plewako J., *Application of an iterative method of fundamental solutions for the analysis of quasi-stationary electromagnetic field in the presence of non-linear magnetic bodies*, Przeglad Elektrotechniczny (in Polish), vol. 89, no. 11, pp. 304-308 (2013).
[9] Apanasewicz S., Pawłowski S., Plewako J., *Analysis for quasi-stationary electromagnetic field with ferromagnetic objects present within*, Przeglad Elektrotechniczny, vol. 89, no. 12, pp. 169-173 (2013).
[10] Pawłowski S., Plewako J., *The matrix method of calculating the parameters of multilayer electromagnetic screens*, Przeglad Elektrotechniczny, vol. 91, no. 12, pp. 185-188 (2015).
[11] Pawłowski S., Plewako J., *Analysis of nonlinear problems in electrodynamics by means of surface impedance boundary conditions* (*SIBC*) *combined with transfer matrix method*, in IEEE Selected Issues of Electr. Engineering and Electronics (WZEE) (2016), DOI: 10.1109/WZEE.2016.7800192.
[12] Zakrzewski K., *Determination of electromagnetic field in solid iron with application of digital method*, Archives of Electrical Engineering, vol. 18, no. 3, pp. 569-585 (1969).
[13] Zakrzewski K., *Berechnung der Wirk- und Blindleistung in einem ferromagnetischen Blech unter Berücksichtigung der komplexen magnetischen Permeabilität*, Wiss. Z. TH Ilmenau, vol. 5, no. 16, pp. 101-105 (1970).
[14] Zakrzewski K., Kuśmierek Z., *Analytic sensitiveness of power losses in electrical steels on an accuracy of determination of the elliptic hysteresis angle*, Przeglad Elektrotechniczny (in Polish), vol. 2, no. 80, pp. 96-99 (2004).
[15] Trajdos T., *Engineers Handbook. Mathematics* (in Polish), PWN Warszawa (1986).

70th Anniversary of the Faculty of Electrical Engineering of the West Pomeranian University of Technology, Szczecin

KRZYSZTOF OKARMA, PAWEŁ DWORAK, MARCIN WARDACH

Faculty of Electrical Engineering
West Pomeranian University of Technology, Szczecin

Dean's foreword

This paper presents a short story of 70 years of existence of the Faculty of Electrical Engineering in Szczecin. Starting from 1947 as one of 3 faculties founded at the Engineering School in Szczecin, it became, as a result of the school transformation in 1955, one of six Faculties of Technical University of Szczecin. Since 2009, after merging with Agricultural University, our Faculty is one of 10 faculties of the West Pomeranian University of Technology, Szczecin.

At present, we teach students in three fields of study: *Electrical Engineering*, *Automatic Control and Robotics* as well as the *Information and Communication Technology* (*ICT*) with the 1st (engineering) and the 2nd (master) degrees for all three fields of study. Quality of education has been confirmed by the institutional evaluation of the Polish Accreditation Commission which has distinguished two categories: development strategy as well as material and human resources. Close relationships with industrial partners allow flexible adaptation of our study programs to the needs of industry and dynamic progress of technology. One of the methods used to achieve this goal is the Industry-Program Council of the Faculty founded in 2009 as one of the first such structures in our region.

We have educated over 8500 graduates so far, employed by various companies and public administration, not only in our region. Currently the Faculty employs over 80 members of academic staff, including 11 professors, 8 associate professors and 6 assistant professors with habilitation degree and has over 1000 students. A high level of scientific research has been confirmed by the Committee for the Evaluation of Scientific Units awarding the Faculty with the "A" category in 2013. Our Faculty has the full academic rights in two scientific disciplines, with doctoral studies as well, and is authorized to confer Ph.D. and habilitation (D.Sc.) degrees in *Electrical Engineering* as well as in *Automatic Control and Robotics*.

In 2017 we are celebrating the 70th Anniversary of our Faculty. Apart from the main celebrations on May 20th together with a picnic and alumni meeting, there are some accompanying events organized as well, such as conferences and special scientific sessions.

Ph.D., D.Sc. Eng. Krzysztof Okarma, Assoc. Prof. – Faculty Dean

1. The origins of the Faculty of Electrical Engineering

Immediately after World War II, the society and the authorities of Szczecin realized that in the face of the lack of cadres with higher education, preparations should be made as soon as possible to set up a higher school in this city, which should educate the highly needed specialists. In Szczecin before World War II there was no university providing higher education. There was, however, State Technical University of Ship Builders and Ship Engineers (*Vereinigte Technische Staatslehranstalten für Schiffsingenieure und Seemaschinisten zu Stettin*) currently located in the building at Sikorskiego 37 Street.

The Faculty of Electrical Engineering was established on the basis of an official act of the Minister of Education on January 20th, 1947, formally establishing the University on December 1st, 1946. At that time, the School consisted of three faculties: Electrical, Mechanical and Civil Engineering, and M.Sc. Ryszard Bagiński was appointed its Director. Shortly afterwards, the two further faculties were set up: Chemical and Architecture.

The rise, formation and development of the Faculty was strongly connected with the organization of electricians in the Szczecin Branch of the Association of Polish Electricians (SEP) – the activities of its first three presidents – Jan Słomiński, Zygmunt Paryski and Witold Gładysz left an indelible mark on the history pages of the Faculty.

After a short period of dynamic development, the central authorities (regulation of Minister of Higher Education dated 31.12.1952) established the organizational structure of the faculty comprising four departments and decided to liquidate the telecommunication as a field of study and additionally limit the number of specialties in the energy field. This caused already recognized specialists to leave the Department.

2. Faculty of Electrical Engineering at the Technical University of Szczecin

On September 1st, 1955, the Council of Ministers upgraded the Engineering School to Technical University of Szczecin. Unfortunately, 15 years later, due to the ongoing personnel crisis, the Ministry of Education and Higher Education reorganized the University transforming the Faculty into the Electrotechnical Institute with the rights of a faculty. Nevertheless, in a short time, due to the tremendous efforts of the community, this situation was changed and the Institute obtained the rights to confer the doctorate degrees starting from December 1971.

The Institute of Automation started functioning on 23.01.1973 and thus the Faculty of Electrical Engineering, composed of two institutes, was reactivated. The third one – Institute of Electronics and Computer Science was established on September 1st, 1989 and another independent unit – Department of Theoretical Electrical Engineering and Computer Science – was established on November 12th, 1990. At the beginning of 2000 the Department of Signal Processing and Multimedia Engineering separated from the Institute of Electronics, Telecommunications and Computer Science. Both these Departments continue to operate to this day.

In June 2002, the Faculty of Electrical Engineering obtained full academic rights in the discipline of electrical engineering. This enabled the Faculty to launch a doctoral program, transferred from the Faculty of Mechanical Engineering in February 2003, which allowed Ph.D. students to defend their dissertations in electrical engineering. The first graduate from this group of people defended his doctoral dissertation on April 3rd, 2003.

The dynamic scientific development of the staff during this period resulted also in the rights to confer the degree of doctorate in the discipline of automatic control and robotics (since 2004).

(a) (b)

Fig. 1. The two buildings of the Faculty of Electrical Engineeging: at 37 Sikorskiego Street – before the Second World War (a) and at number 10 on 26 Kwietnia Street in the 1980's (b)

3. Faculty at the West Pomeranian University of Technology, Szczecin

Under the Act of 5 September 2008 on the establishment of the West Pomeranian University of Technology, Szczecin (ZUT), our Faculty became one of the ten faculties of the new university, created by merging Szczecin University of Technology and the University of Agriculture in Szczecin, and starting its activity on January 1st, 2009.

On January 25th, 2010, our Faculty has obtained the rights to confer doctoral degree in automatic control and robotics. This achievement, having regard to the number of teaching and research staff, has led to the inclusion of the Faculty among a small number of units of this size having full academic rights in two disciplines. It contributed both to the development of academic staff in this discipline as well as to the further extension of the didactic offer for second degree studies in the aforementioned field of ICT, whose graduates acquire knowledge, skills and competencies covering selected topics from three disciplines: computer science, telecommunications as well as automation and robotics.

Literally a few days after obtaining these rights, on January 31st, 2010, the organizational structure of the Faculty has also changed. The institutes of Industrial Automation, Electronics and Telecommunications and Electrical Engineering were abolished and a department based structure consisting of 6 new departments (chairs) has been created in addition to the two existing ones. The youngest unit in the Faculty is the Department of Applied Computer Science established on 1.11.2012.

Changing the organizational structure and gaining habilitation rights in the second discipline coincided in time with scientific advancements, in particular of young workers who have obtained habilitation degrees. During that period, this degree was awarded to 11 faculty members. Three grades have been obtained in accordance with a pre-existing procedure, including habilitation colloquium, whereas one of the doctors was habilitated at Częstochowa University of Technology. Among the habilitations conferred by our Faculty the employees have obtained 5 degrees in the discipline of *Electrical Engineering* and 5 in *Automatic Control and Robotics*. This allowed to significantly rebuild the scientific staff, drained in the last few years by retirements and unfortunately deaths of some professors.

At present, the Faculty of Electrical Engineering employs about 80 academic teachers, including 11 with a professor title and 14 with a habilitation degree. As one of four out of 10 faculties of the West Pomeranian University of Technology, Szczecin, it holds the "A" category in the evaluation of the Committee for Evaluation of Scientific Units. In 2013, the Faculty received a positive institutional assessment of the Polish Accreditation Commission (PKA), with distinctions in two areas (for the development strategy as well as material, financial and human resources).

The priority areas of research conducted at the Faculty of Electrical Engineering, adopted by a resolution of the Faculty Council, include:

– non-destructive testing using electromagnetic methods,
– innovative technologies for the processing, transmission and use of energy,
– high-voltage engineering and diagnostics,
– modeling and management of technical and biological systems,
– real-time diagnostics and control systems,
– photonics and optoelectronics in technology, biomedicine and telecommunications,
– exploration, processing and transmission of signals and data,
– processing and analysis of images in technology and biomedicine.

(a) (b)

Fig. 2. The two buildings of Faculty of Electrical Engineeging at present: at 37 Sikorskiego Street (a) and at number 10 on 26 Kwietnia Street (b)

Since 1994 our Faculty is also the organizer of one of the largest regional scientific events in Europe related to automatic control and robotics, namely *International Conference on Auto-*

mation and Robotics (MMAR) held each year, usually in the Międzyzdroje resort, under the patronage of *IEEE Robotics & Automation Society, IEEE Control Systems Society, International Federation of Automatic Control* (IFAC) and *Committee on Automatic Control and Robotics of the Polish Academy of Sciences*. MMAR conference proceedings appear on the IEEE Xplore platform and are indexed in major global databases: Web of Science (CPCI), Scopus or dblp.

Recent years also include the development of the Faculty's didactic and laboratory base. The most visible part of it is putting into use in 2014 a new part of the building on 26 Kwietnia Street with modern science and didactic laboratories and the Auditorium named after Prof. Stanisław Skoczowski. It is a modern conference and training facility consisting of 3 rooms, together with 533 places, being the largest of its kind in Szczecin universities, with a spacious foyer with a unique gallery of the Szczecin branch of the Union of Artist Photographers of Poland (ZPAF).

Fig. 3. Auditorium named after Prof. Stanisław Skoczowski inside

4. Study offer and cooperation with industry partners

Currently, the Faculty of Electrical Engineering conducts three-cycle studies in the fields of *Automatic Control and Robotics* and *Electrical Engineering* and two-cycle in the field of ICT. The *Electrical Engineering* studies have been conducted since the beginning of the Faculty, the field of *Automatic Control and Robotics* since 1994, and the youngest ICT from 2011, currently also as second cycle studies, with its first graduates in 2017.

In 2009 the Council of the Faculty of Electrical Engineering established the Industry-Program Council of the Faculty and approved its statute. As the first such collegiate structure at the University and in the region, it consists of representatives of leading companies and enterprises in the region from industry sectors related to automation, electronics, electrical engineering, information technology and telecommunications, as well as representatives of the Department and the local authorities. It is also worth emphasizing that the activities of the

Council contributed to the development and improvement of the didactic offer of the Faculty, mentioned above, including the new field of study – ICT (*Teleinformatics*), established as the third in the country after the Wrocław University of Technology and the UTP University of Science and Technology in Bydgoszcz. Currently, the ICT studies gain popularity also in other technical universities e.g. AGH University of Science and Technology in Cracow, Silesian University of Technology or Poznan University of Technology.

Parallel to the operation of the Industry-Program Council, the Faculty cooperates closely with industrial partners, being also active in international cooperation. The results can be observed as the increasing number of international students within the Erasmus + programme as well as increasing number of international scientific projects conducted in cooperation with industrial partners.

Current cooperation with industry allows us to make the study programs more attractive, including the possibility to gain the industrial certificates by our students e.g. under the Samsung Labo course, Siemens Academy or National Instruments LabVIEW Academy. Some other certificates can also be obtained after chosen classes e.g. issued by ASTOR Infel and Bernecker&Rainer companies. The Faculty closely cooperates also with partners from the ICT industry such as Tieto (founded by one of our professors as RTS Networks company), brightONE, GlobalLogic, Apptimia or AVID Technology Poland. Automatic control and robotics is supported additionally by DGS Company, HIAB Cargotec Poland, and recently also AMPER, Kongsberg Maritime and Sonion. Examples of typically electrical companies cooperating with our Faculty are ENEA, TWN or Schneider Electric Energy Poland with a strong support from the Association of Polish Electricians (SEP).

Most of the companies mentioned above support the organization of the 70th Anniversary of the Faculty of Electrical Engineering taking place on May 20th, 2017. The whole event, apart from its official part, consists of alumni meeting and an open air family picnic with the possibility of visiting the older and newer fragments of both our buildings as well as to participate in school reunions, games and competitions for youth and discussions with our industrial partners illustrated by music, i.e. performed by our unique student's music band.

5. Conclusions

The Faculty of Electrical Engineering in Szczecin after 70 years is one of the most relevant faculties of the West Pomeranian University of Technology, Szczecin. Despite its average size, both in terms of number of students and staff, it can be considered as scientifically efficient and effective. Facing new challenges posed by changing external conditions, observing the great involvement of the vast majority of Faculty members, we can look with optimism to the future development of our Faculty.

ARCHIVES OF ELECTRICAL ENGINEERING

SPONSORS

Polish Academy of Sciences

**Faculty of Electrical Engineering,
Poznan University of Technology**

THE AEE JOURNAL IS ALSO CO-SPONSORED BY

Faculty of Electrical, Electronic,
Computer and Control Engineering,
Lodz University of Technology

Faculty of Electrical Engineering,
Automatic Control and Informatics,
Opole University of Technology

Faculty of Electrical and Computer Engineering,
Krakow University of Technology

Faculty of Electrical and Computer Engineering,
Rzeszow University of Technology

Faculty of Electrical Engineering,
West Pomeranian University of Technology, Szczecin

Faculty of Electrical Engineering,
Automatics, Computer Science
and Biomedical Engineering, AGH-UST